2019

# Coupled Thermal-Hydrological-Mechanical-Chemical Processes In Geothermal And Shale Energy Developments

Arash Kamali-Asl
*University of Vermont*

# COUPLED THERMAL-HYDROLOGICAL-MECHANICAL-CHEMICAL PROCESSES IN GEOTHERMAL AND SHALE ENERGY DEVELOPMENTS

A Dissertation Presented

by

Arash Kamali-Asl

to

The Faculty of the Graduate College

of

The University of Vermont

In Partial Fulfillment of the Requirements
for the Degree of Doctor of Philosophy
Specializing in Civil and Environmental Engineering

May, 2019

Defense Date: November 29, 2018
Dissertation Examination Committee:

Ehsan Ghazanfari, Ph.D., Advisor
Nicolas Perdrial, Ph.D., Chairperson
Donna Rizzo, Ph.D.
George Pinder, Ph.D.
Mandar Dewoolkar, Ph.D.
Cynthia J. Forehand, Ph.D., Dean of the Graduate College

# ABSTRACT

Coupled Thermal-Hydrological-Mechanical-Chemical (THMC) processes that exist in the development of different geo-resources (e.g. deep geothermal and shale gas) affect the fracture response (i.e. aperture and permeability), which in turn influences the reservoir production. The main goal of this study was to experimentally evaluate the impact of THMC processes on the response of rock specimens relevant for deep geothermal and shale gas formations. The effects of THMC processes were investigated on: (i) success of the hydraulic fracturing/hydro-shearing mechanism during stimulation stage, and (ii) closure of the created network of fractures during production stage.

The elastic, cyclic, creep, and failure characteristics of different intact reservoir rocks in both short- and long-term were investigated to evaluate their response in stimulation stage. In addition, a series of flow tests on fractured reservoir cores were conducted to evaluate how THMC processes affect fracture response subjected to different stress levels, temperatures, composition of injected fluid, and injection rate. Moreover, the sensitivity of ultrasonic signatures (i.e. velocity, amplitude, attenuation, and time-frequency content) to (i) microstructural changes in the intact rocks, and (ii) flow-induced alterations of aperture/permeability in the fractured rocks were investigated. Analysis of hydraulic data, chemical composition of the effluent, ultrasonic signatures, and X-Ray micro-CT and SEM images, provided invaluable information that facilitated interpretation of the effects of coupled THMC processes on fracture response.

# CITATIONS

Material from this dissertation has been published in the following forms:

Kamali-Asl, A., Ghazanfari, E., Perdrial, N., and Bredice, N.. (2018). Experimental study of fracture response in granite specimens subjected to hydrothermal conditions relevant for enhanced geothermal systems. *Geothermics*, 72, pp. 205 – 224.

Kamali-Asl, A., Ghazanfari, E., Newell, P., and Stevens, M.. (2018). Elastic, viscoelastic, and strength properties of Marcellus Shale specimens. *Journal of Petroleum Science and Engineering*, 171, pp. 662 – 679.

Kamali-Asl, A., Ghazanfari, E., Hedayat, A., and Deering, L.. (2018). Investigation of static/dynamic moduli and plastic response of shale specimens. *International Journal of Rock Mechanics and Mining Sciences*, 110, pp. 231 – 245.

Kamali-Asl, A., K-C, B., Foroutan, M., Ghazanfari, E., Cladouhos, T.T., and Stevens, M.. (2018). Stress-strain response and seismic signature analysis of phyllite reservoir rocks from Blue Mountain geothermal field. *Geothermics*, 77, pp. 204 – 223.

And

Material from this dissertation has been submitted for publication to Geophysics on July 2018 and the revised version submitted on January 2019 in the following form:

Kamali-Asl, A., K-C, B., Ghazanfari, E., and Hedayat, A.. Flow-induced alterations of ultrasonic signatures and fracture aperture under constant state-of-stress in a single-fractured rock.

And

Material from this dissertation has been submitted for publication to Geothermics on November 2018 in the following form:

Kamali-Asl, A., Ghazanfari, E., Perdrial, N., and Cladouhos, T.. Investigation of the effects of different injected fluids on permeability evolution in fractured rocks.

# DEDICATION

To my parents,

Naser and Farideh

To my love,

Samereh

# AKNOWLEDGEMENTS

I would like to thank my family for supporting me throughout writing this dissertation and my life in general. I am very grateful to my PhD advisor, Professor Ehsan Ghazanfari, who consistently supported me during my studies and behaved as my older brother in many hardships I had in my studies. Special thanks to my committee members for their contribution to the improving the quality of my research. I would also like to thank my many officemates through the years (Maria, Yujie, Saleh, Zhuang, Maziar, etc.) for making my office life enjoyable. I am also grateful to Professor Nico Perdrial, Professor Ahmadreza Hedayat, Professor Pania Newell, Dr. Trenton Cladouhos, Mr. Marco van Gemeren, Mrs. Michele Von Turkovich, my groupmates, Maziar Foroutan and Bijay K-C, and undergraduate students, Mathew Stevens, Louisa Deering, and Nicholas Bredice.

# TABLE OF CONTENTS

# LIST OF FIGURES

# LIST OF TABLES

# CHAPTER 1

# INTRODUCTION

## 1.1 MOTIVATION AND SIGNIFICANCE

To meet the energy demand for the growing US population (EIA Report, 2017; Figure 1.1a), development of a wide range of energy resources is necessary. Fossil fuels such as petroleum, natural gas, and coal account for around 80% of the energy source in the US energy portfolio, as illustrated in Figure 1.1b. Renewable energy, however, contributes to only 11% of the US energy consumption with geothermal share being only 0.22%.

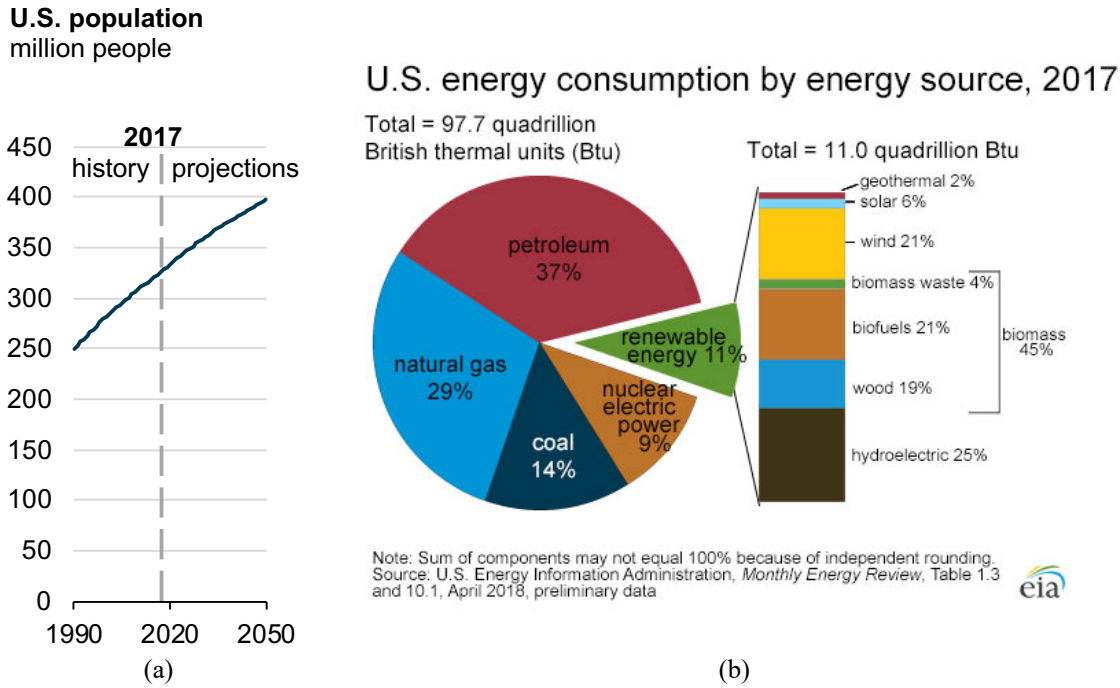


Figure 1-1. (a) US population growth, and (b) US energy consumption by energy source (EIA Report, 2017).

Despite the desire to transition from fossil fuel- to renewable-based energy systems and recent technological and societal advancements in renewable energy production, there is still a substantial gap between energy produced from renewables and fossil fuel resources, even for 2050 projections in the US, as shown in Figure 1.2. The projections for coal and crude oil by 2050 are decreasing and almost-constant, respectively (EIA Report, 2017), while, the projections for natural gas and renewables are increasing, with the former at a higher rate.

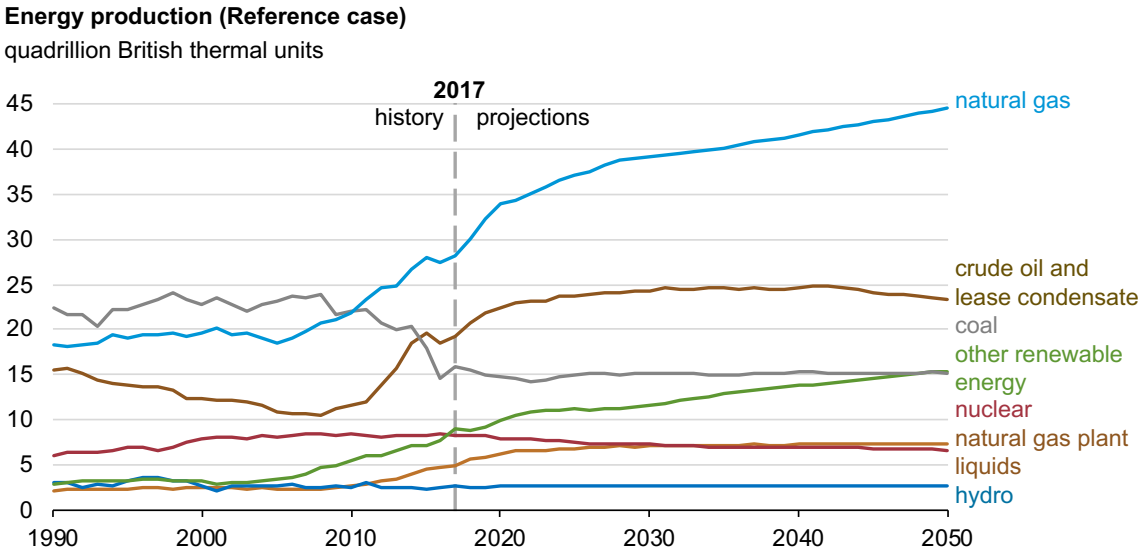


Figure 1-2. Energy production estimates by 2050 (EIA Report, 2017).

Enhanced Geothermal Systems (EGS), or deep geothermal energy, is a clean and renewable source of energy. Despite its significant potential, due to existing practical limitations and knowledge gaps, EGS has not gained enough attention and the 2050 projections for the US indicate small increase in geothermal electricity generation (EIA, 2017; Figure 1.3). Although it is desired to fully transition away from fossil fuels toward

renewable energy resources, the existing gap can be filled with cleaner sources of fossil fuel, such as natural gas. Shale gas, one of the unconventional resources of natural gas, can be used to fill the existing gap as we move toward renewable energy-based infrastructure.

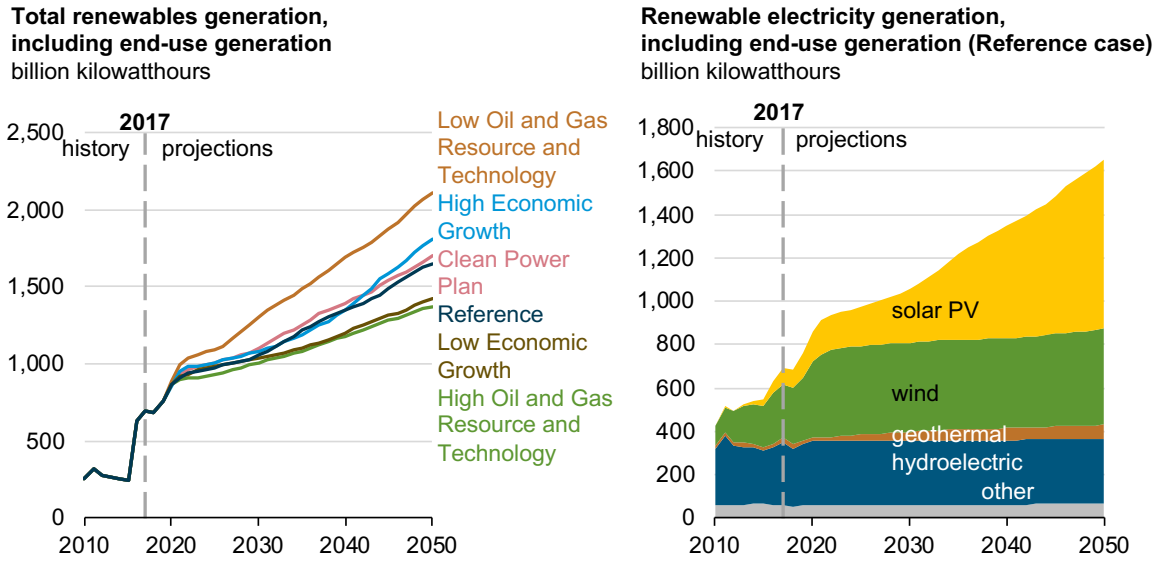


Figure 1-3. The projections of total electricity generation from renewable energy resources (EIA Report, 2017).

In both of these energy resources (i.e. shale gas and EGS), it is necessary to create and/or sustain a network of fractures in the reservoir. Geomechanics plays an important role in optimizing the process of fracture creation and keeping them open during production. In shale gas development, the formation is hydraulically-fractured to extract the stored natural gas, while, in EGS either existing fractures are opened up using hydro-shearing process (e.g. Cladouhos et al., 2016) or new fractures are created through hydraulic fracturing process (e.g. Ghassemi and Suarez-Rivera, 2012). Despite recent advancements in both energy fields, hydro-shearing and hydraulic fracturing processes are

not optimized, in part due to lack of thorough understanding of geomechanical characteristics of reservoirs (e.g. Sone and Zoback, 2013a,b). For example, the created hydraulic fractures in different shale formations are typically extended about 100 to 1000 ft from the stimulation well (e.g. Davies, 2012), as shown in Figure 1.4a. However, the first 100 to 200 ft length of the created fractures can be usually kept open for gas extraction (e.g. Fisher, 2010), as shown in Figure 1.4b, indicating inefficiencies of the current industrial practices for energy intensive reservoir development.

Induced seismicity associated with hydraulic fracturing and/or hydro-shearing processes is a major public concern (e.g. Diechmann and Giardini, 2009). A better understanding of the response of shale and geothermal reservoir rocks during stimulation program (i.e. hydraulic fracturing and/or hydroshearing) is necessary to mitigate the risk of induced seismicity. In addition, geomechanical characterization of shale rocks and their response to hydraulic fracturing is necessary to avoid potential groundwater contamination caused by methane seepage through interaction of created fractures with the existing fractures/faults and abandoned oil/gas wells (Montague and Pinder, 2015).

Maintaining an open network of fractures is a vital task in successful energy extraction from shale gas/EGS reservoirs. Shale gas formations typically possess high clay/organic content. This can lead to significant viscoelastic deformations under in-situ stresses and consequently, closure of fractures over the course of reservoir operation (e.g. Davey, 2012; Sone and Zoback, 2013b; Kamali-Asl et al., 2018b). In EGS reservoirs, chemo-mechanical processes (e.g. pressure solution) contribute to gradual closure of fractures, leading to reservoir production drop over time (e.g. Polak et al., 2003; Faoro et

al., 2016; Kamali-Asl et al., 2018a). Although the use of proppant can mitigate the fracture closure problem in short-term, it does not eliminate this issue in the long-term. Figure 1.5 shows a schematic of the usage of proppants to keep the fracture open in short-term, and gradual closure of fracture in the long-term.

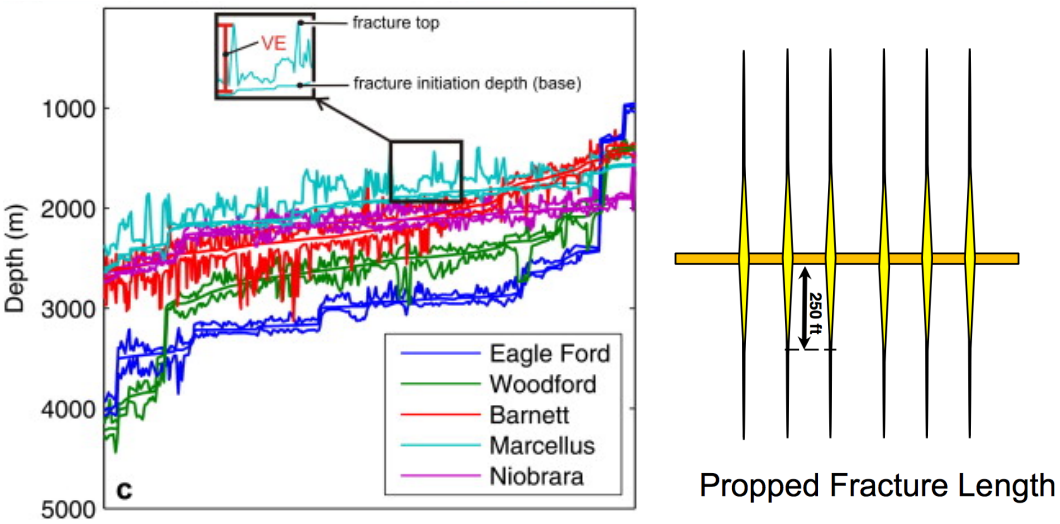


(a) (b)

Figure 1-4. (a) The extent of hydraulic fractures in different shale formations (Davies et al., 2012), and (b) comparison of open hydraulic fractures during and after treatment (Fisher, 2010)

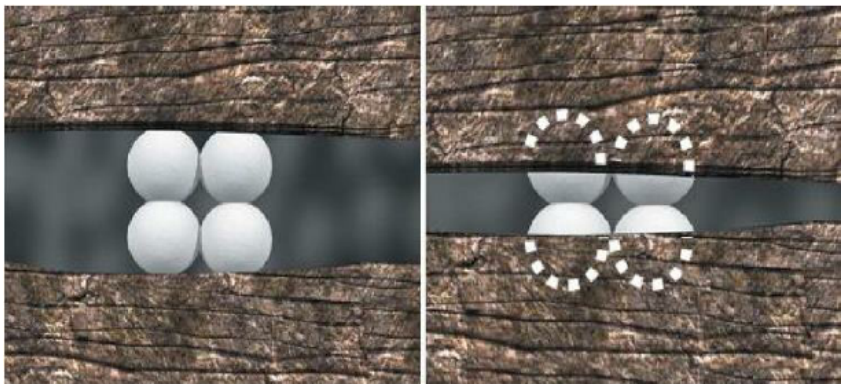

Figure 1-5. A schematic showing the usage of proppants to avoid the closure of fracture, and gradual closure of fracture in long-term (www.chk.com).

In general, coupled Thermal-Hydrological-Mechanical-Chemical (THMC) processes that exist in both shale gas and EGS reservoirs affect the fracture response (i.e. aperture and permeability), which in turn, influences the reservoir production. Therefore, it is critical to investigate the effects of THMC processes on the response of fractured reservoirs to better: (i) design stimulation program, (ii) understand the response of the fractured reservoirs, and (iii) optimize the reservoir production.

In this research, a suite of experiments was performed to evaluate the impact of THMC processes on the response of different reservoir/shallow rock specimens. In particular, mechanical-chemical-thermal characterization of outcrop and reservoir Marcellus Shale rocks and Blue Mountain geothermal reservoir rocks were performed to investigate the (i) outcome of hydraulic fracturing/hydro-shearing mechanism during stimulation stage and (ii) closure of the created network of fractures during production stage. The testing program included an extensive analysis of mechanical properties of specimens under different stress levels. Cyclic, elastic, visco-elastic, strength, and ultrasonic characteristics of shale and geothermal reservoir rocks are important to evaluate how reservoirs respond to different stress conditions in both short- and long-term. In addition, a series of flow-through tests on granite and phyllite specimens were conducted to evaluate how THMC processes affect fracture response under reservoir conditions. To achieve this goal, the experiments were conducted under different stresses, temperatures, composition of injected fluid, and injection rate. Moreover, ultrasonic signals were concurrently recorded during flow-through tests to evaluate their sensitivity to the flow-induced changes in fracture aperture/permeability. Analysis of hydraulic data, chemical composition of the effluent, X-Ray Computed Tomography (CT) images, Back-Scattered

Electron (BSE) images, and Secondary Electron Microscopy (SEM) images, provided invaluable information that enables interpretation of the effects of coupled THMC processes on fracture response, which is critical to the productivity of fractured reservoirs.

## 1.2 DEEP GEOTHERMAL ENERGY

Deep geothermal systems take advantage of exchanged heat between hot dry bedrock and injected water for electricity production or direct heating, as shown in Figure 1.6a. These reservoirs are typically located in areas where fracture permeabilities and heat flow are high. In these projects, the natural hydrothermal system is exploited by drilling geothermal production wells into permeable rock masses containing hot liquids or steam. However, if the permeability of an injection and/or production well is not sufficient, the method of enhanced geothermal systems (EGS) is explored to increase the heat/electricity production from the reservoir. In order to create a network of connected fractures with high permeability, the so-called "Hydro-shearing" process is implemented (e.g. Cladouhos et al., 2016), as shown in Figure 1.6b. In this process, highly-pressurized fluid is injected into sealed fractures to open them and increases their permeability.

In an EGS, the reservoir often experiences closure of fractures over the course of its operation, which is often attributed to the coupled THMC processes (e.g. Ghassemi, 2012; Caulk et al., 2016). Chemical alteration of fracture surface, pore pressure increase, temperature change, and volume change due to fluid withdrawal/injection are the main contributing mechanisms to the change of permeability in EGS reservoir operations. These processes act at different time scales and subsequently, affect the permeability/productivity of the reservoir (e.g. Yasuhara et al., 2004; Taron and Elsworth, 2010).

Figure 1.7 shows the coupling between different processes in an EGS reservoir. Note that the thickness of the arrows indicates the strength of link/coupling between different THMC processes. Thermal processes have considerable influence on both mechanical and chemical processes and intermediate influence on hydrological processes. Mechanical processes, on the other hand, have an intermediate coupling with chemical processes when pressure solution occurs, while they do not substantially affect thermal and hydrological processes. When mineral dissolution/precipitation occurs, the effects of chemical processes on hydrological processes are considerable, although they do not contribute to changes in mechanical and thermal processes. Finally, hydrological processes considerably affect thermal processes, with a weaker coupling with chemical processes, and negligible effects on mechanical processes.

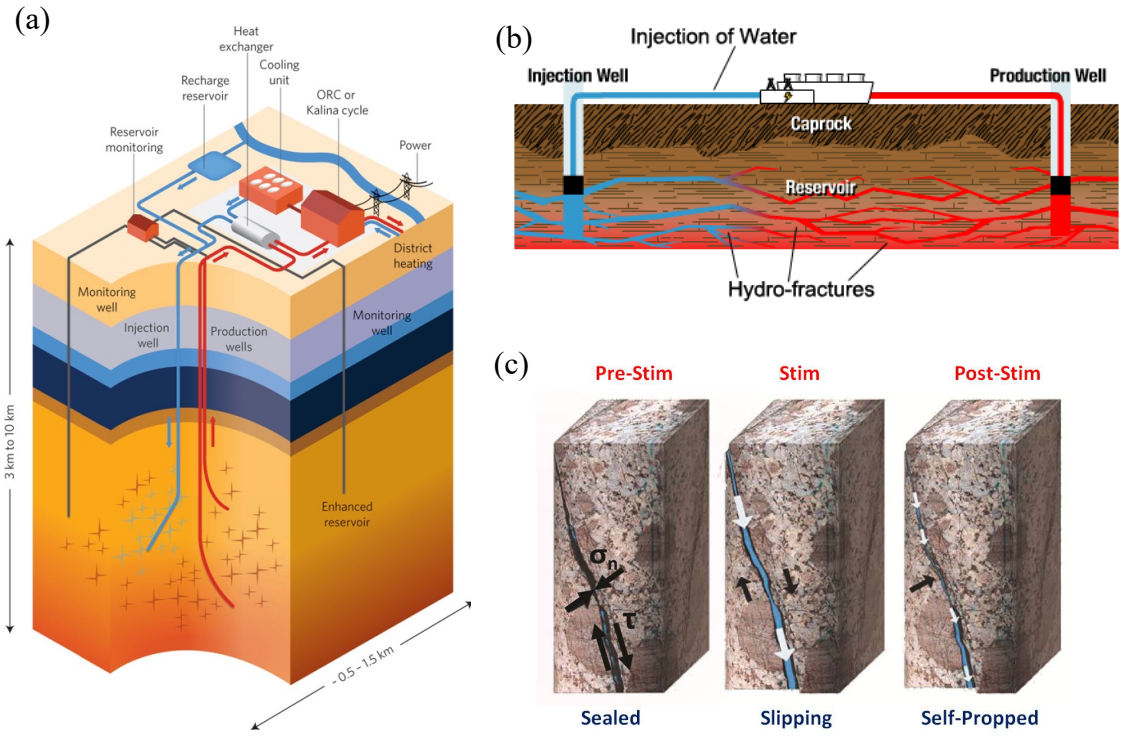


Figure 1-6. Schematics of (a) deep geothermal systems at (adapted from http://www.natures.com), (b) fracture network in reservoir (adapted from http://www.renewablegreenenergypower.com/); and (c) hydro-shearing process (adapted from www.altarockenergy.com)

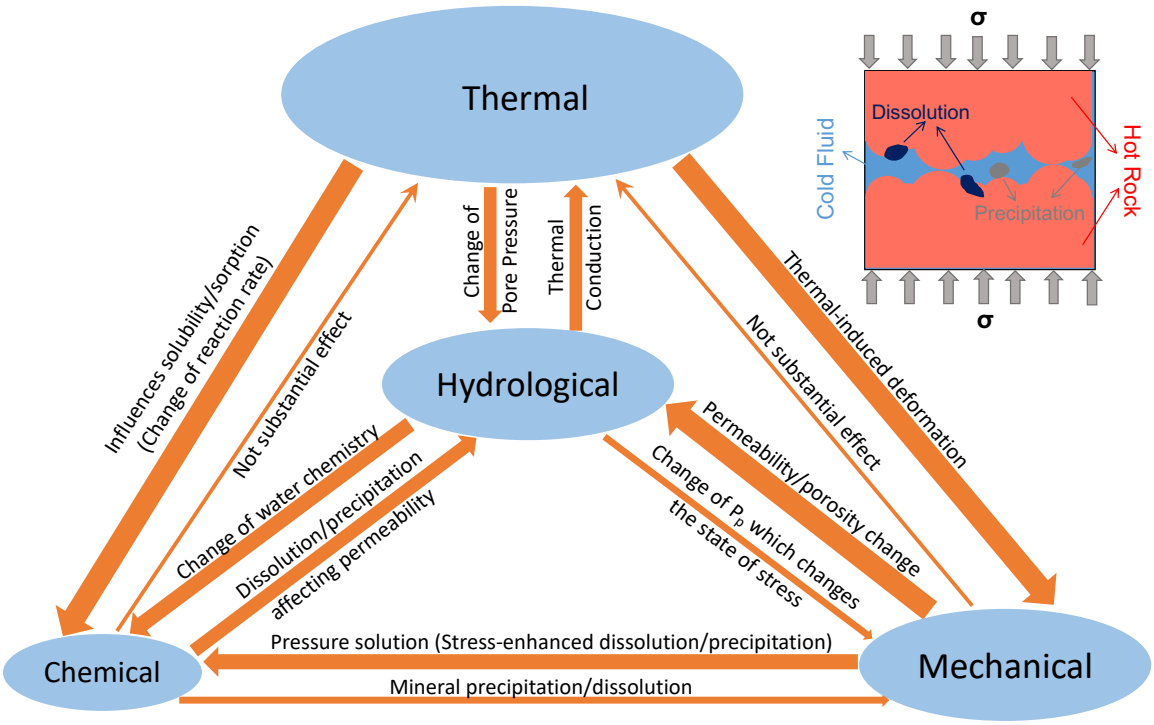


Figure 1-7. Schematic of the coupling between thermal-hydrological-mechanical-chemical processes in fractured geothermal reservoirs (adapted and modified from Manepally et al., 2011) triggered by fluid-fracture surface interactions (upper right schematic)

Note: The thickness of arrows indicates how influential is the contribution of one process on another process. The size of ovals show how influential is a process on other three processes in aggregate.

## 1.3 SHALE GAS

In the US, there are more than 39 billion barrels of proved oil/gas reservoirs, the highest since 1972, with significant contribution of unconventional oil/gas resources such as shale gas and tight oil (EIA Report, 2017). Figure 1.8 shows the distribution of the proved shale gas reservoirs around the globe, some of which are already contributing to the produced energy in the globe.

Shale gas reservoirs in the US are predicted to be the dominant source of natural gas by 2020 and even increase their share by 2040, according to EIA, as shown in Figure

1.9a. Development of Barnett, Haynesville, Marcellus, and Utica Shale among others has led to increased interest in evaluating properties of shale gas formations. In US, Marcellus Shale gas production has reached ~20 bcf/day by September 2018, as shown in Figure 1.9b.

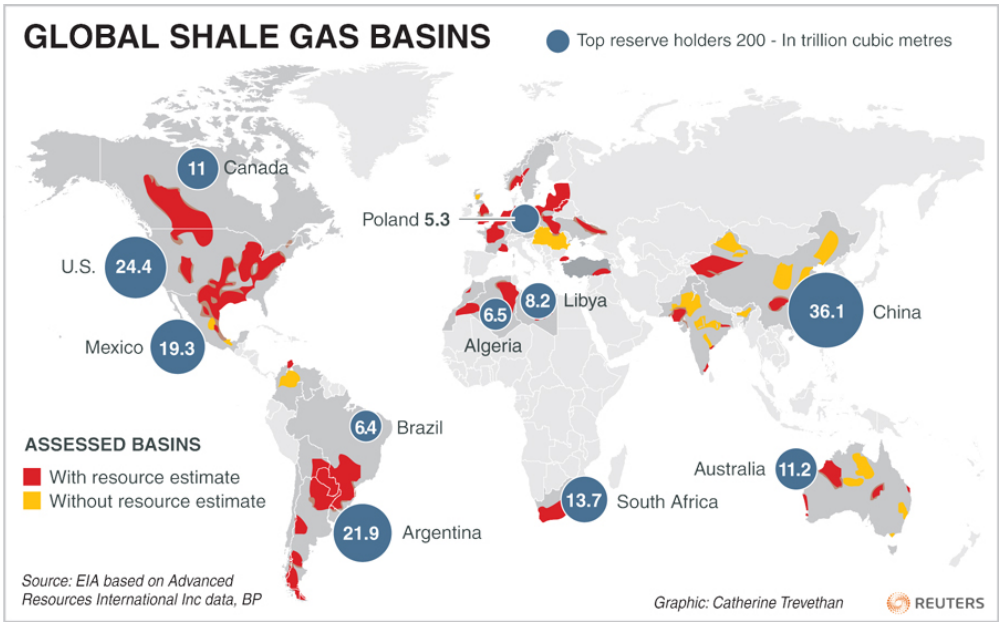


Figure 1-8. Distribution of shale gas formations around the globe (www.reuters.com)

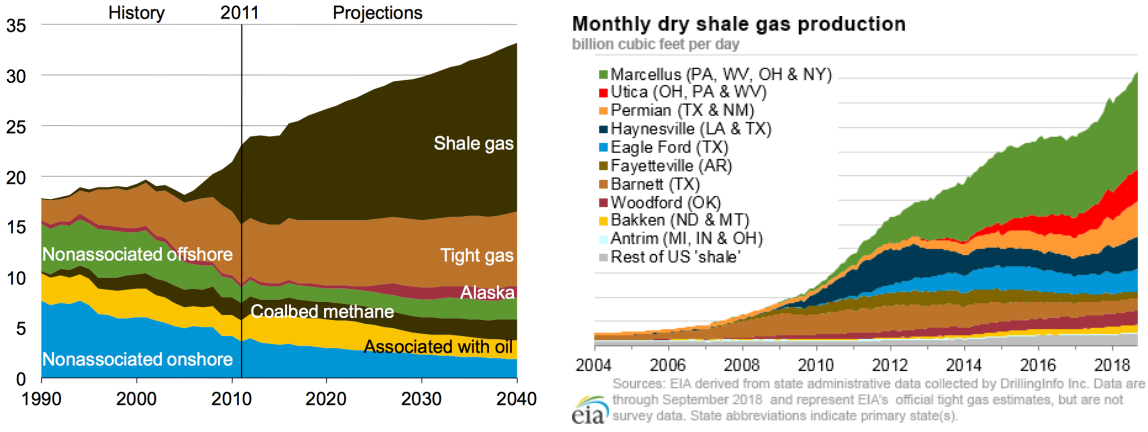


(a) (b)

Figure 1-9. (a) US dry natural gas production by source, 1990-2040 (EIA Report, 2013), (b) Dry shale gas production in different formations 2004-2018 (EIA Report, 2018)

For development of shale gas reservoirs, it is necessary to create a network of fractures through hydraulic fracturing process in horizontal wells to enhance the production rate, as shown in Figure 1.10. Typically, so-called "multi-stage hydraulic fracturing" is performed to increase the production rate and optimize the extraction of natural gas from these reservoirs. The current practice of hydraulic fracturing is not optimized, a lot of energy is wasted (e.g. Fisher, 2010; Davies et al., 2012), and the concerns of induced seismicity and groundwater contamination have not yet fully addressed. Therefore, it is essential to better understand the behavior of shale gas reservoirs under different states-of-stress relevant to the process of hydraulic fracturing.

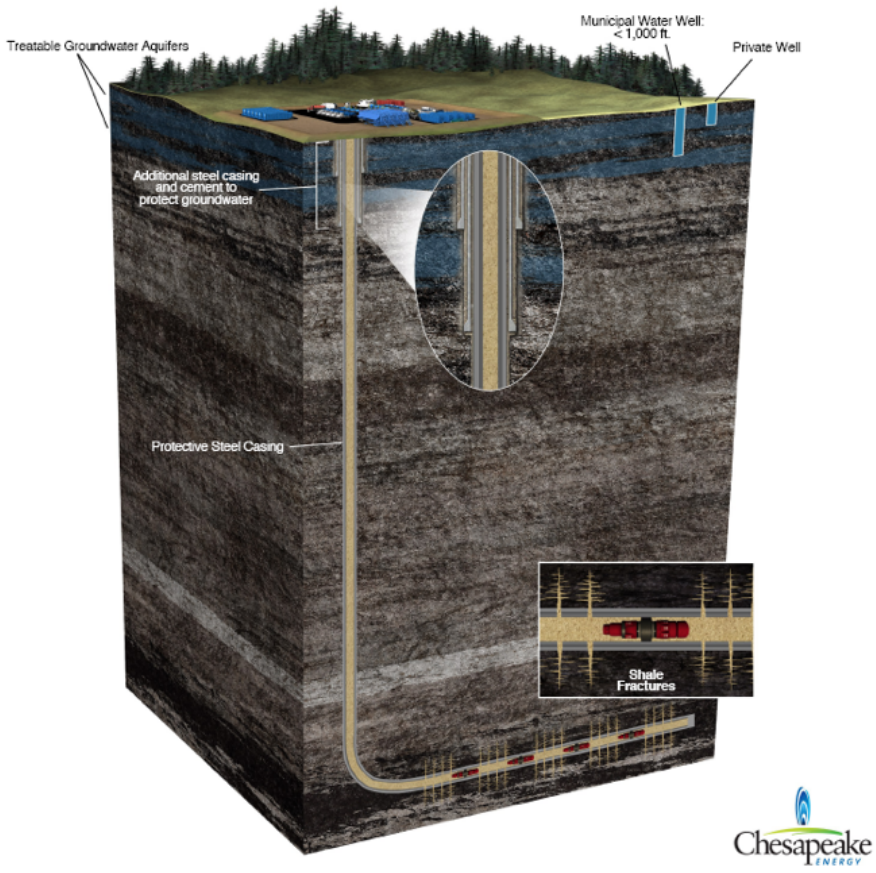


Figure 1-10. Schematic of hydraulic fracturing in shale gas (adapted from http://www.chk.com)

## 1.4 RESEARCH QUESTIONS

The research questions have been divided into two parts: (1) how the elastic, visco-elastic, failure, and hysteresis characteristics of host rocks affect the success of shale gas and geothermal reservoir development during both stimulation and production stages, and (2) how THMC processes impact the fracture aperture/permeability evolution in deep geothermal systems at different reservoir conditions.

### 1.4.1 EFFECTS OF GEOMECHANICAL CHARACTERISTICS ON SUCCESS OF SHALE/GEOTHERMAL RESERVOIR DEVELOPMENT

Despite recent advancements, the outcome of hydraulic fracturing or hydro-shearing operations as well as the fracture closure over time are variable and unpredictable (e.g. Curtis, 2002; Sone, 2012; Bažant et al., 2014). In order to optimize the required energy for hydraulic fracturing or hydro-shearing operation, and production in different geo-energy resources, it is important to evaluate both elastic-plastic and visco-elastic-plastic behavior of the rock formation. Since, rocks could be highly-nonlinear material, it is very important to evaluate their pressure-dependent characteristics. Moreover, the created fractures gradually close under in-situ stresses. Re-stimulation process is typically performed to enhance the production rate in these reservoirs, and therefore, the hysteresis behavior of these rocks should be thoroughly characterized. In addition, the rate of visco-elastic deformations in different reservoirs should be identified, since creep deformation affects both short- and long-term response of these rocks. Ultrasonic wave propagation is another piece of information that is useful in evaluation of elastic properties of rocks in laboratory experiments. Shear and compressional wave velocities can be affected by

closure of existing micro-cracks, potential porosity reduction, and creation of new micro-cracks.

There is a need to better characterize the mechanical properties of the reservoir rocks. In this research, a suite of mechanical testing, including multi-stage elastic and failure, cyclic, and creep tests were performed to evaluate how hydraulic fracturing/re-fracturing, and production rates can affect the stimulation/production stages. The rock cores used in this study were retrieved from deep wells in (i) Marcellus Shale in West Virginia, and (ii) Blue Mountain geothermal field in Nevada, and their elastic, time-dependent, hysteresis, and strength properties were characterized. The specific research questions in this part are as follow:

1. *How the elastic-plastic, failure, visco-elastic, and hysteresis characteristics of shale and deep geothermal reservoir rocks affect the success of reservoir development during both stimulation and production stages?*
2. *How ultrasonic velocities are affected by the changes in the internal micro-structure of reservoirs rocks under different stress conditions?*

### 1.4.2 EFFECTS OF THMC PROCESSES ON TRANSPORT PROPERTIES OF DEEP GEOTHERMAL ROCKS

The sustainability and production efficiency of a geothermal reservoir are the main obstacles toward commercialization of this type of renewable energy. Coupled THMC processes, triggered by injection of cold water into hot dry bedrock, contribute to the permeability reduction and subsequently, production decline over the course of operation

for a geothermal reservoir (e.g. Faoro et al., 2016). These processes often act at different time-scales, which makes it difficult to de-couple them.

Geothermal reservoirs are typically located 3-5 km deep in earth, which makes them good candidates for heat extraction. At these depths, the kinetic reaction rates for different minerals are higher compared to those at lower temperatures. Thermal processes have two immediate effects on the response of the deep geothermal reservoirs. Firstly, the difference between the temperature of the reservoir and the injected fluid exerts thermal stresses and deformations, which can lead to alteration of the mechanical stresses on the rock mass. Secondly, this difference in the temperature of the injected fluid and the rock mass can alter the involved chemical processes, which alters the outcome of mineral precipitation/dissolution processes. The mineral dissolution/precipitation contributes to the change of fracture permeability in geothermal reservoirs. In a deeper reservoir, it is harder to sustain the network of connected fractures, as they get closed in a shorter period of time compared to shallower reservoirs due to higher effective stresses.

Ultrasonic waves can be considered as high-resolution proxy to investigate the flow-induced alterations of fracture aperture/permeability, as they are sensitive to different elements of geological formations. The characteristics of these waves can be influenced by hydro-mechanical and geochemical alterations at the fracture surface. Therefore, investigation of their sensitivity to flow-induced alterations of fracture aperture/permeability can provide insights into characteristics of fracture network in deep geothermal systems.

In order to evaluate the effects of different THMC processes on fracture response in EGS reservoirs, the following sub-research-questions need to be addressed in an attempt to minimize the production decline, which in turn contributes to the development of geothermal energy. In this research, a suite of flow tests on low-porosity artificially-fractured rock specimens were designed and performed to address the following research questions:

1. *How the outcome of chemical dissolution/precipitation and evolution of fracture aperture/permeability might be affected at different stress conditions?*
2. *How different temperatures of rock and injected fluid can affect the rate of chemical dissolution/precipitation, and evolution of fracture aperture/permeability?*
3. *How sensitive are the ultrasonic signatures (namely, velocity, amplitude, attenuation, and time-frequency content) to the flow-induced changes in fracture aperture/permeability at constant and varying states-of-stresses?*
4. *What are the effects of the injected fluid type on the rate of chemical dissolution/precipitation, and evolution of fracture aperture/permeability?*

## 1.5 INTELLECTUAL MERIT

The experimental results of this study provide a unique dataset, which (i) advances our understanding of THMC processes in fractured reservoirs, and (ii) allows improving predictive capability of existing models for prediction of fracture response during

stimulation and production stages in fractured reservoirs. In addition, this study contributes to the improved understanding of the underlying reasons for production decline in shale and EGS reservoir, as well as providing insight for addressing some of the public concerns (e.g. induced seismicity) associated with development of these reservoirs. Most importantly, the elastic and transport properties of different geo-resource formations are investigated through propagation of ultrasonic waves. In particular, the interaction of longitudinal and transverse ultrasonic waves with the rock and/or fractured/fluid provide a better insight into the response of intact/fractured rocks during stimulation/production stages of a geo-resource formation.

## 1.6 BROADER IMPACTS

Reliable development of EGS and/or shale gas reservoirs requires a thorough understanding of geomechanical and hydrothermal characterization of these reservoirs and their response to different in-situ stress conditions. This research contributes to facilitating the transition to cleaner sources of energy and decrease the national dependency on foreign energy resources. In particular, shale gas has the potential to significantly contribute to the energy demand of the US population, given its abundance across different locations in the US. In addition, this research helps addressing some of the environmental concerns such as induced seismicity and groundwater contamination associated with EGS and shale gas energy development.

## 1.7 DISSERTATION OVERVIEW

The dissertation is organized as follows:

- Chapter 2: The effects of mineralogical content on elastic, viscoelastic, and strength properties of deep Marcellus Shale cores (from depths of ~7400 to 7600 ft) were experimentally investigated. In addition, the sensitivity of ultrasonic velocities to the changes in the micro-structure of the rock in creep and cyclic loadings were evaluated. The robustness of power-law and Burger's rheological models in predicting the longer-term time-dependent viscoelastic response of Marcellus shale rocks were investigated. Moreover, the applicability of Mohr-Coulomb and Hoek-Brown failure criteria were studied.
- Chapter 3: The static and dynamic moduli under different levels of confining pressure and differential stress were investigated by conducting multi-stage elastic and cyclic tests on clay-rich and carbonate-rich deep Marcellus shale rocks. The elastic moduli (namely Young's modulus, Poisson's ratio, and shear modulus) of these rocks at different loading, unloading, and reloading conditions. In addition, the hysteresis behavior and sensitivity of P- and S-wave ultrasonic velocities to changes in the state-of-stress were investigated.
- Chapter 4: The effects of material anisotropy on mechanical characteristics of a geothermal reservoir core rock were investigated in this chapter. Elastic, cyclic, viscoelastic, and failure response of two phyllite reservoir rocks (retrieved from a depth of 1.26 km) along with the concurrent measurements

of ultrasonic signatures were studied. To better understand the stress-induced changes in the time-frequency content of seismic signals, wavelet transform was conducted on signals recorded during cyclic, multi-stage elastic, and creep tests.

- Chapter 5: The pressure solution phenomenon at different states-of-stress, different temperatures of injected fluid, and different temperatures of rock specimen was investigated through performing flow-through experiments on fractured Barre granite specimens. To better understand the rate of mineral dissolution/precipitation relatively-long experiments were performed at two different levels of effective pressure. In addition, experiments with loading and unloading paths with various temperatures of injection fluid and rock specimen were conducted along with obtaining X-Ray Micro-CT images and chemical analysis of the effluents to better understand the coupled thermal-hydrological-mechanical-chemical processes on permeability evolution and the degree of permeability recovery.
- Chapter 6: Sensitivity of ultrasonic signatures to flow-induced alterations of fracture aperture/permeability of fractured phyllite specimens under constant state-of-stress were investigated in this chapter. In particular, ultrasonic velocities, amplitudes, attenuations, and time-frequency content were studied to gain a better insight into the changes of ultrasonic signatures. In addition, radial strains were recorded and used as a mechanical deformation proxy on fracture closure.

- Chapter 7: The alterations of ultrasonic signatures under different varying confining and pore pressures were experimentally investigated to better understand how these signatures might be affected. Ultrasonic velocities, amplitudes, attenuations, and time-frequency contents were evaluated. In addition to hydraulic aperture (or equivalently fracture permeability), radial strains were recorded and used as a mechanical deformation proxy on fracture closure.
- Chapter 8: The effects of different circulated fluids on permeability evolution of deep geothermal systems were investigated through flow-through experiments on a phyllite reservoir rock. In particular, deionized water, super- and under-saturated fluids with respect to silica, and a geothermal fluid (retrieved from production wells at Blue Mountain geothermal field) were injected into the fractured rock specimen under the same pressures and temperatures. Chemical analysis of the effluents, CT-scan images, and secondary and backscattered electron microscopy images were used as supporting evidence in addition to hydraulic data (i.e. fracture permeability) during the experiments.
- Chapter 9: Conclusions and suggestions for future works are provided.

# CHAPTER 2

# ELASTIC, VISCOELASTIC, AND STRENGTH PROPERTIES OF MARCELLUS SHALE SPECIMENS

## ABSTRACT

Shale gas rocks are characterized as clastic sedimentary rocks, with features such as obvious bedding planes, presence of micro-cracks, and high clay and organic content. These rocks are anisotropic, and inhomogeneous exhibiting a nonlinear response under loading. In order to optimize the required energy for hydraulic fracturing operation and production in shale gas reservoirs, and for constitutive and numerical modeling, it is important to characterize these shale gas rocks. In this study, the hysteresis, elastic-plastic, viscoelastic, and strength properties of Marcellus Shale specimens retrieved from a deep well located in West Virginia were evaluated through performing a series of creep, cyclic, and triaxial multi-stage failure tests on these specimens. The results suggest that both elastic moduli and plastic deformations show significant levels of pressure dependency. Moreover, higher creep compliance and lower Young's modulus values were observed for clay-rich specimens. Both Power-Law and Burgers models were found to capture the creep response of these specimens reasonably-well. The dynamic moduli estimated from the ultrasonic velocity measurements at different stress levels were found to be higher than static moduli estimations. In addition, the changes in the internal micro-structure of the specimens resulted from variations in the stress condition, were found to affect the

ultrasonic velocity measurements. The strength properties of the calcite/quartz-rich specimen, using multi-stage triaxial failure test, were estimated through both Mohr-Coulomb and Hoek-Brown failure criteria.

## 2.1 INTRODUCTION

Development of shale gas reservoirs around the world has led to increased interest in and demand for geomechanical characteristics of shale gas formations (EIA Report, 2017; Soeder, 2018). Shale gas rocks are characterized as sedimentary rocks with fine grains, high clay and organic content, low permeability and porosity, high heterogeneity and anisotropy, and wide range of Total Organic Content (TOC) and mineralogy (e.g. Curtis, 2002; Huang and Zhao, 2017). Due to their low permeability, hydraulic fracturing is used to create fractures in shale gas formations and extract natural gas (Hossain et al., 2000; Davies et al., 2012; Ghassemi et al., 2013; Sone and Zoback, 2013a and 2013b; Rezaee, 2015).

In shale gas reservoir development, a key step toward optimizing both stimulation and production stages is to evaluate elastic-plastic, visco-elastic-plastic, and strength properties of these rocks (e.g. Sone 2012; Johri and Zoback, 2013; Feng, 2017) as they influence the success of hydraulic fracturing and fracture response during stimulation and production stages, respectively (e.g. Montgomery and Smith, 2010; Vermylen, 2011; Ghassemi and Suarez-Rivera, 2012; Pireh et al., 2015). Different petrophysical and geomechanical tests are often conducted for laboratory characterization of shale rocks (Davey, 2012; Schon, 2015). Geomechanical characterization of these organic-rich rocks usually includes estimation of elastic moduli, strength properties, hysteresis behavior, and

creep deformation (e.g. Vermylen, 2011; Kivi et al., 2015; Schon, 2015; Villamor Lora, 2015).

Triaxial experiments performed in drained/undrained conditions, along with measurements of ultrasonic wave velocities at different stress conditions (e.g. Sone and Zoback 2013a; Villamor Lora et al., 2016) facilitate determination of the aforementioned characteristics/properties in laboratory. These geomechanical and petrophysical properties can be used to (i) optimize the hydraulic fracturing stimulation program, (ii) feed the required parameters for constitutive models, and (iii) improve the accuracy of hydrocarbon production models (e.g. Jarvie et al., 2007; Vermylen, 2011; Villamor Lora et al., 2016).

Elastic moduli of shale gas rocks are influenced by several factors including fabric composition and anisotropy, presence of microcracks, orientation of bedding planes, and stress conditions among others (e.g. Sone, 2012). Typically, shale gas rocks exhibit brittle and nonlinear response, when subjected to axial loading (e.g. Villamor Lora et al., 2016). Strength properties (e.g. unconfined compressive, failure, and ultimate strengths) of these rock formations can be evaluated in laboratory through performing single- and Multi-Stage Failure (MSF) tests (e.g. Sone and Zoback, 2013b; Villamor Lora et al., 2016).

Creep deformation is important in both short- and long-term response assessment of shale gas reservoirs (e.g. Ghassemi and Suarez-Rivera, 2012; Sone, 2012). In short-term, change in the state of stress due to viscoelastic-plastic deformations affects the success of hydraulic fracturing (e.g. Sone and Zoback, 2013b); while, in long-term, the transport processes (permeability-dependent) and productivity of the reservoir (fracture aperture-dependent) are significantly affected by the time-dependent behavior of shale rocks as it

influences closure of fracture (e.g. Villamor Lora and Ghazanfari, 2014; Sone and Zoback, 2014). Given the significance of creep deformation for both short- and long-term success of shale gas development (e.g. Ghassemi and Suarez-Rivera, 2012), it is important to evaluate the creep response of these organic-rich rocks.

Creep tests are usually consisted of two stages, hydrostatic and triaxial. In general, shale rocks do not exhibit significant creep response, when subjected to isotropic compression during hydrostatic stage (e.g. Fjar et al, 2008; Sone, 2012), with several exceptions reported in the literature (e.g. Ghassemi and Suarez-Rivera, 2012). However, these rocks tend to creep significantly while subjected to constant differential stress during triaxial stage. The increase in organic and clay content in shale specimens is linked to enhanced creep response (e.g. Li and Ghassemi, 2012). Therefore, the clay/organic content can be considered as good indications of the viscoelastic-plastic behavior of shale rocks (Sone and Zoback, 2013b). As opposed to calcite/quartz minerals, clay minerals show stable time-dependent sliding response due to their low friction and velocity strengthening frictional properties (Moore and Lockner, 2004; Sone and Zoback, 2013b). It is worth noting that creep deformation of shale rocks is not significantly affected by poroelastic effects (e.g. Sone and Zoback, 2014).

Creep compliance, defined as time-dependent creep strain normalized by applied differential stress, can be used as an index of tendency of the rock to creep (e.g. Chang et al., 1997; Yang and Zoback, 2016). Creep compliance is influenced by clay and organic content of shale rocks, and orientation of bedding planes with respect to differential load (e.g. Sone and Zoback, 2013b). Often times Power-Law and Burgers models are used to

model and predict the time-delayed response of shale rocks (e.g. Li and Ghassemi, 2012; Sone and Zoback, 2014; Rassouli and Zoback, 2015). These models are helpful in capturing the time-delayed response of shale rocks and can be useful in predicting the long-term closure response of the created fractures under reservoir conditions in shale gas formations (Ghassemi and Suarez-Rivera, 2012).

Ultrasonic wave velocities can be measured at different stress levels during triaxial tests on rock specimens at different stress levels and used to estimate the elastic properties of the rocks (i.e. dynamic moduli), which are usually higher than the corresponding static ones (e.g. Paterson and Wong, 2005; Fjar, 2008). As the propagation of ultrasonic waves in rocks is affected by volume, geometry, and distribution of pores and fractures (Chapman, 2003; Jia, 2004; Li and Pyrak-Nolte, 2010; Hedayat et al., 2014 and 2017; Hiraiwa et al., 2017; Zhou et al., 2017), these velocity measurements can be potentially used to indirectly infer additional information about the changes in the internal micro-structure of the rock specimen due to changes in the state-of-stress (Eslami et al., 2010; Ding and Song, 2016). The ultrasonic velocities usually increase during isotropic compression (hydrostatic stage), and show an increasing/decreasing trend during triaxial stage (e.g. Sarout et al., 2007; Sondergeld and Rai, 2011; Schon, 2015).

Although shale gas rocks typically have low porosity, their high clay content leads to high compressibility (e.g. Sone, 2012; Villamor Lora et al., 2016). Closure of existing micro-cracks, potential porosity reduction as a result of pore collapse, potential particle crushing, and creation of new micro-cracks (e.g. Menendez et al., 1996; Fortin et al., 2006; Pellet and Fabre, 2007; Modiriasari et al., 2017) can affect the measured ultrasonic wave

velocities during a triaxial test. In addition, the type of pore fluid, and saturation level (e.g. Moore and Lockner, 2004; Ghrobani et al., 2009), along with the inclination of the maximum principal stress with respect to the bedding planes (Fjar, 2008; Holt et al., 2015), significantly affect ultrasonic wave velocities.

Although the Marcellus Shale is the largest formation in the United States, very limited studies are devoted to characterization of Marcellus Shale formation (e.g. Villamor Lora 2015, Villamor Lora et al., 2016), as opposed to other formations (e.g. Li and Ghassemi, 2012; Davey, 2012; Rassouli and Zoback, 2018). Due to an increasing demand for fundamental properties of this formation, this study reports on the results of creep, cyclic, and multi-stage failure experiments on Marcellus Shale specimens, retrieved from a deep well in West Virginia, in order to characterize their time-dependent, elastic, hysteresis, and strength properties. The experimental program is provided in Section 2.2, the results and discussion are provided in Section 2.3. Finally, Section 2.4 provides the conclusions of this study. Appendix A provides the information about the rock specimens used in this study. Specimen preparation and experimental methodology are provided in Appendices B and C, and matrix representation of stress-strain relationship and estimation of static and dynamic moduli are provided in Appendix D.

## 2.2 EXPERIMENTAL PROGRAM

### 2.2.1 TESTING PLAN

A series of creep, cyclic, and multi-stage failure tests were conducted in this study to characterize the viscoelastic, elastic, and strength properties of Marcellus Shale

specimens. The ultrasonic P- and cross-polarized S-wave velocities were measured along the stress path during creep and cyclic tests. Details of the performed tests are provided in the following sections.

#### 2.2.1.1 CREEP TESTS

Figure 2.1a shows a schematic, identifying different stages of the time-dependent response of a viscoelastic material subjected to a creep test, consisted of (i) initial elastic strain, (ii) primary (transient) creep, (iii) secondary (steady-state) creep, and (iv) tertiary (accelerating) creep, followed by material failure (Fjar, 2008; Brantut et al., 2012). Depending on the stress magnitude, duration of the applied stress, and material properties, secondary and tertiary stages of creep might occur. In general, the primary stage is comprised of a smooth strain increase with a decelerating rate, which is attributed to an increase in stable micro-cracks (Fjar, 2008; Brantut et al., 2012). In the secondary stage, the strain rate is constant, and permanent deformations are induced in the material upon unloading (Fjar, 2008; Brantut et al., 2012). Finally, rapid and unstable fracture growth occurs in tertiary stage of creep, followed by failure of the material (Fjar, 2008; Brantut et al., 2012). In this study, the primary and secondary creep stages were investigated.

Creep experiments were performed to evaluate the time-dependent response of the shale specimens. First, the hydrostatic stage was conducted in which, the CP was increased step-wise in 5 MPa increments up to 30 MPa. In each step, CP was held constant for 2 hours to ensure that the compaction/equilibrium of the specimen was achieved (i.e. no further changes in the axial and radial strains), as shown in Figure 2.1b. Then, three stages of step-wise increase of DS were conducted, and during each stage, the DS was held

constant for 12 hours. At the end, DS was removed and held constant at zero for 6 hours. During both hydrostatic and triaxial stages of the creep tests, the ultrasonic wave velocities were measured (i) immediately after loading, (ii) after 2 hours of creep during hydrostatic stage, and (iii) after 12 hours of creep during triaxial stage, as illustrated on the stress path shown in Figure 2.1b.

#### 2.2.1.2 CYCLIC TESTS

While determining the elastic moduli and strength properties of a rock specimen using triaxial tests, after subjecting the specimen to differential stress, one might expect to observe five different regions in stress-strain response as depicted in Figure 2.1c. These are (I) "crack closure, (II) linear elastic deformation, (III) crack initiation (CI) and stable crack growth, (IV) crack damage (CD) and unstable crack growth, and (V) ultimate failure" (Hoek and Martin, 2014; Walton et al., 2017). At low DS levels, usually the micro-cracks are closed and a highly-nonlinear behavior is observed in region I (Hoek and Martin, 2014; Walton et al., 2017). Increasing the differential stress leads to the initiation of the elastic and linear portion of the stress-strain response in region II. Then, in region III, the damage of grain boundaries due to further increase of DS occurs, which results in crack initiation (CI), with cracks that are stable. Due to the Poisson's effect, these cracks would be aligned with the direction of differential stress. The CI threshold can be identified when there is a deviation from linear response in stress-strain curves (Hoek and Martin, 2014; Walton et al., 2017). In region IV, as DS further increases, the crack damage (CD) threshold is reached, where the specimen experiences unstable crack growth (Hoek and Martin, 2014; Walton et al., 2017). A significant deviation in the stress-strain curve (particularly

volumetric strain) is an indication of the initiation of this region. Finally, the failure is reached in region V, as the applied DS reaches to the peak (failure) strength of the specimen.

The hysteresis and non-linear behavior, and gradual degradation of stiffness of rocks can be evaluated using cyclic tests. In a cyclic test, the CP is first increased to the desired level and kept constant during the test. Then, in order to capture the (i) potential changes in loading/unloading moduli, and (ii) plastic deformations, a few cycles of loading/unloading are performed. In this study, CP was increased to 30 MPa, in steps with 5 MPa increments (each step two hours). Then, differential stress ranging from 0 to 45 MPa was applied in 8-9 consecutive cycles with DS increasing by 5 MPa, as shown in Figure 2.1d.

#### 2.2.1.3 MULTI-STAGE FAILURE TESTS

Strength properties (e.g. failure and ultimate strengths) are often estimated at different confining levels by performing multiple single-stage triaxial experiments. Due to specimen scarcity and variability, MSF tests can be rather performed (e.g. Kovari and Tisa, 1975; Kim and Ko, 1979; Youn and Tonon, 2010; Yang, 2012; Villamor Lora et al., 2016) to obtain strength properties of rocks, and construct the failure envelope using a single specimen. To perform the MSF test, the CP is first increased to the desired level, followed by axial loading of specimen up to the vicinity of the failure point. Since identification of the dilation threshold and failure point (Figure 2.1c) is often based on visual observation of slope of stress-strain curve (e.g. Youn and Tonon, 2010; Villamor Lora et al., 2016), it is very difficult to identify the exact failure point. Before reaching to the failure point, the

differential stress is removed. CP is then increased to the next level, followed by application of differential stress up to the vicinity of failure point. This process is repeated at several CP levels. Using MSF test, it is possible to construct failure criteria for the tested specimen (Kim and Ko, 1979; Youn and Tonon, 2010), however, it should be acknowledged that the residual plastic deformations and induced damage in the earlier stages of the test might affect the accuracy of the test results at latter stages. Figure 2.1e shows the stress path followed in MSF test performed on shale specimens, consisting of six stages performed at CP levels of 5, 10, 20, 30, 40, and 50 MPa.

### 2.2.2 SUMMARY OF EXPERIMENTS

Details of the experimental conditions for the set of experiments reported in this study are presented in Table 2.1. The XRD analysis revealed that two of the specimens are clay-rich and the other two are calcite/quartz-rich. Creep tests were performed on CL1 and CR1. Cyclic tests were performed on CL2 and CR2 specimens, followed by MSF experiments on the same specimens. It should be noted that experiments were conducted on dry specimens due to concerns with (i) potential damage to the internal structure caused by re-hydration process (Villamor Lora et al., 2016), and (ii) the long time (e.g. weeks to months) needed to perform drained tests due to very low permeability of shale rocks (e.g. Islam and Skalle, 2013).

Table 0-1. The information about shale specimens specimens

| Specimen | Specimen dimensions | | Depth (ft) | Mineralogy (wt. %) | | | | | | | Performed Test | CP*[3] (MPa) | DS*[4] (MPa) |
|---|---|---|---|---|---|---|---|---|---|---|---|---|---|
| | D*[1] (mm) | L*[2] (mm) | | Illite | Muscovite | Quartz | Pyrite | Calcite | Dolomite | Gypsum | | | |
| CR1 | 38.04 | 56.87 | 7404 | - | 30.2 | 26.1 | - | 38.5 | 5.2 | - | Creep | 0 to 30 | 0 to 30 |
| CR2 | 38.07 | 65.26 | 7404 | | | | | | | | Cyclic and *[5]MSF | 30 and 0 to 50 | 0 to 45 |
| CL1 | 38.03 | 60.34 | 7467 | 69 | - | 20.8 | 3.1 | 2.9 | - | 4.1 | Creep | 0 to 30 | 0 to 30 |
| CL2 | 38.05 | 65.42 | 7467 | | | | | | | | Cyclic and MSF | 30 and 0 to 50 | 0 to 45 |

*[1]D: Diameter of the Specimen

*[2]L: Length of the Specimen

*[3]CP: Confining Pressure

*[4]DS: Differential Stress

*[5]MSF: Multi-Stage Failure

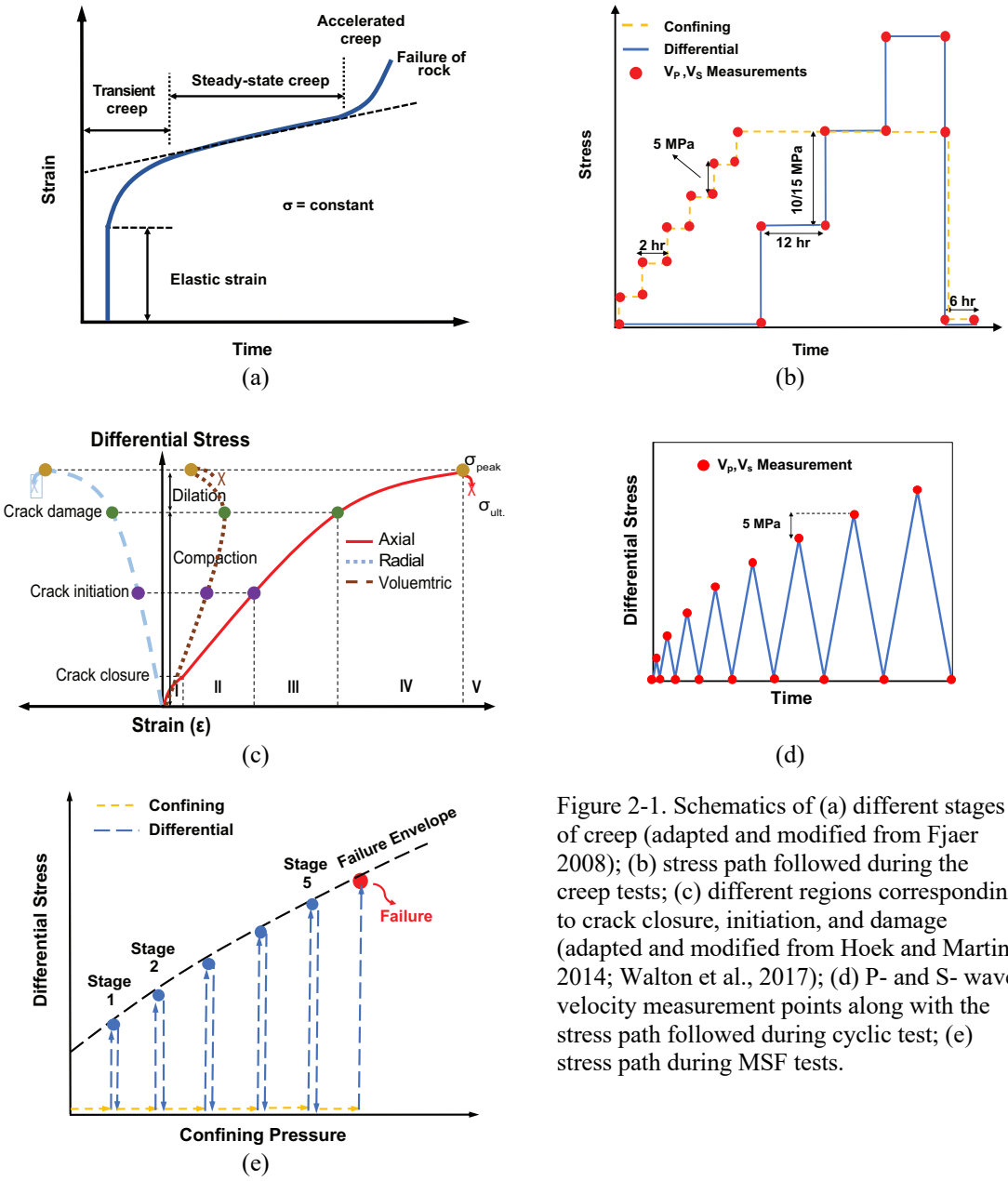


Figure 2-1. Schematics of (a) different stages of creep (adapted and modified from Fjaer 2008); (b) stress path followed during the creep tests; (c) different regions corresponding to crack closure, initiation, and damage (adapted and modified from Hoek and Martin, 2014; Walton et al., 2017); (d) P- and S- wave velocity measurement points along with the stress path followed during cyclic test; (e) stress path during MSF tests.

## 2.3 RESULTS AND DISCUSSION

The strain and ultrasonic P- and S-wave velocity measurements are provided for: (i) creep tests on CL1 and CR1 specimens in Section 2.3.1, (ii) cyclic tests on CL2 and

CR2 specimens in Section 2.3.2. The results of MSF test on CR2 specimen are presented in Section 2.3.3.

### 2.3.1 CREEP TESTS

#### 2.3.1.1 STRAIN MEASUREMENTS

Figures 2.2a and 2.2b illustrate the axial and radial strains during both hydrostatic and triaxial stages for CL1 (clay-rich) and CR1 (calcite/quartz-rich) specimens, which are super-imposed on stress path. During hydrostatic (isotropic compression) stage, axial strains increase from 0 to ~3.2 for CL1 and from 0 to ~0.5 mili-strains for CR1, while radials increase from 0 to ~0.7 for CL1 and from 0 to ~0.35 mili-strains for CR1. As expected, during hydrostatic compression, the measured strains during this stage indicate shortening and shrinkage in axial and radial directions, respectively.

During triaxial stage, axial strains increase from ~3.2 to ~7.3 for CL1 and from ~0.5 to ~1.9 mili-strains for CR1, while radials increase from ~0.7 to ~ -0.6 (cumulative of ~1.3) for CL1 and from ~0.35 to ~ -0.1 (cumulative of ~0.45) mili-strains for CR1, as illustrated in Figures 2.2a and 2.2b. As expected, upon application of differential stress, the specimens exhibit shortening and expansion in axial and radial directions, respectively. Although CR1 was subjected to DS of 30 MPa (compared to DS of 45 MPa for CL1) in the last stage of triaxial creep, this does not explain the significantly higher cumulative strains during triaxial stage for CL1 compared to CR1. Given the same organic content of the both specimens, this substantial difference can be attributed to different mineralogical content. As evident from Figures 2.2a and 2.2b, the radial strains are much lower than axial.

This could be an indication of compaction of organic matter and closure of microcracks, leading to volume loss (Sone and Zoback, 2014; Villamor Lora et al., 2016).

For CL1, at the beginning of triaxial stage (DS increasing from 0 to 15 MPa), there is a significantly-higher increase in axial strain compared to latter stages of the creep test (i.e. DS from 15 to 30 MPa, and from 30 to 45 MPa). This could be due the fact that, although some of the existing micro-cracks were closed during hydrostatic stage, the majority of the micro-cracks were closed during the first application of differential stress. The radial strains, on the other hand, show uniform deformation, transitioning from one DS stage to the next. Upon unloading, the strains indicate permanent plastic deformations in both specimens, attributed to the secondary stage of creep.

Variation of cumulative strain (elastic, viscoelastic and total) with differential stress during triaxial stage of the creep test for CL1 and CR1 are shown in Figures 2.2c and 2.2d, respectively. The elastic strain was calculated when the applied differential stress was increasing, while viscoelastic strain was calculated when differential stress was keeping constant. The total strains were estimated by adding the elastic and viscoelastic strains. At the tested stress levels, the variation of cumulative elastic, time-dependent, and total strains with differential stress show a linear trend as was also observed by other studies (Li and Ghassemi, 2012; Sone and Zoback, 2013; Sone and Zoback, 2014).

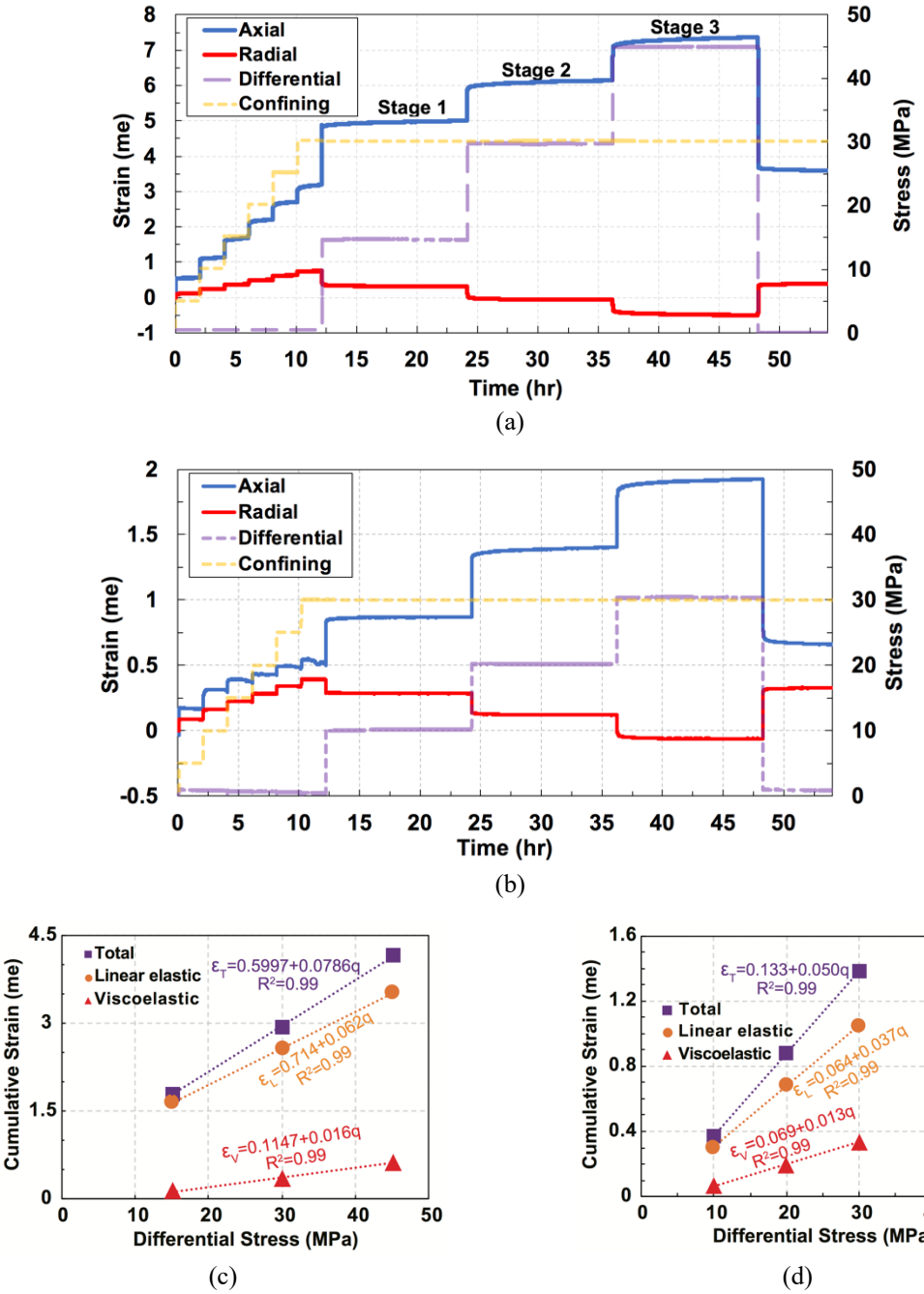


Figure 2-2. Stress and strains during creep test on (a) CL1 (clay-rich) and (b) CR1 (calcite/quartz -rich) specimen; cumulative strain versus differential stress (elastic, viscoelastic and total) for (c) CL1 (clay-rich) and (d) CR1 (calcite/quartz-rich) specimen.

Figures 2.3a and 2.3b show the viscoelastic strains during hydrostatic stage for CL1 and CR1 specimens, respectively. For CL1, the majority of the viscoelastic deformations

occur in the first half-hour of each stage of CP. After that, this specimen shows additional viscoelastic deformations at higher CP levels, and consequently, as expected, increasing the confining level leads to higher magnitudes of viscoelastic deformation in latter times. Compared to CL1 specimen, CR1 does not show notable secondary creep.

Figures 2.3c and 2.3d show the viscoelastic strains during triaxial stage for CL1 and CR1, respectively, indicating more creep in axial direction compared to the radial. It can be observed that the rate of axial and radial viscoelastic strains decreases as the creep stages progress. For both specimens, the majority of the viscoelastic deformations occur in the first ~6 hours of each stage in the axial direction, while, it occurs in the first ~3 hours in the radial direction. As the differential stress increases, moving from one stage to the next, both specimens exhibit higher viscoelastic deformations. For both specimens, the ratio of the magnitude of 12-hour creep between Stages 1 and 2 to that of between Stages 2 and 3 is higher in the axial direction, however, there is a relatively-linear increase in radial strain transitioning from Stage 1 to 2 to that of Stage 2 to 3. High clay/organic content can be identified as responsible causes for observed creep during both hydrostatic and triaxial stages. In shale rocks, since most of the pores are located within clay and organic matters (e.g. Sone and Zoback, 2013b), compaction of pore volume and subsequently, porosity reduction and pore stiffening (Sone and Zoback, 2013b) can cause stiffening of the specimen. The higher creep observed in CL1 compared to CR1 can be explained by: (i) the fact that increasing clay content leads to higher rates of viscoelastic deformation in shale sediments, and (ii) unlike calcite/quartz minerals, clay minerals show stable time-dependent sliding response due to their low friction and velocity strengthening frictional properties (Sone and Zoback, 2013b). The creep response of CR1 specimen could be also

resulted from pore collapse, and micro-crack propagation. Sone and Zoback (2013a) found that softer specimens show higher creep compliance. As shown in Figures 2.3e and 2.3f, higher creep compliance observed for CL1 compared to CR1, can be explained by stiffness difference between these specimens.

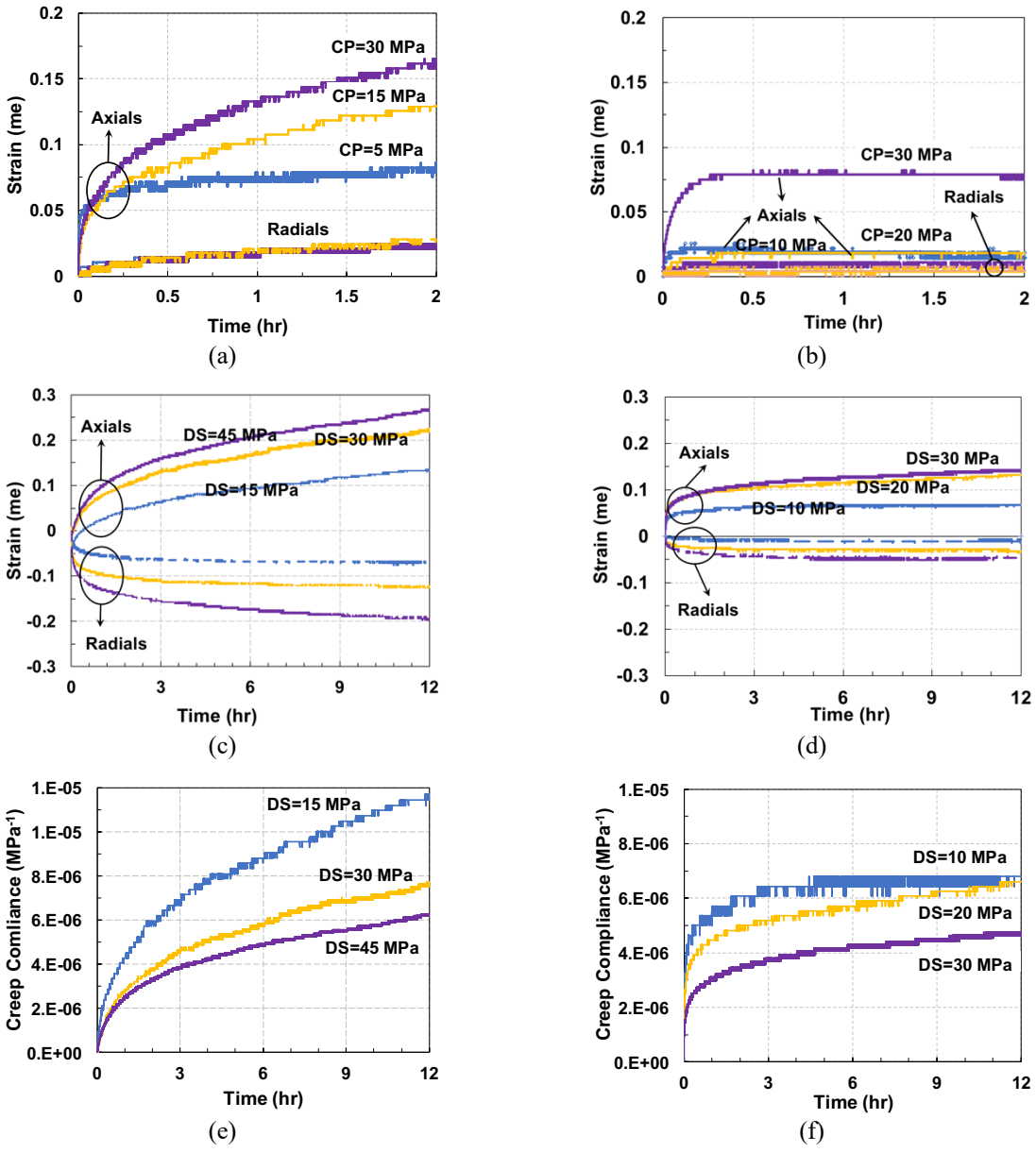


Figure 2-3. Creep strains during hydrostatic stage on (a) CL1 (clay-rich), and (b) CR1 (calcite/quartz-rich); creep strains during triaxial stage on (c) CL1 (clay-rich), and (d) CR1 (calcite/quartz-rich); creep compliance for (e) CL1 (clay-rich), and (f) CR1 (calcite/quartz-rich) specimens.

#### 2.3.1.2 CREEP MODELS

In order to predict the long-term viscoelastic behavior of the shale gas reservoirs, it is useful to fit the experimental data to different creep models, including Power-Law and Burgers models. The Power-Law model can be explained as follows:

$$\varepsilon = \sigma \times Bt^n \tag{2.1}$$

in which $\sigma$ is the applied differential stress (MPa), $\varepsilon$ is the axial strain, and B and n are empirical parameters. The viscoelastic behavior (creep strain hardening) can be explained by n parameter in the power-law model, while, structure of the rock specimen is controlling the B factor which has a higher impact on the compliance and hence, on the elastic response of the specimen (Sone and Zoback, 2014; Rassouli and Zoback, 2017 and 2018).

The Burgers model, on the other hand, is a rheological model consisting of a Maxwell unit $(E_1, \eta_1)$ and a Voight-Kelvin unit $(E_2, \eta_2)$ as shown in Figure 2.4. The differential equation for Burgers model under a constant differential stress is:

$$\frac{\eta_1\eta_2}{E_2}\ddot{\varepsilon} + \eta_1\varepsilon = \frac{\eta_1\eta_2}{E_1E_2}\ddot{\sigma} + \left(\frac{\eta_1}{E_1} + \frac{\eta_1}{E_2} + \frac{\eta_2}{E_2}\right)\dot{\sigma} + \sigma \tag{2.2}$$

The solution to this differential equation can be obtained as:

$$\varepsilon = \frac{\sigma_1}{E_1}\left[1 + \frac{E_1}{\eta_1}t + \frac{E_1}{E_2}\left(1 - e^{-\frac{E_2}{\eta_2}t}\right)\right] \tag{2.3}$$

where $E_1$ and $E_2$ are in units of MPa, representing the springs, and $\eta_1$ and $\eta_2$ are in units of MPa.Sec, representing the dashpots. The estimated parameters B, n, $E_1$, $E_2$, $\eta_1$, and $\eta_2$ for CL1 and CR1 specimens are presented in Table 2.2.

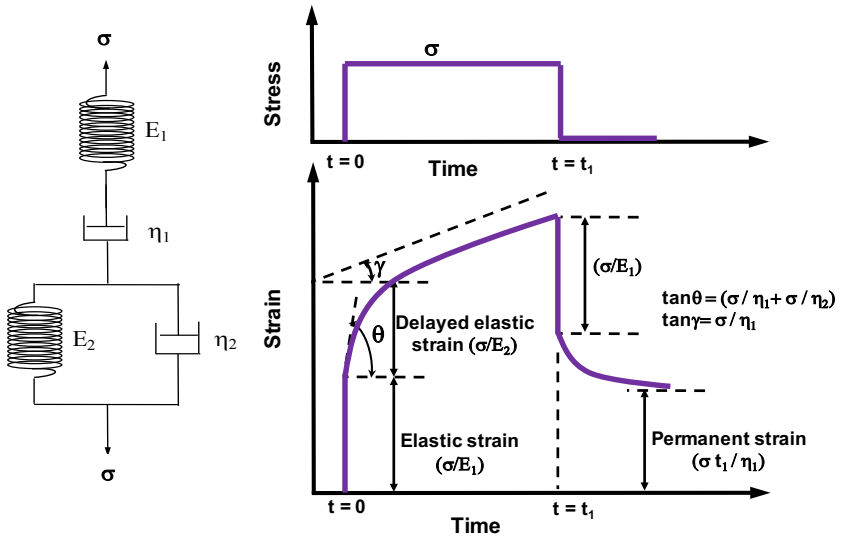


Figure 2-4. Schematics of a Burgers model for creep test (adapted and modified from Puzrin (2012)).

It can be observed that n values are higher for CL1 compared to CR1, attributed to the more ductile response in specimens with higher clay content. As higher stresses are applied, the n value for CR1 increases, however, there is not a viable trend for n value in CL1. For the calcite/quartz-rich specimen, the decrease of B parameter at higher stress levels indicates a creep-hardening process as was also observed by Rassouli and Zoback (2017 and 2018), however, for the clay-rich specimen, the decrease of B value at higher stress levels shows a creep-softening behavior (Rassouli and Zoback, 2017). It can be observed that as higher stresses are applied, the estimated values of $E_2$, $\eta_1$, and $\eta_2$ increase, pointing to the fact the creep response is not purely viscoelastic. The higher values of $E_2$ and $\eta_2$ for CL1 compared to CR1, both at DS of 30 MPa, indicate that there is a higher tendency for specimen with higher clay to show viscoelastic response compared to the specimen with higher calcite/quartz content.

Table 2-2. Parameters of Burgers' and Power-Law Models for CL1 and CR1 specimens

| Specimen | Model | Parameter | Stage | | | |
|---|---|---|---|---|---|---|
| | | | I | II | III | Unloading |
| CL1 (Clay-rich) | Burger's | $E_1$ (GPa) | 15.0 | 16.3 | 16.0 | 16.5 |
| | | $E_2$ (GPa) | 187 | 332 | 401 | 382 |
| | | $\eta_1$ (GPa.h) | 1800 | 2553 | 3223 | 4031 |
| | | $\eta_2$ (GPa.h) | 141 | 190 | 221 | 21 |
| | Power-Law | n | 0.414 | 0.481 | 0.453 | 0.152 |
| | | B ($MPa^{-1}$) | 1.43E-07 | 4.58E-08 | 4.89E-08 | -8.43E-07 |
| CR1 (Calcite/quartz –rich) | Burger's | $E_1$ (GPa) | 27.2 | 25.3 | 26.7 | 25.0 |
| | | $E_2$ (GPa) | 179.26 | 261.53 | 419.74 | 325 |
| | | $\eta_1$ (GPa.h) | 10888.98 | 7254.58 | 10091.10 | 5939 |
| | | $\eta_2$ (GPa.h) | 37.47 | 73.84 | 133.55 | 30 |
| | Power-Law | n | 0.0955 | 0.152 | 0.184 | 0.113 |
| | | B ($MPa^{-1}$) | 2.38E-06 | 1.03E-06 | 4.93E-07 | -1.29E-06 |

Using the estimated values for Power-Law model (B and n) and Burgers model ($E_1, E_2, \eta_1$, and $\eta_2$), the predicted viscoelastic response (for each level of differential stress as well unloading) against experimental data are illustrated in Figures 2.5 and 2.6 for CL1 and CR1, respectively. As evident in Figures 2.5 and 2.6, both models can potentially predict the creep response, with the Burgers model yielding better predictions.

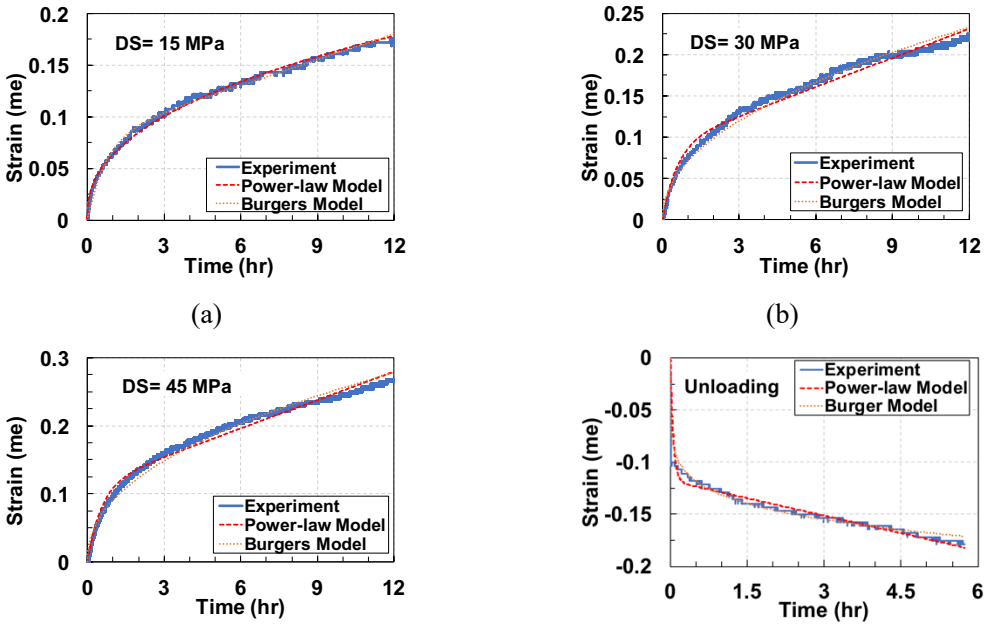


Figure 2-5. Comparison of Power law and Burgers' model prediction against experimental data for CL1 (clay-rich) at different differential stress levels: (a) 15, (b) 30, (c) 45 MPa, and (d) unloading stage.

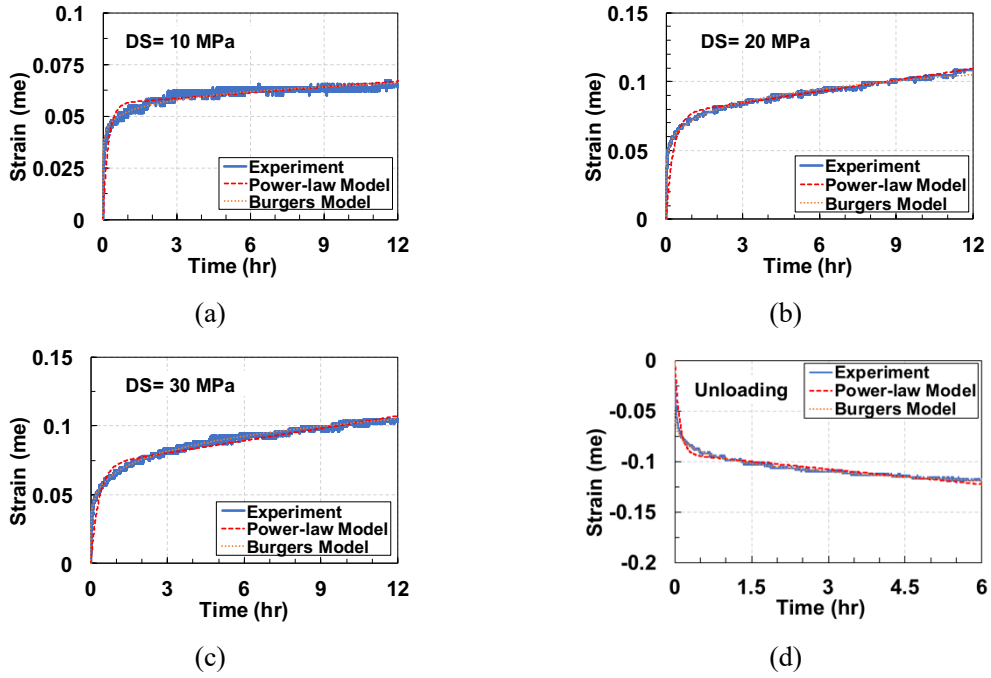


Figure 2-6. Comparison of Power law and Burgers' model prediction against experimental data for CR1 (calcite/quartz-rich) at different differential stress levels: (a) 10, (b) 20, (c) 30 MPa, and (d) unloading stage.

#### 2.3.1.3 ESTIMATION OF DYNAMIC MODULI AND SENSITIVITY OF ULTRASONIC VELOCITY MEASUREMENTS

The measured P- and S-wave velocities, super-imposed on stress path, are illustrated for CL1 and CR1 in Figures 2.7a and 2.7b, respectively. As higher stress levels are applied (both CP and DS), the ultrasonic P- and S-wave velocities increase, which can be attributed to closure of fractures. There is a substantial increase in ultrasonic velocities in both specimens during hydrostatic stage, with higher increase in earlier stages of hydrostatic loading. The significant increase of P- and S-wave velocity measurements during earlier stages of hydrostatic loading can be attributed to the fact that at lower stresses the created fractures, due to retrieval and relieving specimens from in-situ stresses, can be closed with a higher rate compared to those closed at higher stresses. During the triaxial stage, the velocity measurements linearly increase with an increase in DS level. In addition, as evident in Figures 2.7a and 2.7b, the increase of P-wave velocity due to the increase of DS at the beginning of each stage is the highest in Stage 1 and gradually decreases in Stages 2 and 3. This could be an indication of an increase in the stiffness of the specimens during the first stage of triaxial loading, which becomes less pronounced in Stages 2 and 3.

On the other hand, it should be noted that during the viscoelastic stage of the experiment (constant DS and CP), in both hydrostatic and triaxial stages, there is a slight increase in velocity measurements, potentially indicating additional closure of the micro-cracks and/or further compaction of clay and organic content.

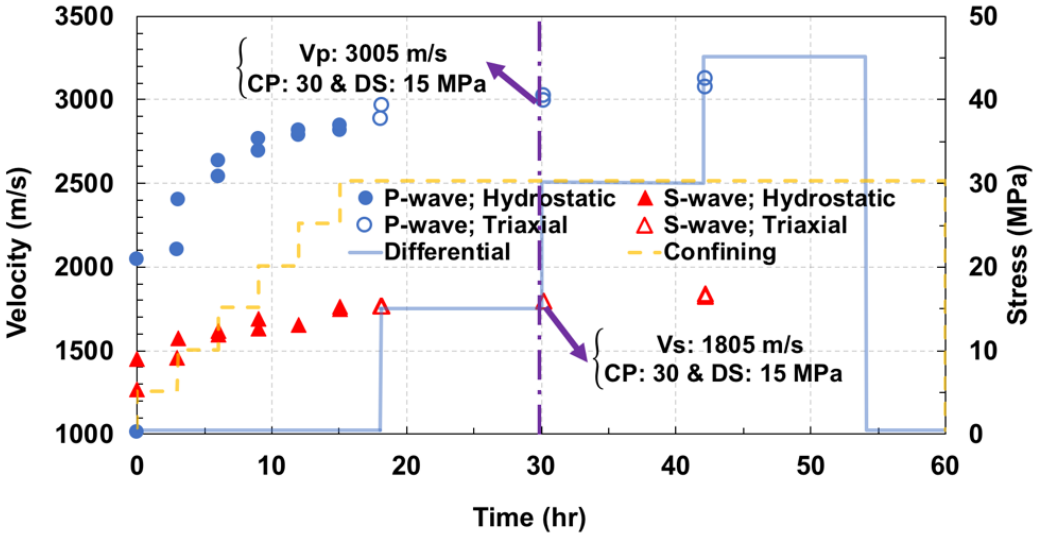


(a)

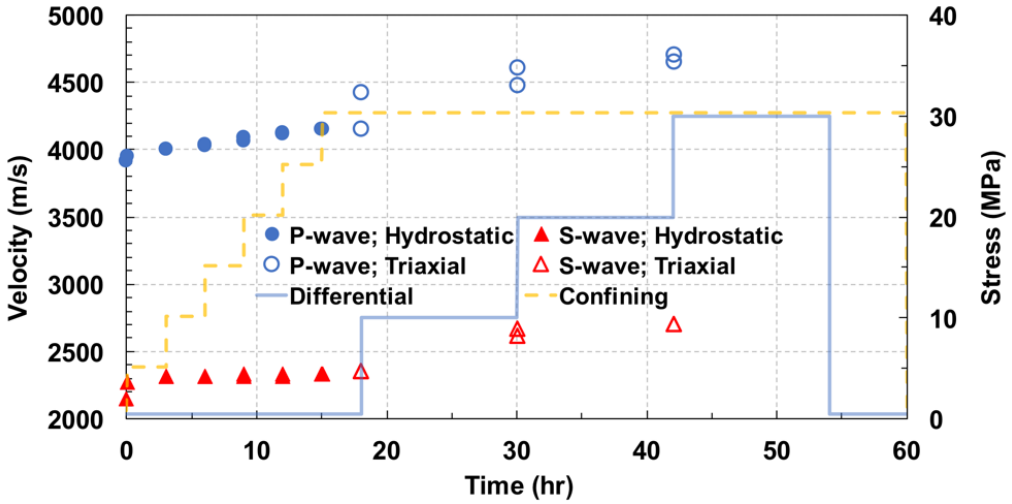


(b)

Figure 2-7. P- and S- wave velocity measurements superimposed on stress path during the creep tests on: (a) CL1 (clay-rich), and (b) CR1 (calcite/quartz-rich).

The estimated static bulk modulus (K) values at different CP levels for CL1 and CR1 specimens are shown in Figures 2.8a and 2.8b, respectively, indicating lower bulk modulus for CL1 compared to CR1, which can be, in part, attributed to its higher clay content, leading to higher compressibility during hydrostatic stage. Coupling moduli (J) estimations for different confining levels, are presented in Figures 2.8c and 2.8d for CL1

and CR1 specimens, respectively. The range of coupling modulus for CL1 specimen is one order of magnitude less than that of CR1, which can be in part attributed to the different degrees of anisotropy for these specimens.

Figures 2.8e and 2.8f show the estimated static and dynamic Young's modulus (E) values at three stages of DS for CL1 and CR1 specimens, respectively. Subjecting shale specimens to higher differential stresses can lead to (i) increase/decrease in static moduli, and (ii) increase in dynamic moduli. Since shale rocks typically contain high clay and organic content, new micro-cracks may develop within the specimen as higher differential stresses are applied. For the tested shale rocks in this study, as higher differential stresses were applied during the tests, both CL1 and CR1 specimens exhibited (i) decrease in the estimated static Young's modulus, and (ii) increase in estimated dynamic Young's modulus. While subjecting specimens to higher differential stresses, CL1 specimen showed higher decrease in estimated static Young's modulus, compared to CR1, which might be contributed to its higher clay content. A similar trend was also observed in other studies (e.g. Dewhurst et al., 2011; Rassouli and Zoback, 2018). The estimated dynamic Young's modulus increased for both specimens, as higher differential stresses are applied, a trend which was also observed in several studies (e.g. Sarout et al., 2007; Kuila et al., 2011; Dewhurst et al., 2011; Sone and Zoback, 2013a; Villamor Lora, 2015). This increase in dynamic Young's modulus reflected in the measured P- and S-wave velocities, as higher differential stresses are applied, might be explained by (i) closure of some of the existing micro-cracks and other defects, (ii) increased grain-grain contact, and (iii) decrease in porosity (Schon, 2015).

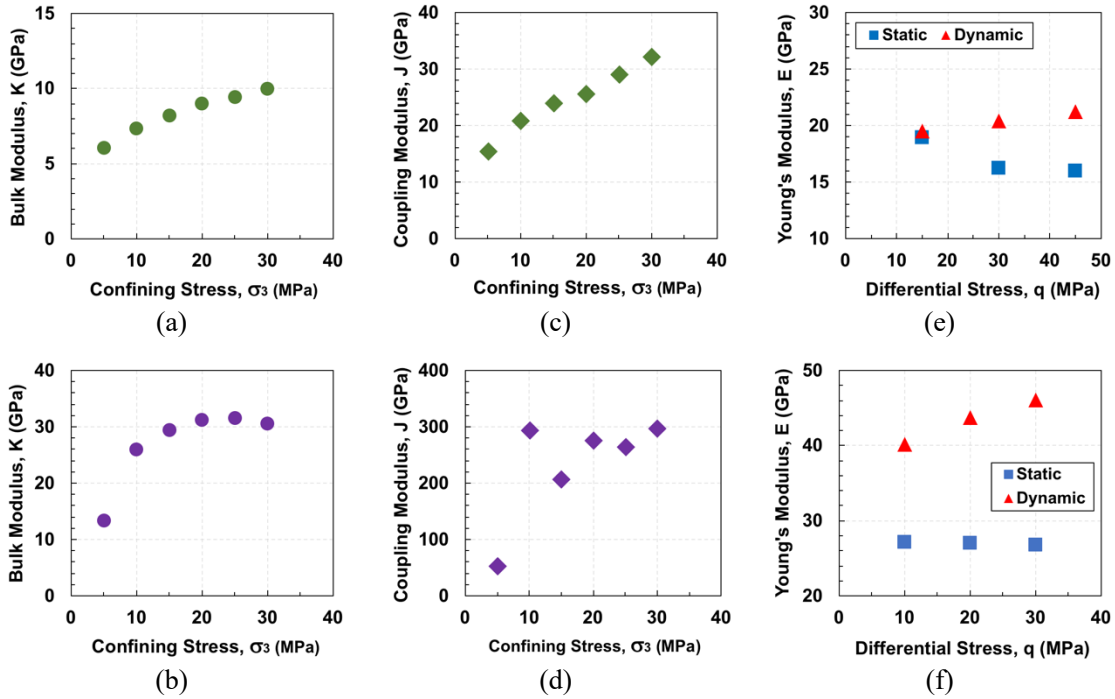


Figure 2-8. Estimated static bulk modulus during hydrostatic stage for: (a) CL1 (clay-rich), and (b) CR1 (calcite/quartz-rich) specimens; estimated static coupling modulus during hydrostatic stage for: (c) CL1 (clay-rich), and (d) CR1 (calcite/quartz-rich) specimens; estimated static and dynamic Young's modulus during triaxial stage for: (e) CL1 (clay-rich), and (f) CR1 (calcite/quartz-rich) specimens.

### 2.3.2 CYCLIC TESTS

Figure 2.9b shows the time evolution of axial and radial strains for CR2 specimen in cyclic test with stress path presented in Figure 2.9a. Significantly higher strains in axial direction compared to radial direction can be seen in Figure 2.9b. The specimen does not exhibit significant plastic deformations, with linear behavior in both loading and unloading paths, up to DS of 30 MPa. However, beyond this stress level, both axial and radial strains show some degree of non-linearity. Figure 2.9c shows the axial, radial, and volumetric strains against differential stress. Although axial and radial strains seem linear along the stress path, the volumetric strains indicate nonlinearity, particularly above the differential

stress of 30 MPa. The estimated static moduli at different cycles are presented in Table 2.3, indicating slightly higher values of Young's modulus during unloading compared to loading. For example, the static Young's modulus during loading and unloading with application of DS from 0 to 40 MPa are 26 and 26.2 GPa, respectively.

P- and S-wave velocity measurements at different stress levels during the test are illustrated in Figure 2.9d. The magnitude of P- and S-wave velocities ranging from 4500 to 4800 and 2650 to 2950 m/s, respectively. Both P- and S-wave velocities increase/decrease follow the increase/decrease in differential stress. In general, transitioning from one cycle to the next, both ultrasonic wave velocities increase as differential stress increases, indicating that within the range of applied stresses, the closure of the existing micro-cracks (perpendicular to the direction of loading) is more dominanat than creation of new micro-cracks. The estimated dynamic moduli, based on these velocity measurements, are presented in Table 2.3, indicating an increasing trend with the applied differential stress. For example, the dynamic Young's modulus at DS levels of 15, 30, and 45 MPa are 48.9, 51.1, and 51.3 GPa, respectively.

Rock specimens show an elastic-plastic response during loading, while, elastic response is more dominant during unloading (Fjar, 2008). This can explain the higher values of static Young's modulus during unloading compared to loading. Hence, the elastic behavior of the rock can be better explained by unloading Young's modulus. On the other hand, the estimated dynamic Young's modulus is not affected by loading/unloading. This might be attributed to the fact that dynamic moduli reflect the elastic properties of the rock, rather than capturing plastic deformations.

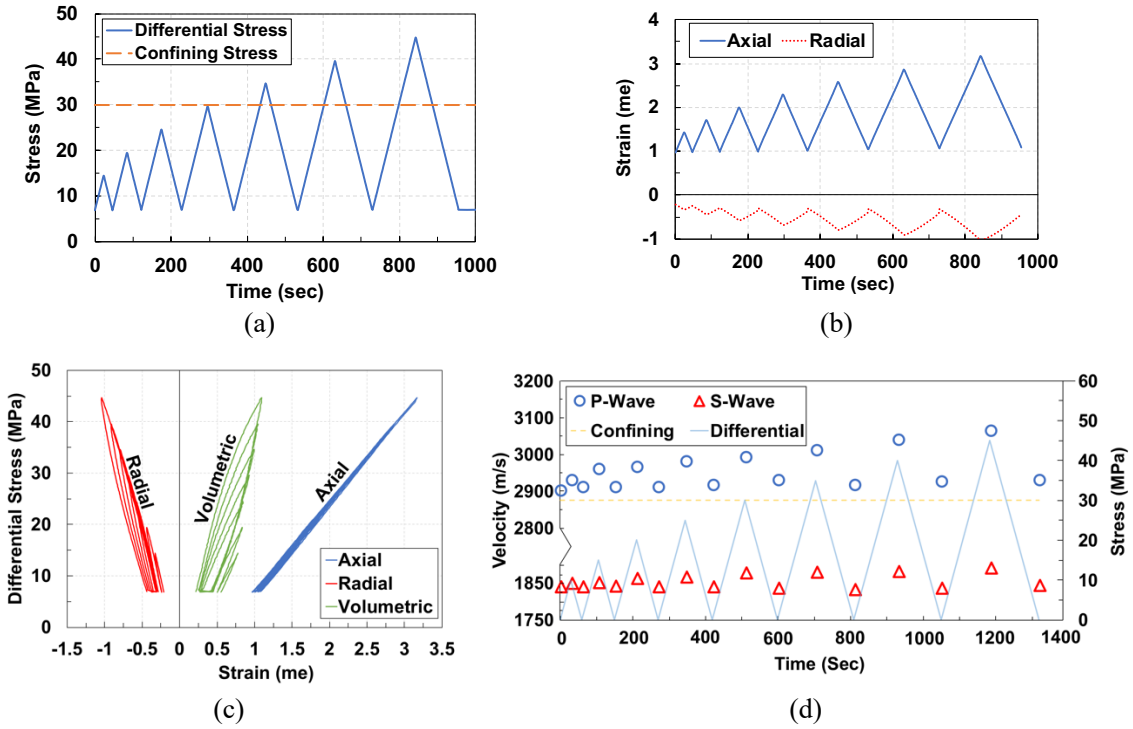


Figure 2-9. Results from cyclic test on CL2 specimen: (a) stress path followed during the test; (b) variation of strains versus time; (c) variation of strains versus differential stress; and (d) P- and S- wave velocity measurements during the test superimposed on the stress path.

*Note that the velocity axis has been broken for better illustration.

At close-to-zero differential stresses and as the cycles progress, the measured P- and S-wave velocities might provide some insight into the state of the internal structure of the specimen. The measured P-wave velocities increase/decrease at these points with no identifiable trend. This observation indicates that either closure/opening of existing/new micro-cracks are the dominant mechanism, which in turn, depends on the initial state of the specimen (e.g. distribution of micro-cracks) and the previous loading/unloading cycles that the specimen has undergone.

Table 2-3. The estimated dynamic/static moduli for the CR2 and CL2 specimens under cyclic test (confining stress is constant at 30 MPa)

| Type | | DS (MPa) | Specimen | | | | | |
|---|---|---|---|---|---|---|---|---|
| | | | CR2 (Calcite/quartz-rich) | | | CL2 (Clay-rich) | | |
| | | | E (GPa) | ν (%) | G (GPa) | E (GPa) | ν (%) | G (GPa) |
| Static | Loading | 0-5-0 | 24.7 | 24.4 | 9.3 | N/A | N/A | N/A |
| | Unloading | | 25.4 | 23.7 | 9.6 | N/A | N/A | N/A |
| Dynamic | | 5 | N/A | N/A | N/A | 20.9 | 18.1 | 8.8 |
| Static | Loading | 0-10-0 | 26.9 | 24.5 | 10.1 | N/A | N/A | N/A |
| | Unloading | | 27.4 | 24.4 | 10.2 | N/A | N/A | N/A |
| Dynamic | | 10 | 48.3 | 20.9 | 20 | 21 | 18.4 | 8.8 |
| Static | Loading | 0-15-0 | 27.4 | 24.7 | 10.2 | 16.7 | 25.3 | 6.2 |
| | Unloading | | 27.8 | 25 | 10.3 | 16.4 | 19.6 | 6.4 |
| Dynamic | | 15 | 48.9 | 20.9 | 20.2 | 21.2 | 18.4 | 8.9 |
| Static | Loading | 0-20-0 | 27.1 | 25.6 | 10.1 | 17.5 | 26.8 | 6.4 |
| | Unloading | | 27.2 | 25.8 | 10.1 | 17 | 21.4 | 6.5 |
| Dynamic | | 20 | 49.1 | 21.5 | 20.2 | 21.4 | 18.5 | 9 |
| Static | Loading | 0-25-0 | 26.7 | 26 | 9.9 | 17.7 | 28.5 | 6.4 |
| | Unloading | | 26.8 | 26.2 | 9.9 | 17.2 | 23.6 | 6.5 |
| Dynamic | | 25 | 49.5 | 21 | 20.4 | 21.5 | 18.6 | 9 |
| Static | Loading | 0-30-0 | 26.3 | 26.6 | 9.7 | 17.9 | 30.2 | 6.4 |
| | Unloading | | 26.2 | 26.6 | 9.7 | 17.5 | 24.9 | 6.5 |
| Dynamic | | 30 | 51.1 | 21.4 | 21.1 | 21.7 | 19.4 | 9.1 |
| Static | Loading | 0-35-0 | 26.1 | 27.3 | 9.6 | 18.1 | 31.6 | 6.4 |
| | Unloading | | 26.3 | 27.3 | 9.6 | 17.9 | 27 | 6.5 |
| Dynamic | | 35 | 51 | 19.6 | 21.3 | 21.9 | 19.1 | 9.1 |
| Static | Loading | 0-40-0 | 26 | 28.4 | 9.5 | 18.3 | 33.5 | 6.4 |
| | Unloading | | 26.2 | 27.8 | 9.6 | 18.2 | 28.8 | 6.6 |
| Dynamic | | 40 | 51.3 | 20.2 | 21.3 | 22.1 | 19.1 | 9.2 |
| Static | Loading | 0-45-0 | N/A | N/A | N/A | 18.2 | 34.7 | 6.3 |
| | Unloading | | N/A | N/A | N/A | 18.2 | 29.7 | 6.5 |
| Dynamic | | 45 | 51.3 | 21.2 | 21.2 | 22.3 | 19 | 9.2 |

On the other hand, the measured S-wave velocities at these points in the earlier cycles (up to cycle 5) of the test, remain almost constant, while, in the latter cycles of the test (cycles 6 to 8), starts to decrease slightly. This could be an indication of the onset of crack initiation (region III in Figure 2.1a) as higher differential stresses are applied.

Figure 2.10b illustrates the time evolution of axial and radial strains for CL2 specimen subjected to cyclic test, with stress path presented in Figure 2.10a. It should be noted that the strain measurements for differential stresses of less than 7 MPa are not shown in Figure 2.10b. The strain measurements between DS of 0 to 7 MPa were highly-scattered and did not follow a reasonable trend, due to closure of initial micro-fractures. Axial strains show a linear response, with very small plastic deformations, whereas, radial strains exhibit a nonlinear response, with more pronounced plastic deformations, as opposed to CR2. Figure 2.10c shows the variation of axial, radial, and volumetric strains with differential stress. As it can be seen from Figure 2.10c, the axial strains show no hysteresis, while, radial and volumetric show significant hysteresis.

The estimated static moduli at different cycles are presented in Table 2.3, indicating that in successive cycles, the estimated static Young's modulus is decreasing from the 1st to the 7th cycle for CR2 (calcite/quartz-rich) specimen, while, it is increasing for the CL2 (clay-rich) specimen. However, the estimated dynamic Young's modulus increases with the successive cycles for both specimens, which could be due to closure of micro-cracks in the successive cycles given that within the applied stresses, the specimens are below the crack initiation threshold. For example, the estimated static Young's modulus during

loading at DS from 0 to 15, 0 to 30, and 0 to 45 MPa are 16.7, 17.9, and 18.2 GPa, respectively, which indicates ~9% increase.

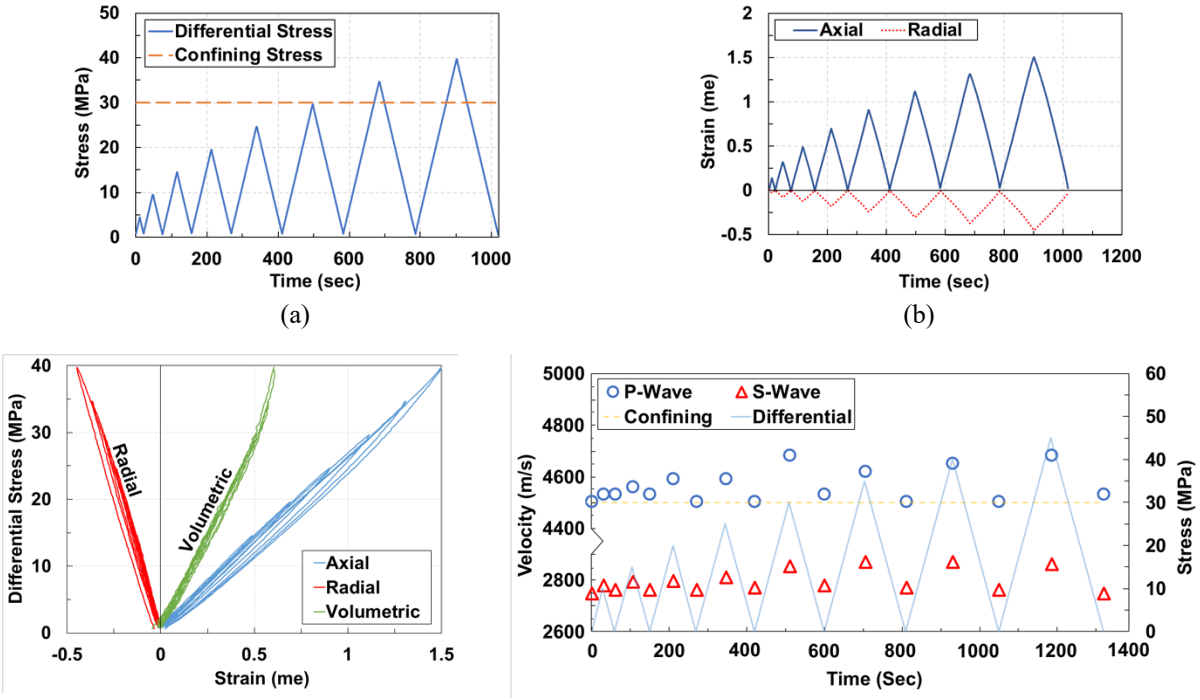


Figure 2-10. Results from cyclic test on CR2 specimen: (a) stress path followed during the test; (b) variation of strains versus time; (c) variation of strains versus differential stress; and (d) P- and S- wave velocity measurements during the test superimposed on the stress path.

*Note that the velocity axis has been broken for better illustration.

The estimated Young's modulus (from both static and dynamic) during unloading is typically higher than those measured during loading as was also observed for CR2, explained by the fact that some of the micro-cracks that were closed at a specific stress level during loading, do not re-open during unloading at the same stress level. For CL2 specimen, however, the estimated Young's modulus during loading is higher than that during unloading. This observation could be attributed to the fact that since the lower bound

of the applied stress level is around 7 MPa (not zero), the initial non-linearity and plastic deformations are not present. Therefore, the estimated Young's modulus during unloading might be affected by the almost-zero plastic deformations. The estimated cumulative plastic strains at different stress levels are presented in Table 2.4. The cumulative plastic strains were calculated by subtracting the axial strain before loading from that of after loading.

Table 2-4. The estimated plastic strain (cumulative) under cyclic test

| Specimen | DS (MPa) | Plastic strain (micro strain) |
|---|---|---|
| CR2 (Calcite/quartz-rich) | 0-to-10 | 11 |
| | 0-to-15 | 11 |
| | 0-to-20 | 20 |
| | 0-to-25 | 0 |
| | 0-to-30 | 18 |
| | 0-to-35 | 12 |
| | 0-to-40 | 0 |
| | 0-to-45 | -132 |
| CL2 (Clay-rich) | 7-to-10 | N/A |
| | 7-to-15 | 7 |
| | 7-to-20 | 6 |
| | 7-to-25 | 7 |
| | 7-to-30 | 20 |
| | 7-to-35 | 39 |
| | 7-to-40 | 14 |
| | 7-to-45 | 21 |

P- and S-wave velocity measurements at different stress levels during the test are shown in Figure 2.10d. The magnitude of P- and S-wave velocities ranges from 2900 to 3200 and 1800 to 1900 m/s, respectively. Both P- and S-wave velocities are sensitive to variation of differential stress in each cycle and closely follow the stress path trend. In

addition, in all cycles, the measured P- and S-wave velocities after unloading (at DS of close to zero) are higher than those prior to loading (at DS of close to zero). The estimated dynamic moduli, based on these velocity measurements, are presented in Table 2.3, indicating an increasing trend with the applied DS as observed for CR2 specimen. For example, the dynamic Young's modulus at DS of 15, 30, and 45 MPa are 21.2, 21.7, and 22.3 GPa, respectively.

The variation of the measured ultrasonic velocities with differential stress for both specimens is presented in Figure 2.11. As evident in Figures 2.11a-d, within the range of applied differential stresses, the measured P- and S-wave velocities linearly increase with DS, with good regression values (i.e. $R^2$=0.97) for the CL2 specimen and reasonable values for CR2. This might be an indication that within the range of the applied stresses, the specimens were below the CI threshold (region II in Figure 2.1c).

It is commonly-accepted that the estimated dynamic moduli are higher than those of static (e.g. Paterson and Wong, 2005; Sone and Zoback, 2014; Schon, 2015). This discrepancy can be attributed to: (i) significantly lower strain amplitudes for dynamic measurements compared to static, (ii) exceeding the elastic limit of the minerals due to stress concentration at grain contact, and (iii) stress-induced porosity reduction (Fjar, 2008). This discrepancy can be exacerbated in shale rocks, due to their heterogeneous micro-structure, non-linearity, and plasticity effects (Fjar, 2008). We observed that the ratio of dynamic Young's modulus to that of static, namely $\frac{E_{dynamic}}{E_{static}}$, is higher for specimen with stiffer (calcite/quartz) minerals, i.e. CR1 and CR2, compared to those with softer (clay)

minerals, i.e. CL1 and CL2. Therefore, this ratio might imply that there is a link between the clay content and $\frac{E_{dynamic}}{E_{static}}$ ratio.

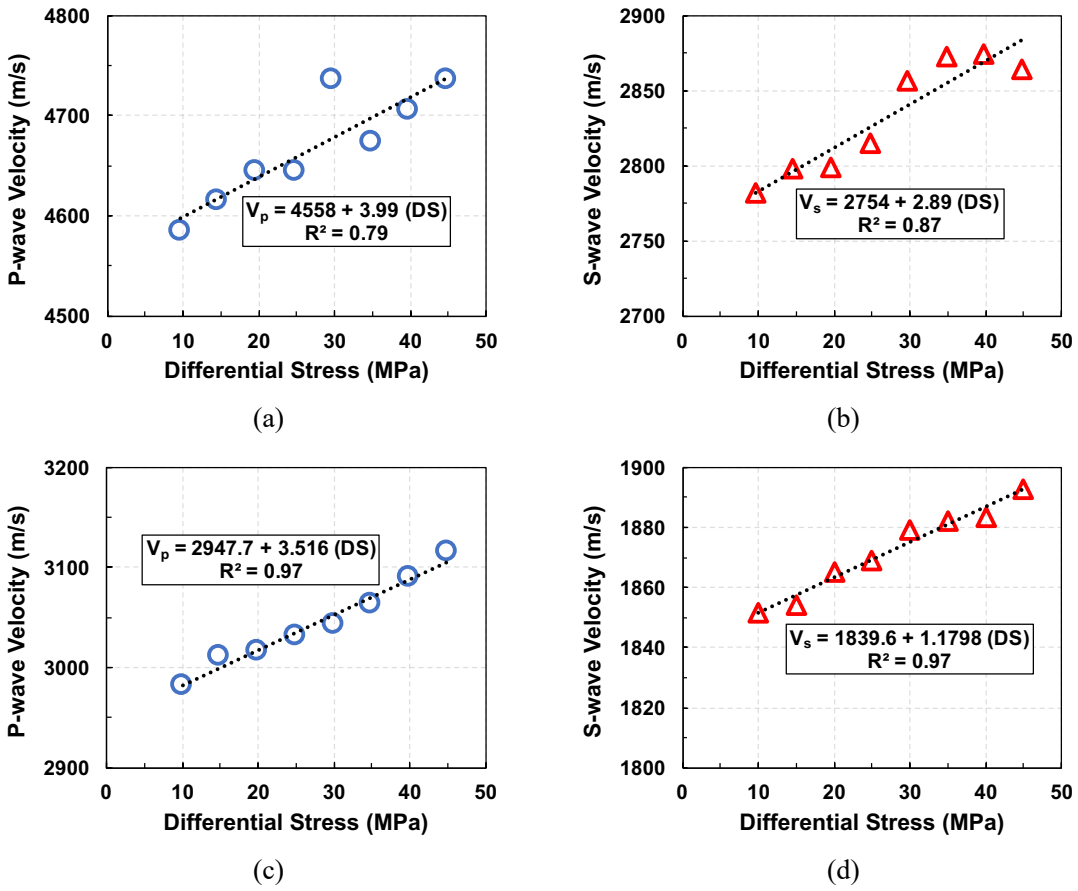


Figure 2-11. Variation of P-wave and (b) S-wave velocity measurements with differential stress during cyclic test on (a) and (b) CL2 specimen, and (c) and (d) CR2 specimen.

### 2.3.3 MSF TEST

The MSF test was first performed on CL2 specimen. Unfortunately, due to difficulties involved in performing the test, particularly identifying the crack damage threshold and failure strength from stress-strain data, the specimen was failed pre-maturely in the first stage of the test (CP of 5 MPa). In addition, the embedded ultrasonic transducers

were damaged in this experiment due to failure of this specimen, and therefore, for performing the MSF test on CR2, regular core holders (without ultrasonic transducers) were used. Figure 2.12 presents the variation of axial and radial strains with differential stress for all six stages of the MSF test performed on CR2. It can be observed from Figure 2.12a that the peak strength values are increasing in successive stages (with confining level).

Plastic deformation induced in the first stage of the test is ~0.4 mili-strains, which increases to ~0.9 in the last stage of the test. Figure 2.12b shows an example of axial, radial, and volumetric strains corresponding to the Stage 4 of the test (CP of 30 MPa), indicating that the specimen reached to the crack damage (dilation) threshold at DS of ~112 MPa, and to the proximity of the peak (failure) strength at DS of ~126 MPa, before DS was removed. Volumetric strain is initially dominated by compaction behavior until the crack damage threshold is reached, then the volumetric strain follows a dilatancy-dominated behavior. Based on the strain data, the failure points were identified and the variation of axial and radial strains during only loading are illustrated in Figure 2.12c for better clarity. As expected, increasing the confinement level leads to higher strength, with higher rate of increase at lower confinement levels. At low DS levels (i.e. up to ~10 MPa), there is a significant non-linearity corresponding to region I in Figure 2.1c, associated with closure of micro-cracks, with higher degree of nonlinearity at lower confinement levels.

Figure 2.13 shows the post-mortem X-Ray CT-images (side views and cross section) of the specimen. The planes of weakness (horizontal) can be observed in the images. Multiple fractures, both shear and tensile, resulted from performing different

stages of the test can be observed in the images. Although not conclusive, the orientation of the failure plane with respect to the major principal stress (in this case, cylindrical axis), measured in the middle section of the core to avoid end effects, was estimated as ~60 degree. Fractures sub-parallel to the identified failure plane could have been formed during different stages of the test.

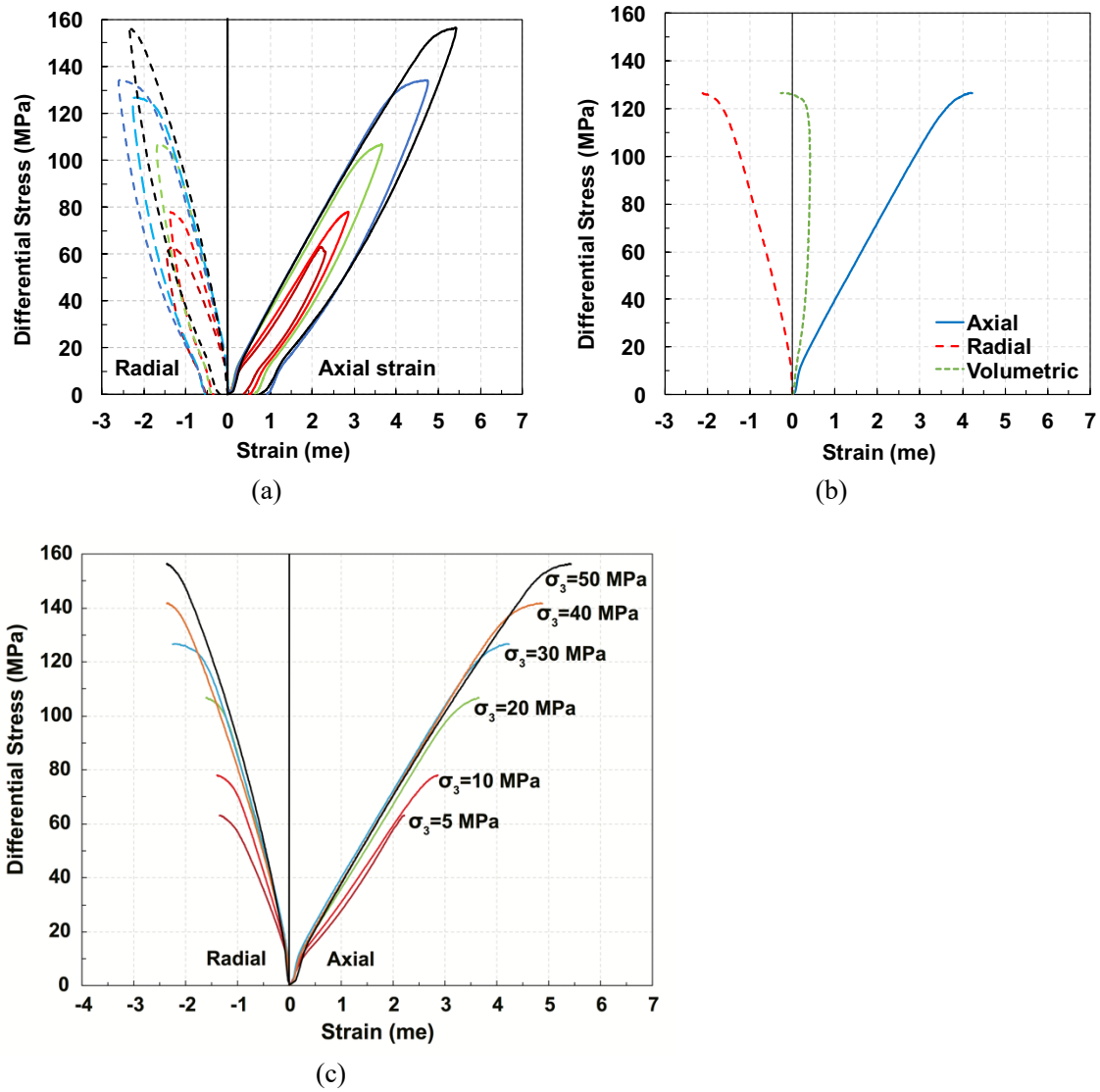


Figure 2-12. MSF test on CR2 specimen: (a) variation of axial and radial strains with differential stress for different stages of the test; (b) example of strain vs. differential stress at CP=30 MPa; and (c) axial and radial strain versus differential stress up to failure point at different stages.

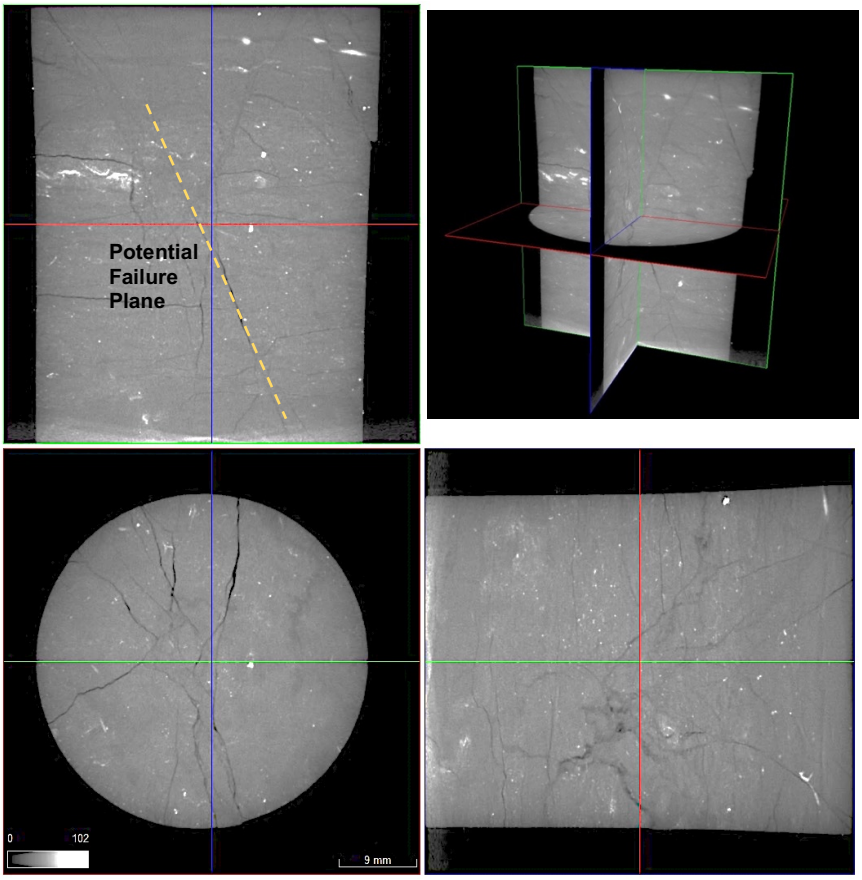

Figure 2-13. Post-mortem X-Ray CT images (3D, cross section, and side views) of the CR2 specimen after MSF test.

Figure 2.14a shows the Mohr's circles and Coulomb failure envelope. Figure 2.14b compares the Linearized Mohr-Coulomb and Hoek-Brown failure criteria against experimental data. The estimated orientation of failure plane using Coulomb envelope is ~60.5°, which is within the range observed from X-Ray CT-images, and the coefficient of internal friction was estimated as ~0.6 using Mohr-Coulomb criterion. Table 2.5 summarizes both Linearized Mohr-Coulomb and Hoek-Brown model parameters estimated using least-square regression. As evident in Figure 2.14b, both criteria are in good agreement with the measured strengths, within the range of applied confining levels. Figure

2.14c illustrates the variation of axial and radial strains at failure with confining level. Both axial and radial strains peaks, are increasing with the confining level. The axial strains exhibit a linear relationship with CP, however, there is a weaker linearity in the radial direction. It should be acknowledged that due to relatively-high number of stages involved in the test (six stages) and reaching to crack damage (dilation) threshold in most of the stages, additional damage has occurred within the specimen as evident in Figure 2.13. In the latter stages of the test, the cumulative effect of damage and plastic deformations might had led to inaccurate estimations of the strength properties. However, almost-linear relationship was observed between failure strains and confining level. In addition, very good regression values ($R^2$) values for Mohr-Coulomb and Hoek-Brown models can indicate that the estimated strength parameters are close to those at true failure. One can validate the results of MSF test with those obtained from single-stage triaxial failure test, which was not possible in this study due to lack of specimen.

Table 2-5. The parameters of Linearized Mohr-Coulomb and Empirical Hoek-Brown

| Linearized Mohr-Coulomb Criterion* | | | | | Empirical Hoek-Brown Criterion** | | | |
|---|---|---|---|---|---|---|---|---|
| $C_0$ (MPa) | $\beta$ (°) | $S_0$ (MPa) | $\mu$ | RMSE*** (MPa) | $C_0$ (MPa) | m | $s^a$ | RMSE (MPa) |
| 56.05 | 60.5 | 14.5 | 0.6 | 5 | 44.7 | 9.88 | 1.05 | 2.72 |

*Linearized Mohr-Coulomb Criterion: $\sigma_1=C_0+\sigma_3\tan^2(\beta)$

**Empirical Hoek-Brown Criterion: $\sigma_1=\sigma_3+ C_0(m\sigma_3/ C_0)^{0.5}$

***RMSE: Root Mean Square Error

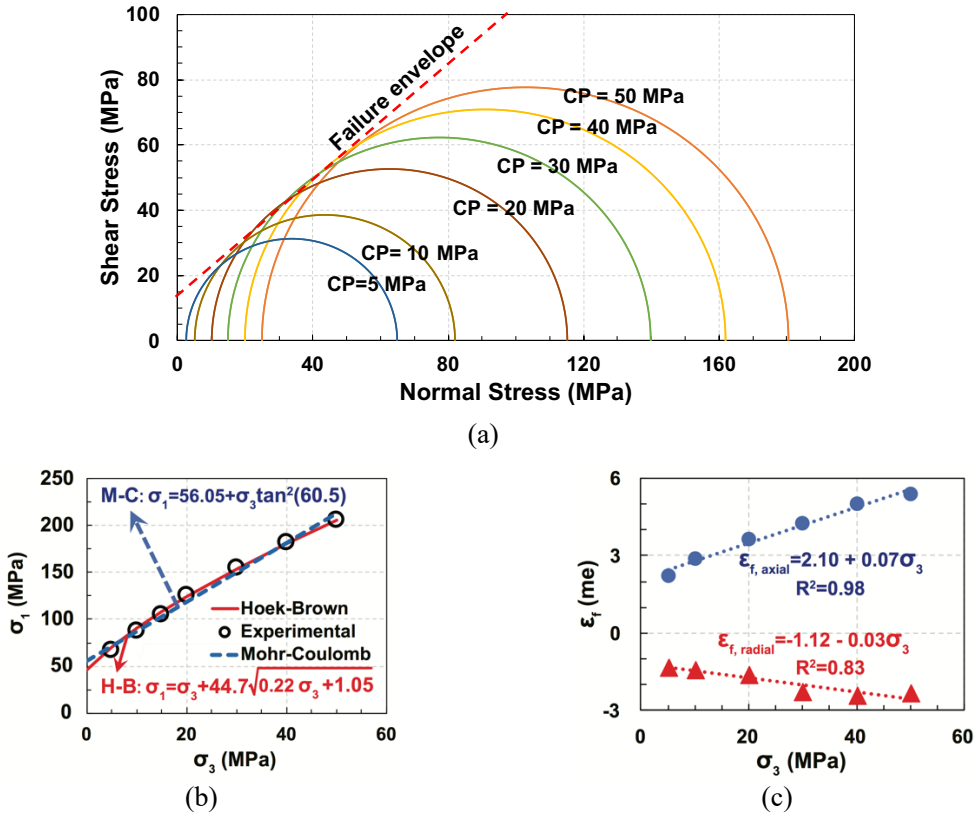


Figure 2-14. Estimated failure parameters for CR2 specimen: (a) Mohr's circles and Coulomb failure envelope; (b) comparison between Linearized Mohr-Coulomb and Hoek-Brown criteria; (c) variation of axial and radial strains at failure with confining level.

## 2.4 CONCLUSIONS

In order to optimize the design and operation of hydraulic fracturing in shale gas reservoirs, and for developing production models, laboratory characterization of shale gas rocks is necessary. A series of triaxial tests accompanied with measurements of ultrasonic P- and S-wave velocities at different stress levels were conducted on Marcellus Shale specimens, retrieved from a deep well in West Virginia. With respect to mineralogy, the specimens were found to be either clay-rich or calcite/quartz-rich. The response of these specimens was influenced by planes of weakness and presence of micro-cracks.

A set of creep, cyclic, and multi-stage failure tests were conducted on these specimens in order to characterize the elastic, time-dependent, hysteresis, and strength properties of these rock. It was found that the specimens tend to significantly creep under the applied range of stresses, with enhanced creep rate in clay-rich specimen. Both Power-Law and Burgers models were successfully able to capture the time-dependent behavior of specimens, with the Power-Law being in closer agreement with experimental data. The ultrasonic velocity measurements revealed that during viscoelastic deformation, for both isotropic compression and triaxial stages, there is a slight increase in both P- and S-wave velocities, mostly caused by the compaction of the clay and organic matter.

Within the range of the applied stresses, the cyclic test revealed higher Young's modulus and velocity measurements for calcite/quartz-rich specimen compared to clay-rich, which was attributed to its higher stiffness, due to its mineralogical content. This increase of both estimated static Young's modulus and measured ultrasonic velocities can be an indication that, within the range of applied stresses, the closure of existing micro-cracks was the dominant phenomenon compared to creation of new micro-cracks. The strength of the calcite/quartz-rich specimen at different levels of confinement was obtained by performing multi-stage triaxial failure test. It was found that the peak strength increased in successive stages (i.e. increased confining level). The strength properties were estimated through both Mohr-Coulomb and Hoek-Brown failure criteria, based on the constructed failure envelope. The Linearized Mohr-Coulomb criteria yielded an unconfined compressive strength of ~56 MPa, and a coefficient of internal friction as ~0.6, which is in the medium-upper range for shale gas rocks.

# CHAPTER 3

# INVESTIGATION OF STATIC/DYNAMIC MODULI AND PLASTIC RESPONSE OF SHALE SPECIMENS

## ABSTRACT

High clay and organic content, irregular voids, presence of micro-cracks, and obvious bedding planes are among features of shale gas rocks that affect their mechanical response. These sedimentary rocks exhibit substantial degree of anisotropy and inhomogeneity, with non-linear response when subjected to axial loading. The laboratory characterization of these rocks is necessary to design an optimized hydraulic fracturing program, and for reliable constitutive and numerical modeling of these formations. In this study, a series of triaxial multi-stage elastic and cyclic tests were performed on Marcellus Shale specimens, retrieved from a deep well (~2270 m deep) located in West Virginia, to characterize their elastic-plastic and hysteresis response subjected to loading/unloading cycles. The experimental results indicated a nonlinear response, particularly at low differential stress levels. In addition, the specimens with higher clay content exhibited a softer response with lower estimated static and dynamic moduli at different stress levels compared to those of specimens with higher calcite/quartz content. The ultrasonic P- and S-wave velocity measurements were found to be sensitive to the changes in the micro-structure of the rock caused by variation in stress condition. In general, the estimated Young's modulus during unloading was found to be higher than loading. The plastic

deformations were pronounced in the first cycle of loading, followed by a decreasing trend in the subsequent cycles.

## 3.1 INTRODUCTION

According to EIA Report (2017), there are more than 39 billion barrels of proved oil/gas reservoirs, the highest since 1972. Unconventional oil/gas resources such as shale gas and tight oil are significantly contributing to the oil/gas production (EIA Report, 2017). Shale gas reservoirs have been exploited with a total technically-recoverable resources of about 660 trillion cubic feet (EIA Report, 2017) around the globe in countries such as China, United States, Mexico, South Africa, and Australia to name a few (Zou et al., 2010; Rezaee, 2015). In the United States, development of Barnett, Haynesville, Marcellus, and Utica Shale among others has led to increased interest in evaluating properties of shale gas formations (EIA Report, 2017).

Shale rocks, categorized into clastic sedimentary rock (e.g. Rezaee, 2015), usually contain very fine grains resulting in very low permeability, and therefore, extraction of natural gas from these organic-rich rocks requires creation of fractures in the reservoir via hydraulic fracturing (e.g. Croize, 2013; Liu et al., 2016). Despite recent advancements in understanding of the mechanics of hydraulic fracturing, the outcome of hydraulic fracturing operation, and also the fracture closure over time are variable and unpredictable in different shale/clayey formations (Davies et al., 2012; Sone and Zoback, 2013a and b; Rezaee, 2015; Liu et al., 2017). This is, in part, due to lack of knowledge about the shale rock properties controlling the fracture initiation, propagation, and closure under reservoir conditions (Chang and Zoback, 2009; Sone and Zoback, 2013a; Villamor Lora et al., 2016).

In order to optimize the required energy for hydraulic fracturing operation and production in shale gas reservoirs, it is important to evaluate both elastic-plastic and visco-elastic-plastic behavior of these rocks (e.g. Britt et al., 2009; Maxwell, 2011; and Sone, 2012; Liu et al., 2018).

Shale/clayey rocks are typically recognized by their extremely low porosity and permeability (Vermylen, 2011; Ghassemi and Suarez-Rivera, 2012; Liu et al., 2015), with a wide range of mineralogy and Total Organic Content (TOC) and are highly heterogeneous and anisotropic (e.g. Islam and Skalle, 2013; Sone and Zoback, 2013a; Villamor Lora et al., 2016). These characteristics significantly affect the outcome of hydraulic fracturing during stimulation stage and fracture closure during production stage in a shale gas reservoir (e.g. Bazant et al., 2014). For example, during hydraulic fracturing, shale/clayey formations with higher clay content, exhibit a more ductile behavior, and therefore tend to deform instead of shattering (Rezaee, 2015; Liu and Shao, 2016).

The presence of clay/organic matters in shale/clayey formations results in significant visco-elastic deformations, which in turn, affect both short- and long-term deformation of these formations (e.g. Sone and Zoback, 2013b; Liu and Shao, 2016; Liu et al., 2016; Kamali-Asl et al., 2018). Time-dependent (i.e. visco-elastic) deformations might lead to change in the state of the stress, elastic and failure characteristics, and permeability of shale/clayey rocks (Ghassemi and Suarez-Rivera, 2012; Sone and Zoback, 2014; Liu et al., 2017). Liu et al. (2015) found that structural anisotropy significantly influences the creep response of Cox argillite specimens, with increased strength due to visco-elastic-plastic deformations. Liu et al. (2018) studied the effects of mineralogical composition,

relative humidity, confining pressure, and structural anisotropy on creep response of re-saturated and desaturated Cox claystone specimens and reported that active clay minerals significantly influence the creep strains. Burgers' and Power-Law models have shown to be able to reasonably capture the long-term creep response of shale rocks (e.g. Sone and Zoback, 2013b; Sone and Zoback, 2014; Kamali-Asl et al., 2018).

Laboratory characterization of shale rock specimens typically includes non-destructive and destructive petrophysical and geomechanical testing (Dewhurst et al., 2011; Josh et al., 2012). Elastic moduli (including Young's and shear moduli and Poisson's ratio), strength properties (i.e. cohesion, coefficient of internal friction, and unconfined compressive strength), hysteresis behavior (i.e. plastic deformation), and creep response are important to be addressed for geomechanical characterization of these shale formations (e.g. Islam and Skalle, 2013; Sone and Zoback, 2013a and 2013b; Villamor Lora et al., 2016). Typically, these characteristics can be determined in laboratory by performing triaxial experiments in drained/undrained conditions, and by measurements of ultrasonic wave velocities at different stress conditions (e.g. Sone and Zoback 2013a; Villamor Lora et al., 2016). Both geomechanical and petrophysical properties are important for the optimized design of hydraulic fracturing stimulation program, and improved accuracy of production models.

Shale rocks are reported to be highly-nonlinear material (e.g. Islam and Skalle, 2013; Sone and Zoback, 2013a; Villamor Lora et al., 2016) with presence of micro-cracks, that affect their elastic properties, particularly at lower confining levels of up to ~10 MPa (e.g. Vermylen, 2011; Josh et al., 2012; Sone, 2012). Moreover, fabric anisotropy and

composition are reported to have a substantial influence on elastic moduli (Dewhurst et al., 2008; Piane et al., 2009; Josh et al., 2012; Sone and Zoback, 2013a), resulting in higher degree of pressure-dependency of stiffness compared to other rocks (e.g. Villamor Lora et al., 2016). Furthermore, shale rocks exhibit significant variations in the measured static moduli during loading/unloading/reloading (Sone and Zoback, 2013a; Villamor Lora et al., 2016). In addition, irrecoverable deformations make it difficult to interpret the static moduli as elastic properties (e.g. Sone and Zoback, 2013a; Villamor Lora et al., 2016).

In shale reservoirs, due to creep deformation, the created fractures gradually close under in-situ stresses (e.g. Ghassemi and Suarez-Rivera, 2012; Liu et al., 2015). In order to maintain continued reservoir production, it is necessary to re-stimulate the reservoir. The response of shale rocks subjected to cyclic loading is more complex compared to other rocks due to their inherent fabric complexity. These rocks show a brittle, nonlinear, and highly-anisotropic plastic response as well as initiation of micro-cracks under successive loading/unloading cycles, which affect their stiffness and strength properties (e.g. Niandou et al., 1997; Liang et al., 2012; Islam and Skalle, 2013). The permanent plastic deformations and degradation of elastic moduli due to fatigue of shale formations play a significant role in design and operation of re-stimulation process (e.g. Eshkalak et al., 2015).

Ultrasonic wave propagation is often used to estimate the elastic properties of the rocks, referred to as dynamic moduli. Typically, the estimated dynamic moduli are higher than the corresponding static ones (e.g. Toksoz et al., 1976; Fjar, 2008). The propagation of ultrasonic waves in rocks depends on volume, geometry, and distribution of pores and

fractures (Jia, 2000; Bachrach and Avseth, 2008; Manjunath et al., 2012; Hedayat et al., 2014 and 2018). In a triaxial test, usually during isotropic compression (hydrostatic stage), the ultrasonic velocities increase, however, during triaxial stage, the ultrasonic velocities show an increasing/decreasing trend (e.g. Castanga et al., 1985; Dewhurst et al., 2008; Kuila et al., 2011).

In general, shale rocks exhibit irregular intergranular spaces as void (Jones and Wang, 1981), and, high compressibility due to high clay content (e.g. Sone and Zoback, 2014). During hydrostatic and triaxial stages, shear and compressional wave velocities can be affected by closure of existing micro-cracks, potential porosity reduction, and creation of new micro-cracks (e.g. Fortin et al., 2007; Wichtmann and Triantafyllidis, 2009; Zhu et al., 2010; Yang and Gu, 2013). For low porosity shale specimens, typically by increasing the mean stress, the P- and S-wave velocities monotonically increase during hydrostatic stage followed by subsequent decrease during triaxial stages (e.g. Kuila et al., 2011). It is worth noting that ultrasonic wave velocities are significantly affected by: (i) the type of pore fluid (Fjar, 2008), (ii) the level of saturation (e.g. Moore and Lockner, 2004; Ghrobani et al., 2009), and (iii) the orientation of bedding planes with respect to applied differential stress (Dewhurst et al., 2011; Gao et al., 2015). It should be mentioned that in shales, existing/created fractures impact the transmitted waves by: (i) filtering high frequency content of the wave, and (ii) attenuating the signal (Cook, 1992).

Although several studies are available on geomechanical characterization of different shale formations (e.g. Liang et al., 2012; Islam and Skalle, 2013; Sone and Zoback, 2013a and 2013b), very limited studies are available on Marcellus Shale (e.g.

Villamor Lora 2015, Villamor Lora et al., 2016). Given that Marcellus Shale is the largest shale formation in the United States, and there is an increasing demand for fundamental rock properties of this formation, this study focused on characterization of Marcellus Shale specimens retrieved from a deep well. This study reports the results from a set of multi-stage elastic and cyclic experiments on Marcellus Shale specimens, in attempt to characterize the elastic-plastic properties of the specimens. The time-dependent and strength properties of the shale specimens were investigated by performing creep and multi-stage failure tests on the specimens, and the results are reported in a companion manuscript by the authors.

Section 3.2 provides the experimental program, Section 3.3 presents the results followed by analysis and discussion in Section 3.4. Finally, the conclusions of this study are provided in Section 3.5. Appendix A provides the information about the rock specimens used in this study. Specimen preparation and experimental methodology are provided in Appendices B and C, and matrix representation of stress-strain relationship and estimation of static and dynamic moduli are provided in Appendix D.

## 3.2 EXPERIMENTAL PROGRAM

### 3.2.1 TESTING PLAN

Multi-Stage Elastic (MSE) and cyclic tests were conducted in this study to characterize the non-linear, pressure-dependent, and inelastic response of the Marcellus Shale specimens. P-wave and cross-polarized S-wave velocities were measured at different points along the stress path to (i) estimate dynamic moduli, and (ii) investigate the

sensitivity of the velocity measurements to changes in the micro-structure of the specimen due to variation in stress conditions. Details of the stress path for MSE and cyclic tests are provided in the following sections.

#### 3.2.1.1 MULTI-STAGE ELASTIC TESTS

Due to rock specimen variability and scarcity, MSE test can be performed on a single specimen to obtain the geo-mechanical parameters, instead of performing multiple single-stage triaxial tests on multiple specimens (e.g. Islam and Skalle 2013; Villamor Lora et al., 2016). Several studies have shown that the results from an MSE test on shale specimens (e.g. Kim and Ko, 1979, Villamor Lora et al., 2016) or on Berea Sandstone specimens (e.g. Pagoulatos, 2004) agree well with those from single stage triaxial tests. Although the design of stress path is unique in each study, MSE tests are usually performed at multiple stages, where each stage consists of applying a constant CP, followed by few cycles of differential stress (loading/unloading) to fully characterize the specimen's elastic properties, non-linearity, and plastic deformations at different stress levels.

Five different regions in stress-strain response of a rock specimen subjected to triaxial loading can be observed (Hoek and Martin, 2014; Walton et al., 2017) as depicted in Figure 3.1a, including "(I) crack closure, (II) linear elastic deformation, (III) crack initiation (CI) and stable crack growth, (IV) crack damage (CD) and unstable crack growth, and (V) ultimate failure" (Hoek and Martin, 2014; Walton et al., 2017). In region I (low differential stress levels), the behavior of the rock is usually nonlinear, in part, due to closure of micro-cracks (Hoek and Martin, 2014; Walton et al., 2017). In region II, rock exhibits linear elastic response with the increase in differential stress. In region III, crack

initiation (CI), with stable cracks, due to damage of grain boundaries occurs. In region IV, crack damage (CD) threshold and unstable crack growth occur (Hoek and Martin, 2014; Walton et al., 2017). In region V, the peak (failure) strength is reached. While performing an MSE test, in order to stay within the elastic range, usually the differential stress is kept below 50% of Unconfined Compressive Strength (UCS) and 3 times of CP. This implies that only regions I and II are present in stress-strain response in MSE tests.

Figure 3.1b shows the stress path followed during MSE tests, which consisted of seven stages. For each stage of the test, CP was applied and held constant for 2 hours to ensure that the compaction and equilibrium of the specimen were achieved (i.e. no further changes in axial and radial strains). Then, one to two cycles of differential stress were applied as depicted in Figures 3.1c-e. The loading/unloading rate for both CP and DS was set as 0.333 MPa/sec. At the completion of each stage, CP was increased to the next level as shown in Figure 3.1f. Throughout the test, CP was increased step-wise in 5 MPa increments up to 50 MPa (the approximate in-situ overburden stress for the tested shale specimens). The ultrasonic P- and S-wave velocities were measured at different points along the stress path as shown in Figure 3.1f for Stage 3 of the test, as an example. At each stage, the seismic velocities were measured (i) immediately after application of CP, (ii) after achieving equilibrium (after 2 hours), and (iii) during application of differential stress at different stress levels as shown in Figure 3.1f. Figure 3.1g shows the labeling of static measurements at each stage. In this study, static moduli (including Young's, and shear moduli, and Poisson's ratio) were evaluated at different stress levels through MSE test.

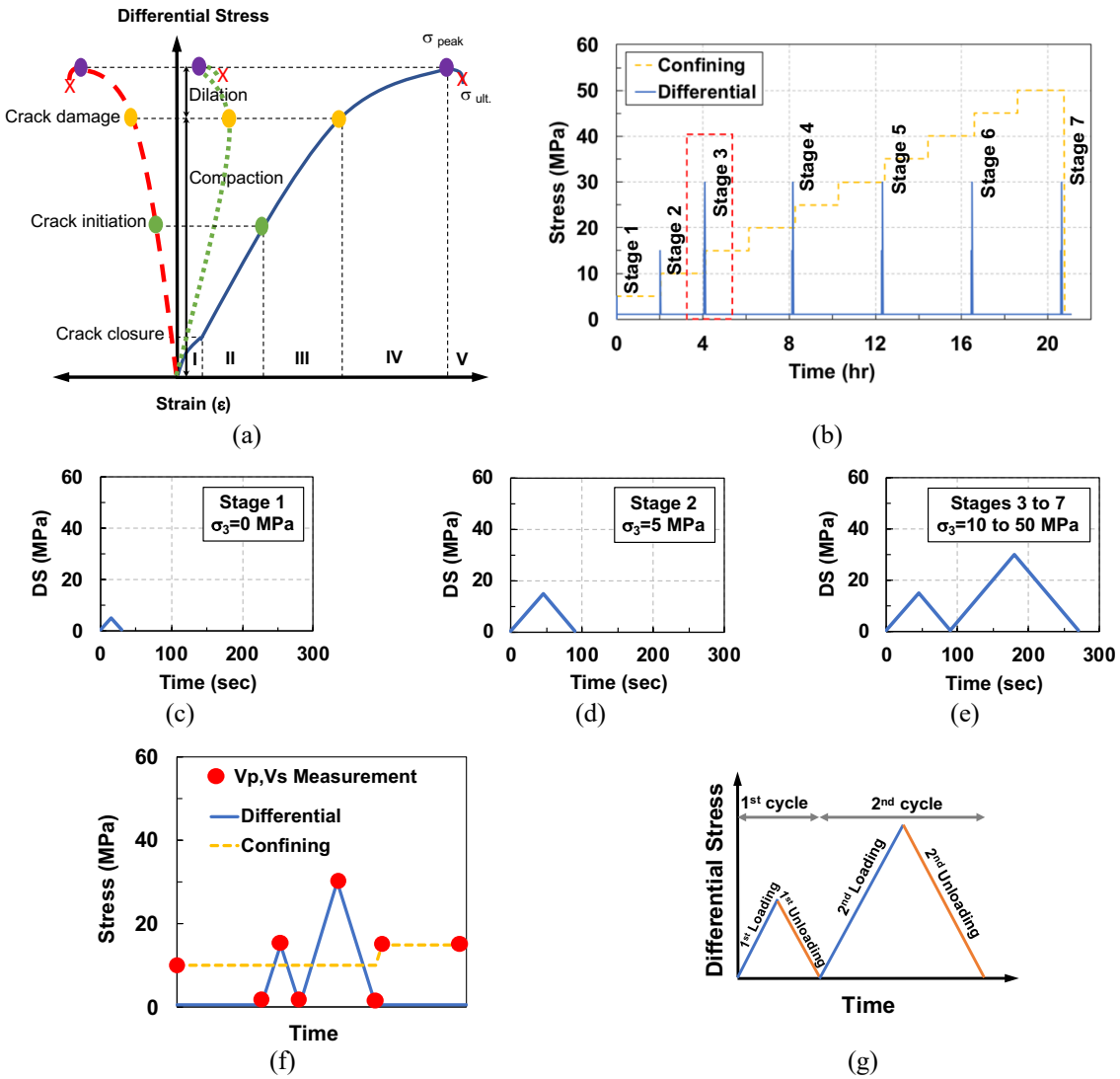


Figure 3-1. (a) schematic of different regions corresponding to crack closure, initiation, and damage (adapted and modified from Hoek and Martin, 2014; Walton et al., 2017); (b) stress path followed during the MSE tests; differential stress during (c) stage 1, (d) stage 2, and (e) stages 3 to 7 of the test; (f) example of the stress conditions, P- and S- wave velocity measurement points along the stress path during stage 3; (g) determination of static moduli from 1st loading, 1st unloading, 2nd loading and 2nd unloading in stages 3 to 7.

### 3.2.1.2 CYCLIC TESTS

Cyclic tests are helpful in evaluating the gradual degradation, non-linear, and hysteresis behavior of rocks. In cyclic tests, the CP is first increased to the desired level

and kept constant during the test. Then, the cycles of loading/unloading are performed, as shown in Figure 3.2a. The lower and upper bounds of differential stress can be prescribed, and a few cycles be performed to investigate (i) the potential degradation in loading/unloading moduli, and (ii) plastic deformations.

First CP was increased step-wise in 5 MPa increments up to 30 MPa. In each step, CP was held constant for 2 hours to ensure the compaction/equilibrium of the specimen was achieved (i.e. no further changes in axial/radial strains). Then, differential stress ranging from 0 to 48 MPa was applied as shown in Figure 3.2b. When characterizing non-linear material (e.g. shale), it is recommended to perform loading/unloading cycles at different stress levels to better characterize the response of the specimen within the elastic range (Fjar et al., 2008). Within each cycle, loading/unloading/reloading sub-cycles were performed at multiple stress levels as shown in Figure 3.2b. In addition, ultrasonic velocities were measured at different points along the stress path as shown in Figures 3.2b.

### 3.2.2 SUMMARY OF EXPERIMENTS

Table 3.1 presents the details of the experimental conditions for the set of experiments reported in this study. MSE tests were performed on R1 (calcite/quartz-rich) and R3 (clay-rich) specimens. The cyclic type I test was performed on R2 (calcite/quartz-rich) and R4 (clay-rich) specimens. It should be also noted that all the experiments were performed on dry specimens as (i) re-saturation process could damage these specimens (Villamor Lora et al., 2016), and (ii) low permeability of the specimens necessitates long time (e.g. weeks to months) to perform drained test (e.g. Islam and Skalle, 2013).

Table 3-1. The information about shale specimens

| Specimen | Specimen dimensions | | Depth (ft) | Mineralogical Content (wt. %) | | | | | | | Performed Test | CP*[3] (MPa) | DS*[4] (MPa) |
|---|---|---|---|---|---|---|---|---|---|---|---|---|---|
| | D*[1] (mm) | L*[2] (mm) | | Calcite | Dolomite | Gypsum | Illite | Muscovite | Pyrite | Quartz | | | |
| R1 | 38.04 | 56.87 | 7486 | 38.5 | 5.2 | - | - | 30.2 | - | 26.1 | MSE*[5] | 0 to 50 | 0 to 30 |
| R2 | 38.07 | 65.26 | | | | | | | | | Cyclic | 30 | 0 to 45 |
| R3 | 38.03 | 60.34 | 7467 | 2.9 | - | 4.1 | 69 | - | 3.1 | 20.8 | MSE | 0 to 50 | 0 to 30 |
| R4 | 38.05 | 65.42 | | | | | | | | | Cyclic | 30 | 0 to 45 |

*[1]D: Diameter of the Specimen

*[2]L: Length of the Specimen

*[3]CP: Confining Pressure

*[4]DS: Differential Stress

*[5]MSE: Multi-Stage Elastic

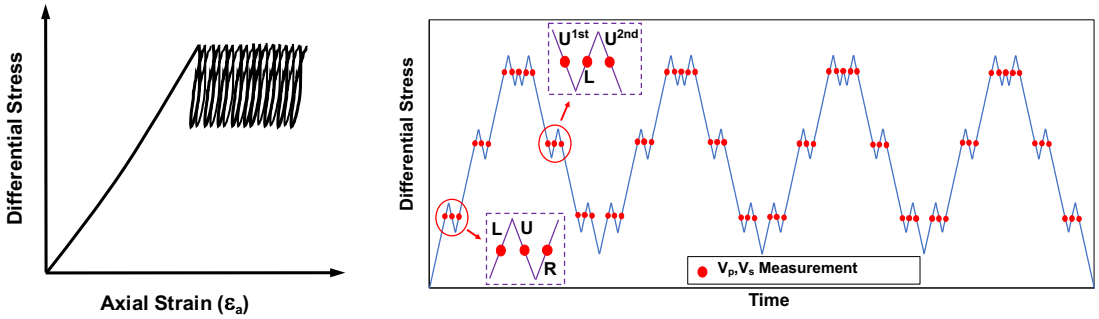


(a) (b)

Figure 3-2. Schematic stress-strain curve for cyclic test (adapted and modified from Gatelier et al., 2002), with cyclic loading between two prescribed limits; stress path and P- and S-wave velocity measurement points for cyclic test. L: loading; U: unloading; R: re-loading; $U^{1st}$: first unloading; $U^{2nd}$: second unloading.

## 3.3 RESULTS

The strain and P- and S-wave velocity measurements are provided for (i) MSE tests on R1 and R3 specimens in Section 3.3.1, (ii) cyclic tests on R2 and R4 specimens in Section 3.3.2. More in-depth discussions are provided in Section 3.4.

### 3.3.1 MSE TESTS

Figure 3.3 shows the variation of axial and radial strains (average of the two pairs of strain gauges) with differential stress at different levels of confining levels for the MSE test on R1 (calcite/quartz-rich) specimen. As evident from Figure 3.3, at all stages of the test, the radial strains are much lower than axials, an indication of volume loss, which is possibly accommodated by the closure of microcracks and compaction of organic matter (Sone and Zoback, 2013a; Villamor Lora et al., 2016). At very low confining levels (i.e. 0, 5, 10 MPa), the specimen exhibits substantial degree of non-linearity (axial stress-strain response) and plastic deformations. In addition to the mineral elastic deformations that

occur during loading, frictional sliding and micro-crack growth could induce energy-dissipative inelastic deformations (Zoback and Byerlee, 1975; Sone, 2012). These plastic deformations can change the micro-structure of the rock specimen and subsequently, affect the response of the rock specimen.

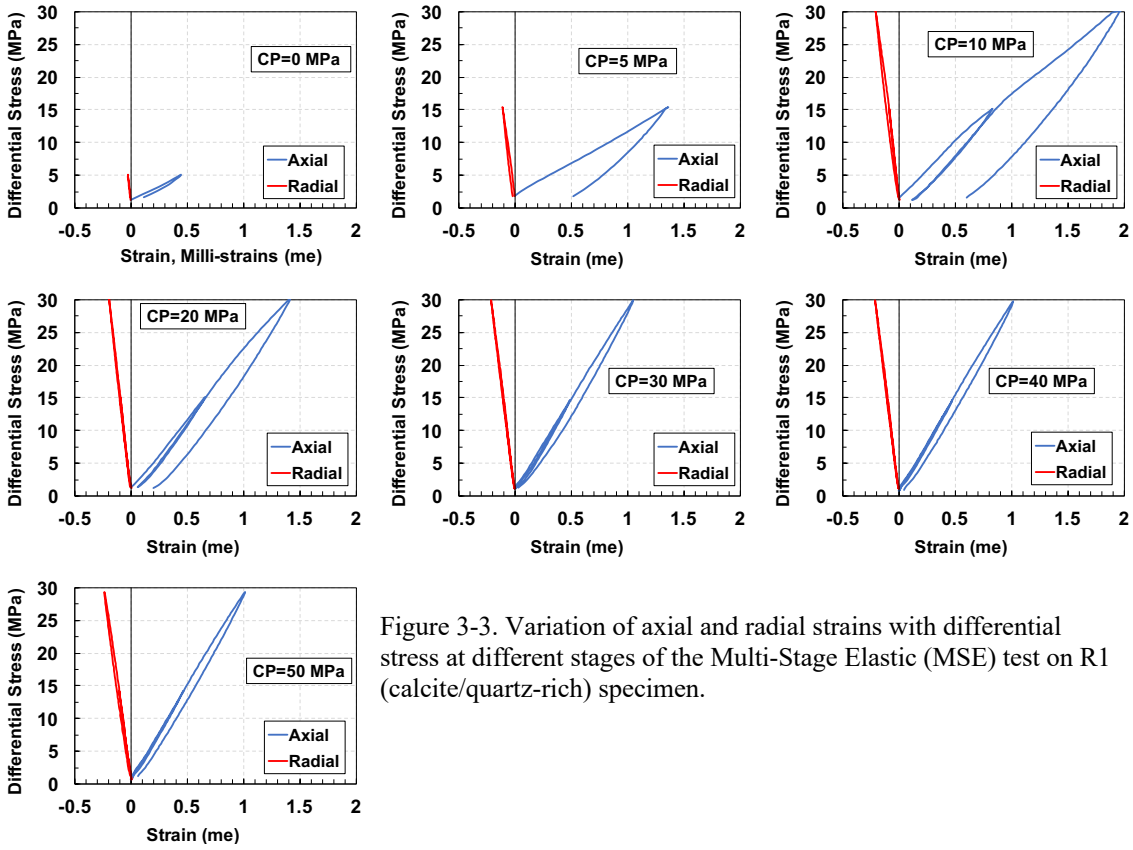


Figure 3-3. Variation of axial and radial strains with differential stress at different stages of the Multi-Stage Elastic (MSE) test on R1 (calcite/quartz-rich) specimen.

As expected, increasing the confinement level significantly affects the response of the specimen. As it can be seen in Figure 3.3, at higher confining levels, the plastic deformations and the degree of non-linearity of the specimen's response decrease. The plastic deformations at CP levels of 30, 40, and 50 MPa decrease significantly (close to zero) compared to those at lower CP levels, which might be due to combination of high confining levels and successive loading. The estimated static moduli at different confining

levels for different loading/unloading conditions (as illustrated in Figure 3.1g) are presented in Table 3.2. As expected, static measurements of Poisson's ratio, Young's, and shear moduli increase with increase in confining level. For example, the Young's modulus corresponding to first loading at CP=5, 20, and 50 MPa are estimated as 12, 23, and 29 GPa, respectively.

Figure 3.4 shows the variation of axial and radial strains with differential stress at different confining levels for the MSE test on R3 (clay-rich) specimen. As evident in Figure 3.4, the radial strains are lower than axials, and the plastic deformations and the non-linear behavior become less pronounced at higher confinement levels, as was also observed for the R1 specimen. At low differential stress levels (i.e. up to ~6 MPa), the specimen exhibits a significant degree of non-linearity, which could be attributed to the closure/creation of existing/new micro-cracks. Similar to R1 specimen, as evident in Table 3.2, static measurements of Poisson's ratio, Young's, and shear moduli increase with increase in confining level. For example, the Young's modulus corresponding to first loading at CP=5, 20, and 50 MPa are estimated as 7, 10, and 13 GPa, respectively.

Table 3-2. Estimated static/dynamic moduli from MSE test for R1 and R3 specimens

| Specimen | CP (MPa) | DS (MPa) | Type | E (GPa) | ν (%) | G (GPa) |
|---|---|---|---|---|---|---|
| R1 (Calcite/quartz-rich) | 0 | 0-15-0 | Static | 9.1L$^{1st}$-11.1U$^{1st}$ | 6.0L$^{1st}$ -6.7U$^{1st}$ | 4.0L$^{1st}$ -4.8U$^{1st}$ |
| | | 15 | Dynamic | 33.9 | 114.9 | 7.9 |
| | 5 | 0-15-0 | Static | 11.5L$^{1st}$ -17.4U$^{1st}$ | 9.3L$^{1st}$ -11.3U$^{1st}$ | 4.8L$^{1st}$ -6.9U$^{1st}$ |
| | | 15 | Dynamic | 35.1 | 13.6 | 15.5 |
| | 10 | 0-15-0-30-0 | Static | 18.2L$^{1st}$ -20.7U$^{1st}$ - 17.9R$^{2nd}$-22.4U$^{2nd}$ | 11.0L$^{1st}$ -13.1U$^{1st}$ - 11.9R$^{2nd}$ -14.4U$^{2nd}$ | 7.2L$^{1st}$ -7.9U$^{1st}$ - 7.0R$^{2nd}$ -8.4U$^{2nd}$ |
| | | 15,30 | Dynamic | 37.8,41.8 | 17.3,20.7 | 16.1,17.3 |
| | 20 | 0-15-0-30-0 | Static | 22.8L$^{1st}$ -25.0U$^{1st}$ - 23.8R$^{2nd}$ -25.8U$^{2nd}$ | 15.4L$^{1st}$ -16.5U$^{1st}$ - 16.0R$^{2nd}$ -17.9U$^{2nd}$ | 8.4L$^{1st}$ -9.1U$^{1st}$ - 8.7R$^{2nd}$ -9.2U$^{2nd}$ |
| | | 15,30 | Dynamic | 41.8,44.9 | 19.0,18.7 | 17.6,18.9 |
| | 30 | 0-15-0-30-0 | Static | 28.6L$^{1st}$ -29.8U$^{1st}$ - 29.4R$^{2nd}$ -30.0U$^{2nd}$ | 20.8L$^{1st}$ -21.4U$^{1st}$ - 21.7R$^{2nd}$ -22.0U$^{2nd}$ | 9.9L$^{1st}$ -10.2U$^{1st}$ - 10.0R$^{2nd}$ -10.0U$^{2nd}$ |
| | | 15,30 | Dynamic | 47.5,48.5 | 23.0,24.7 | 19.3,19.5 |
| | 40 | 0-15-0-30-0 | Static | 30.0L$^{1st}$ -30.6U$^{1st}$ - 30.4R$^{2nd}$ -31.0U$^{2nd}$ | 22.5L$^{1st}$ -23.2U$^{1st}$ - 23.6R$^{2nd}$ -24.0U$^{2nd}$ | N/A |
| | | 15,30 | Dynamic | 48.6,48.6 | 23.1,23.1 | 19.8,19.8 |
| | 50 | 0-15-0-30-0 | Static | 29.2L$^{1st}$ -30.4U$^{1st}$ - 30.0R$^{2nd}$ -31.0U$^{2nd}$ | 23.3L$^{1st}$ -23.6U$^{1st}$ - 24.6R$^{2nd}$ -25.0U$^{2nd}$ | N/A |
| | | 15,30 | Dynamic | 48.8,49.7 | 24.4,23.2 | 19.6,20.2 |
| R3 (Clay-rich) | 0 | 0-15-0 | Static | 6.4L$^{1st}$ -6.7U$^{1st}$ | 11.6L$^{1st}$ -10.9U$^{1st}$ | 2.8L$^{1st}$ -2.9U$^{1st}$ |
| | | 15 | Dynamic | 4.9 | -59.7 | 6.1 |
| | 5 | 0-15-0 | Static | 7.3L$^{1st}$ -8.8U$^{1st}$ | 9.5L$^{1st}$ -11.0U$^{1st}$ | 3.2L$^{1st}$ -3.8U$^{1st}$ |
| | | 15 | Dynamic | 18.6 | 13 | 8.2 |
| | 10 | 0-15-0-30-0 | Static | 8.8L$^{1st}$ -9.6U$^{1st}$ - 8.6R$^{2nd}$ -9.6U$^{2nd}$ | 10.4L$^{1st}$ -11.8U$^{1st}$ - 13.5R$^{2nd}$ -14.7U$^{2nd}$ | 3.8L$^{1st}$ -4.1U$^{1st}$ - 3.6R$^{2nd}$ -4.0U$^{2nd}$ |
| | | 15,30 | Dynamic | 14.8,16.7 | (-12.2),(-6.2) | 8.4,8.9 |
| | 20 | 0-15-0-30-0 | Static | 10.0L$^{1st}$ -10.9U$^{1st}$ - 9.8R$^{2nd}$ -10.7U$^{2nd}$ | 11.6L$^{1st}$ -13.3U$^{1st}$ - 14.4R$^{2nd}$ -15.6U$^{2nd}$ | 4.3L$^{1st}$ -4.6U$^{1st}$ - 4.1R$^{2nd}$ -4.4U$^{2nd}$ |
| | | 15,30 | Dynamic | 16.5,17.8 | (-6.1),1.8 | 8.8,8.8 |
| | 30 | 0-15-0-30-0 | Static | 11.5L$^{1st}$ -12.0U$^{1st}$ - 11.0R$^{2nd}$ -11.5U$^{2nd}$ | 12.7L$^{1st}$ -14.2U$^{1st}$ - 15.7R$^{2nd}$ -16.6U$^{2nd}$ | 4.8L$^{1st}$ -5.0U$^{1st}$ - 4.5R$^{2nd}$ -4.7U$^{2nd}$ |
| | | 15,30 | Dynamic | 18,18.7 | 2.8,7.5 | 8.8,8.7 |
| | 40 | 0-15-0-30-0 | Static | 12.4L$^{1st}$ -12.6U$^{1st}$ - 11.8R$^{2nd}$ -12.2U$^{2nd}$ | 13.0L$^{1st}$ -15.0U$^{1st}$ - 16.2R$^{2nd}$ -17.3U$^{2nd}$ | N/A |
| | | 15,30 | Dynamic | 18.9,19.4 | 3.3,8.8 | 9.1,8.9 |
| | 50 | 0-15-0-30-0 | Static | 13.1L$^{1st}$ -13.2U$^{1st}$ - 13.2R$^{2nd}$ -13.1U$^{2nd}$ | 13.7L$^{1st}$ -15.6U$^{1st}$ - 17.7R$^{2nd}$ -18.4U$^{2nd}$ | N/A |
| | | 15,30 | Dynamic | 19.5,19.9 | 7.9,10 | 9.0,9.1 |

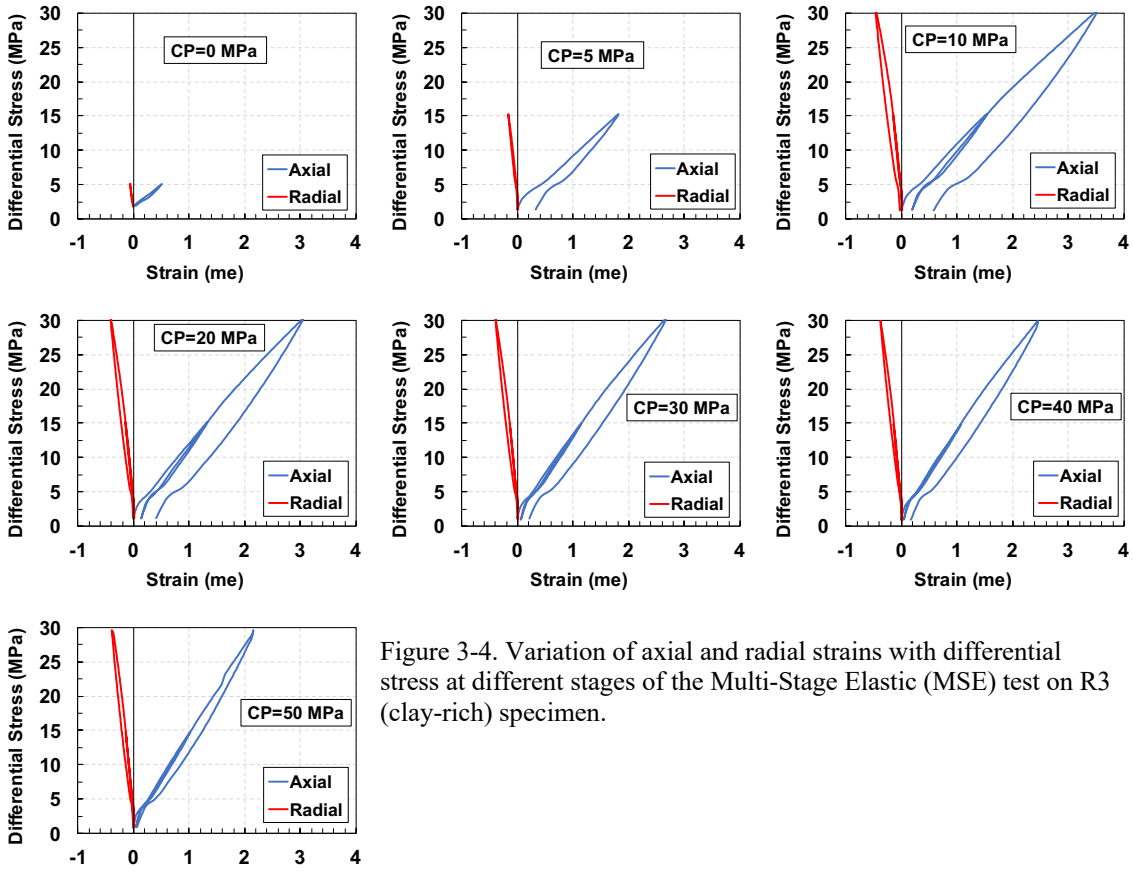


Figure 3-4. Variation of axial and radial strains with differential stress at different stages of the Multi-Stage Elastic (MSE) test on R3 (clay-rich) specimen.

Figures 3.5a and 3.5b show the P- and S-wave velocity measurements super-imposed on the stress path followed during MSE tests on R1 and R3 specimens, respectively. The magnitude of P- and S-wave velocities for R1 specimen ranges from 1400 to 4800 and 1000 to 2950 m/s, respectively. On the other hand, the magnitude of P- and S-wave velocities for R3 specimen ranges from 1000 to 2600 and 1400 to 1900 m/s, respectively. The higher P- and S-wave velocity measurements for R1 specimen compared to R3, given the same frequency of velocity measurements constant at 750 kHz, could be attributed to the higher stiffness of this specimen due to the fact that it is composed of stiffer minerals.

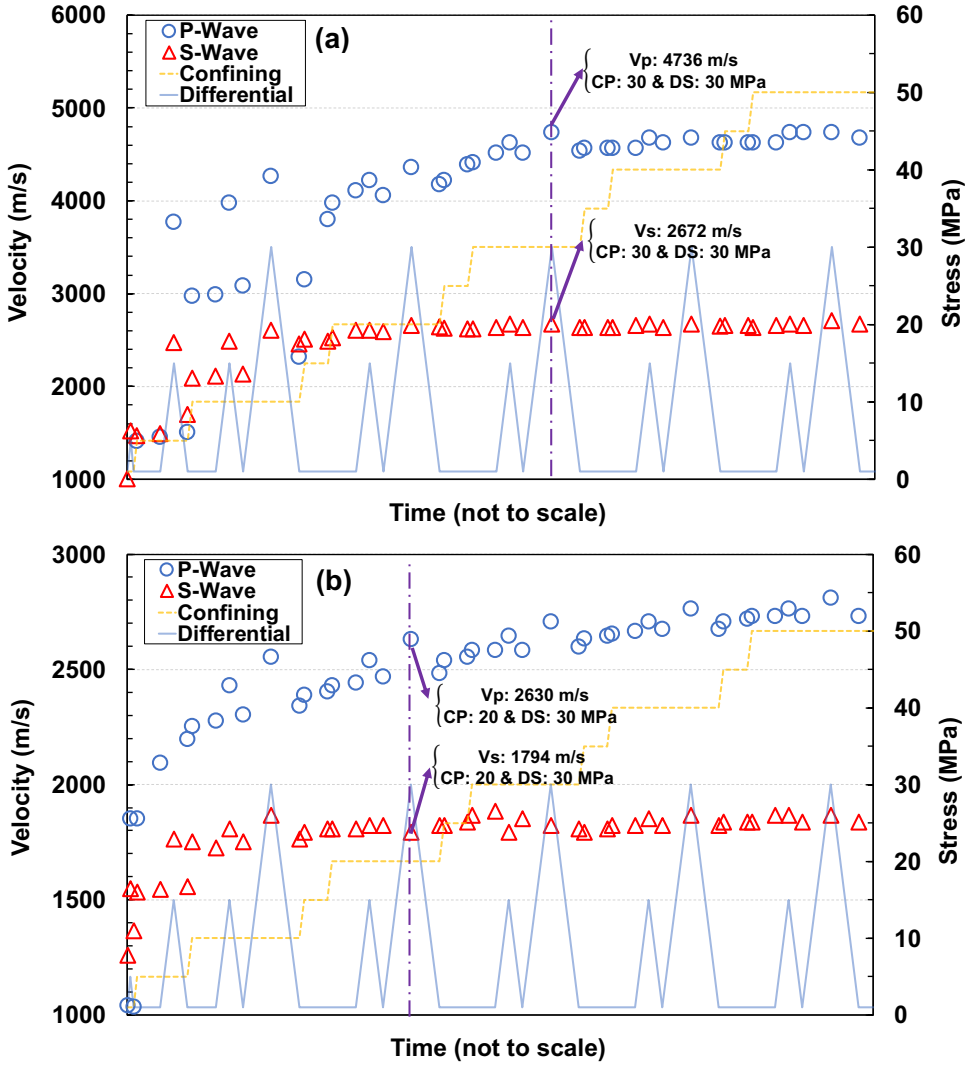


Figure 3-5. P- and S- wave velocity measurements during multi-stage elastic tests on (a) R1 (calcite/quartz-rich), and (b) R3 (clay-rich) specimens.

The estimated dynamic moduli at different confining levels for different loading/unloading conditions are presented in Table 3.2. For example, the estimated dynamic Young's modulus for R1 specimen at CP=5, 20, 50 MPa were estimated as 35, 42, 49 GPa, respectively, which are 192%, 83%, and 69% higher than static measurements, respectively. On the other hand, the values of dynamic Young's moduli for R3 specimen

at CP=5, 20, 50 MPa were estimated as 19,17, and 20 GPa, respectively, which are 171%, 70%, and 54% higher than static measurements, respectively.

The P- and S-wave velocity measurements for both R1 and R3 specimens substantially increase during Stage 1 (CP=0; Figure 3.1c) of the tests. In the subsequent stages, the S-wave velocity measurements stay relatively-constant, however, the P-wave velocity measurements follow the loading/unloading trend of the stress path, that is lower velocities at lower differential stress levels and higher velocities at higher levels. This indicates that the stress level (i.e. both confining and differential) directly affects the ultrasonic velocities. Also, it can be observed from Figures 3.5a and 3.5b that at higher confinement levels, the velocities are increasing, indicating the closure of the existing micro-cracks.

### 3.3.2 CYCLIC TESTS

Figure 3.6b illustrates the time-history axial and radial strains for R2 (calcite/quartz-rich) specimen subjected to cyclic test, with stress path as presented in Figure 3.6a. Since the specimen was axially loaded during triaxial stage, the axial strains were higher compared to radials as also observed during MSE tests. The range of axial strain variation in the latter cycles of the test, under the same upper and lower bound of differential stress, is smaller than those during earlier cycles of the test. This could be an indication of slight hardening of the specimen. In addition, transitioning from the first cycle to the second, there is an apparent plastic deformation (~0.3 milli-strains), however, in the subsequent cycles, no obvious additional plastic deformations can be observed. Therefore, the permanent plastic deformation at the end of the experiment appears to be caused during

the first cycle. Figure 3.6c shows the variation of axial, radial, and volumetric strains against differential stress. Highly non-linear behavior and hysteresis are observed during loading/unloading/reloading cycles, particularly during the first cycle.

The estimated static moduli at different loading/unloading/reloading conditions are presented in Table 3.3. In general, the estimated static Young's modulus during (i) unloading is the highest, (ii) loading is the lowest, and (iii) reloading is the intermediate. For example, the static Young's modulus in the first cycle at DS of 30 MPa measured during loading, unloading, and reloading stages are 23.3, 29.4, and 26.5 GPa, respectively. In the successive cycles, the static Young's modulus is continuously increasing under the same stress conditions. For example, the reloading Young's modulus at DS of 30 MPa measured during loading path for cycles 1 to 4 are 26.5, 31.4, 32.9, and 38.1 GPa, indicating 44% increase in the estimated Young's modulus.

Ultrasonic velocities were measured during all loading/unloading/reloading cycles of the test on R2 specimen. For clarity, only measured velocities immediately after loading or immediately before unloading (Figure 3.2b) are shown in Figure 3.6d. The magnitude of P- and S-wave velocities ranges from 4500 to 4800 and 2650 to 2950 m/s, respectively. Table 3.3, based on these velocity measurements, presents the estimated dynamic moduli. In general, the dynamic Young's modulus is not altering in sub-cycles of loading/unloading/reloading within a cycle. For example, the estimated dynamic Young's modulus in the first cycle at DS of 30 MPa measured during loading, unloading, and reloading stages are 50.1, 51.4, and 51.4 GPa, respectively. In the earlier cycles, the dynamic Young's modulus increases following by a decrease in the latter cycles under the

same stress conditions. For example, the dynamic reloading Young's modulus at DS of 30 measured during loading stage for cycles 1 to 4 are 51.4, 52.1, 51.4, and 50.7 GPa.

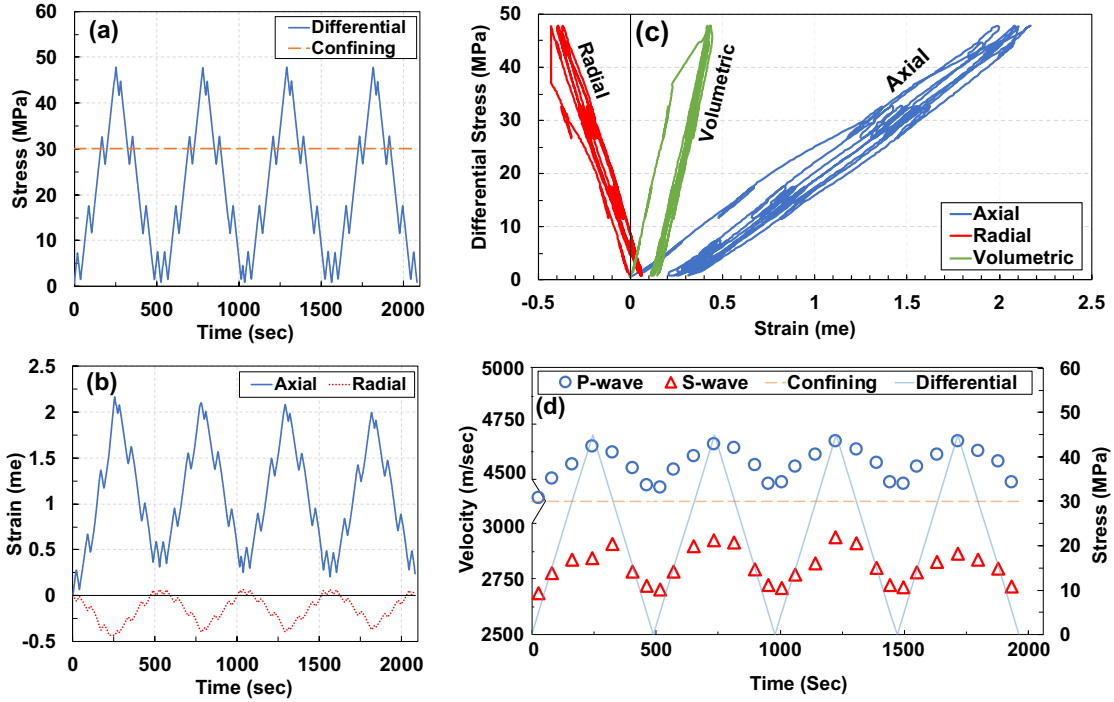


Figure 3-6. Results from cyclic test on calcite/quartz-rich sample (a) stress path; (b) variation of strains versus time; (c) variation of strains versus differential stress; and (d) P- and S- wave velocity measurements during the test superimposed on the stress path. Note that the velocity axis is broken down for better illustration.

Table 3-3. Static/dynamic moduli for R2 specimen under cyclic loading (CP is constant at 30 MPa)

| Cycle | Moduli | Type | Differential Stress (MPa) | | | | | |
|---|---|---|---|---|---|---|---|---|
| | | | 15 | | 30 | | 45 | |
| | | | Loading | Unloading | Loading | Unloading | Loading | Unloading |
| 1 | E (GPa) | Static | 27.1L-28.6U-31.5R | 24.0U$^{1st}$-30.6L-28.5U$^{2nd}$ | 23.3L-29.4U-26.5R | 27.4U$^{1st}$-30.3L-27.4U$^{2nd}$ | 13.7L-41.5U-29.3R | 41.5U$^{1st}$-29.3L-35.1U$^{2nd}$ |
| | | Dynamic | 48.3L-48.4U-48.5R | 48.9U$^{1st}$-48.9L-48.8U$^{2nd}$ | 50.1L-51.4U-51.4R | 52.0U$^{1st}$-52.1L-52.1U$^{2nd}$ | 50.9L-52.9U-53.0R | 50.9L-52.9U-53.0R |
| | ν (%) | Static | 24.8L-21.3U-25.3R | 29.5U$^{1st}$-23.8L-23.7U$^{2nd}$ | 34.7L-32.0U-23.2U | 26.1U$^{1st}$-22.6L-25.4U$^{2nd}$ | 0L-37.7U-26.1R | 37.7U$^{1st}$-26.1L-24.5U$^{2nd}$ |
| | | Dynamic | 21.4L-21.5U-21.4R | 21.9U$^{1st}$-21.9L-22.0U$^{2nd}$ | 20.7L-19.6U-19.4R | 19.4U$^{1st}$-19.5L-19.5U$^{2nd}$ | 22.0L-19.1U-19.8R | 22.0L-19.1U-19.8R |
| | G (GPa) | Static | 10.1L-10.9U-11.6R | 8.7U$^{1st}$-11.4L-10.7U$^{2nd}$ | 8.2L-10.3U-10.0R | 10.1U$^{1st}$-11.4L-11.2U$^{2nd}$ | 6.5L-13.7U-10.8R | 13.7U$^{1st}$-10.8L-12.8U$^{2nd}$ |
| | | Dynamic | 19.9L-19.9U-20.0R | 20.1U$^{1st}$-20.1L-20.0U$^{2nd}$ | 20.7L-21.5U-21.5R | 21.8U$^{1st}$-21.8L-21.8U$^{2nd}$ | 20.8L-22.2U-22.1R | 20.8L-22.2U-22.1R |
| | | | | | | | | |
| 2 | E (GPa) | Static | 27.7L-30.7U-29.4R | 19.0U$^{1st}$-31.7L-29.4U$^{2nd}$ | 27.6L-33.4U-31.4R | 25.6U$^{1st}$-29.3L-31.3U$^{2nd}$ | 37.9L-35.2U-31.2R | 35.2U$^{1st}$-31.2L-35.7U$^{2nd}$ |
| | | Dynamic | 48.7L-49.0U-48.7R | 49.5U$^{1st}$-49.2L-49.1U$^{2nd}$ | 51.7L-51.6U-52.1R | 52.3U$^{1st}$-52.0L-52.4U$^{2nd}$ | 52.8L-53.4U-53.4R | 52.8L-53.4U-53.4R |
| | ν (%) | Static | 23.5L-24.8U-18.2R | 25.6U$^{1st}$-25.2L-23.9U$^{2nd}$ | 25.9L-24.5U-22.2R | 23.8U$^{1st}$-22.5L-22.0U$^{2nd}$ | 37.6L-32.0U-27.8R | 32.0U$^{1st}$-27.8L-22.2U$^{2nd}$ |
| | | Dynamic | 22.0L-21.7U-22.2R | 21.4U$^{1st}$-21.8L-22.1U$^{2nd}$ | 19.5L-20.0U-19.6R | 19.6U$^{1st}$-19.4L-19.7U$^{2nd}$ | 19.6L-19.6U-19.3R | 19.6L-19.6U-19.3R |
| | G (GPa) | Static | 10.4L-11.3U-11.5R | 7.2U$^{1st}$-11.6L-11.0U$^{2nd}$ | 10.2L-12.3U-11.8R | 9.7U$^{1st}$-11.0L-11.8U$^{2nd}$ | 12.8L-12.2U-11.3R | 12.2U$^{1st}$-11.3L-13.3U$^{2nd}$ |
| | | Dynamic | 20.0L-20.1U-19.9R | 20.4U$^{1st}$-20.2L-20.1U$^{2nd}$ | 21.6L-21.5U-21.8R | 21.9U$^{1st}$-21.8L-21.9U$^{2nd}$ | 22.1L-22.3U-22.4R | 22.1L-22.3U-22.4R |

Table 3.3. cont'd.

| Cycle | Moduli | Type | Differential Stress (MPa) | | | | | |
|---|---|---|---|---|---|---|---|---|
| | | | 15 | | 30 | | 45 | |
| | | | Loading | Unloading | Loading | Unloading | Loading | Unloading |
| 3 | E (GPa) | Static | 28.1L-31.2U-29.9R | 25.6U[1st]-30.3L-30.7U[2nd] | 25.7L-33.1U-32.9R | 26.8U[1st]-30.7L-30.9U[2nd] | 28.2L-31.9U-34.9R | 31.9U[1st]-34.9L-35.9U[2nd] |
| | | Dynamic | 48.5L-48.7U-48.8R | 49.2U[1st]-49.4L-49.3U[2nd] | 50.1L-50.1U-51.4R | 52.0U[1st]-52.1L-52.3U[2nd] | 53.2L-53.2U-52.9R | 53.2L-53.2U-52.9R |
| | ν (%) | Static | 26.3L-19.1U-22.8R | 22.7U[1st]-25.4L-23.2U[2nd] | 23.8L-20.3U-23.0R | 23.1U[1st]-19.5L-25.2U[2nd] | 28.1L-25.2U-24.1R | 25.2U[1st]-24.1L-27.5U[2nd] |
| | | Dynamic | 22.6L-22.4U-21.9R | 21.8U[1st]-21.7L-22.1U[2nd] | 22.0L-22.1U-20.2R | 19.8U[1st]-19.9L-19.6U[2nd] | 19.5L-19.5U-19.8R | 19.5L-19.5U-19.8R |
| | G (GPa) | Static | 10.3L-12.0U-11.2R | 9.7U[1st]-11.2L-11.5U[2nd] | 9.7L-12.6U-12.2R | 10.1U[1st]-11.8L-11.4U[2nd] | 10.2L-11.7U-12.8R | 11.7U[1st]-12.8L-12.9U[2nd] |
| | | Dynamic | 19.8L-19.9U-20.0R | 20.2U[1st]-20.3L-20.2U[2nd] | 20.5L-20.5U-21.4R | 21.7U[1st]-21.7L-21.9U[2nd] | 22.3L-22.3U-22.1R | 22.3L-22.3U-22.1R |
| | | | | | | | | |
| 4 | E (GPa) | Static | 30.4L-35.3U-34.9R | 27.4U[1st]-34.6L-28.4U[2nd] | 27.6L-30.3U-38.1R | 31.5U[1st]-37.3L-35.0U[2nd] | 29.9L-38.2U-27.8R | 38.2U[1st]-27.8L-27.9U[2nd] |
| | | Dynamic | 48.7L-48.8U-48.8R | 49.2U[1st]-49.2L-49.3U[2nd] | 50.3L-50.6U-50.7R | 52.5U[1st]-52.3L-50.6U[2nd] | 51.5L-51.5U-53.5R | 51.5L-51.5U-53.5R |
| | ν (%) | Static | 23.5L-24.1U-22.9R | 22.3U[1st]-27.3L-21.4U[2nd] | 24.1L-20.9U-22.3R | 26.4U[1st]-21.6L-27.4U[2nd] | 28.4L-30.3U-22.3R | 30.3U[1st]-22.3L-24.0U[2nd] |
| | | Dynamic | 22.3L-22.1U-22.1R | 22.1U[1st]-22.6L-22.2U[2nd] | 21.8L-22.4U-21.8R | 19.9U[1st]-19.9L-21.9U[2nd] | 21.9L-21.8U-18.2R | 21.9L-21.8U-18.2R |
| | G (GPa) | Static | 11.4L-13.0U-13.0R | 10.4U[1st]-12.5L-10.8U[2nd] | 10.3L-11.6U-14.1R | 11.5U[1st]-13.9L-12.5U[2nd] | 10.8L-13.4U-10.7R | 13.4U[1st]-10.7L-10.4U[2nd] |
| | | Dynamic | 19.9L-20.0U-20.0R | 20.1U[1st]-20.1L-20.2U[2nd] | 20.6L-20.7U-20.8R | 21.9U[1st]-21.8L-20.8U[2nd] | 21.1L-21.1U-22.6R | 21.1L-21.1U-22.6R |

The variations of both P- and S-wave velocities follow those of differential stress, which indicates the sensitivity of measured velocities in response to the change in the internal structure of the rock specimen (i.e. closure/opening of existing/new micro-cracks). For example, as indicated from axial strain measurements in Figure 3.6b, the permanent plastic deformation in the specimen was caused during the first cycle. This is reflected in the increase of P-wave measurements at the beginning of the second cycle, compared to that of the first cycle. As evident in Figure 3.6d, at a specific differential stress level, the measured velocities during the unloading part of each cycle are slightly higher than those during the loading part. This could be in part due to the fact that some of the closed micro-cracks during loading, do not open up after unloading, which in turn, leads to the increased velocity measurements.

Figure 3.7b shows the time evolution of axial and radial strains for R4 specimen subjected to cyclic test, with stress path presented in Figure 3.7a. Although the followed stress path during this experiment was very similar to that for specimen R2, the lower bound of the differential stress in this test was prescribed as ~7 MPa. As it can be seen from Figure 3.7b, the specimen exhibits plastic deformations (total of ~0.7 milli-strains) distributed in successive loading cycles, as opposed to the R2 specimen, which exhibited plastic deformation mostly in the first cycle (~0.3 milli-strains). In addition to the observed plastic deformations in the axial direction, plastic deformations are observed in the radial direction in each cycle (total of ~0.8 milli-strains).

Figure 3.7c shows the variation of axial, radial, and volumetric strains against differential stress. A non-linear response is observed at different stress levels within each

cycle, particularly, the first cycle. As successive cycles continue, the hysteresis in volumetric strains becomes more pronounced, which can be attributed to the closure of the existing microcracks and compaction of organic and clay content. The estimated static moduli at different loading/unloading/reloading cycles are presented in Table 3.4. In general, the estimated static Young's modulus during 2nd unloading in unloading part of a cycle is higher than static Young's modulus during loading in the loading part of a cycle. For example, the Young's modulus in the first cycle during loading and 2nd unloading stages at DS of 30 MPa are 14.8 and 16.9 GPa, respectively.

Figure 3.7d shows the measured P- and S-wave velocities during cyclic test on R4 specimen. The magnitude of P- and S-wave velocities ranges from 2900 to 3200 and 1750 to 1900 m/s, respectively. Similar to R2 specimen, the variations of both P- and S-wave velocities follow those of differential stress, although, the magnitudes of velocities are less than those for R2 specimen, due to the difference in the mineralogical composition. The estimated dynamic moduli, based on these velocity measurements, are presented in Table 3.4, indicating that they are relatively-constant except those of the second cycle. For example, the average dynamic Young's modulus (for loading/unloading/reloading) in cycles 1 to 4 during loading stage at DS of 30 MPa are 21.8, 22.2, 22.1, and 21.9 GPa, respectively.

Table 3-4. Static/dynamic moduli for R4 specimen under cyclic loading (CP is constant at 30 MPa)

| Cycle | Moduli | Type | Differential Stress (MPa) | | | | | |
|---|---|---|---|---|---|---|---|---|
| | | | 15 | | 30 | | 45 | |
| | | | Loading | Unloading | Loading | Unloading | Loading | Unloading |
| 1 | E (GPa) | Static | 15.1L-15.9U-15.7R | 16.1U$^{1st}$ - 15.4L-15.3U$^{2nd}$ | 14.8L-16.8U-16.0R | 17.7U$^{1st}$-16.3L-16.9U$^{2nd}$ | 17.6L-16.7U-17.1R | 16.7U$^{1st}$-17.1L-16.3U$^{2nd}$ |
| | | Dynamic | 20.9L-21.0U-21.0R | 21.6U$^{1st}$-21.7L-21.7U$^{2nd}$ | 21.8L-21.8U-21.9R | 22.1U$^{1st}$-22L-22.2U$^{2nd}$ | 22.3L-22.4U-22.4R | 22.3U$^{1st}$-22.4L-22.4U$^{2nd}$ |
| | ν (%) | Static | 24.3L-17.6U-18.7R | 34.0U$^{1st}$-18.0L-19.2U$^{2nd}$ | 31.3L-18.1U-20.2R | 29.1U$^{1st}$-18.1L-19.6U$^{2nd}$ | 47.9L-15.8U-21.0R | 15.8U$^{1st}$-21.0L-17.9U$^{2nd}$ |
| | | Dynamic | 20.8L-20.6U-21.3R | 21.4U$^{1st}$-21.3L-21.0U$^{2nd}$ | 21.9L-21.6U-21.9R | 21.3U$^{1st}$-21.7L-21.7U$^{2nd}$ | 21.9L-22.3U-22.4R | 21.9U$^{1st}$-22.3L-22.4U$^{2nd}$ |
| | G (GPa) | Static | 5.7L-6.3U-6.2R | 5.6U$^{1st}$-6.1L-6.0U$^{2nd}$ | 5.3L-6.6U-6.2R | 6.4U$^{1st}$-6.4L-6.6U$^{2nd}$ | 5.6L-6.7U-6.6R | 6.7U$^{1st}$ - 6.6L-6.4U$^{2nd}$ |
| | | Dynamic | 8.6L-8.7U-8.7R | 8.9U$^{1st}$-8.9L-9.0U$^{2nd}$ | 9.0L-9.0U-9.0R | 9.1U$^{1st}$-9.1L-9.1U$^{2nd}$ | 9.1L-9.2U-9.2R | 9.1U$^{1st}$-9.2L-9.2U$^{2nd}$ |
| | | | | | | | | |
| 2 | E (GPa) | Static | 16.6L-16.5U-16.6R | 16.5U$^{1st}$-15.4L-15.3U$^{2nd}$ | 16.3L-17.3U-16.5R | 17.7U$^{1st}$-16.6L-16.7U$^{2nd}$ | 15.6L-16.8U-16.7R | 16.8U$^{1st}$-16.7L-16.6U$^{2nd}$ |
| | | Dynamic | 21.9L-21.6U-21.6R | 21.7U$^{1st}$-21.7L-21.8U$^{2nd}$ | 22.1L-22.2U-22.2R | 22.3U$^{1st}$-22.1L-22.2U$^{2nd}$ | 22.4L-22.8U-22.6R | 22.4U$^{1st}$-22.8L-22.6U$^{2nd}$ |
| | ν (%) | Static | 27.9L-18.7U-20.6R | 34.2U$^{1st}$-18.3L-19.3U$^{2nd}$ | 34.5L-18.7U-21.3R | 30.5U$^{1st}$-20.0L-20.0U$^{2nd}$ | 37.3L-17.6U-21.0R | 17.6U$^{1st}$-21.0L-19.1U$^{2nd}$ |
| | | Dynamic | 21.2L-21.5U-21.9R | 21.3U$^{1st}$-21.9L-20.9U$^{2nd}$ | 21.9L-21.6U-22.5R | 21.9U$^{1st}$-21.5L-21.7U$^{2nd}$ | 22.5L-23.5U-22.6R | 22.5U$^{1st}$-23.5L-22.6U$^{2nd}$ |
| | G (GPa) | Static | 6.0L-6.5U-6.4R | 5.7U$^{1st}$-6.1L-6.0U$^{2nd}$ | 5.7L-6.7U-6.3 | 6.3U$^{1st}$-6.4L-6.5U$^{2nd}$ | 5.3L-6.6U-6.4R | 6.6U$^{1st}$-6.4L-6.5U$^{2nd}$ |
| | | Dynamic | 9.1L-8.9U-8.9R | 8.9U$^{1st}$-9.0L-8.9U$^{2nd}$ | 9.1L-9.1U-9.1R | 9.1U$^{1st}$-9.1L-9.1U$^{2nd}$ | 9.1L-9.2U-9.2R | 9.1U$^{1st}$-9.2L-9.2U$^{2nd}$ |

Table 3.4. cont'd.

| Cycle | Moduli | Type | Differential Stress (MPa) | | | | | |
|---|---|---|---|---|---|---|---|---|
| | | | 15 | | 30 | | 45 | |
| | | | Loading | Unloading | Loading | Unloading | Loading | Unloading |
| 3 | E (GPa) | Static | 17.2L-16.2U-19.1R | 17.0U[1st]-15.5L-15.6U[2nd] | 16.7L-17.3U-17.0R | 18.0U[1st]-16.6L-16.8U[2nd] | 15.9L-17.0U-17.1R | 17.0U[1st]-17.1L-16.3U[2nd] |
| | | Dynamic | 21.7L-21.7U-21.7R | 21.5U[1st]-21.7L-21.6U[2nd] | 22.1L-22.2U-22.1R | 22.3U[1st]-22.0L-22.1U[2nd] | 22.5L-22.3U-22.5R | 22.5U[1st]-22.3L-22.5U[2nd] |
| | ν (%) | Static | 28.5L-18.7U-18.9R | 34.8U[1st]-18.5L-19.0U[2nd] | 36.0L-18.5U-21.0R | 29.4U[1st]-19.4L-19.7U[2nd] | 36.3L-18.3U-20.8R | 18.3U[1st]-20.8L-18.0U[2nd] |
| | | Dynamic | 21.2L-21.3U-21.9R | 21.5U[1st]-20.0L-19.2U[2nd] | 21.3L-21.9U-22.1R | 20.5U[1st]-20.8L-19.9U[2nd] | 22.1L-21.2U-22.2R | 22.1U[1st]-21.2L-22.2U[2nd] |
| | G (GPa) | Static | 6.2L-6.4U-7.4R | 5.9U[1st]-6.1L-6.1U[2nd] | 5.8L-6.8U-6.5R | 6.5U[1st]-6.5L-6.5U[2nd] | 5.5L-6.7U-6.6R | 6.7U[1st]-6.6L-6.4U[2nd] |
| | | Dynamic | 8.9L-8.9U-8.9R | 9.0U[1st]-8.9L-9.0U[2nd] | 9.1L-9.1U-9.1R | 9.1U[1st]-9.1L-9.1U[2nd] | 9.2L-9.2U-9.2R | 9.2U[1st]-9.2L-9.2U[2nd] |
| | | | | | | | | |
| 4 | E (GPa) | Static | 17.6L-16.1U-16.7R | 17.3U[1st]-15.7L-15.5U[2nd] | 16.9L-17.4U-17.2R | 18.1U[1st]-16.7L-17.4U[2nd] | 16.5L-17.0U-16.6R | 17.0U[1st]-16.6L-16.4U[2nd] |
| | | Dynamic | 21.3L-21.6U-21.5R | 21.4U[1st]-21.5L-21.6U[2nd] | 21.8L-21.9U-22.0R | 22.0U[1st]-22.1L-22.1U[2nd] | 22.3L-22.4U-22.4R | 22.3U[1st]-22.4L-22.4U[2nd] |
| | ν (%) | Static | 29.1L-18.4U-20.9R | 36.7U[1st]-18.4L-19.8U[2nd] | 34.6L-19.8U-21.9R | 30.0U[1st]-19.7L-20.5U[2nd] | 37.6L-19.0U-20.6R | 19.0L-20.6L-18.7U[2nd] |
| | | Dynamic | 19.5L-20.3U-20.9R | 19.3U[1st]-19.9L-19.9U[2nd] | 20.5L-20.3U-20.9R | 21.2U[1st]-20.7L-19.8U[2nd] | 20.9L-21.2U-21.1R | 20.9U[1st]-21.2L-21.1U[2nd] |
| | G (GPa) | Static | 6.4L-6.3U-6.4R | 5.9U[1st]-6.2L-6.0U[2nd] | 5.9L-6.7U-6.5R | 6.5U[1st]-6.5L-6.7U[2nd] | 5.6L-6.6U-6.4R | 6.6U[1st]-6.4L-6.4U[2nd] |
| | | Dynamic | 9.0L-9.0U-8.9R | 8.9U[1st]-9.0L-9.0U[2nd] | 9.0L-9.1U-9.1R | 9.1U[1st]-9.1L-9.1U[2nd] | 9.2L-9.2U-9.2R | 9.2U[1st]-9.2L-9.2U[2nd] |

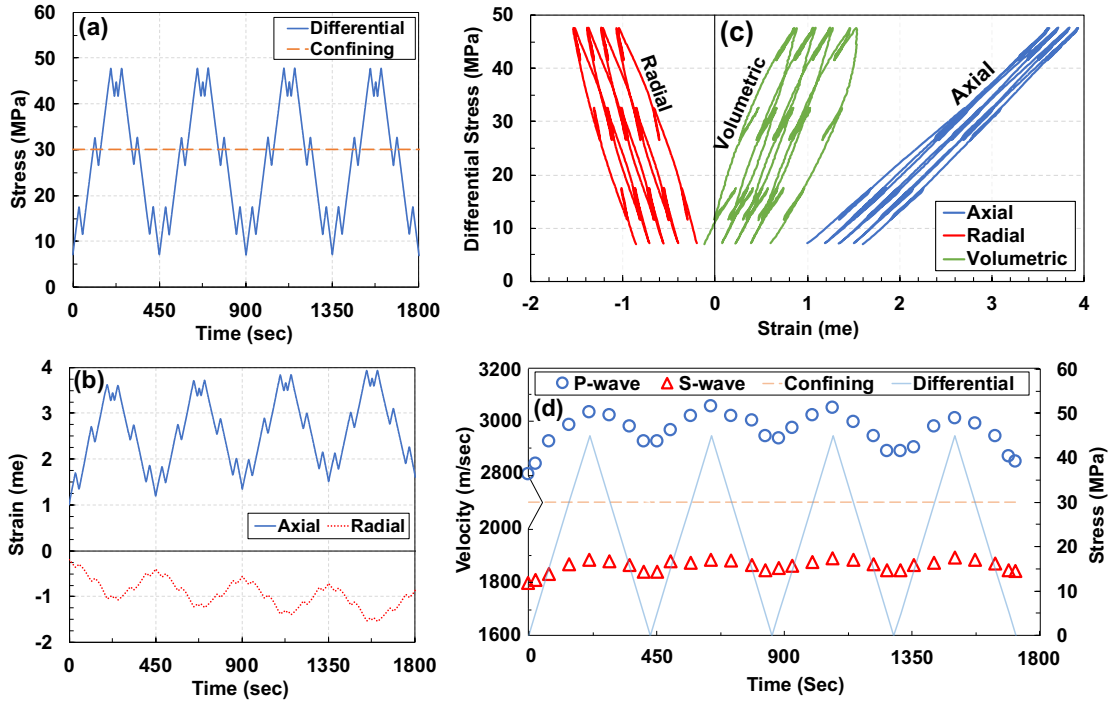


Figure 3-7. Results from cyclic test on clay-rich sample (a) stress path; (b) variation of strains versus time; (c) variation of strains versus differential stress; and (d) P- and S- wave velocity measurements during the test superimposed on the stress path. Note that the velocity axis is broken down for better illustration.

Since the direction of axial loading in MSE and cyclic tests was perpendicular to the bedding planes, compaction of bedding planes was expected to significantly contribute to the axial strain. The difference between axial and radial strains during isotropic compression was used to investigate the deformation anisotropy of the tested shale specimens. At the beginning of the cyclic tests, the confining stress was increased from ~1 to ~30 MPa (rate: 0.333 MPa/sec). Figure 3.8a and 3.8b show the variation of $\varepsilon_a$-$\varepsilon_r$ against confining stress for the R2 (calcite/quartz-rich) and R4 (clay-rich) specimens, respectively, during isotropic compression. As evident in Figure 3.8a, R2 specimen exhibits some degree of anisotropy, with less pronounced anisotropy levels at higher confining stresses. More significant anisotropy level can be observed for R4 specimen (see Figure 3.8b) compared

to R2 specimen, which can be in part attributed to the different mineralogical content of these two specimens.

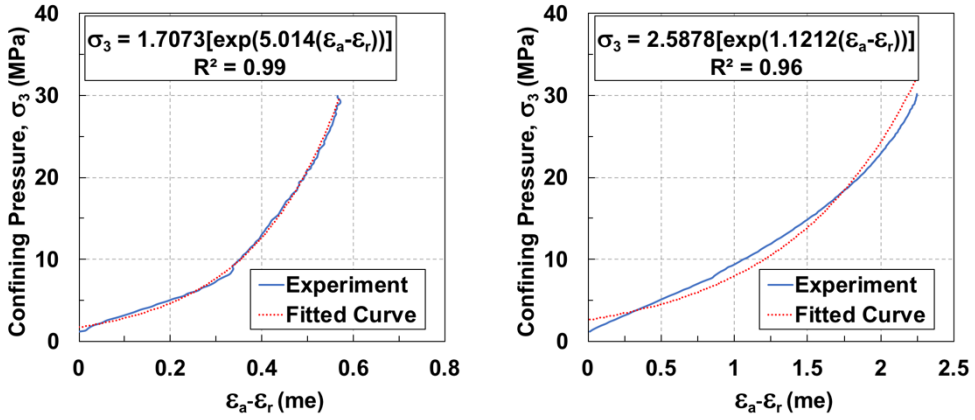


Figure 3-8. Variation of $\varepsilon_a$-$\varepsilon_r$ against confining stress during isotropic compression for (a) R2 (calcite/quartz-rich), and (b) R4 (clay-rich) specimens.

## 3.4 ANALYSIS AND DISCUSSION

The shale rocks are typically highly-inhomogeneous and anisotropic which make them inelastic material (e.g. Sone, 2012; Rezaee, 2015). In addition, the tested rock specimens in this study had multiple micro-cracks, resulted from stress relief during coring process, in the direction of the bedding planes (see Figure A1.1d), which cannot transfer the applied stress (Fjar et al., 2008). Therefore, the closure/opening of these micro-cracks during loading/unloading leads to variation in elastic moduli. In addition, these characteristics of shale rocks lead to pressure dependency and non-linear behavior, particularly upon application of differential stress.

### 3.4.1 RESPONSE OF SPECIMEN TO LOADING/UNLOADING/RELOADING CYCLES

Both calcite/quartz- and clay-rich specimens show a nonlinear axial stress-strain response with a higher non-linearity observed for the clay-rich specimens. This might be due to their higher clay content compared to the calcite/quartz-rich specimens. At lower differential stress levels, a higher degree of non-linearity is observed which could be attributed to the closure of the initial micro-cracks at very low stress levels, with an accelerated pace. On the other hand, a significant amount of non-linearity is observed for radial stress-strain for the clay-rich specimens under cyclic tests.

There is an increasing trend in the estimated static Young's modulus with differential stress for both calcite/quartz- and clay-rich specimens. This can be attributed to the fact that within the range of the applied differential stresses, the specimens are below the crack initiation threshold (see Figure 3.1a), and therefore, new micro-cracks are not created, rather some of the existing micro-cracks are being closed. As evident in Tables 3.3 and 4, the estimated static Young's modulus is affected by the loading/unloading/reloading cycles. As also observed in other studies (e.g. Sone and Zoback, 2013a; Villamor Lora et al., 2016), the estimated static Young's modulus is (i) the highest during unloading, (ii) the lowest during loading, and (iii) the intermediate during reloading. For example, the estimated static Young's modulus in unloading is 7% higher than that of loading. Although, this ratio is affected by the confinement level and is reduced from 1.51 at CP=10 MPa to 1.04 at CP=50 MPa.

The observed difference between Young's modulus in loading and unloading could be, in part, attributed to the fact that during loading both elastic and inelastic deformations occur, while during unloading, elastic deformations are more dominant (Sone and Zoback, 2013a; Villamor Lora et al., 2016). Therefore, the unloading Young's modulus might be a better indication of the elastic properties of the rock specimens (Zoback, 2010; Villamor Lora et al., 2016). On the other hand, the estimated dynamic Young's modulus is not affected by loading/unloading/reloading cycles. This observation is in-line with the fact that dynamic measurements do not capture plastic deformations of the rock specimen regardless of the type of loading/unloading/reloading, rather indicate the elastic properties of the rock (Fjar, 2008).

In all experiments, in general, the estimated static and dynamic Young's moduli at a specific stress level during the unloading path are slightly higher compared to the loading path under the same stress level. This can be an indication of the closure of some of the fractures upon loading and not opening up after releasing the stress.

### 3.4.2 SENSITIVITY OF ULTRASONIC VELOCITIES TO VARIATIONS IN STRESS CONDITIONS

Both P- and S-wave velocities are sensitive to changes in differential stress during loading and unloading. At low stress levels, the existing micro-cracks (coring/stress-relieved) are closed (region I in Figure 3.1a), and as DS increases (within region II), additional closure of existing/inherent micro-cracks occurs. Upon unloading, some of the closed fractures open up again. The closure/opening of these microfractures during loading/unloading affects the ultrasonic velocities. At lower differential stresses, the

relationship between velocity and applied stress is almost linear (e.g. Dewhurst and Siggins, 2006 and Kuila et al., 2011).

There are two sources of non-linearity as the shale specimen is loaded: (i) closure of micro-cracks, and (ii) potential plastic response of solid matrix (e.g. Dewhurst and Siggins, 2006 and Kuila et al., 2011; Villamor Lora et al., 2016). Other materials such as sandstone can show a high degree of non-linearity between velocity and stress (e.g. Eberhart-Phillips et al., 1989 and Sayers et al., 1990), which is usually attributed to grain contact stiffening and micro-crack closure (Kuila et al., 2011). As obvious from SEM images (see Figures A1.1e and A1.1f), the shales in this study have micro-cracks, and therefore, it is hypothesized that the fractures in shales behave in a different way than those in sandstone. This observation could be related to differences in shale matrix compressibility, shale fracture compliance compared to sandstone (Kuila et al., 2011).

At a particular DS level in successive cycles, the measured velocities continuously increase for both calcite/quartz- and clay-rich specimens (see Figures 3.6d and 3.7d), except for the last cycle of the clay-rich specimen. The increase of ultrasonic velocities in successive cycles could be due to compaction of the specimen and permanent closure of some of the micro-cracks, while, the decrease of the measured velocities transitioning from 3rd to 4th cycle in the clay-rich specimen could be due to the fact that some new micro-cracks are created, which is the onset of crack initiation (region III in Figure 3.1a).

By increasing the confining level, the ratio of Vp/Vs versus Vp continuously increases as shown in Figure 3.9a, indicating the effect of confinement on the velocity measurements. On the other hand, as it can be seen from Figure 3.9b, under constant

confining level, the Vp/Vs ratio versus Vp remains almost constant, indicating that increasing/decreasing differential stress does not change Vp/Vs at a constant confining level, consistent with the observation in other studies (e.g. Castanga et al., 1985).

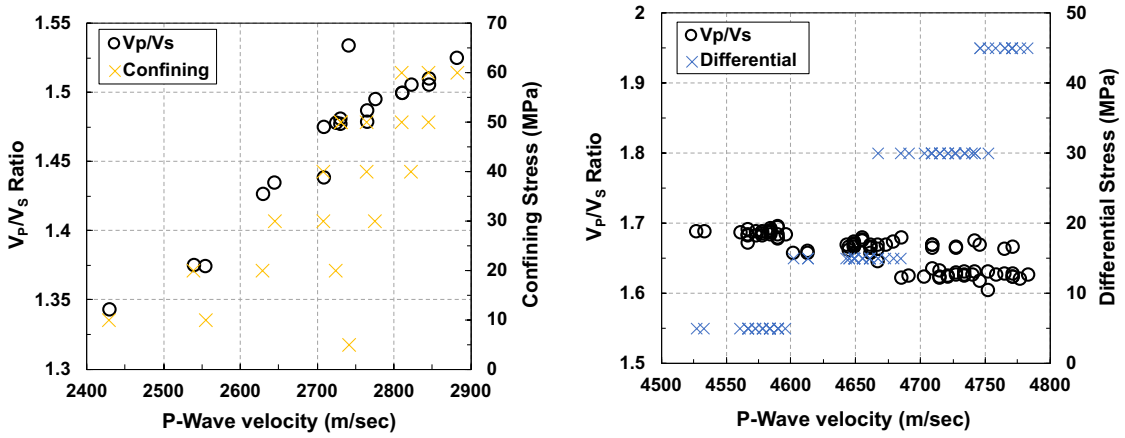


(a) (b)

Figure 3-9. Variation of $V_P/V_S$ ratio versus P-Wave velocity at (a) varying confining level, and (b) constant confining level.

### 3.4.3 PRESSURE-DEPENDENCY OF YOUNG'S MODULUS AND POISSON'S RATIO

The variation of estimated static and dynamic Young's modulus and Poisson's ratio with confining level are illustrated in Figures 3.10a and 3.10b for R1 (calcite/quartz-rich) specimen, and in Figures 3.10c and 3.10d for R3 (clay-rich) specimen, respectively. As expected and evident in Figures 3.10a-d, the estimated Young's modulus and Poisson' ratio from both static and dynamic measurements increase with the increase in confining level. In general, the variation of both static and dynamic Young's modulus follow a linear trend with relatively good regression values, except that of estimated dynamic Young's modulus for R4 specimen. It should be noted that two different trends are identifiable for CP levels

below and above 30 MPa, indicating that the closure of micro-cracks becomes less dominant as higher levels of CP are applied. This could be explained by the smaller number of open micro-cracks at higher confinement levels compared to those at lower confinement levels. Therefore, there is less room for further changes in Young's modulus at higher confinement levels. Estimations of static and dynamic Poisson's ratio, on the other hand, show a nonlinear relationship with confining level. At close-to-zero confining level, the very low Poisson's ratio estimations are attributed to the initial closure of horizontal cracks, which leads to high axial strain compared to radial strain, as also observed by Villamor Lora et al. (2016).

The combined effect of CP and DS on the estimated static and dynamic Young's modulus for R1 and R3 specimens are shown in Figures 3.10e and 3.10f, respectively, where the variation of P- and S-wave velocities with mean stress are illustrated. It can be observed that at a constant CP, as higher differential stress is applied (i.e. higher mean stress at a constant CP), the estimated dynamic Young's modulus for both specimens and static Young's modulus for the calcite/quartz-rich specimen increases, while, the estimated static Young's modulus for clay-rich specimen decreases. This difference in response of the specimens is be attributed to difference in mineralogy composition.

### 3.4.4 COMPARISON OF STATIC AND DYNAMIC MODULI ESTIMATION

In general, the estimated dynamic moduli are higher than those of static (e.g. Simmons and Brace, 1965; Fjar, 2008; Villamor Lora et al., 2016). This difference can be attributed to: (i) significantly higher strain amplitudes for static measurements compared to dynamic measurements, (ii) stress concentration at grain contact and consequently

exceeding elastic limit of minerals, and (iii) stress-induced changes in porosity (Fjar, 2008). For shale rocks, non-linearity effects as well as the heterogeneous micro-structure can further contribute to this difference between static and dynamic moduli (Fjar, 2008).

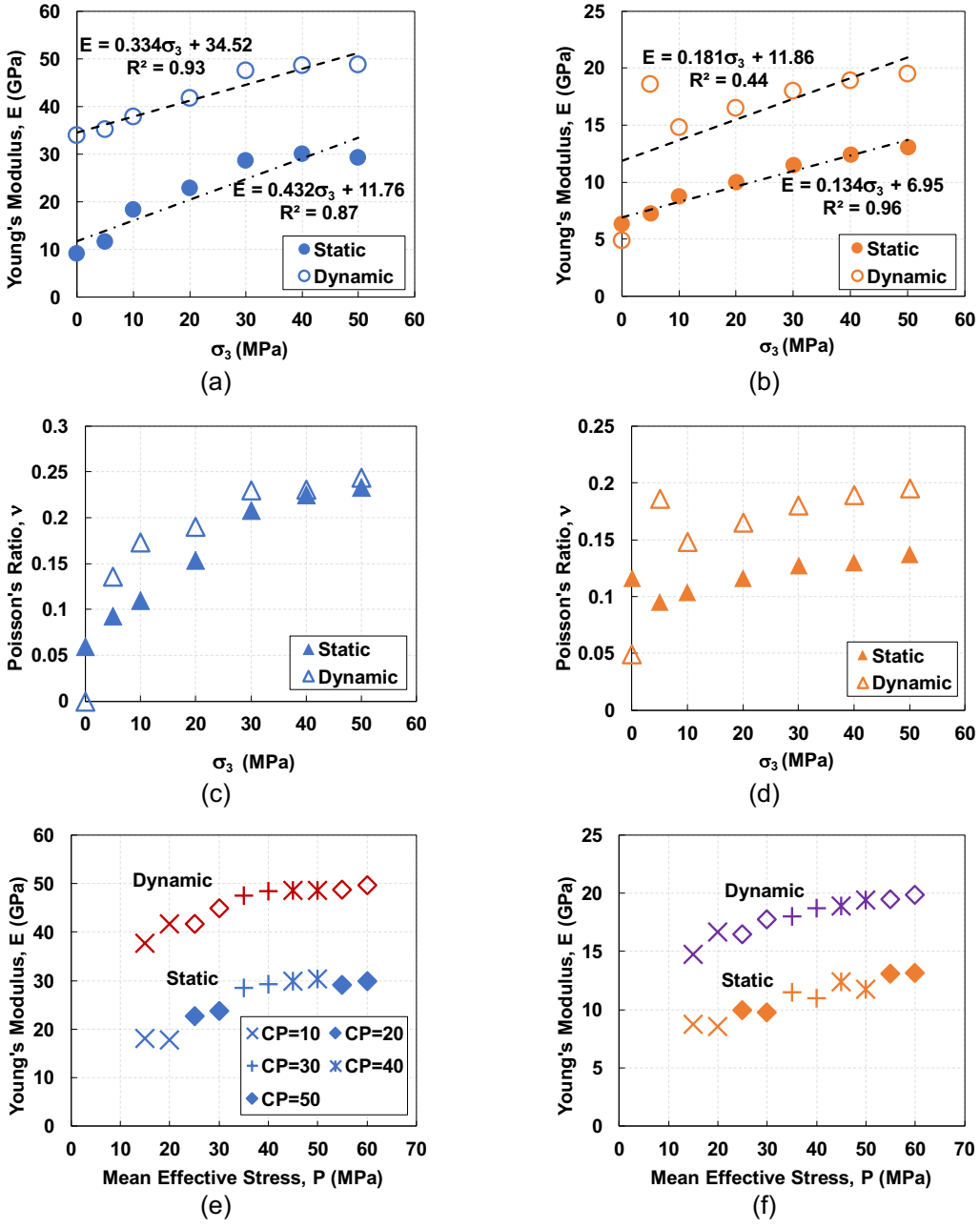


Figure 3-10. Effect of confining pressure on Young's modulus for (a) R2 and (b) R4 specimens; and on Poisson's ratio for (c) R2 and (d) R4 specimen; joint effect of confining and differential pressure on the Young's modulus for (e) R2 and (f) R4 specimens.

As evident in Figure 3.10, the dynamic moduli are higher than static. It should be noted that at low confinement levels, the relationship between the static and dynamic moduli is not reliable, however, as the confinement level increases the difference becomes smaller. This observation, in part, can be explained by the fact that the microcracks affect the strain data more than velocities (Simmons and Brace, 1965). Strain amplitude and consequently the static moduli estimated from unloading/reloading cycles are intermediate between static moduli estimated during loading and dynamic moduli (either loading/unloading/reloading).

The ratio of Young's modulus estimated based on velocity measurements to that estimated based on strain measurements, i.e. $\frac{E_{dynamic}}{E_{static}}$, can be affected by clay and organic content of the specimen. The average $\frac{E_{dynamic}}{E_{static}}$ is about 1.7 and 1.4 for calcite/quartz-rich and clay-rich specimens, respectively.

### 3.4.5 HYSTERESIS EFFECTS

The evolution of plastic deformation with CP and DS levels for both calcite/quartz-rich and clay-rich specimens is presented in Table 3.5 implying that under the same level of differential stress, the plastic deformations decrease as confinement level increases. In addition, it is worth noting that at CP=0 MPa, the applied differential stress is around 5 MPa, leading to relatively-small plastic deformation. Furthermore, at a specific confinement level, the plastic deformations increase with increase in differential stress. The clay-rich specimen follows a trend similar to that observed for calcite/quartz specimen, with few discrepancies. In addition, as it can be found from Figures 3.6d and 3.7d, during

cyclic loading, the S-wave velocities do not show hysteresis effects, while the P-wave velocities show some degree of hysteresis, similar observation to Jones and Wang (1981) for dry shale rocks.

Table 3-5. The estimated plastic strain (cumulative) under MSE test

| Specimen | CP (MPa) | DS (MPa) | Plastic strain (micro_strain) |
|---|---|---|---|
| R1 (Calcite/quartz-rich) | 0 | 0-15 | 65 |
| | 5 | 0-15 | 500 |
| | 10 | 0-15, 0-30 | 140,440 |
| | 20 | 0-15, 0-30 | 66,127 |
| | 30 | 0-15, 0-30 | 8,17 |
| | 40 | 0-15, 0-30 | 7,46 |
| | 50 | 0-15, 0-30 | 6,43 |
| R3 (Clay-rich) | 0 | 0-15 | 28 |
| | 5 | 0-15 | 333 |
| | 10 | 0-15, 0-30 | 195,393 |
| | 20 | 0-15, 0-30 | 139,266 |
| | 30 | 0-15, 0-30 | 73,151 |
| | 40 | 0-15, 0-30 | 42,131 |
| | 50 | 0-15, 0-30 | 58,24 |

## 3.5 CONCLUSIONS

The design of an optimized hydraulic fracturing program and the development of production models require the laboratory characterization of shale gas formations. In this study, Marcellus Shale rock core plugs, retrieved from a deep well in West Virginia at a depth of ~2270 m, were characterized through a series of triaxial tests with concurrent measurements of ultrasonic P- and S-wave velocities at different stress conditions. Based on the mineralogy, the specimens were categorized into calcite/quartz-rich and clay-rich.

It was found that the planes of weakness and the existing microcracks (residing in clay content and sub-parallel to the bedding planes) play a major role in response of these rocks.

For characterization of elastic, hysteresis, and plastic properties of the specimens tested in this study, a series of multi-stage elastic and cyclic test, supplemented by velocity measurements, were performed. It was found that both type of specimens show a substantially-nonlinear response, with higher degree of nonlinearity for clay-rich specimens. The nonlinear response was more pronounced at low differential stress levels, where the closure of microcracks might occur. The ultrasonic P- and S-wave velocities were found to be sensitive to changes in the internal structure of the rock caused by variation in stress conditions. The changes in measured velocities were more significant during isotropic compression stages of the tests, where confining level was increased, compared to triaxial stages of the tests. Both static and dynamic estimations of Young's modulus and Poisson's ratio increased with increase in confining level. At higher stress levels, both estimated static and dynamic moduli increased, an indication that the compaction of the specimens has occurred.

The estimated dynamic Young's modulus was found to be affected by the very small strain amplitudes, and therefore, significantly higher than the static estimations at corresponding stress level. The ratio of the estimated dynamic Young's modulus to static can be considered as a proxy of the clay and organic content of the specimen. Therefore, the specimens with higher clay content showed a lower ratio of dynamic to static Young's modulus, compared to that of calcite/quartz-rich specimens. However, the static reloading/unloading Young's modulus in sub-cycles of the cyclic tests were found to be

the intermediate value between dynamic and static (during loading). The slightly higher Young's modulus during unloading path was attributed to the fact that some of the closed microcracks upon loading, were not opened up again after unloading, and subsequently, the plastic deformations were not as substantial as those during loading path. It was found that as the confining level increases, the plastic deformations become less significant, while, increasing the differential stress on the specimens caused more significant plastic deformations.

# CHAPTER 4

# STRESS-STRAIN RESPONSE AND SEISMIC SIGNATURE ANALYSIS OF PHYLLITE RESERVOIR ROCKS FROM BLUE MOUNTAIN GEOTHERMAL FIELD

## ABSTRACT

Geothermal energy is the heat contained in rock and fluid in the earth's crust. In some areas the geothermal resource can be exploited by drilling wells to extract the heated fluids and piping the fluids to a power plant to generate renewable electricity. Geomechanical characterization of the rocks in geothermal reservoirs is necessary to (i) optimize a well stimulation program, (ii) reduce production decline, and (iii) build more accurate predictive models at reservoir scale. In this study, we present the results of a suite of experiments on mechanical characterization of phyllite rock specimens retrieved from DB-2 well (depth of 1260 m) at the Blue Mountain geothermal field in Nevada, United States. In order to investigate the effects of anisotropy on mechanical response of rock, one vertically-drilled and one horizontally-drilled sub-cores were extracted from the phyllite core. Multi-stage elastic, cyclic, creep, and multi-stage failure tests were performed to characterize the elastic, plastic, time-dependent, and failure properties as well as effects of anisotropy on the behavior of the phyllite specimens. The pressure-dependent static and dynamic moduli revealed that within the elastic region, the Young's modulus increased with the increment of differential stress during the loading stage. While, 10% to 50% difference between the elastic moduli of the two specimens confirmed the anisotropic

nature of the material. Negligible creep response was observed in both specimens, with a more pronounced change in P- and S-waves velocities during hydrostatic stage for vertically-drilled sub-core. The failure envelope developed using the multi-stage failure test on the vertically-drilled specimen, indicated good agreement with both Linearized Mohr-Coulomb and Hoek-Brown failure criteria. On the other hand, significant changes were observed in the time-frequency maps of the transmitted seismic waves during multi-stage elastic test (i.e. change in confining level), however, slight changes in the time-frequency map were observed during creep test (i.e. application of differential stress for a relatively long period).

## 4.1 INTRODUCTION AND BACKGROUND

Geothermal systems take advantage of exchanged heat between hot dry bedrock and injected water for electricity production or direct heating (Tester et al., 2006). Due to several factors such as (i) high capital cost (e.g. Tester et al., 2006), (ii) reduced reservoir productivity (e.g. Ghassemi, 2012; Caulk et al., 2016; Kamali-Asl et al., 2018a), and (iii) environmental concerns, such as induced seismicity (e.g. Majer et al., 2007; Izadi and Elsworth, 2015), development of geothermal reservoirs as a resource of renewable energy has not gained enough attention. The reduced reservoir productivity and induced seismicity are linked to the coupled Thermal-Hydrological-Mechanical-Chemical (THMC) processes resulted from the interaction between host rock and circulating fluid. Thermo-mechanical deformation (e.g. Ghassemi and Zhou, 2011), chemical alteration of fracture surface (e.g. Taron and Elsworth, 2010), shear dilation (e.g. McClure and Horne, 2014), chemical-mechanical creep (e.g. Taron and Elsworth, 2010), and reservoir volume change due to

fluid injection/withdrawal (e.g. Ellsworth, 2013) are among the processes that are shown to have significant influence on the geothermal reservoir production.

Although greenfield Enhanced Geothermal Systems (EGS) are not yet common, single-well stimulations are sometimes conducted to overcome the low productivity or injectivity of geothermal wells and create an EGS reservoir or expand an existing reservoir, which has been practiced at different geothermal fields (e.g. Chabora et al., 2012; Kelkar et al., 2012; Bradford et al., 2016). To create a productive EGS reservoir, a network of connected fractures is created in the reservoir through stimulation program, in which either new fractures are created through hydraulic fracturing (e.g. Li et al., 2016) or existing sealed fractures are re-opened using hydro-shearing process (e.g. Cladouhos et al., 2009 and 2016; Frash et al., 2014). Both of these stimulation strategies are conducted by injecting moderate pressure (for hydro-shearing) or high pressure (for hydraulic fracturing) fluid into the reservoir, which leads to perturbations in the state-of-stress (e.g. McClure and Horne, 2014; Wang et al., 2016).

Geomechanical characterization of geothermal reservoir rocks usually involves estimation of fundamental rock properties such as elastic moduli, strength and failure properties, and viscoelastic deformations under different stress conditions. These properties are crucial as they influence the activation of the discontinuities, long-term permeability and induced seismicity in a geothermal reservoir (e.g. Lutz et al. 2010). Moreover, these fundamental material properties are essential input for advanced multi-physical constitutive models for geothermal reservoirs (e.g. Zimmermann and Reinicke, 2010).

The elastic properties of reservoir rocks are affected by variation of the composing materials of the reservoir rock, geological structures, in-situ state-of-stress, temperature, and pore pressure (e.g. Sone and Zoback, 2013; Kamali-Asl et al., 2018b). Accordingly, evaluation of the short-term static moduli (i.e. those estimated from stress-strain response) and dynamic moduli (i.e. those estimated from seismic wave velocities) of reservoir rocks can improve our understanding of a geothermal reservoir response (Lockner et al., 1982). The minimum pressure required to initiate a hydraulic fracture is contingent on the magnitude of the least principal stress (e.g. Fjar, 2008), while, hydro-shearing can take place at stress levels lower than the minimum horizontal principal stress (e.g. Cladouhos et al., 2009). Therefore, characterizing the failure mechanism of the formation rock and principal stress regime are necessary to design an optimum reservoir stimulation program (e.g. Zoback, 2010).

On the other hand, viscoelastic deformation of reservoir rocks might have a significant negative influence on both short- and long-term performance of geothermal reservoirs. In short-term, mechanical creep causes stress perturbations, subsidence, and affects the stimulation process (e.g. Majer et al., 2007; Ghassemi, 2012; Schmittbuhl et al., 2014). In long-term, under in-situ reservoir conditions, mechanical creep is one of the phenomena that contribute to gradual closure of fracture, and thereby decreasing the permeability of a geothermal reservoir. In order to maintain the optimal flow, shear stimulation is conducted in geothermal reservoirs to re-open the closed fractures (e.g. Cha et al. 2017), in some cases, using cyclic rate injection scheme (Zhuang et al. 2017). Therefore, evaluation of mechanical creep and cyclic load response of reservoir rocks is an

important component of geomechanical characterization of a geothermal/EGS reservoir rock.

Ultrasonic wave propagation is a non-destructive method to evaluate rock behavior under different loading/unloading conditions (e.g. Simmons and Brace, 1965; Sone and Zoback, 2013; Kamali-Asl et al., 2018c). In this method, the compressional-wave velocity (Vp) and the cross-polarized shear-wave velocities (Vs) are used to estimate the dynamic properties (e.g. elastic moduli) of a rock (e.g. Simmons and Brace, 1965; Ayling et al., 1995). Compared to the static estimation of the elastic moduli of rocks, the dynamic ones are usually higher (e.g. Sone and Zoback, 2013; Choi et al., 2014; Kamali-Asl et al., 2018c). Generally, the ultrasonic wave velocities are sensitive to presence of micro-cracks/fractures and loading/unloading-induced changes in the micro-cracks and fractures within the rock (e.g. Schubnel and Gueguen, 2003; Kamali-Asl et al., 2018b). Fracture closure and pore collapse under hydrostatic condition (i.e. isotropic compression) increase the ultrasonic wave velocities, however, crack propagation under triaxial loading condition can reduce P- and S-waves velocities (e.g. Sone and Zoback, 2013; Hedayat and Walton, 2016; Kamali-Asl et al., 2018b).

Conventional geothermal energy projects are located in rare areas where fracture permeabilities and heat flow are high. In these projects, the natural hydrothermal system is exploited by drilling geothermal production wells into permeable rock masses containing convecting hot liquids or steam (e.g. Lockner et al., 1982). Often these hydrothermal systems result in surface manifestation such as hot springs, geysers, or fumaroles where they breach the surface (e.g. Stimac et al., 2008). Hydrothermal systems can also be blind,

where the convective cell is capped by impermeable layers (e.g. Faulds and Melosh, 2008). Even in geothermal fields with generally productive wells, some wells do not have sufficient permeability to serve as economically viable producers or injectors, in which case the techniques of EGS can be used to make idle wells productive and expand the field (e.g. Ghassemi, 2012). This has been successfully performed at Raft River, Idaho (Bradford et al., 2016) and Desert Peak, Nevada (Chabora et al., 2012; Kelkar et al., 2012).

Crystaline (e.g. granite) (e.g. Caulk et al., 2016) and sedimentary (e.g. sandstone) (e.g. Legarth et al., 2005) rocks are the typical rock types encountered in deep geothermal reservoirs. However, in many cases, the reservoir rock is comprised of metamorphic rocks (e.g. Sumner et al., 2015; Swyer et al., 2016) such as phyllite, which is classified as low-grade metamorphic rocks that commonly have thin-foliated texture (Arnold, 1998). Flow and recrystallization of the rocks under high pressure and temperature is reflected in the anisotropic characteristic of metamorphic rocks (e.g. Nasseri et al., 2003). The intrinsic anisotropy of phyllite rocks affect its physical and mechanical properties (McLamore and Gray, 1967; Ramamurthy et al., 1993). Therefore, the permeability, strength, deformation, and elastic moduli, can be different in different loading directions (Ramamurthy et al., 1993; Nasseri et al., 2003).

### 4.1.1 BLUE MOUNTAIN GEOTHERMAL FIELD

Blue Mountain is a relatively small fault block consisting of different types of rocks including quartzites, slate, and phyllite (Faulds and Melosh, 2008; Casteel et al., 2009) located 50 km east of Winnemucca, Nevada, United States (see Figure 4.1). Although

sometimes labeled as a blind geothermal field (i.e., no active surface manifestations) (Faulds and Melosh, 2008), there is an evidence for prolonged hydrothermal activity along faults exposed on the flanks of Blue Mountain (Casteel et al., 2009) and hydrothermally-altered ground at the surface near the DB-2 core hole (T. Cladouhos, pers. Comm, 2017). Several studies have been performed to model the geological structure of the geothermal field and identify the physical properties (i.e., grain density, dry and saturated bulk density) and lithology of Blue Mountain reservoir rock specimens (e.g. Ponce et al., 2009; Calvin et al., 2010; Ponce, 2012). According to the structural model suggested by Faulds and Melosh (2008), this geothermal field is situated where NE-striking, normal-sinistral, and WNW-striking normal-dextral fault zones intersect. Ponce (2012) conducted a site investigation using two different boreholes (DB-1 and DB-2) and reported an average saturated bulk density of 2650 kg/m$^3$.

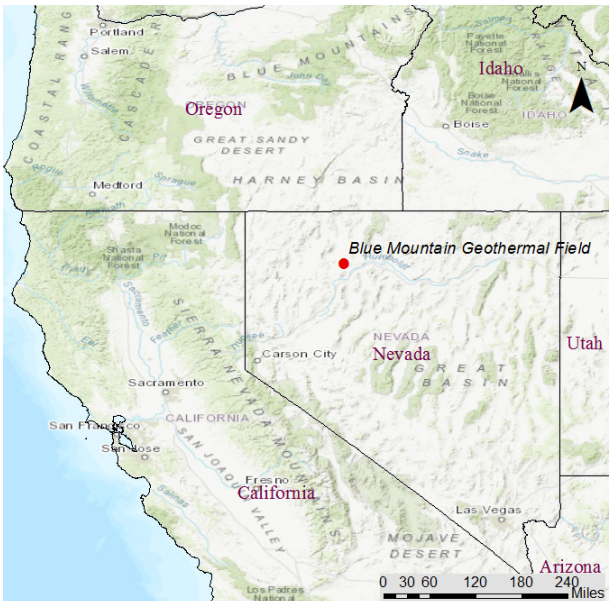


Figure 4-1. The location of Blue Mountain geothermal field (Map created using ArcGIS)

The geothermal resource of Blue Mountain was discovered accidentally during a mineral exploration process (Faulds and Melosh, 2008). This geothermal reservoir is categorized into hot brine geothermal field that contains neutral-pH, dilute alkaline-chlorine waters (Casteel et al., 2009). Furthermore, the injection test at the depth of 5600 ft has revealed that the reservoir has high injectivity potential, where the maximum initial temperature was in the order of 210 °C (Casteel et al., 2009). Aeromagnetic and gravity data have indicated that the geothermal field is located along the pre-existing crustal fracture (Ponce et al., 2009), which is mostly consisted of mafic dike. However, characterization of fracture connectivity demonstrated that calcite scaling could occur at the average temperature of 160 °C, which is a common temperature at the Blue Mountain geothermal field (Sumner et al., 2015). Calcite precipitation can impact the fracture connectivity and reduce the productivity of the geothermal field. Monitoring of the micro-seismic events can provide useful information about the behavior and characteristics of the reservoir (e.g., fluid transport characteristics) (Shapiro et al., 2002). Templeton et al. (2017) monitored 600 micro-earthquakes to identify the fracture characteristics of the Blue Mountain geothermal field under the influence of fluid injection or temperature changes and concluded that only one-third of the seismic events occurred inside the reservoir (Templeton et al., 2017). When AltaRock took over the project in 2013, the Blue Mountain geothermal reservoir had experienced over 20 °F temperature drop due to the initial injection strategy, which resulted in power output decrement (Swyer et al., 2016). A new geothermal conceptual model was developed (Swyer et al., 2016), which better explains the well connectivities and led to an alternative injection strategy; moving the injection

flow to the wells located in northern part of the field and closing the western deep wells (Swyer et al., 2016).

Prior to development of the geothermal field at Blue Mountain from 2006-2009, two core holes, Deep Blue 1 and 2 (DB-1 and DB-2), were drilled in 2002 and 2004-2005 to depths of 672 m (2205 ft) and 1522 m (4993 ft), respectively. To study the geomechanical, hydrothermal and transport properties of the reservoir rock, AltaRock Energy provided a phyllite rock core, from DB-2 from a depth of 1260 m, the depth of the geothermal reservoir in wells drilled 1-2 km to the west (see Figure 4.2a). Four sub-cores were successfully extracted, two in the direction of coring axis (i.e. vertically-drilled sub-core) and two side-drilled (i.e. horizontally-drilled sub-core) specimens, as shown in Figure 4.2b. Two specimens were artificially fractured and used to conduct flow-through tests and investigate the hydrothermal and transport properties. The results of these experiments are summarized in a companion paper by the authors. In this study, the results of a suite of experiments for mechanical characterization and potential anisotropy effects of one intact vertically-drilled (PH1) and one intact horizontally-drilled (PH2) specimens are presented. Section 4.2 presents the material used in this study, followed by experimental program in Section 4.3. Section 4.4 presents the results and Section 4.5 provides discussions and analysis, respectively. Finally, the conclusions are provided in Section 4.6. Specimen preparation is provided in Appendix B, experimental procedure is provided in Appendix C, a matrix representation of stress-strain response and derivation of static and dynamic moduli is provided in Appendix D, and introduction to wavelet analysis are provided in Appendix E.

## 4.2 MATERIALS

As shown in Figure 4.2a, the original phyllite core had a diameter of 2.5 inches, a length of 9 inches, and a dry density of 2.69 g/cm$^3$. No apparent micro-cracks were identified in the texture of the core, and a quartz vein was observed in the core, as it can be seen in Figure 4.2a. The foliation for PH1 specimen was 23° from horizontal ends of the specimen. PH2 specimen is along the strike of the foliation, and hence, the angle between the horizontal ends of PH2 and the foliation is 90 degrees.

The X-Ray Diffraction (XRD) analysis indicated that the rock contained 67.4% quartz, 18.8% albite, 10.5% biotite, and 3.2% chlorite. Using the comparison between average grain density and the bulk density of the specimen (Mavko et al., 2009), the porosity of the specimens was estimated as 0.74%. The permeability of the core at close to in-situ conditions (i.e. an overburden stress of 30 MPa, and temperature of bedrock ~155 °C) was measured in the lab as ~$5\times10^{-20}$ m$^2$. Figure 4.2c shows the CT-scan image of the cross-section of PH1 specimen prior to any loading. Figure 4.2d shows small region selected for Scanning Electron Microscopy (SEM) images. At these scales (i.e. X2500 and X6000) no major micro-cracks, voids and inclusions can be identified. However, the grain boundaries can be easily identified, particularly, in the magnified region (i.e. X6000).

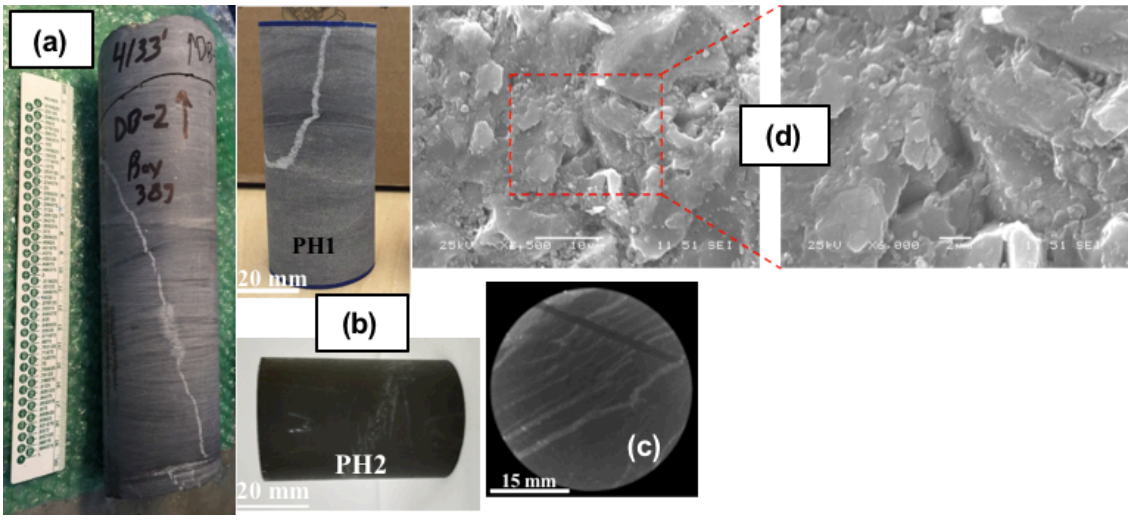


Figure 4-2. Photo of (a) the phyllite core from Blue Mountain geothermal reservoir, and (b) PH1 and PH2 specimens, (c) CT-scan image of the cross-section of the PH1 specimen prior to any loading, (d) SEM images of the phyllite core at X2500 and X6000 magnifications.

## 4.3 EXPERIMENTAL PROGRAM

### 4.3.1 TESTING PLAN

For characterization of elastic, viscoelastic, hysteresis, and failure response, a series of Multi-Stage Elastic (MSE), creep, cyclic, and Multi-Stage Failure (MSF) tests were conducted on vertically-drilled sub-core (PH1) and horizontally-drilled sub-core (PH2) phyllite specimens, in addition to characterization of anisotropic effects on the response of these rocks. Moreover, during MSE, creep, and cyclic tests, the seismic signatures (i.e. velocities and frequency content) were collected in order to (i) estimate dynamic moduli at different stress levels, and (ii) investigate the sensitivity of seismic signatures to the changes in the micro-structure of these rocks. The rationale and details of each test are provided in the following sections.

#### 4.3.1.1 MULTI-STAGE ELASTIC (MSE) AND FAILURE (MSF) TESTS

Reservoir rocks are typically scarce and variable in their geomechanical properties, and therefore, multi-stage triaxial tests are usually helpful as substitute to multiple single-stage triaxial tests (e.g. Islam and Skalle 2013; Villamor Lora et al., 2016; Kamali-Asl et al., 2018c). Pressure-dependent elastic, failure, and non-linear properties of a reservoir rock can be investigated through MSE and MSF tests. Several studies have shown the effectiveness of MSE test for determination of elastic properties (e.g. Kim and Ko, 1979; Villamor Lora et al., 2016; Kamali-Asl et al., 2018c) as well as MSF test for (i) characterization of strength properties, and (ii) constructing failure envelope (Kovari and Tisa, 1975; Kim and Ko, 1979; Youn and Tonon, 2010; Yang, 2012; Villamor Lora et al., 2016; Kamali-Asl et al., 2018b). The design of MSE/MSF tests are specific to the type of the rock and stress conditions. In MSE test, usually several stages of confining stress are applied to the specimen, followed by a few cycles of differential stress in each stage to investigate the static and dynamic moduli as well as hysteresis behavior at different confining/differential levels. To stay within the elastic region, the applied differential stress to the rock specimen should not exceed 50% of UCS and 3 times of CP.

As shown in Figure 4.3a, in MSF test, at each stage with a specific CP, the differential stress is increased up to close-to-failure point; then the differential stress is removed, CP is increased to the next desired level in the next stage, and differential stress is increased to close-to-failure point, and finally the rock is failed at the last stage. This allows constructing failure envelope, estimating Unconfined Compressive Strength (UCS) and pressure-dependent failure strength properties (Kim and Ko, 1979; Youn and Tonon,

2010; Kamali-Asl et al., 2018b). In performing MSF test, it should be noted that the dilatancy threshold of a specimen at close-to-failure stress level is identified based on visual monitoring of stress-strain data (e.g. Youn and Tonon, 2010; Villamor Lora et al., 2016; Kamali-Asl et al., 2018b), and hence, it is not easy to identify the failure point. It should be noted that the accuracy and reliability of the results of MSF test in its latter stages might be affected by the induced damage and plastic deformations in the earlier stages.

As shown in Figure 4.3b, a rock specimen typically exhibits up to five regions in its stress-strain response under triaxial loading (Hoek and Martin, 2014; Walton et al., 2017), which are: "I) crack closure, (II) linear elastic deformation, (III) crack initiation (CI) and stable crack growth, (IV) crack damage (CD) and unstable crack growth, and (V) ultimate failure" (Hoek and Martin, 2014; Walton et al., 2017). At low differential stress levels (i.e. region I), the closure of micro-cracks caused by stress relief during coring process could be one of the underlying reasons for the nonlinear behavior of rock (e.g. Villamor Lora et al., 2016; Kamali-Asl et al., 2018b). A linear stress-strain relationship can be observed in region II, followed by damage in the boundaries of grains, as higher differential stresses are applied, leading to initiation of stable cracks in region III (Hoek and Martin, 2014; Walton et al., 2017). Unstable crack growth and crack damage threshold occurs in region IV, followed by reaching to failure strength in region V (Hoek and Martin, 2014; Walton et al., 2017). In an MSF test, all of these regions might be present as the specimen is loaded up to the vicinity of its failure strength. However, in MSE test, only Regions I and II are present in stress-strain response, since the applied differential stress to the rock specimen is within 3 times of CP and 50% of UCS.

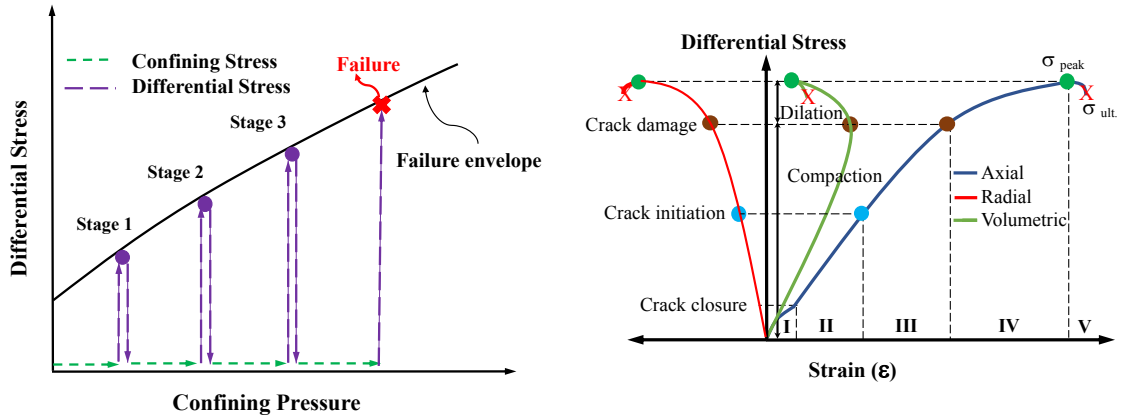


Figure 4-3. (a) Stress path during MSF tests (adopted and modified from Kamali-Asl et al., 2018), and (b) schematic of different regions corresponding to crack closure, initiation, and damage (adopted and modified from Hoek and Martin, 2014; Walton et al., 2017).

The stress path followed during MSE test, with seven stages, is illustrated in Figure 4.4a. CP was first applied and kept constant for 2 hours in each stage, to ensure that the compaction of the specimen has been fully achieved, followed by application of 1 to 4 cycles of differential stress depending on the confining level, as illustrated in Figure 4.4b-e. A rate of 0.333 MPa/sec was selected for applying CP and DS (ASTM D7012). After subjecting a rock specimen to loading/unloading process at desired DS levels, the CP was increased in 5 MPa increments to the next level up to 50 MPa, as illustrated in Figure 4.4a, followed by performing loading/unloading stage at the desired DS levels. At different stress levels along the stress path, the ultrasonic P- and S-waves were measured. Figure 4.4f shows an example of the instances of seismic signature collection during Stage 4 of MSE test, indicating that in each stage the ultrasonic velocities were measured (i) immediately after application of CP, (ii) after 2 hours of equilibrium, and (iii) immediately before and after application of DS.

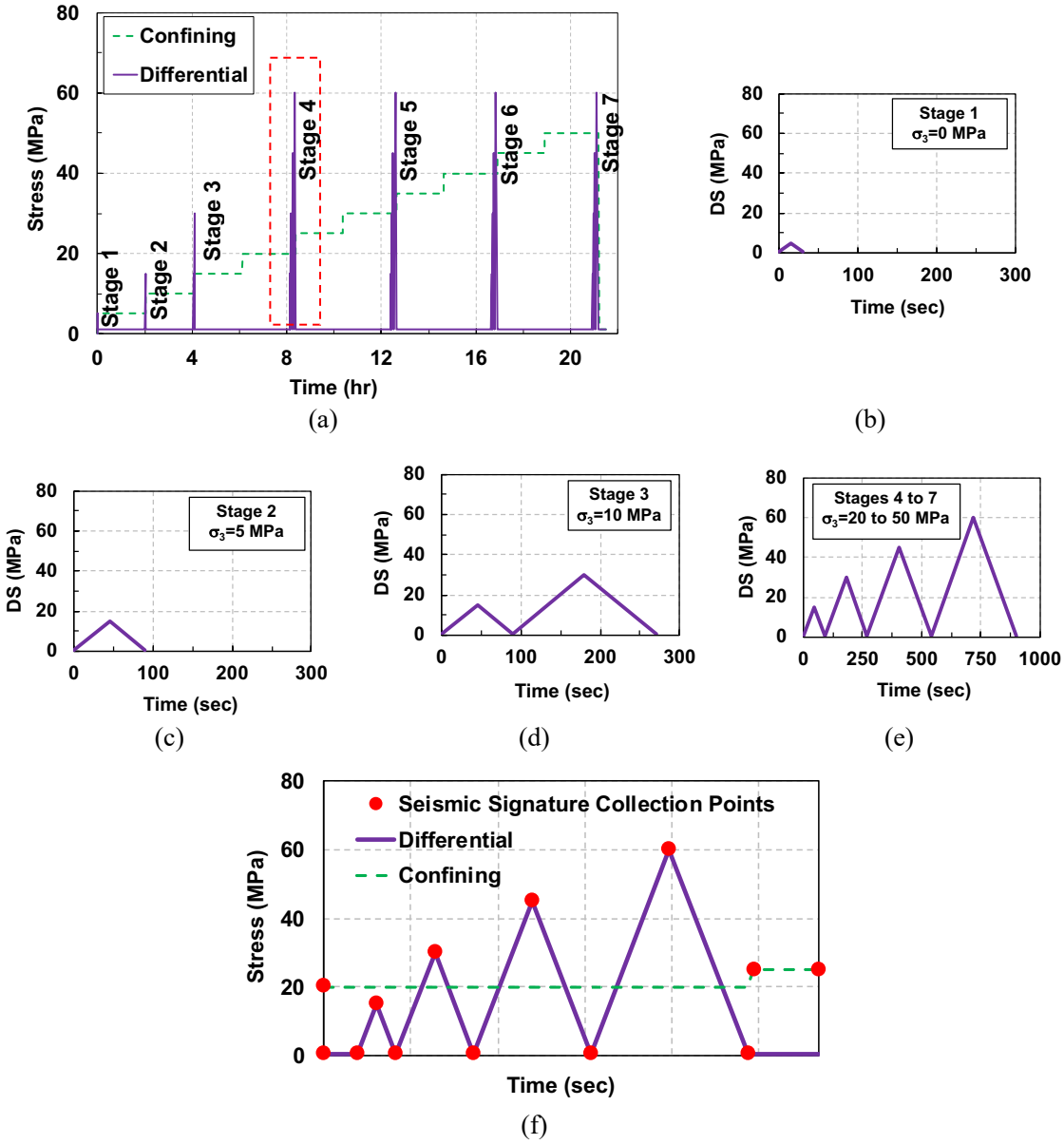


Figure 4-4. (a) stress path followed during the MSE tests; differential stress during (b) Stage 1, (c) Stage 2, (d) Stage 3, and (e) Stages 4 to 7 of the test; and (f) example of the stress conditions, P- and S- wave velocity measurement points along the stress path during Stage 4.

### 4.3.1.2 CREEP TESTS

As illustrated in Figure 4.5a, a viscoelastic material exhibits a time-dependent response under creep tests, which is consisted of four stages (Fjar, 2008; Brantut et al.,

2012) including: (i) initial elastic strain, in which the elastic strains are observed due to application of differential stress, (ii) primary creep with a decelerating rate in viscoelastic response due to increase in stable micro-cracks, (iii) secondary creep with a constant strain rate and permanent residual deformations after unloading, and (iv) tertiary creep due to growth of unstable cracks, followed by material failure.

The viscoelastic response of phyllite specimens were evaluated through hydrostatic and triaxial stages of creep tests. Hydrostatic stage consisted of six levels of CP up to 30 MPa, with each CP held constant for 3 hours, while during the triaxial stage the CP was held constant at 30 MPa (i.e. in-situ stress level), and four stages of DS increasing from 15 MPa up to 60 MPa were performed, with each DS held constant for 12 hours. Upon completion of stages of triaxial creep test, the DS was removed, and CP held constant at the in-situ stress for 6 hours. As shown on stress path in Figure 4.5b, the seismic signatures were collected immediately after loading and after completion of 3 hours of hydrostatic creep or 12 hours of triaxial creep.

#### 4.3.1.3 CYCLIC TESTS

Cyclic tests are useful in order to evaluate the gradual degradation of elasticity, non-linear, and hysteresis behavior of rocks (e.g. Yang, 2012; Kamali-Asl and Ghazanfari, 2018). These characteristics could be useful for optimizing the (re)stimulation of reservoir rocks, to re-open the network of fractures that have been closed (e.g. Cha et al. 2017; Zhuang et al., 2017). In a typical cyclic test, the confining level is first increased to the in-situ stress level, followed by application of a number of cycles of differential stress. Then, plastic deformations due to hysteresis/nonlinear behavior, and alteration of elastic moduli

in different loading/unloading scenarios can be investigated. Similar to creep tests, CP was increased to the in-situ stress level (i.e. 30 MPa), followed by application of 9 cycles of differential stress from 0 to 60 MPa, as illustrated in Figure 4.6.

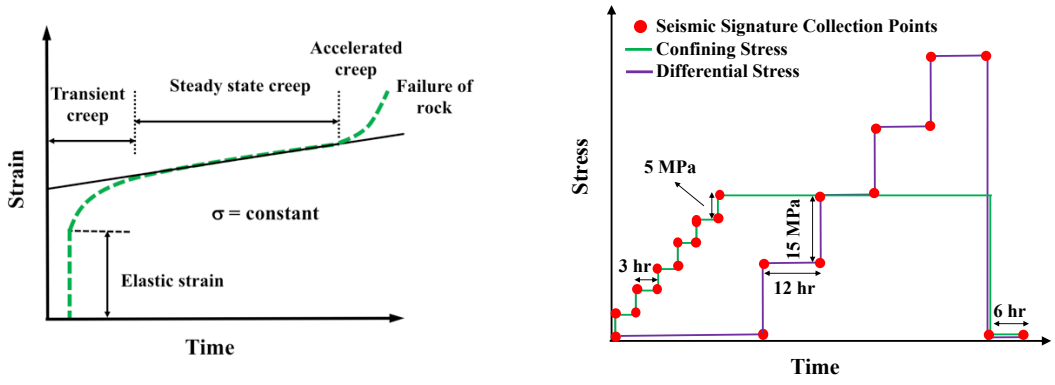


Figure 4-5. Schematics of (a) different stages of creep (adopted and modified from Fjaer 2008); (b) stress path followed during the creep tests.

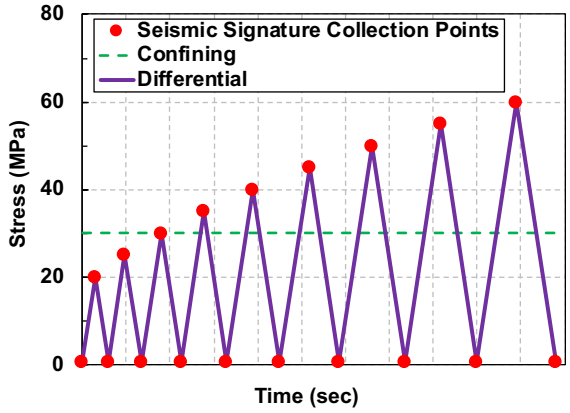


Figure 4-6. Stress path followed in cyclic test with the instances of velocity measurements

### 4.3.2 SUMMARY OF EXPERIMENTS

A series of the mechanical characterization tests including MSE, cyclic, creep, and MSF tests, in addition to investigation of the effects of material anisotropy. The tests were performed on dry specimens due to the fact that saturation of the very low porosity phyllite

specimens was extremely difficult. The order of the experiments was selected to minimize the effects of an earlier test on the results of a later test, however, it should be acknowledged that performing the tests on one single specimen might create permanent deformations, leading to some degree of inaccuracy in the results.

## 4.4 RESULTS

### 4.4.1 ISOTROPIC COMPRESSION

Prior to all the triaxial tests, isotropic compression tests were performed on both specimens. In this test, the confining level was increasing step-wise from 0 to 30 MPa (i.e. in-situ stress level), in increments of 5 MPa and at each stage, CP was kept constant for 2 hours, similar to hydrostatic stage of creep test. Using stress-strain data, static bulk and coupling moduli were estimated for both specimens. In addition, dynamic bulk modulus for both specimens was estimated using the measured P- and S-waves velocities. Figures 4.7a and 4.7b show the estimated static and dynamic bulk moduli for PH1 and PH2 specimens, respectively. It can be observed that both static and dynamic moduli for both specimens increase with confining level, except a discrepancy in static bulk modulus and a discrepancy in dynamic bulk modulus, both for PH2 specimen.

For better illustration of the anisotropy behavior, the ratio of the static-to-dynamic bulk modulus at different confining levels for both specimens are provided in Figure 4.7c. The range of variation of static-to-dynamic bulk modulus ratio is ~0.4 to ~0.9 for both specimens and this ratio increases with increased confining pressure. It can be observed that at higher confining levels, this ratio is higher, as also observed in other studies (e.g.

Fjar, 2008; Sone and Zoback, 2013). This observation indicates that the estimated static and dynamic values are closer at higher confining levels, or equivalently, the dynamic measurements are more-reliable at higher confining levels. The change in the ratio of static-to-dynamic bulk modulus at different confining levels for the intact phyllite specimens can be attributed to the facts that (i) the dynamic strain amplitudes are 3-4 orders of magnitude less than those of static counterparts, (ii) micro-structure of the rock specimens is heterogenous, and (iii) there is stress concentration at the grain contact, which might exceed the elasticity limit. It should be, however, noted that the trends of variation of the static-to-dynamic bulk modulus ratio with confining level is not similar in the two specimens, indicating some degree of anisotropy."

The estimation of static coupling moduli for PH1 and PH2 specimens are illustrated in Figures 4.7d and 4.7e. It can be observed that as higher confining levels are applied, the coupling modulus for both specimens increases. Up to confining level of 20 MPa, the coupling moduli of PH1 and PH2 specimens are very close (~5% higher for PH2 specimen). However, at confining levels of 25 and 30 MPa, PH2 specimen yielded significantly higher coupling modulus values compared to PH1 specimen. This can indicate that the tested phyllite rock exhibits some degree of anisotropy at confining levels close to in-situ conditions.

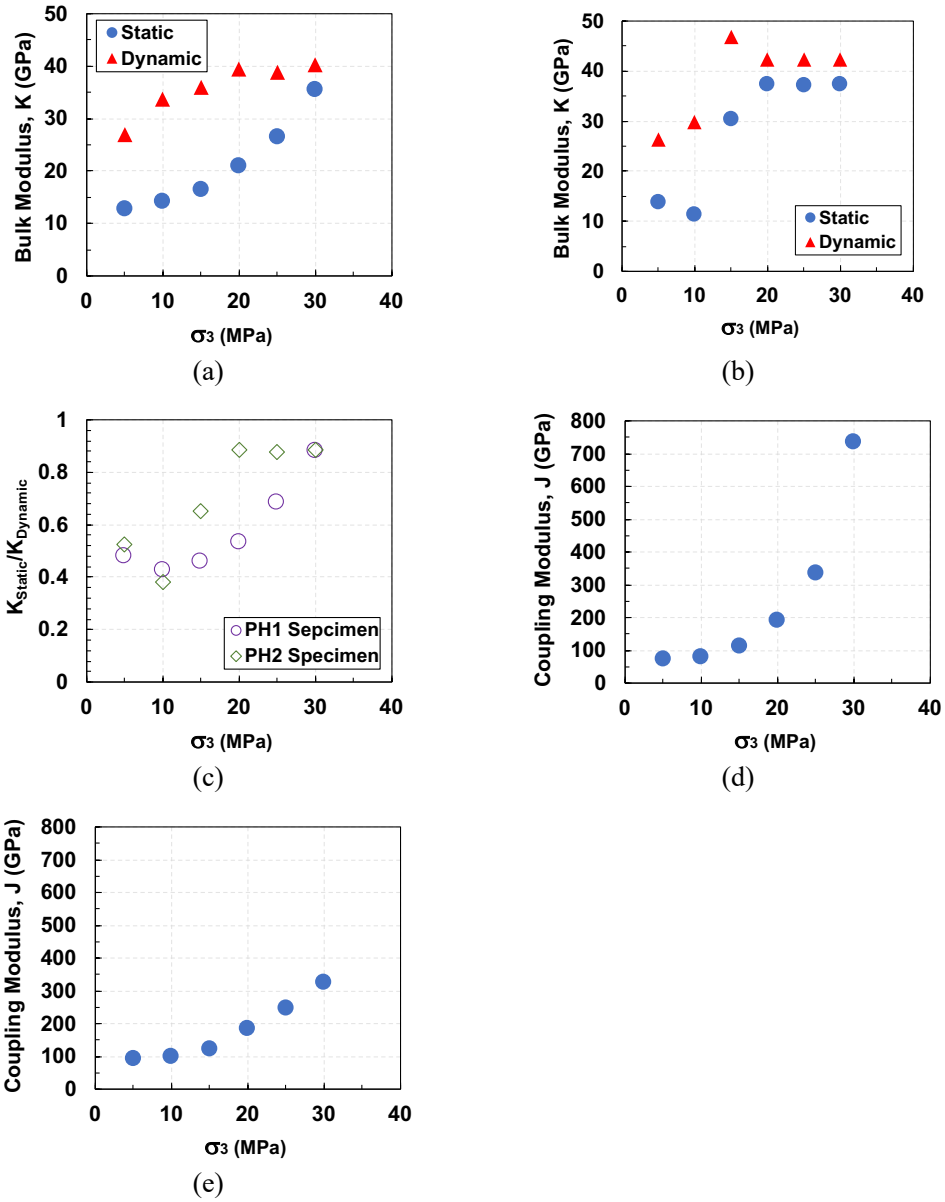


Figure 4-7. Estimated values of static and dynamic bulk modulus for (a) PH1, and (b) PH2 specimens; (c) the ratio of static to dynamic bulk modulus at different confining levels; the estimated values of static coupling modulus for (c) (d) PH1, and (d) (e) PH2 specimens.

### 4.4.2 MSE TESTS

Figure 4.8 shows the stress-strain curves in axial and radial directions during MSE test for PH1 specimen at different confining levels, indicating relatively-elastic response

with negligible plastic deformations in all CP levels. At lower CP levels (i.e. below 30 MPa), as higher differential stresses are applied, a strain-hardening behavior with some degree of hysteresis can be observed in stress-strain curves. However, at higher CP levels (i.e. greater than 30 MPa), stress-strain curve becomes linear with very small hysteresis behavior. Inelastic deformations occur due to energy dissipation as a result of micro-crack growth and frictional sliding (Zoback and Byerlee, 1975; Sone and Zoback, 2013). The stress-strain response in axial and radial directions for PH2 specimen under MSE test at different CP levels is illustrated in Figure 4.9.

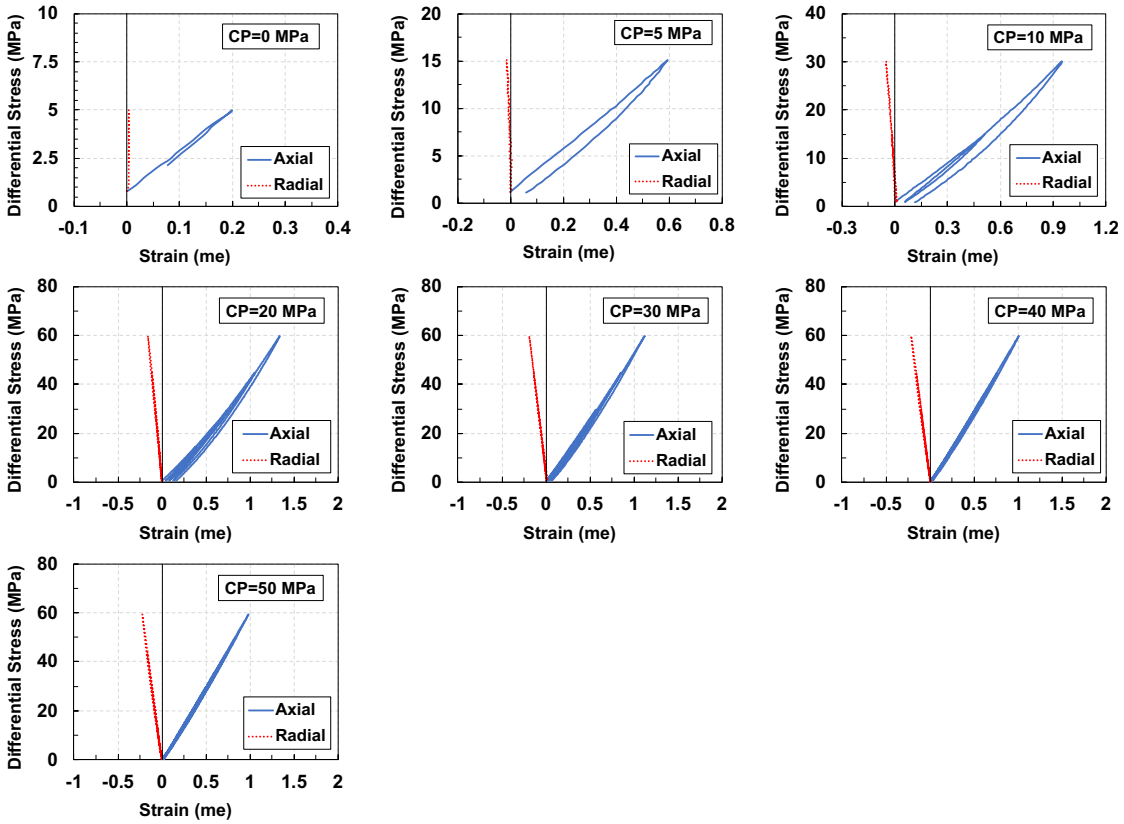


Figure 4-8. Stress-strain response of PH1 specimen at different levels of confining pressure from 0 to 50 MPa.

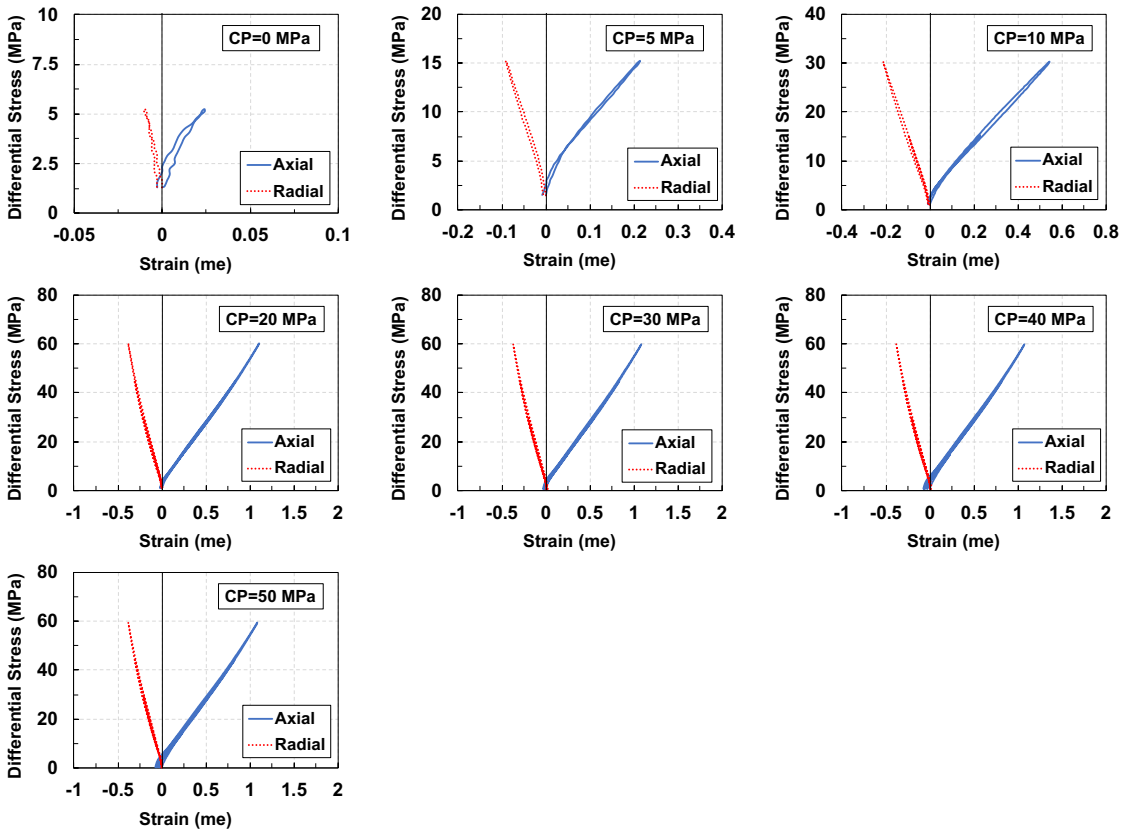


Figure 4-9. Stress-strain response of PH2 specimen at different levels of confining pressure from 0 to 50 MPa.

Steeper slope of stress-strain curve (i.e. higher Young's modulus) can be observed for very low DS levels (i.e. below 10 MPa) compared to higher DS levels, however, in each region (i.e. below and above 10 MPa) the stress-strain response is linear. Regardless of the confining level, the stress-strain curves do not show hysteresis and plastic response. The difference in stress-strain response for PH1 and PH2 specimens indicates significant anisotropy effects for the phyllite specimens tested in this study. The estimated static moduli at different stress levels for both specimens are presented in Table 4.1. It can be observed that for PH1 specimen, Young's modulus is higher during unloading path, while for PH2 specimen, the Young's modulus is higher during loading path. In addition, at

higher confining levels, the Young's modulus is higher, with a more pronounced increase at lower CP levels. This could be due to closure of some of the micro-cracks that were created due to in-situ stress relief while extracting the core from the deep well. Application of higher DS levels leads to an increase in the estimated Young's modulus values. For example, at CP=30 MPa, the Young's modulus for PH1 at DS levels of 0-15, 0-30, 0-45, and 0-60 MPa are 48.3, 52.1, 54.4, and 55.9 GPa, respectively. Table 4.2 presents the estimated dynamic moduli for PH1 and PH2 specimens obtained from MSE test, indicating a significant difference in the estimated moduli for PH1 specimen compared to those of PH2. This difference is more pronounced at lower CP levels and diminishes at higher confining levels.

### 4.4.3 CYCLIC TESTS

Figure 4.10a shows the variation of axial, radial, and volumetric strains against differential stress for PH1 specimen, indicating negligible hysteresis behavior at the applied moderate stress levels. Axial and radial strains show a strain hardening behavior beyond DS=30 MPa, with a more pronounced strain hardening in radial direction. Volumetric strains, however, show an almost-linear stress-strain response. The variation of axial, radial, and volumetric strains for the PH2 specimen are shown in Figure 4.10b. It can be observed that the axial and radial strains show very lower degree of hysteresis compared to PH1 specimen, indicating the effects of anisotropy. In addition, volumetric strains show more plastic residual deformations compared to PH1 specimen.

Table 4-1. The estimated static moduli (Young's and shear moduli, and Poisson's ratio) for PH1 and PH2 specimens during MSE test

| CP (MPa) | DS (MPa) | Specimen | Young's Modulus, E (GPa) | | Poisson's Ratio, ν (%) | | Shear Modulus, G (GPa) | |
|---|---|---|---|---|---|---|---|---|
| | | | Loading | Unloading | Loading | Unloading | Loading | Unloading |
| 0 | 0-5 | PH1 | 21.1 | 22.8 | 43.7 | 43.9 | N/A | N/A |
| | | PH2 | 170.3 | 133.6 | 42.4 | 25.2 | N/A | N/A |
| 5 | 0-15 | PH1 | 23.3 | 23.5 | 39.3 | 39.7 | 9.9 | 10.8 |
| | | PH2 | 60.8 | 56.9 | 42.5 | 38.2 | 17.4 | 16.9 |
| 10 | 0-15 | PH1 | 27.3 | 31.8 | 37.1 | 37.4 | 11.4 | 12.3 |
| | | PH2 | 60 | 54.9 | 42.4 | 38.5 | 17.5 | 16.6 |
| | 0-30 | PH1 | 32.5 | 36.4 | 37.1 | 37.3 | 12.8 | 13.5 |
| | | PH2 | 51.1 | 49.6 | 37.8 | 36.2 | 15.6 | 15.4 |
| 20 | 0-15 | PH1 | 36.8 | 41.1 | 36.5 | 36.6 | 15.7 | 17.0 |
| | | PH2 | 60.1 | 54.5 | 42.4 | 38.2 | 18.2 | 17.4 |
| | 0-30 | PH1 | 41.7 | 44 | 36.3 | 36.4 | 17.3 | 18.0 |
| | | PH2 | 51.5 | 49.6 | 38 | 36 | 16.7 | 16.3 |
| | 0-45 | PH1 | 45.8 | 49.2 | 36.8 | 32.5 | 18.5 | 19.1 |
| | | PH2 | 49.9 | 49 | 36.1 | 35.4 | 16.6 | 16.5 |
| | 0-60 | PH1 | 49.6 | 53.5 | 36 | 35.7 | 19.5 | 19.9 |
| | | PH2 | 51.2 | 50.7 | 34.7 | 34.1 | 17.2 | 17.1 |
| 30 | 0-15 | PH1 | 48.3 | 51 | 34.9 | 35.3 | 20.3 | 21.0 |
| | | PH2 | 54.8 | 51.8 | 38.2 | 36.8 | 18.7 | 17.9 |
| | 0-30 | PH1 | 52.1 | 52.7 | 34.7 | 35.1 | 21.6 | 22.0 |
| | | PH2 | 51 | 49.1 | 37.1 | 36.4 | 17.6 | 17.0 |
| | 0-45 | PH1 | 54.4 | 57 | 35 | 34.9 | 22.3 | 22.6 |
| | | PH2 | 50.3 | 49.2 | 35.6 | 35.5 | 17.5 | 17.2 |
| | 0-60 | PH1 | 55.9 | 58.2 | 35.2 | 34.9 | 22.8 | 23.0 |
| | | PH2 | 51.7 | 51 | 34.7 | 34.3 | 18.1 | 17.9 |
| 40 | 0-15 | PH1 | 55.3 | 55.7 | 31.4 | 32.1 | N/A | N/A |
| | | PH2 | 59.4 | 50.4 | 43.3 | 36.9 | N/A | N/A |
| | 0-30 | PH1 | 57.7 | 58.5 | 32.1 | 32.5 | N/A | N/A |
| | | PH2 | 50.7 | 47.4 | 38.4 | 36.4 | N/A | N/A |
| | 0-45 | PH1 | 59.2 | 60.1 | 32 | 32.8 | N/A | N/A |
| | | PH2 | 49.2 | 47.6 | 36.2 | 35.4 | N/A | N/A |
| | 0-60 | PH1 | 60 | 61.3 | 31.6 | 31.6 | N/A | N/A |
| | | PH2 | 50.2 | 49.6 | 34.5 | 34.2 | N/A | N/A |
| 50 | 0-15 | PH1 | 58.5 | 59.1 | 33.7 | 33.9 | N/A | N/A |
| | | PH2 | 59 | 49.9 | 41.9 | 36.5 | N/A | N/A |
| | 0-30 | PH1 | 60.5 | 60.8 | 33.2 | 33.9 | N/A | N/A |
| | | PH2 | 50.3 | 47.1 | 37.8 | 36.2 | N/A | N/A |
| | 0-45 | PH1 | 60.9 | 61.4 | 30.5 | 33.4 | N/A | N/A |
| | | PH2 | 49 | 47.4 | 35.9 | 35.3 | N/A | N/A |
| | 0-60 | PH1 | 61.4 | 61.7 | 31.6 | 32.7 | N/A | N/A |
| | | PH2 | 50 | 49.1 | 34.5 | 34.3 | N/A | N/A |

Table 4-2. The estimated dynamic moduli (Young's and shear moduli, and Poisson's ratio) for PH1 and PH2 specimens during MSE test

| CP (MPa) | DS (MPa) | Specimen | Young's Modulus, E (GPa) | Poisson's Ratio, ν (%) | Shear Modulus, G (GPa) |
|---|---|---|---|---|---|
| 0 | 5 | PH1 | 40.5 | 3.4 | 19.6 |
| | | PH2 | 74.7 | 20.2 | 31.0 |
| 5 | 15 | PH1 | 48.3 | 10.1 | 21.9 |
| | | PH2 | 79.4 | 19.2 | 33.3 |
| 10 | 15 | PH1 | 51.8 | 12.0 | 23.1 |
| | | PH2 | 80 | 19.2 | 33.6 |
| | 30 | PH1 | 58.6 | 16.7 | 25.1 |
| | | PH2 | 81.4 | 18.3 | 34.4 |
| 20 | 15 | PH1 | 60.4 | 18.5 | 25.5 |
| | | PH2 | 81 | 18.8 | 34.1 |
| | 30 | PH1 | 64.7 | 20.0 | 27.0 |
| | | PH2 | 82.5 | 19.1 | 34.6 |
| | 45 | PH1 | 67.9 | 20.3 | 28.2 |
| | | PH2 | 83.9 | 18.2 | 35.5 |
| | 60 | PH1 | 70.3 | 20.4 | 29.2 |
| | | PH2 | 85.1 | 18.2 | 36.0 |
| 30 | 15 | PH1 | 70.9 | 22.0 | 29.1 |
| | | PH2 | 82.2 | 18.1 | 34.8 |
| | 30 | PH1 | 72.3 | 21.6 | 29.7 |
| | | PH2 | 83.2 | 18.3 | 35.1 |
| | 45 | PH1 | 73.6 | 20.9 | 30.4 |
| | | PH2 | 84.4 | 17.6 | 35.9 |
| | 60 | PH1 | 74.7 | 20.7 | 30.9 |
| | | PH2 | 85.6 | 18.4 | 36.1 |
| 40 | 15 | PH1 | 74.6 | 21.0 | 30.8 |
| | | PH2 | 82.7 | 18.8 | 34.8 |
| | 30 | PH1 | 75.5 | 20.7 | 31.3 |
| | | PH2 | 83.5 | 17.9 | 35.4 |
| | 45 | PH1 | 76.6 | 20.4 | 31.8 |
| | | PH2 | 85.5 | 18.5 | 36.0 |
| | 60 | PH1 | 77.2 | 20.4 | 32.0 |
| | | PH2 | 85.8 | 18.1 | 36.3 |
| 50 | 15 | PH1 | 76.6 | 20.4 | 31.8 |
| | | PH2 | 82.8 | 18.7 | 34.8 |
| | 30 | PH1 | 77.3 | 20.2 | 32.1 |
| | | PH2 | 84.5 | 18.2 | 35.7 |
| | 45 | PH1 | 78.1 | 20.2 | 32.4 |
| | | PH2 | 85.2 | 18.7 | 35.9 |
| | 60 | PH1 | 78.8 | 20.3 | 32.7 |
| | | PH2 | 86.1 | 17.8 | 36.5 |

Figure 4.10c shows the measured ultrasonic P- and S-waves velocities, superimposed on the followed stress path. Higher P- and S-waves velocities for PH2 specimen compared to PH1, indicates the effects of anisotropy. In addition, it can be observed that P-wave velocities are increasing as higher DS levels are applied, however, S-waves velocities are not notably affected by increase of DS. Table 4.3 presents the estimated static and dynamic moduli for both specimens at different DS levels, indicating much lower static and dynamic Young's modulus for PH1 specimen compared to PH2. As also observed in MSE test, application of higher DS levels leads to higher estimated Young's modulus, regardless of the type of the measurement (i.e. static or dynamic), with a smaller difference between the estimated moduli at higher DS levels.

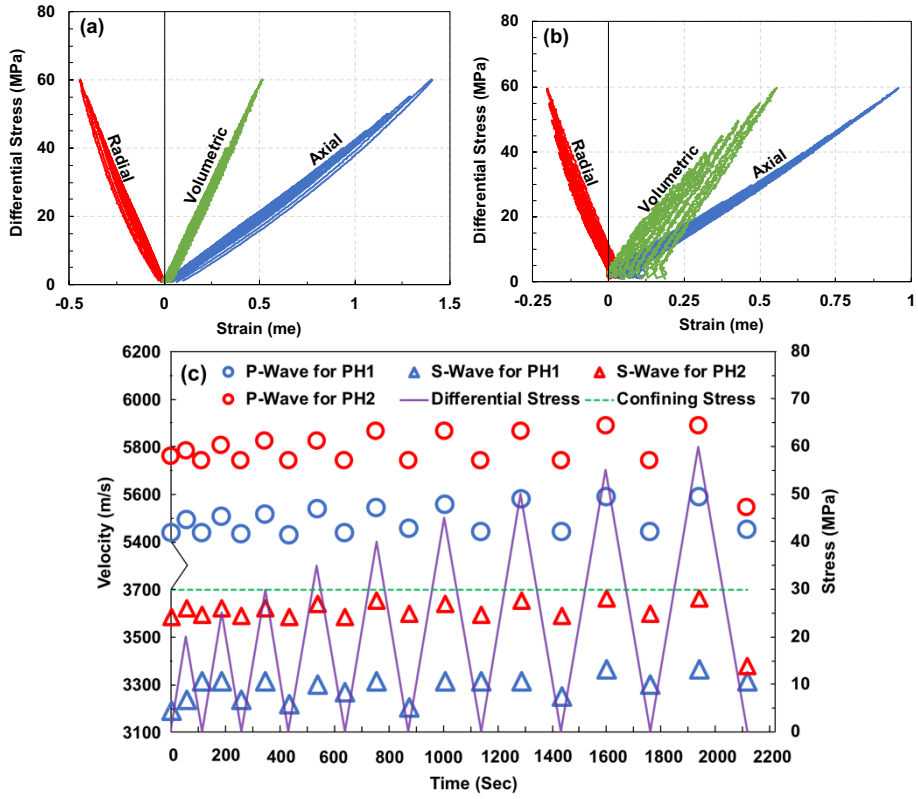


Figure 4-10. Axial, radial, and volumetric strains versus differential stress for (a) PH1, and (b) PH2 specimens, and (c) Measured P- and S-waves velocities during cyclic for PH1 and PH2 specimens.

Table 4-3. Static and dynamic estimations of Young's and shear moduli and Poisson's ratio in cyclic tests for PH1 and PH2 specimens

| DS (MPa) | Specimen | Young's Modulus, E (GPa) | | | Poisson's Ratio, ν (%) | | | Shear Modulus, G (GPa) | | |
|---|---|---|---|---|---|---|---|---|---|---|
| | | Loading | Unloading | Dynamic | Loading | Unloading | Dynamic | Loading | Unloading | Dynamic |
| 0-20 | PH1 | 41.5 | 41.1 | 69.6 | 31.6 | 31.8 | 23.4 | 15.4 | 15.2 | 28.2 |
| | PH2 | 57.8 | 53.0 | 83.0 | 38.8 | 35.4 | 17.8 | 21.0 | 20.8 | 35.2 |
| 0-25 | PH1 | 41.1 | 41.3 | 71.9 | 31.8 | 32.4 | 21.5 | 15.3 | 15.2 | 29.6 |
| | PH2 | 54.9 | 52.1 | 83.3 | 37.6 | 35.6 | 18.1 | 21.1 | 20.9 | 35.2 |
| 0-30 | PH1 | 41.2 | 41.3 | 72.0 | 32.3 | 32.5 | 21.7 | 15.2 | 15.2 | 29.6 |
| | PH2 | 53.9 | 51.2 | 83.7 | 37.1 | 35.4 | 18.4 | 21.3 | 21.2 | 35.3 |
| 0-35 | PH1 | 41.4 | 41.5 | 71.8 | 32.4 | 32.5 | 22.5 | 15.3 | 15.3 | 29.3 |
| | PH2 | 53.2 | 50.4 | 84.1 | 37.1 | 35.4 | 17.9 | 21.5 | 21.3 | 35.6 |
| 0-40 | PH1 | 41.6 | 42.1 | 72.3 | 32.5 | 32.4 | 22.2 | 15.4 | 15.5 | 29.6 |
| | PH2 | 53.0 | 50.3 | 85.0 | 37.5 | 35.5 | 18.3 | 21.9 | 21.6 | 35.9 |
| 0-45 | PH1 | 42.0 | 42.5 | 72.4 | 32.6 | 32.1 | 22.4 | 15.5 | 15.7 | 29.6 |
| | PH2 | 52.6 | 50.1 | 84.6 | 37.2 | 35.1 | 18.7 | 22.3 | 22.1 | 35.6 |
| 0-50 | PH1 | 42.5 | 43.4 | 72.6 | 32.6 | 31.9 | 22.7 | 15.7 | 16.0 | 29.6 |
| | PH2 | 51.7 | 50.2 | 85.0 | 36.0 | 34.7 | 18.3 | 22.7 | 22.4 | 35.9 |
| 0-55 | PH1 | 43.1 | 44.1 | 74.1 | 32.6 | 31.8 | 21.6 | 15.9 | 16.3 | 30.4 |
| | PH2 | 51.8 | 50.6 | 85.6 | 35.6 | 34.6 | 18.4 | 23.1 | 22.9 | 36.1 |
| 0-60 | PH1 | 43.8 | 45.1 | 74.1 | 32.6 | 31.4 | 21.6 | 16.2 | 16.7 | 30.4 |
| | PH2 | 52.8 | 51.1 | 85.6 | 36.1 | 34.1 | 18.4 | 23.5 | 23.3 | 36.1 |

### 4.4.4 CREEP TESTS

Figures 4.11a and 4.11b show the variation of axial and radial strains during hydrostatic and triaxial stages of the creep test for PH1 and PH2 specimens, respectively,

indicating negligible viscoelastic deformations in all the stages. This observation could be justified by the fact that these specimens do not have clay/organic content, which are responsible minerals for creep in rocks (e.g. Zoback, 2010; Schon, 2015). Rather, sliding behavior at the interface of the grains is responsible for the observed response during creep tests (Moore and Lockner, 2004). Figure 4.11c illustrates the measured P- and S-waves velocities during creep tests for both specimens, indicating higher velocities for PH2 specimen compared to PH1, as also observed in MSE and cyclic tests.

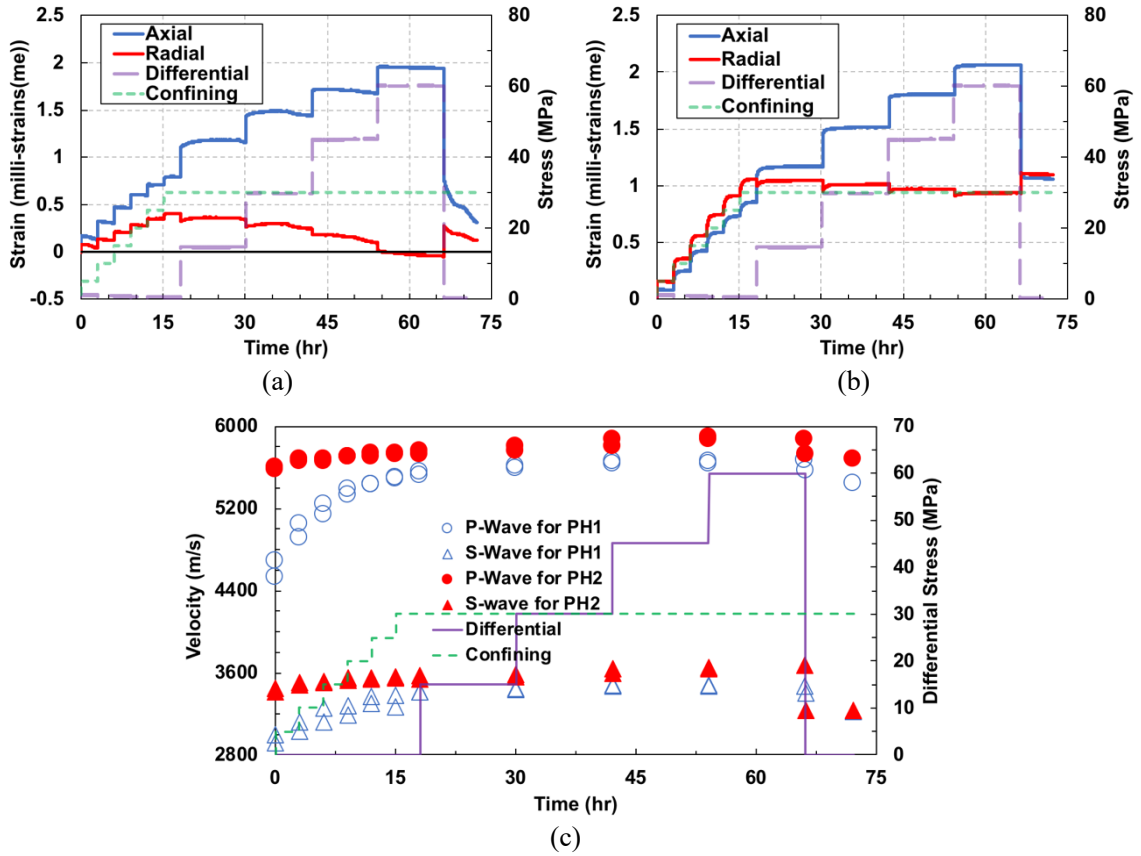


Figure 4-11. (a) Creep response of PH1 specimen, (b) creep response of PH2 specimen, and (c) measured ultrasonic P- and S-waves velocities during creep for both PH1 and PH2 specimens.

### 4.4.5 MSF TESTS

Figure 4.12a shows the variation of axial and radial strains against differential stress at different confining levels during MSF test on PH1 specimen, indicating higher estimations of strength at higher confining levels. The unconfined compressive strength (i.e. strength at CP=0 MPa) of 184 MPa indicates that the phyllite rock is categorized into rocks with "high" strength according to Schon (2015). Figure 4.12b shows the axial, radial, and volumetric strains at CP=30 MPa (close to in-situ overburden stress), where the specimen was purposely failed. At the in-situ stress conditions, the ultimate and failure strengths of the specimen were estimated as 322 and 300 MPa, respectively, as illustrated in Figure 4.12b. This observation implies that this specimen showed a brittle response with a reduction in ultimate strength, as opposed to rocks with a more ductile response at failure such as shale rocks (e.g. Kamali-Asl and Ghazanfari, 2017; Kamali-Asl et al., 2018b). Ultimate and failure axial strains were estimated as 7.5 and 8.4 millistrains, respectively. The variation of volumetric strains against differential stress shows that at DS levels below 20 MPa, the specimen exhibits a softer response due to closure of some of the existing micro-cracks, followed by a linear response at the intermediate stress levels. Then, at DS levels above 250 MPa, the stress-strain response deviates from linear curve, leading to a dilatancy-dominated behavior. Finally, there is a sharp decrease in the strength of the specimen after reaching to ultimate strength.

Figure 4.12c shows the Mohr's circles at different confining levels, and the Mohr-Coulomb failure envelope. The MSF test appears to successfully provide the strength properties at different CP levels as (i) Mohr-Coulomb failure envelope is tangent to Mohr's

circles in all CP levels, and (ii) the specimen was failed in the last CP stage, proves that. Figure 4.13a shows a picture of PH1 specimen after MSF test. Post-mortem X-Ray CT-images (side views, 3D, and cross section) of the specimen are shown in Figure 4.13b. It can be seen that as a result of four stages of MSF test, both tensile and shear fractures were induced in the specimen. The orientation of failure plane with respect to minor principal stress (horizontal axis in this case) was estimated around ~65.4°. The existence of some fractures parallel to the identified major failure plane could have been created due to application of different stages of MSF test.

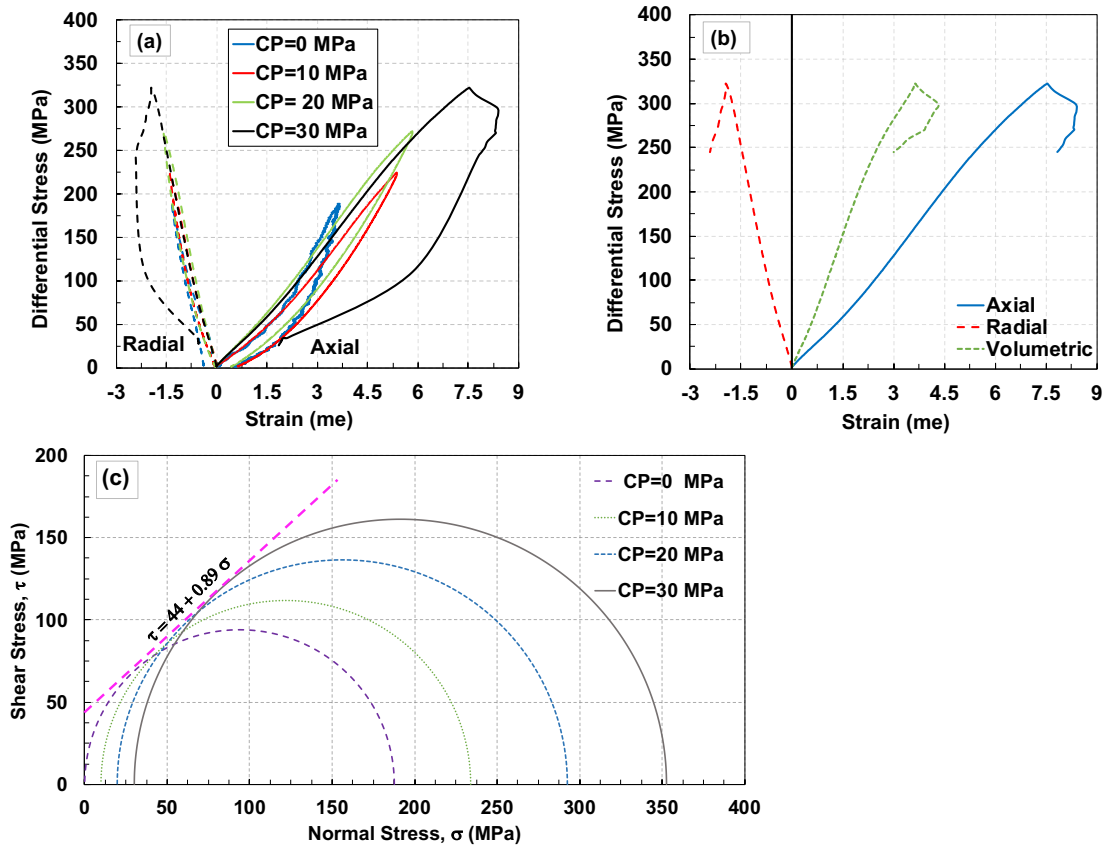


Figure 4-12. MSF test on PH1 specimen: (a) axial and radial strains versus differential stress for different stages, (b) axial, radial, and volumetric strains for CP=30 MPa, and (c) Mohr's circles and Coulomb failure envelope.

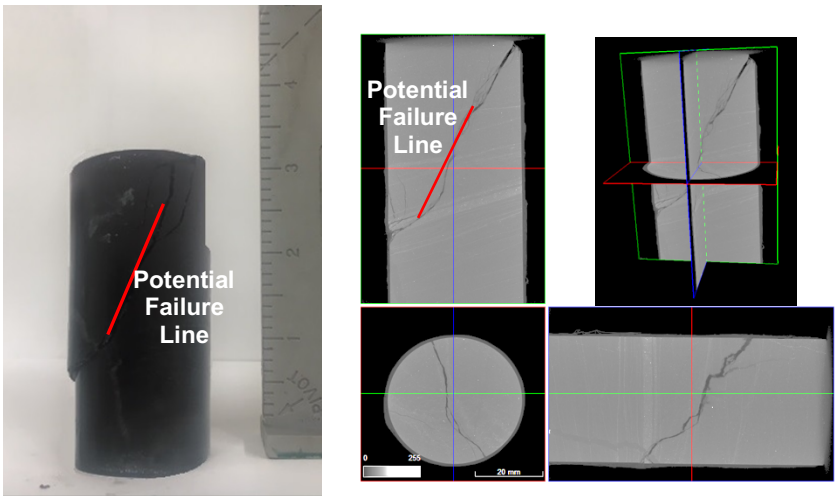


(a) (b)

Figure 4-13. (a) Photo of the PH1 specimen after failure; and (b) post-mortem X-Ray CT images (cross-section, 3D, and side views) of the PH1 specimen after MSF test.

## 4.5 DISCUSSION AND ANALYSIS

### 4.5.1 ELASTIC, FAILURE, AND ANISOTROPY

At the relatively-low-to-intermediate differential stress levels in MSE and cyclic tests, both PH1 and PH2 specimens showed a linear and elastic stress-strain response, particularly, at higher confining levels. After unloading the specimens, very small plastic deformations were observed, except for confining levels below 10 MPa. This could be attributed to the fact that the cracks that were created due to stress relief, were not closed and therefore, some residual deformations occurred. Figure 4.14 shows the variation of static and dynamic Young's modulus with mean stress at different confining levels for both specimens, indicating that as higher differential stresses are applied the Young's modulus increases, except for the static Young's modulus for PH2 specimen. This discrepancy in this specimen could be explained by looking into Figure 4.9, where it can be observed that

regardless of the confining level, PH2 specimen exhibited a very steep slope for DS levels below 10 MPa. This steeper slope of the stress-strain curve, for differential stress levels below 10 MPa, leads to very high estimations of Young's modulus for the differential stress level of 0-15 MPa. As higher differential stresses are applied, the contribution of the initial portion of stress-strain response (which has very steep slope) becomes smaller and Young's modulus decreases. However, transitioning from differential stress of 45 to 60 MPa, and for all CP levels, the Young's modulus increases. This could be attributed to the fact that contribution of increase in differential stress in variation of Young's modulus becomes more pronounced compared to the weakened contribution of the initial high slope of stress-strain response, as higher DS levels are applied.

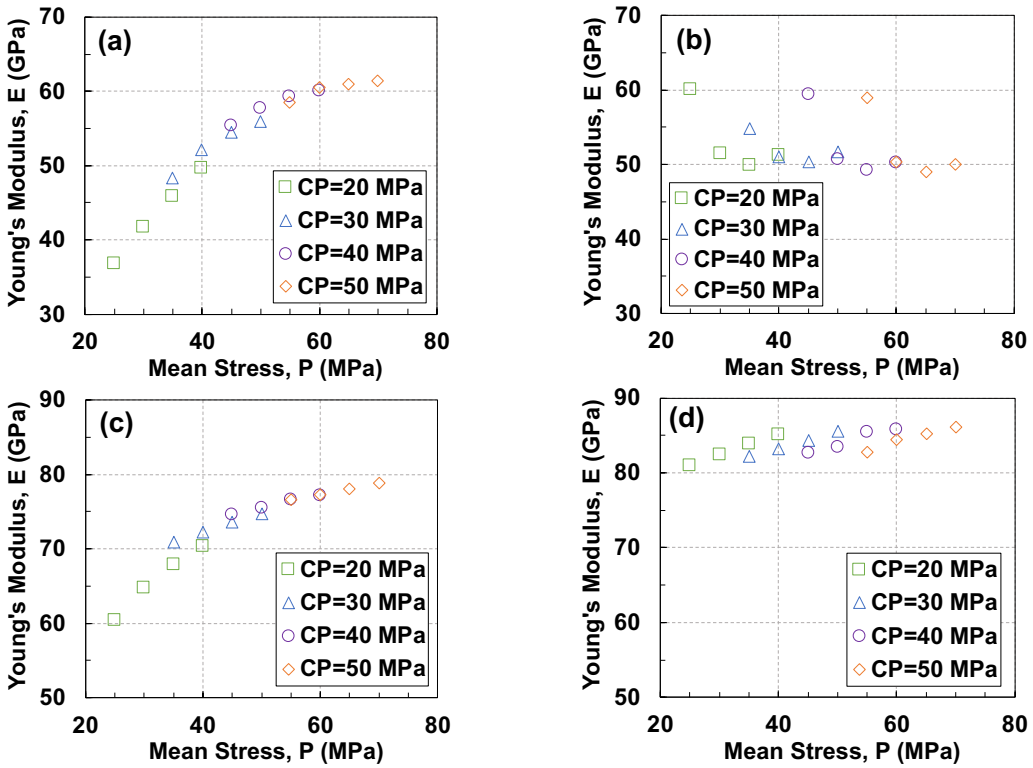


Figure 4-14. Variations of Young's modulus with mean stress at different confining levels for (a) static modulus for PH1, (b) static modulus for PH2, (c) dynamic modulus for PH1, (d) dynamic modulus for PH2.

The relatively intermediate values of coupling moduli for both specimens, as illustrated in Figure 4.7c and 4.7d, implies that there is some degree of anisotropy for the tested specimens. The effects of anisotropy can be also observed in very different values for Young's modulus in PH1 specimen compared to those of PH2, specifically at low CP levels. In addition, the estimations of Poisson's ratio with about 10% to 15% difference in PH1 and PH2 specimens are indicatives of the observed anisotropy effects, although not significant. At in-situ stress level (i.e. CP=30 MPa), the estimated dynamic Young's modulus for PH2 specimen is ~15% higher than that of PH1, reflecting anisotropy effects for the phyllite specimens.

Both Hoek-Brown and Linearized Mohr-Coulomb failure criteria successfully predicted the strength properties at different CP levels, as shown in Figure 4.15a. The orientation of failure plane with respect to horizontal axis was found ~67° based on Linearized Mohr-Coulomb failure criterion, which is in close agreement (within 1-2°) with the observation from post-mortem X-Ray CT-images of the specimen. The coefficient of internal friction was estimated as ~0.89 using Linearized Mohr-Coulomb failure criterion. The variation of axial and radials strains at failure are presented in Figure 4.15b, indicating progressively-higher estimated strains at higher confining levels. It should be acknowledged that application of previous stages might affect the results in a later stage, due to creation of some micro-cracks and plastic deformations.

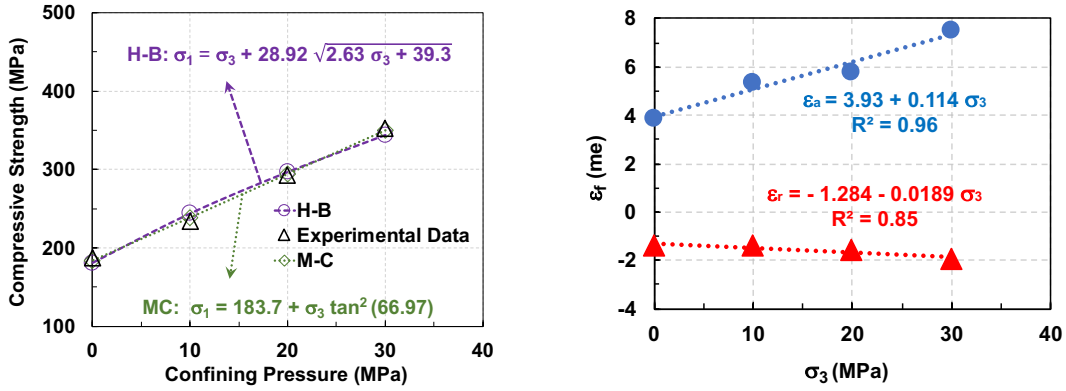


Figure 4-15. (a) Comparison of Hoek-Brown and Linearized Mohr-Coulomb criteria, and (b) variation of axial and radial strains at failure with confining pressure

### 4.5.2 TIME-FREQUENCY ANALYSIS OF ULTRASONIC SEISMIC WAVES

Time-frequency analysis of transmitted seismic waves through rock specimens can reveal valuable information about the frequency characteristics of the rocks, which can be potentially linked to the changes in the micro-structure of the rock caused by application of different stress levels. In order to construct time-frequency maps, Continuous Wavelet Transform (CWT) approach was implemented (see Appendix E).

Figure 4.16a illustrates the six instances (specified with red circle) of seismic signature collection during MSE test for time-frequency analysis. Figures 4.16b-g show the time-frequency maps of the received P-wave signal in MSE test on PH1 specimen for different confining levels at the beginning of each CP stage (i.e. no applied differential stress). It can be observed that as the confining level increases, the frequency content of the P-wave signal changes significantly. For example, a dominant frequency of ~300 kHz can be observed at CP levels of 0 and 10 MPa, becomes less pronounced at intermediate confining levels, and disappears at high confining levels. At different CP levels,

representing different depths or overburden stress, the frequency content of the rock mass is different. In addition, induced micro-cracks in the rock specimen due to stress relief during coring process might be closed at higher confining levels, leading to change in the stiffness of the rock specimen, and in turn, alteration of the frequency content of the rock specimen. Transitioning from lower to higher CP values, the high frequency part of the signal (i.e. frequencies around 750 kHz) becomes less pronounced. This might be attributed to the fact that as the specimen becomes stiffer, due to application of higher confining levels, the transmitted seismic wave attenuates faster (e.g. Gordon and Davis, 1968; Barton, 2007). In addition, analyzing the second-half of the time-frequency maps (i.e. after t=40 μSec) reveals that as the confining level increases, a dominant frequency of ~100 kHz becomes pronounced. In particular, at close to in-situ conditions (i.e. CP=30 MPa) the only dominant frequency is ~100 kHz, which could be attributed to the rock dominant frequency in the field at a depth of 1260 m.

Figure 4.17a illustrates the five instances (specified with red circle) of seismic signature collection during cyclic test for time-frequency analysis. Figures 4.17b-f show the time-frequency map of the transmitted S1-wave signal in cyclic test on PH1 specimen for different levels of differential stress. It can be observed that the frequency content of the received signal does not significantly change at different DS levels, indicating that changes in the micro-structure of a rock specimen due to application of differential stress is not reflected in its frequency content. This could be attributed to the fact that PH1 specimen has a very high elastic moduli, as it can be seen in Table 4.3, and applying the relatively low-to-intermediate stress levels of cyclic test does not create a significant

change in the internal micro-structure of the rock specimen. However, as observed in Section 4.3, the S-waves velocities increase at higher levels of differential stress, indicating that during application of differential stress, the seismic velocities are more sensitive to changes in differential stress compared to frequency content of the rock specimen. It should be noted that analysis of time-frequency map of P-wave velocity during cyclic test led to the same conclusion as S1-wave velocity, and hence, it has not been included in the manuscript.

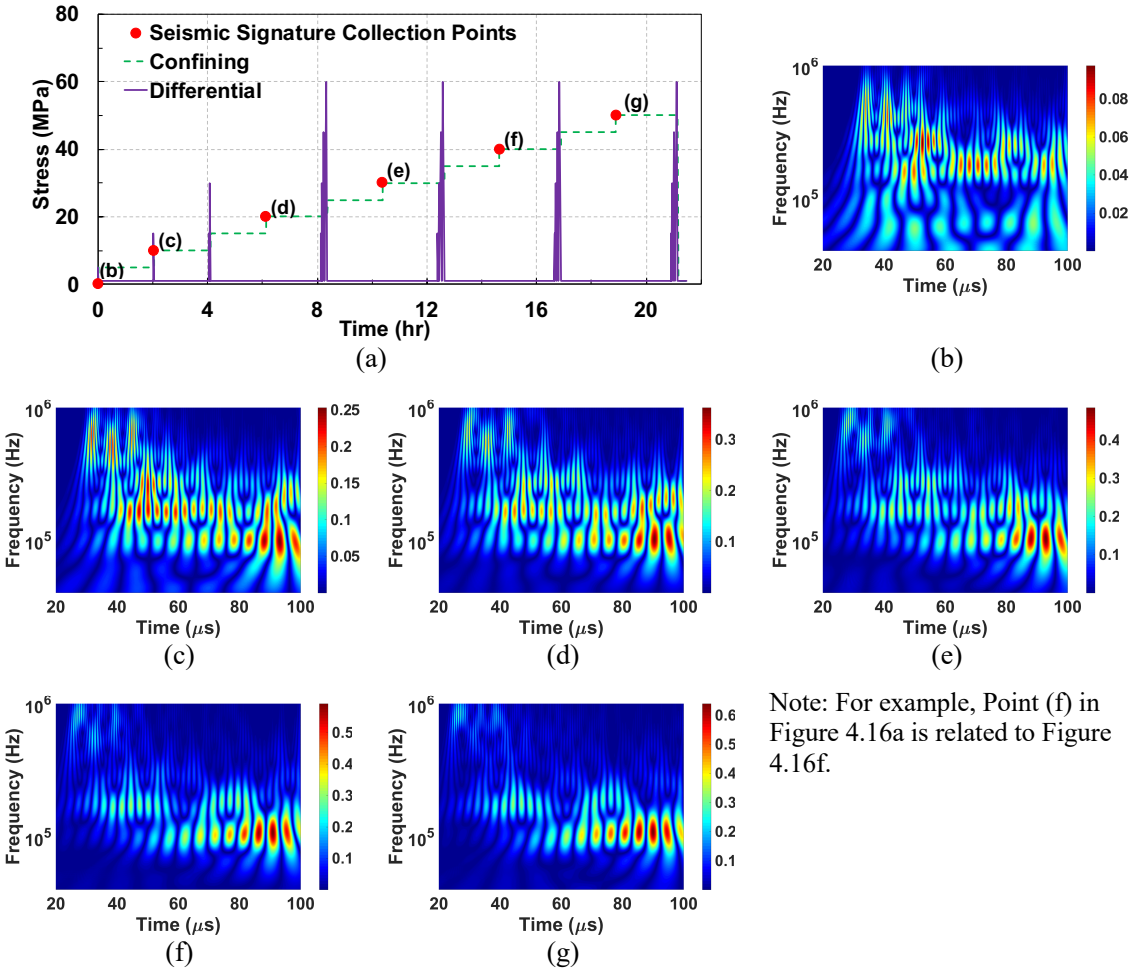


Figure 4-16. (a) schematic of the stress path and points of seismic signature collection; P-wave time-frequency map during MSE test at (b) CP=0; (c) CP=10; (d) CP=20; (e) CP=30; (f) CP=40; (g) CP=50 MPa. Note that frequency axis is in log-scale.

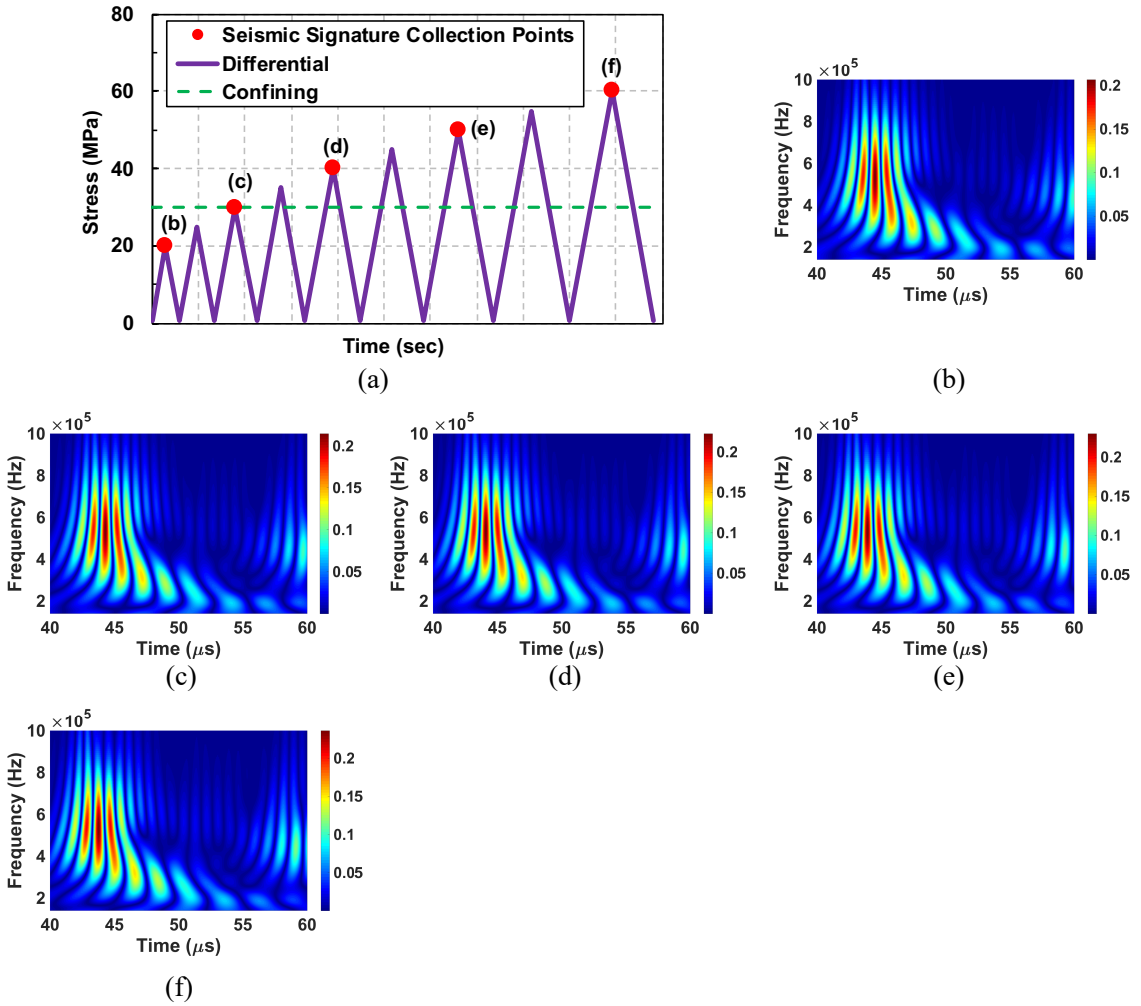


Figure 4-17. (a) schematic of the stress path and the points of seismic signature collection; S-wave time-frequency map during cyclic test at (b) DS=20; (c) DS=30; (d) DS=40; (e) DS=50; (f) DS=60 MPa.

Figure 4.18a illustrates the six instances (specified with red circle) of seismic signature collection during creep test for time-frequency analysis. Figures 4.18b, 4.18d, and 4.18f show the time-frequency map of the received P-wave signal immediately after application of differential stress in different stages of triaxial creep test, while, Figures 4.18c, 4.18e, and 4.18g illustrate the time-frequency map of the signal which was obtained by subtracting the signal immediately after loading from the signal that was recorded after

12 hours of triaxial creep test. It can be seen by comparing 4.20b with 4.20c, 4.20d with 4.20e, and 4.20f with 4.20g that there are slight changes in their time-frequency content.

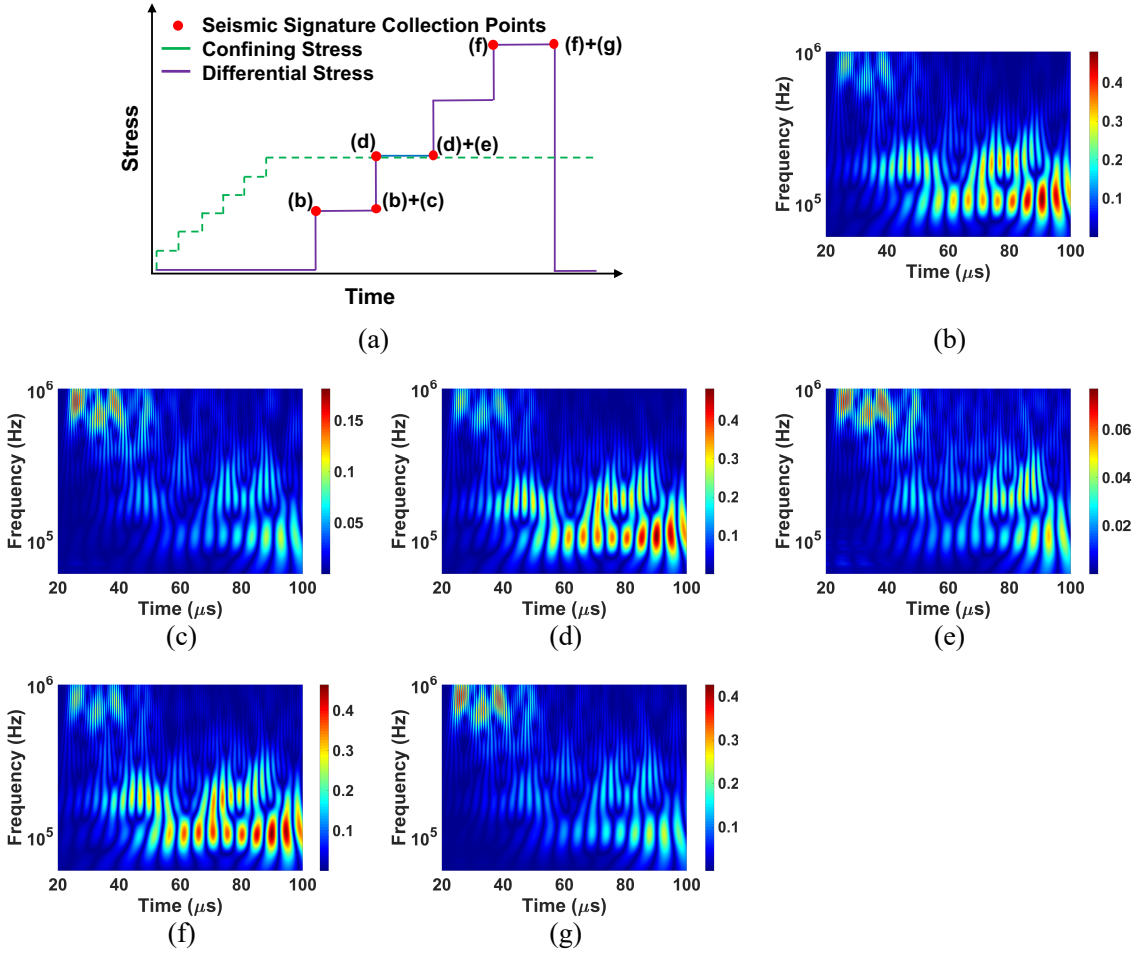


Figure 4-18. (a) schematic of the stress path and the points of seismic signature collection; P-wave time-frequency map for the difference between the P-wave signal at the end of each triaxial creep stage with that of the beginning of the creep for (b) and (c) DS=15, (c) and (d) DS=30, and (e) and (f) DS=60 MPa. Note that frequency axis is in log-scale.

Comparing the time-frequency maps in Figures 4.18b, 4.18d, and 4.18f, it can be observed that the time-frequency content of the rock specimen upon loading at various differential stress levels changes slightly. However, the time-frequency maps for cyclic test (see Figure 4.17) did not show notable changes at different DS levels. This could be

attributed to the fact that application of triaxial creep, i.e. maintaining a constant stress for a relatively-long time, can lead to slight changes in the micro-structure of the rock specimen, which in turn, alters the frequency content of the rock specimen. It should be noted that time-frequency maps of the S-waves during creep test showed same results as P-wave.

### 4.5.3 IMPLICATIONS OF FINDINGS IN GEOTHERMAL RESERVOIRS

Deep geothermal reservoirs are typically located at a depth of 1 to 5 km (e.g. Ghassemi, 2012), with corresponding overburden stress in the range of 20 to 100 MPa (Cladouhos et al., 2016). Therefore, it is necessary to better understand the geomechanical and hydrothermal response of these reservoirs in order to (i) better design the stimulation program (e.g. Majer et al., 2007), (ii) reduce production decline over the course of the reservoir operation (e.g. Ghassemi, 2012), and (iii) build more accurate predictive models at reservoir scale (e.g. Ghassemi, 2012). In this study, it was found that the elastic moduli (i.e. Young's and shear moduli and Poisson's ratio) are pressure-dependent, which implies that in the predictive models, this pressure-dependency should be considered. In addition, the estimated Young's moduli for the tested phyllite specimens categorize the rocks in this geothermal field as "high" elasticity, compared to other typical geothermal fields, which are mostly composed of sandstone and granite (e.g. Ghassemi, 2012).

The range of compressive and failure strength of the tested phyllite specimens fall in "high" strength values (Schon, 2015), which in turn, can affect the outcome of hydraulic fracturing process during reservoir stimulation. The relatively high unconfined compressive strength of the tested phyllite specimen implies that higher injection pressures

are needed to create a network of fractures. This required injection pressure and higher strength properties, compared to the typical injection pressures in geothermal fields with sandstone or granite as bedrock, might lead to a different pattern in fracture propagation. Therefore, these strength properties are very important in the site-specific design of stimulation program (Schon, 2015).

The tested phyllite specimens did not show significant creep, one of the processes that contributes to reservoir permeability reduction (Caulk et al., 2016). There is little production flow decline in this geothermal field of the type related to fracture closure, perhaps due to the strength of the phyllite. However, other processes such as free-face dissolution/precipitation of minerals as well as pressure solution phenomena (e.g. Taron and Elsworth, 2010; Kamali-Asl et al., 2018a) cannot be ruled out and are investigated and reported in a companion paper by the authors. In addition, it is important to investigate the effects of thermal processes in both stimulation and production stages of geothermal reservoir development, although not studied in this paper. The thermal stresses induce thermal cracks during stimulation stage, leading to increase in fracture permeability (e.g. Ghassemi, 2012), but also might affect the elastic and failure characteristics of reservoir. The Blue Mountain geothermal field has experienced significant temperature drawdown, which has resulted in reduced productivity of this reservoir (e.g. Swyer et al., 2016). Therefore, it is necessary to investigate the coupled effect of this temperature drop on (i) mineral dissolution/precipitation processes, and (ii) production decline which are being studied in a companion paper by the authors. In addition, creation of new fractures through hydraulic fracturing process is useful to reduce thermal breakthrough, as was also conducted in Raft River, Idaho (e.g. Bradford et al., 2016), Desert Peak and Soda Lake,

Nevada (e.g. Chabora et al., 2012; Kelkar et al., 2012), and Soda Lake, Nevada (e.g. Lovekin, 2017) geothermal fields. Hence, characterization of mechanical properties of Blue Mountain geothermal field is helpful to better design single-well (i.e. EGS) stimulations.

## 4.6 CONCLUSIONS

Due to growing population of the world, it is necessary to address challenges and issues associated with development of renewable sources of energy. Development of deep geothermal energy, a renewable energy source, has not yet gained enough attention compared to other renewable energy sources. In order to address some of the obstacles toward full-scale commercialization of deep geothermal energy, it is essential to better understand the geomechanical and hydrothermal characteristics of these reservoir rocks.

In this paper, we presented the results from a suite of mechanical characterization tests on phyllite specimens retrieved from a depth of 1260 m from DB-2 core hole, representative of the reservoir at Blue Mountain geothermal field located in, Nevada, United States. A series of triaxial multi-stage elastic and failure, creep, and cyclic tests were performed on one vertically-drilled sub-core and one horizontally-drilled sub-core, allows studying the effects of anisotropy on the response of these specimens. The obtained stress-strain response from these tests allowed identifying the elastic, failure, viscoelastic, and hysteresis behavior of these specimens at different stress levels. In addition, ultrasonic P- and S-waves velocities were measured during the tests, which were used to (i) estimate the dynamic moduli, and (ii) potentially infer the changes in the micro-structure of the specimens at different stress levels.

Both static and dynamic moduli were found to be pressure-dependent at different confining levels, with a more pronounced anisotropy effect on dynamic moduli. The observed difference in the measured ultrasonic P- and S-waves velocities between the two specimens were found to be ~20% and ~14%, respectively. For both specimens, no substantial viscoelastic deformations were observed, however, there is a discrepancy in their creep response, which can be attributed to material anisotropy. Vertically-drilled specimen exhibited a more significant change in measured P- and S-waves velocities during hydrostatic stage of the creep test, compared to the horizontally-drilled specimen. Multi-stage failure test on vertically-drilled specimen revealed a brittle response for this phyllite specimen with increased strength at higher confining levels. Both Hoek-Brown and Linearized Mohr-Coulomb failure criteria could successfully predict the failure strength properties of the vertically-drilled specimen obtained from multi-stage failure test. The coefficient of internal friction and unconfined compressive strength of the vertically-drilled specimen were estimated as 0.89 and 184 MPa, respectively.

The time-frequency maps of the received seismic waves signals revealed that changing confining level alters the frequency content of the rock specimen, which could be attributed to the changes in the micro-structure of the specimen at different confining levels. However, the frequency content of P- and S-waves was almost independent of the level of the applied differential stress, indicating insensitivity of frequency content of the rock specimen to the changes in the differential stress. Applying a constant differential stress for a relatively-long time, i.e. during creep tests, led to slight changes in the frequency content of the rock specimen.

# CHAPTER 5

# EXPERIMENTAL STUDY OF FRACTURE RESPONSE IN GRANITE SPECIMENS SUBJECTED TO HYDROTHERMAL CONDITIONS RELEVANT FOR ENHANCED GEOTHERMAL SYSTEMS

## ABSTRACT

Sustaining a network of connected fractures is critical to the long-term success of Enhanced Geothermal Systems (EGS). In this study, the effects of coupled Thermal-Hydrological-Mechanical-Chemical (THMC) processes on fracture aperture and permeability were examined by conducting a series of flow-through experiments on artificially-fractured granite specimens at effective stresses of 5 MPa to 36 MPa, rock temperatures of 25 °C and 130 °C, and injected fluid temperatures of 25 °C, 75 °C, and 130 ° C. The higher fracture closure rates observed at higher effective stresses and the incomplete recovery of fracture permeability and hydraulic aperture observed during unloading stages highlight the role of pressure solution. The increase in temperature of the injected fluid increases the recovery percentage of fracture aperture and permeability after unloading.

## 5.1 INTRODUCTION

Geothermal energy is a renewable and clean source of energy with a projected capacity of 7.92 GigaWatts (GW) by 2050 in the United States (EIA report, 2017) and 18.3 GW by 2021 worldwide (GEA report, 2016). Enhanced Geothermal System (EGS) is a type of geothermal system that takes advantage of the high temperature of deep hot dry bedrock. EGS has the capacity of covering 20% of electricity needs and contributing up to 100 GW of electricity in the United States by 2050 (MIT Report, 2006). To have a productive EGS reservoir, it is necessary to create a network of connected fractures, using hydro-shearing (e.g. Cladouhos et al., 2016) or hydraulic fracturing (e.g. Frash et al., 2014; Frash et al., 2015; Tomac and Gutierreze, 2017) within the hot dry rock, in addition to the existing natural fractures (e.g. Majer et al., 2007; Ghassemi, 2012; Zang et al., 2014; Izadi and Elsworth, 2015; Safari and Ghassemi, 2015). The injected geothermal fluid (typically water) flows through the primary and secondary fractures, and exchanges heat with the host rock. The produced hot water/steam is then extracted from the production well(s), and used as a source of energy, either for direct heating or for electricity production (MIT report, 2006).

Several research and demonstration projects around the world have significantly contributed to the advancement of knowledge for EGS development (e.g. Deichmann and Giardini, 2009; Wong et al., 2010; Goertz-Allmann et al., 2011; Albaric et al., 2014; Gritto and Jarpe, 2014; Kwiatek et al., 2015; Cladouhos et al., 2016; Fang et al., 2016; Caulk and Tomac, 2017). Despite its potential, several factors have hindered deployment of EGS at

fully-commercial scales. For example, the high capital cost (MIT report, 2006; EIA report, 2017), induced seismicity (e.g. Rutqvist et al., 2006; Majer et al., 2007; Izadi and Elsworth, 2015), and production decline (e.g. Yasuhara et al., 2011; Caulk et al., 2016; Faoro et al., 2016; Farough et al., 2016) over time are some of the concerns that need to be addressed before EGS can be viewed as an economically-viable renewable energy production system.

The potential production decline in EGS reservoir is a pressing challenge yet to be addressed. Sustaining a permeable fracture network over long-term that allows continuous heat exchange between the injected fluid and the host rock is key to the successful development of EGS. Pore pressure increase, temperature change, volume change due to fluid withdrawal/injection and chemical alteration of fracture surface are the main contributing mechanisms to the change of permeability in EGS reservoir operations (e.g. Majer et al., 2007; Ghassemi, 2012; McClure and Horne, 2014). The coupled THMC processes that act at different time scales can significantly affect the fracture response and reservoir permeability. In addition, the triggered THMC processes change the state of stress (e.g. Majer et al., 2007; Schoenball et al., 2014; Martínez-Garzón et al., 2014) and might lead to induced seismicity (e.g. Catalli et al., 2013; Edwards and Douglas, 2014; Gischig, 2015; Ghassemi and Tao, 2016). For instance, induced seismicity as observed in geothermal fields (Geysers, CA - Rutqvist et al., 2006; Garcia et al., 2016; Basel, Switzerland - Meier et al., 2015; Soultz, France - Andre et al., 2006; Genter et al., 2010) were in part linked to the activated THMC processes in the reservoir.

Several experimental and numerical studies (not actual EGS operational data) have predicted the significant contribution of the coupled THMC processes to EGS reservoir

production decline (e.g. Kanagawa et al., 2000; Dobson et al., 2003; Tenthorey et al., 2003; Kumar and Ghassemi, 2005; Yasuhara and Elsworth, 2006; Farough et al., 2016). A brief summary of the studies investigating the effects of these processes on fracture response is provided in the following sections.

### 5.1.1 THERMAL EFFECTS

Several studies have investigated the effects of thermal processes on EGS production using physical and numerical experiments (e.g. Kranz et al., 1979; Brace, 1980; Barnabe, 1986; Polak et al., 2003; Yasuhara et al., 2004; Yasuhara et al., 2005; Ghassemi and Kumar, 2007; Ghassemi et al., 2008; Taron and Elsworth, 2010). For example, using numerical simulation, some studies have shown that the decrease in effective stress due to thermal drawdown in rock texture leads to increased fracture aperture, particularly near the injection well (e.g. Ghassemi et al., 2008; Koh et al., 2011). In addition, the secondary thermal cracks, resulted from cold water injection, can contribute to the increased heat extraction process (e.g. Tarasovs and Ghassemi, 2010; Ghassemi, 2012; Tomac and Gutierrez, 2017).

Savage et al. (1992) performed laboratory flow-through experiments on rock specimens retrieved from Cornwall geothermal field and reported that elevated temperatures enhanced the dissolution rate of some minerals, specifically that of quartz. Morrow et al. (2001) performed a series of flow-through experiments on intact, fractured, and gouge-bearing Westerly granite specimens at an effective stress of 50 MPa and temperatures ranging from 150 °C to 500 °C, and observed higher permeability reduction rates for fractured specimens compared to intact specimens, which was attributed to

mineral precipitation in the fractures. Polak et al. (2003) performed a series of flow-through experiments on naturally-fractured novaculite (crypto-crystalline quartz) specimens at different temperatures to simulate hydrothermal conditions. They reported that under constant effective stress, an increase in temperature of injected water and rock would decrease the fracture aperture. In this study, the temperatures of injected water and fractured rock specimen in flow-through experiments were selected such that the contribution of thermal stresses and mineral dissolution/precipitation processes on fracture response can potentially be investigated separately.

### 5.1.2 MECHANICAL EFFECTS

Mechanical processes including change in state of stress, shear dilation, and mechanical creep affect fracture aperture and permeability in EGS (e.g. Yasuhara et al., 2004; Ghassemi et al., 2008; Yasuhara and Elsworth, 2008; Elsworth and Yasuhara, 2010; Ghassemi and Zhou, 2011; Yasuhara et al, 2011; Hu et al., 2013; Faoro et al., 2016; Vogler et al., 2016). The geometry of the contacting asperities between the two rough surfaces of the fracture and the void spaces adjacent to these asperities influences the mechanical and hydraulic properties of fractured rocks (e.g. Cook, 1992). Loading a fracture causes deformation of void space and consequently changes the contact area, which leads to alteration of hydraulic and mechanical properties of the fractured rock (Pyrak-Nolte et al., 1987; Pyrak-Nolte and Morris, 2000). Mechanical and hydraulic characteristics of a fractured rock specimen are interrelated as: (i) fluid flow depends on aperture distribution and contact area of fracture surface; and (ii) fracture specific stiffness depends on the

number and spatial distribution of the asperities, as well as aperture distribution (e.g. Pyrak-Nolte et al., 1987; Pyrak-Nolte and Morris, 2000; Yasuhara et al., 2004).

Ameli et al. (2014) developed a model that incorporated mechanical deformation and chemical alteration of the fracture asperities and estimated the elastic deformation of rough surfaces of fracture using a semi-analytical approach. They showed that permeability increases monotonically at low flow rates, and at high flow rates transitions to a more complex evolution in which the permeability initially decreases and then increases due to dissolution of contacting asperities. Since fracture surface roughness is an important parameter affecting permeability and flow patterns, different imaging techniques (e.g. X-ray computed tomography, scanning electron microscopy, and optical profilometry) can be implemented for mapping fracture surfaces (e.g. Ameli et al., 2013; Caulk et al., 2016; Faoro et al., 2016). For example, Ameli et al. (2013) suggested a scalable method using optical profilometer to map the fracture surface and reported that the specimen with tensile fracture exhibits better-reconstructed surface topography than the specimen with saw-cut fracture.

At higher effective stresses, the fracture closes and the permeability decreases (e.g. Polak et al., 2003; Yasuhara et al., 2011; Faoro et al., 2016; Caulk et al., 2016). Ghassemi and Zhou (2011) performed numerical Thermal-Hydological-Mechanical (THM) modeling at reservoir scale and concluded that poroelastic effects are dominant in shorter-term, while, thermoelastic effects are dominant in longer time periods. Faoro et al. (2013) performed flow-through experiments on naturally-fractured Basalt and artificially-fractured granite specimens with the latter heated up to temperatures of 500 °C to 800 °C,

concluding that at lower differential stresses the fracture permeability is reduced, while at intermediate differential stresses the permeability increases. Luo et al. (2017) performed flow-through experiments on artificially-fractured granite specimens and observed that higher fracture roughness, (defined as the ratio of the true fracture surface area to the projected surface area on a horizontal plane), leads to higher permeability. In an attempt to gain a better insight into the fracture response subjected to loading/unloading at different effective stresses, the influence of effective stress on fracture permeability and hydraulic aperture was investigated in this study.

### 5.1.3 CHEMICAL EFFECTS

Contribution of chemical processes on the change of fracture permeability in EGS reservoirs has been investigated in experimental (e.g. Savage et al., 1992;Yasuhara et al., 2004; Yasuhara et al., 2005; Yasuhara et al., 2011; Caulk et al., 2016; Farough et al., 2016) and numerical modeling studies (e.g. Xu et al., 2001; Kumar and Ghassemi, 2005; Andre et al., 2006; Ghassemi and Kumar, 2007; Ghassemi, 2012; Rawal and Ghassemi, 2014; Kim et al., 2015; Pandey et al., 2015; Blaisonneau et al., 2016). Kim et al. (2015) performed THMC simulation at reservoir scale and reported that permeability for a fractured reservoir can be significantly altered due to mineral dissolution/precipitation processes. Kumar and Ghassemi (2005) through numerical modeling of a fractured EGS reservoir found that silica dissolution occurs near the injection well, and that higher initial fracture aperture among other parameters (e.g. higher initial water velocity, lower reservoir thermal conductivity) leads to increased dissolution of quartz. Pandey et al. (2015) performed simulations using a numerical THC model to investigate injection of super-saturated and

under-saturated silica water into a geothermal reservoir concluding that in the former case the precipitation occurs within the reservoir and close to the injection well, while in the latter case dissolution occurs far from the injection well.

Farough et al. (2016) performed a series of flow-through experiments on fractured ultramafic cores under effective pressure of 30 MPa, and temperature of 260 °C and observed significant permeability reduction, 1-2 orders of magnitude, due to mineral precipitation. Caulk et al. (2016) performed long-term experiments on artificially fractured granite specimens at temperature of 120 °C, pore pressures of 5 MPa, and confining pressures of 30 and 40 MPa, and reported that feldspar dissolution at asperities led to reduction of fracture permeability and hydraulic aperture. In this study, the influence of the temperature of injected fluid and effective stress on mineral dissolution is investigated. In addition, the permeability change under constant effective stress and temperature conditions is investigated to highlight the role of mineral dissolution/precipitation processes.

### 5.1.4 PRESSURE SOLUTION

Pressure solution, a sub-set of chemo-mechanical processes (Taron and Elsworth, 2010), is among important processes that contribute to deformation and diagenetic compaction in rocks within the upper earth crust (Stephenson et al., 1992; Yasuhara et al., 2003), and can contribute to porosity and permeability reduction (Stephenson et al., 1992; Taron and Elsworth, 2010). There are three mechanisms involved in pressure solution acting in a fracture: (i) dissolution of the asperities in-contact due to high localized stresses, (ii) diffusion of dissolved mass from highly-stressed regions (contacting asperities) to less-

stressed regions (free-faces of the fracture surface) due to chemical potential, and (iii) precipitation of dissolved minerals at free faces of the fracture surface (Yasuhara et al., 2004; Yasuhara et al., 2011). Figure 5.1 shows a schematic of pressure solution, in which fracture aperture change (Δb) due to pressure solution phenomenon leads to permeability change and also volume change (ΔV) based on contact area (Yasuhara et al., 2011).

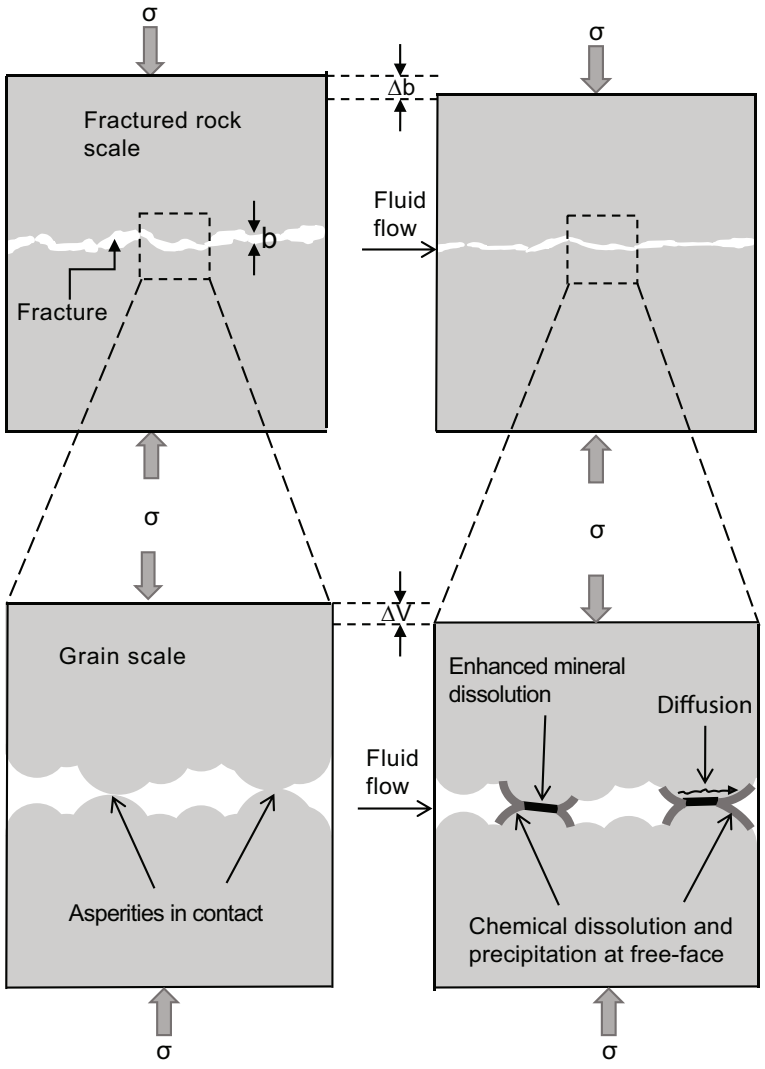


Figure 5-1. Schematic of pressure solution: at asperities contacts, the minerals dissolve due to high localized stresses, dissolved mass diffuses from the interface further down the fracture surface, and precipitation occurs at the free-faces of the fracture surface (adapted and modified from Yasuhara et al., 2004).

σ: stress; Δb: aperture change; ΔV: volume change

Several studies have investigated the role of pressure solution in fracture closure at relatively high temperatures (e.g. Yasuhara et al., 2004; Yasuhara et al., 2005; Faoro et al., 2016). Yasuhara et al. (2004) performed flow-through experiments on Arkansas novaculite specimens with natural fractures at an average confining pressure of 2.73 MPa and found that pressure solution is the dominant mechanism contributing to the permeability reduction at temperatures of 20 to 150 °C. Yasuhara et al. (2005) performed a series of flow-through experiments on naturally-fractured novaculite specimens at temperatures ranged from 20 °C to 120 °C and reported that in the first half of the experiment the fracture gradually closes due to dissolution at asperities, followed by an increase in fracture aperture due to free-face dissolution for the rest of the experiment. They also found that at high temperatures the contribution of free-face dissolution is more pronounced compared to room temperature. Faoro et al. (2016) conducted a series of flow-through experiments on fractured Westerly granite specimens with temperatures ranging from 25 °C to 150 °C and at effective stress ranging from 1.35 MPa to 55 MPa, and found that at low temperature the pressure solution is the main contributing mechanism to fracture permeability reduction, while, at high temperature, both pressure solution and chemical precipitation/dissolution processes contribute to the fracture permeability reduction.

Considering the importance of the effects of coupled processes on fracture permeability/aperture reduction and consequently on EGS production decline (e.g. Morrow et al., 2001; Polak et al., 2003; Ghassemi and Zhang, 2004; Yasuhara et al., 2004; Ghassemi and Zhou, 2011; Caulk et al., 2016), it is critical to further investigate these processes and improve the fundamental understanding of them. In particular, pressure solution can significantly alter the fracture aperture and permeability. Since temperature affects pressure

solution (Faoro et al., 2016), it is necessary to further investigate the effects of temperature for both rock and injected fluid on pressure solution and its significance to fracture aperture and permeability change. The reversibility of fracture aperture/permeability due to pressure solution, and the effects of temperature difference between the injected fluid and rock on fracture response are among important knowledge gaps in this area. In this study, a series of flow-through experiments has been conducted on artificially-fractured granite specimens under effective stress ranges between 5 MPa to 36 MPa, rock temperatures of 25 °C and 130 °C, and injected fluid temperatures of 25 °C, 75 °C, and 130 °C. A total of six flow-through experiments, 5 to 10 days, on fractured granite specimens with mainly quartz and feldspar minerals were performed and the results are reported here.

## 5.2 EXPERIMENTAL PROGRAM

### 5.2.1 SAMPLE PREPARATION

Barre granite (Vermont, USA) specimens, cored from a homogeneous block, were used in this study. Using microscope and image analysis, the plane of foliation was first identified (Caulk et al., 2016) and then coring was performed accordingly (see Figure 5.2a) to facilitate the creation of a tensile artificial fracture along specimen. The cylindrical shaped cores were 38.4 mm in diameter and 38.5 mm in length. The specimens had a dry density of 2.63 g/cm$^3$, and porosity of 0.72%. The X-Ray Diffraction (XRD) analysis revealed that the specimens contained 42.4% quartz, 47.9% feldspars (36.7% oligoclase, 11.2% microcline), 3.9% biotite, 3.2% muscovite, and 2.6% accessory minerals including oxides, calcite, and chlorite (Caulk et al., 2016). The two ends of the specimens were lapped to 0.001 inches. Modified Brazilian test, in which a flattened disk is used to eliminate the

stress concentration at the corners of the specimen (Yu et al., 2009), was performed to create an artificial fracture along the length of each specimen. Figures 5.2b and 5.2c show a picture of one of the fractured specimens used in this study. The two halves of the fractured specimen were mated together cleanly in reported experiments and no attempt was made to cause shear dislocation on fracture.

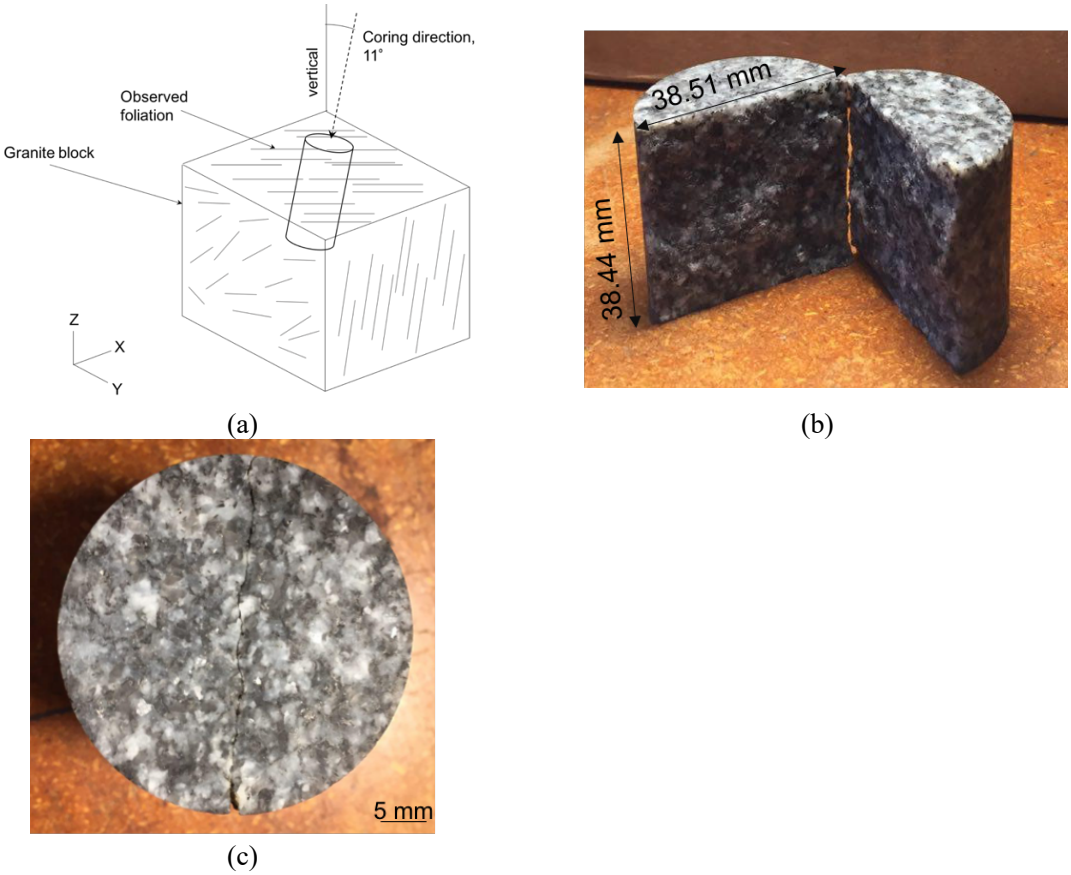


(a) (b)

(c)

Figure 5-2. Images of an artificially fractured specimen used in the experiments, (a) schematic of the foliation and coring direction (adapted and modified from Caulk et al., 2016), (b) two halves of the fractured specimen are separated, and (c) the two halves of the fractured specimen are mated together (plan view)

### 5.2.2 CHEMICAL ANALYSIS

Analysis of the influent (i.e. deionized water) and effluent samples collected at the end of each experiment was performed using a JY Horiba Optima 2 ICP-OES instrument housed at the Geology Department, University of Vermont. Samples were acidified with 1% ultrapure $HNO_3$ and concentrations of Al, Ca, Fe, K, Mg, Mn, Na, and Si were determined. The rate of fracture aperture change over time (db/dt) can be estimated using the concentration of dissolved species in the collected effluent samples (e.g. Polak et al., 2003; Faoro et al., 2016). In this study, quartz and microcline feldspar were selected for estimation of hydraulic aperture change, as several studies have highlighted the importance of quartz and feldspar dissolution/precipitation in EGS reservoir production (e.g. Rawal and Ghassemi, 2014; Pandey et al., 2015). The rate of the fracture aperture change over time is estimated using the following expression (Polak et al., 2003; Yasuhara et al., 2004; Faoro et al., 2016):

$$\frac{db}{dt} = \frac{QC_\alpha}{A_c\rho} \tag{5.1}$$

where $C_\alpha$ is the silicon-derived concentration of quartz or microcline feldspar (kg/m$^3$), $Q$ is the flow rate (m$^3$/s), $\rho$ is the density of the quartz or microcline felsdspar (kg/ m$^3$), and $A_c$ is the contact- surface area between the two halves of the specimen (m$^2$). $C_\alpha$ is computed as the product of molar weight ratio of quartz or microcline feldspar to that of silicon, and silicon concentration in the effluent obtained from ICP-OES analysis. Although oligoclase has an important role in the dissolution process given its high percentage in XRD analysis of the rock specimens, microcline and quartz were used as the two end-members

contributing to silicon production. The molar ratio of quartz to silicon is 1, that of oligoclase to silicon is 2, and that of microcline to silicon is 3. Therefore, the silicon-derived concentration of oligoclase in the effluent falls between those of quartz and microcline. Thus, using Eq. (5.1), the estimated fracture aperture considering oligoclase dissolution falls between estimated fracture apertures considering dissolution of quartz and microcline. $A_c$ is expressed as:

$$A_c = R_c A_f \tag{5.2}$$

where $A_f$ is the entire surface area of the fracture, and $R_c$ is the percentage of the asperities in-contact. In this study, a lower bound of $R_c$=0.4 to account for potential asperity misfit, and an upper bound of $R_c$=0.8 to account for well-mated specimens were selected to capture the irregularity of the created fracture in the specimens. In general, as tensile fracture was created in the tested specimen, and the two halves were mated together as clean as possible higher $R_c$ values (i.e. closer to the upper bound) were expected as also reported by other studies (e.g. Ameli et al., 2013; Caulk et al., 2016).

### 5.2.3 IMAGE ANALYSIS

A Brucker SkyScan 1173 Micro-Computed Tomography (CT), housed in the Imaging Laboratory at the Department of Civil and Environmental Engineering, University of Vermont, was used to scan the pre- and post-test specimens with a resolution of 19.9 microns. The boundary greyscale thresholding of the pre- and post-CT scans were equally performed following the standard approach for CT-image processing (ASTM, 1992). Although it was desired to use pre- and post-test CT-images to estimate the change in

fracture volume along the length of the specimen, the fact that the pre- and post-test CT-images were obtained at atmospheric pressure and room temperature (not experimental condition) prevented performing this analysis. However, the pre- and post-test CT images were used to construct three-dimensional (3D) maps of the fracture surface topography at selected regions on the fracture. 3D models were constructed using several slices along the fracture. Then, using Fusion 360 software, the elevation of each grid point, representing the height of asperities at the fracture surface was evaluated. Afterwards, the 3D matrices of the planar coordinates merged with elevation of grid points for pre- and post-test conditions were created in MATLAB. Finally, the 3D map of the fracture topography for pre- and post-test at the selected region was created using these 3D matrices.

### 5.2.4 TESTING PLAN

The coupled THMC processes contribute to relatively-rapid permeability reduction and production decline in EGS reservoirs (e.g. Ghassemi, 2012; Faoro et al., 2016). Details of the experimental conditions for the six experiments reported in this study are presented in Table 5.1. Although, the performed experiments were relatively-short, the results (Section 5.3) show rapid closure of fracture which can potentially represent the initial rapid closure of fracture in the field. Experiments #1 and #2 were performed to evaluate the evolution of hydraulic aperture and fracture permeability under relatively-low and high effective stresses, with constant effective stress during each experiment. It should be noted that effective stress is defined as the difference between the total stress and the pore water pressure.

In order to further investigate the effects of pressure solution on fracture response, a specific stress path (see Figure 5.3) for experiments #3 to #6 was designed. Effective stress was increased step-wise ( 5, 15, 35, and 55 MPa) during loading stages and decreased step-wise (35, 15, 5 MPa) during unloading stages, and was kept constant for 24 hours during each stage. The loading increase/decrease rate during transition from one loading/unloading stage to the next was 0.333 MPa/sec. The unloading stages were performed as it was desired to evaluate the reversibility of hydraulic aperture and fracture permeability due to pressure solution. In addition, the temperature of injected fluid and the granite specimens were varied in these experiments to gain a better insight into the significance of temperature on contributing processes to fracture behavior. Experiment #3 was designed to improve the understanding of the effects of pressure solution on fracture response, while allowing comparison with experiments #1 and #2 (i.e. similar temperatures for rock specimen and injected water).

Experiments #4 and #5 aimed at evaluating the effects of temperature difference ($\Delta T$) between the injected fluid and rock specimen on physical- and chemical-triggered processes, while allowing comparison with experiments #3 ($\Delta T$~105 °C) and #6 ($\Delta T$~0 °C). Thermal contraction/dilation of the rock is directly affected by the temperature difference ($\Delta T$) between the injected fluid and the rock. Higher $\Delta T$ values leads to higher contraction/dilation rate compared to lower $\Delta T$ values (e.g. Ghassemi and Zhou, 2011). In addition, increasing the temperature of injected fluid directly affects the kinetic rate of mineral dissolution/precipitation (Johnson et al., 1998; Dove, 1999). Since the temperature of injected water potentially affects both thermal contraction/dilation and mineral dissolution/precipitation processes, to evaluate its effect on fracture response, the

temperature of the injected water was set higher in experiments #4 and #5. The higher temperature of the injected water in these two experiments favors higher dissolution rate compared to other experiments, which in turn increases the probability of precipitation on the fracture surface as fluid moves along the fracture.

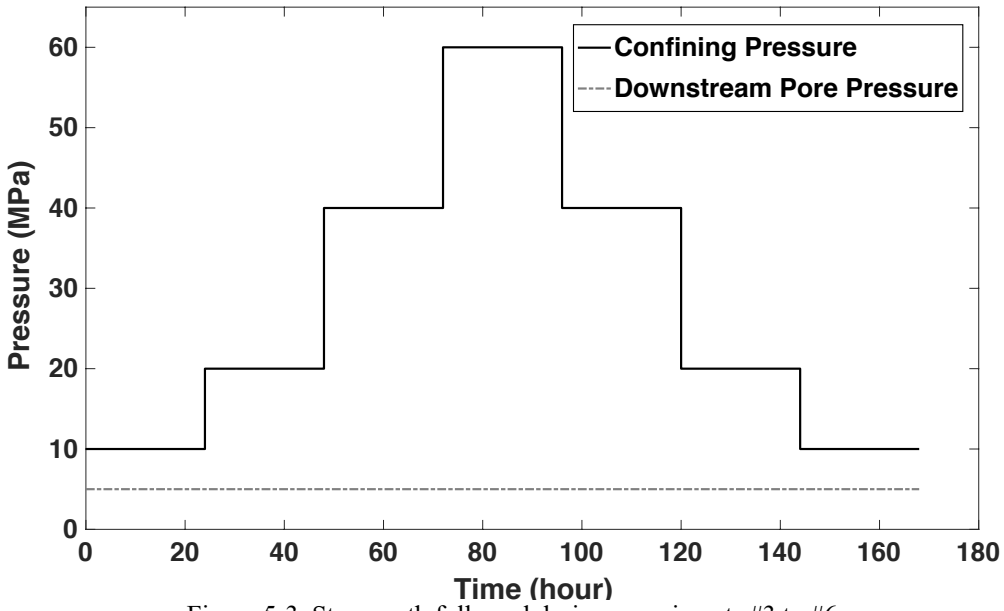

Figure 5-3. Stress path followed during experiments #3 to #6

The rock temperature and the injected fluid temperature in experiments #5 and #6 were set at 130 °C and 25 °C, respectively. One of the main intentions for designing experiments #5 and #6 was to potentially minimize the effects of thermal stresses ($\Delta T=0$ in both experiments), while studying the effects of chemical processes on fracture response, as higher temperature of the injected fluid affects the kinetic rate of mineral dissolution/precipitation. The effect of temperature on mineral dissolution/precipitation is present in experiment #5, while, is minimized in experiment #6.

The tests in this study were performed in displacement-controlled mode, as explained in Appendix F. Very low injection rates (see Table 5.1) were selected to allow enough residence time facilitating the water-rock mineral interactions during the experiments. Other studies (e.g. Yasuhara et al., 2011) have reported that for granite rocks subjected to relatively-similar range of pressure/temperature, the effluent concentration for dissolved quartz reached steady-state within a day. It was assumed that the concentration in the effluent collected in the reported experiments in this study reached steady-state within one day. However, it should be acknowledged that the exact time to reach chemical equilibrium in the experiments was not specifically studied. At the end of each experiment, the effluent sample collected during the experiment was retrieved for Inductively Coupled Plasma Optical Emission Spectrometry (ICP-OES) analysis.

Table 5-1. Relevant information of the experiments

| Experiment ID | Confining Pressure (MPa) | Downstream Pore Pressure (MPa) | Injection rate (ml/min) | Duration of the Experiment (Days) | Rock Temperature (°C) | Injected water Temperature (°C) |
|---|---|---|---|---|---|---|
| Exp. #1 | 15 | 5.5 | 0.00160 | 8 | 130 | 25 |
| Exp. #2 | 57.8 | 21.2 | 0.00119 | 10 | 130 | 25 |
| Exp. #3 | [10, 20, 40, 60, 40, 20,10] | 5.0 | 0.00148 | 7 | 130 | 25 |
| Exp. #4 | [10, 20, 40, 60, 40, 20,10] | 5.0 | 0.00148 | 7 | 130 | 75 |
| Exp. #5 | [10, 20, 40, 60, 40, 20] | 5.0 | 0.00148 | 5 | 130 | 130 |
| Exp. #6 | [10, 20, 40, 60, 40, 20,10] | 5.0 | 0.00148 | 7 | 25 | 25 |

It is worth mentioning that the viscosity of the injected deionized water in the reported experiments substantially changes with temperature and slightly with pressure. For estimation of fracture permeability and hydraulic aperture using Eqs. (A7.1) and (A7.2), the corresponding dynamic viscosity values used in experiments #1 to #6 are: $8.89\times10^{-4}$, $8.86\times10^{-4}$, $8.89\times10^{-4}$, $3.79\times10^{-4}$, $2.82\times10^{-4}$, and $8.89\times10^{-4}$ Pa.s, respectively.

As discussed earlier, the experiments were performed under constant injection rate (i.e. the upstream pore pressure intensifier continuously adjusts the upstream pore pressure to keep the injection rate constant) and constant downstream pore pressure. Since all parameters in Eq. (A7.2) are constant during each experiment (except for $\Delta P$) and recalling that the downstream pore pressure is kept constant during the experiment, the hydraulic aperture varies only with changes in upstream pore pressure ($b \propto \frac{1}{\sqrt[3]{\Delta P}}$). Therefore, during experiments, increase of the upstream pore pressure is an indication of decrease in the hydraulic aperture to maintain the prescribed constant injection rate, and decrease of the upstream pore pressure is an indication of increase in the hydraulic aperture.

## 5.3 RESULTS AND DISCUSSION

Experiments #1 and #2 were conducted at constant effective stresses. On the other hand, experiments #3 to #6 were performed with varying effective stress and at different temperatures. The results of experiments #1 and #2 are presented in section 5.3.1, and those of experiments #3 to #6 are presented in section 5.3.2.

### 5.3.1 EXPERIMENTS WITH CONSTANT EFFECTIVE STRESS

Figure 5.4a shows the variation of upstream pore pressure recorded during experiment #1 conducted at relatively-low confining pressure of 15 MPa, indicating continuous increase of upstream pore pressure under constant downstream pore pressure of 5.5 MPa and constant injection rate of 0.00160 ml/min. Figure 5.4b shows the variation of hydraulic aperture and fracture permeability estimated using pore pressure data based on Darcy's law (Eq. (A7.1)) and modified cubic law (Eq. (A7.2)), respectively. In general, the upstream pore pressure increases with a linear trend (rate of 0.14 Pa/s) indicating decrease of hydraulic aperture and fracture permeability. Hydraulic aperture decreases from 1.1 to 0.91 μm, and the corresponding fracture permeability decreases from $3.3\times10^{-18}$ $m^2$ to $2.1\times10^{-18}$ $m^2$.

(a)

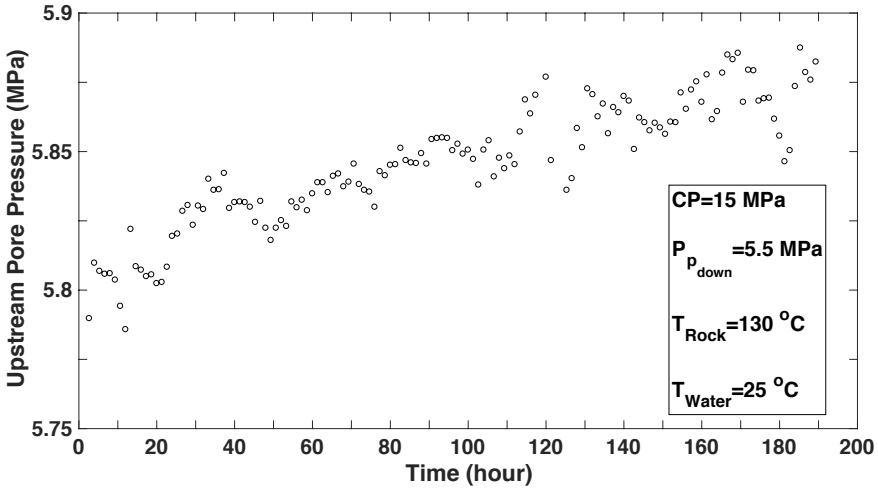

(b)

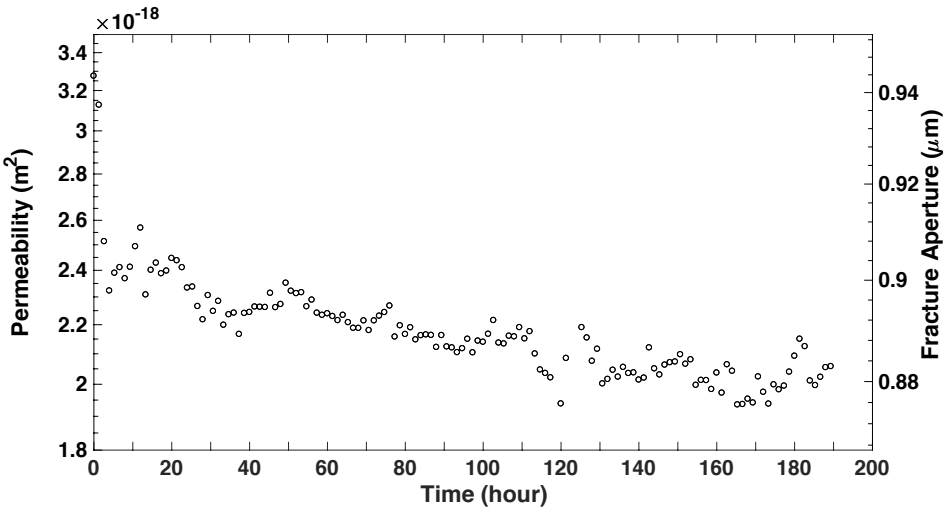


Figure 5-4. Evolution of (a) upstream pore pressure, and (b) fracture permeability and hydraulic aperture during the experiment #1.

CP: confining pressure; $P_{p,down}$: downstream pore pressure; $T_{rock}$: temperature of rock specimen; $T_{water}$: temperature of injected deionized water

Table 5-2. Results of ICP-OES analysis for different experiments

| Element | DL | Influent conc. (ppm) | Effluent conc. (ppm) | | | | |
|---|---|---|---|---|---|---|---|
| | | | Exp. #1 | Exp. #2 | Exp. #3 | Exp. #4 | Exp. #5 |
| Al | 0.100 | bdl | *bdl* | *bdl* | *bdl* | 0.1726 | 0.6142 |
| Ca | 0.050 | <0.500 | 4.8798 | 2.8366 | 4.3038 | 17.4681 | 9.6833 |
| Fe | 0.300 | *bdl* | *bdl* | *bdl* | *bdl* | *bdl* | 0.3547 |
| K | 0.200 | <0.500 | 5.0444 | 4.4976 | 4.8003 | 5.2091 | 6.6092 |
| Mg | 0.050 | NA | 0.1818 | 0.1931 | 0.1890 | 4.5467 | 0.4579 |
| Mn | 0.010 | *bdl* | *bdl* | *bdl* | *bdl* | *bdl* | *bdl* |
| Na | 0.040 | <0.500 | 6.1311 | 4.5764 | 5.9914 | 71.4673 | 159.3813 |
| Si | 0.040 | <0.300 | 6.7219 | 2.7446 | 5.5743 | 0.5370 | 9.6282 |

Figure 5.5a illustrates the evolution of upstream pore pressure for experiment #2 conducted at relatively-high confining pressure of 57.8 MPa and pore pressures of 21.2 MPa. These pressures represent a depth of approximately 2.4 km with confining and pore

pressure gradients of 24 and 8.8 MPa/km, respectively (Cladouhos et al., 2016). The upstream pore pressure tends to increase to maintain the constant prescribed injection rate of 0.00119 ml/min and consequently, both hydraulic aperture and fracture permeability decrease over time (Figure 5.5b). This is an indication of gradual closure of fracture, which is attributed to the coupled THMC processes. The rate of pore pressure increase for this experiment was estimated around 0.17 Pa/s, which is slightly higher than that of experiment #1. Hydraulic aperture decreases from 1.3 μm to 0.95 μm, and the corresponding fracture permeability decreases from $5.9\times10^{-18}$ to $2.4\times10^{-18}$ $m^2$. The results from the chemical analysis of the collected effluent samples are reported in Table 5.2, showing a noticeable increase in concentration of all elements except for aluminum in both experiments #1 and #2, which is an indication of dissolution of quartz and feldspars.

### 5.3.2 EXPERIMENTS WITH VARYING EFFECTIVE STRESS

The evolution of upstream pore pressure with a rate of 2.26 Pa/s (computed during loading stages, from the beginning of CP of 10 MPa until the ending of CP of 60 MPa) and the corresponding hydraulic aperture and fracture permeability changes in experiment #3 appear in Figures 5.6a and 5.6b, respectively. As evident in Figure 5.6b, the fracture permeability decreases almost two orders of magnitude, from $3.8\times10^{-17}$ to $9.7\times10^{-19}$ $m^2$, during loading stages, and gradually increases during unloading stages, and recovers back to $7.0\times10^{-18}$ $m^2$, indicating an incomplete permeability recovery caused mostly by pressure solution phenomena. As shown in Figure 5.6b, the hydraulic aperture has dropped from 2.4 to 0.71 μm during loading stages and recovers back to 1.36 μm during unloading stages. The initial fracture geometry, particularly, the shape, number and spatial distribution of

asperities; hardness of asperities; and the way that the two pieces of the fracture have been mated together are among important factors that influence (i) the initial fracture permeability (Pyrak-Nolte and Morris, 2000; Farough et al., 2016), (ii) mechanical aspect of pressure solution phenomenon (Yasuhara and Elsworth, 2008; Yasuhara et al., 2011); and (iii) the percentage of permeability recovery.

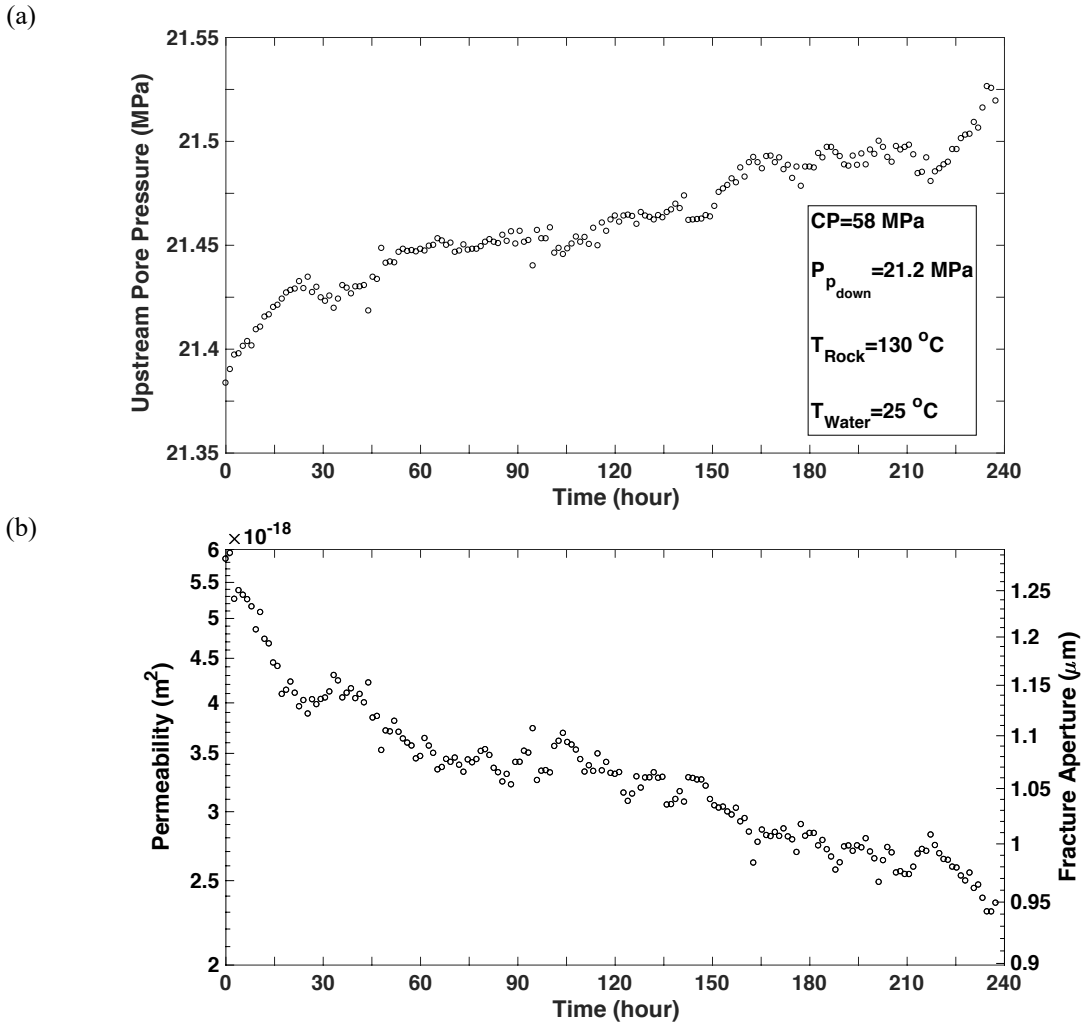


Figure 5-5. Evolution of (a) upstream pore pressure, and (b) fracture permeability and hydraulic aperture during the experiment #2

As it can be seen in Figure 5.6a, the rate of upstream pore pressure increases at higher CP levels (e.g. 40 and 60 MPa) is higher than that of lower CP levels (e.g. 10 MPa). This might be explained by the fact that at higher CP levels, in addition to the increase of the number of asperities in contact (i.e. increasing $R_c$ values), the effect of pressure solution is more pronounced, which leads to higher fracture closure rates. Also, as presented in Table 5.2, the concentrations of Ca, K, Na, and Si has have noticeably increased in the collected effluent samples for experiment #3 compared to those of influent (i.e. deionized water), which is attributed to the dissolution of feldspars and quartz. It is worth noting that the range of concentrations of dissolved elements for experiment #3 is consistent and close to those for experiments #1 and #2, which is attributed to the fact that the temperature of the rock specimen and the temperature of the injected water in all these three experiments were the same.

Figures 5.7a shows a 2D CT image of a slice along the fractured specimen used in experiment #3 and the selected region for morphology analysis (i.e. change in height of asperities). Figure 5.7b shows the location of the selected region, with dimensions of 3.16mm-by-1.65mm, on the fracture surface of the rock specimen. A total number of 83 slices along the fracture length were used to construct the 3D models for pre- and post-test conditions. The elevation at each of the 13197 grid points (159×83), representing height of asperities at the fracture surface was evaluated using these 3D models. Figure 5.7c illustrates the net change in the asperities height (i.e. difference between pre- and post-test), indicating the regions with dissolution (negative values on the 3D map) and precipitation (positive values on the 3D map), which are also shown on the magnified region of study in Figure 5.7d. The results of image analysis confirm the occurrence of dissolution as

indicated by the chemical analysis. It should be noted that the resolution in this analysis was 19.9 μm, and that higher resolution leads to more accurate analysis.

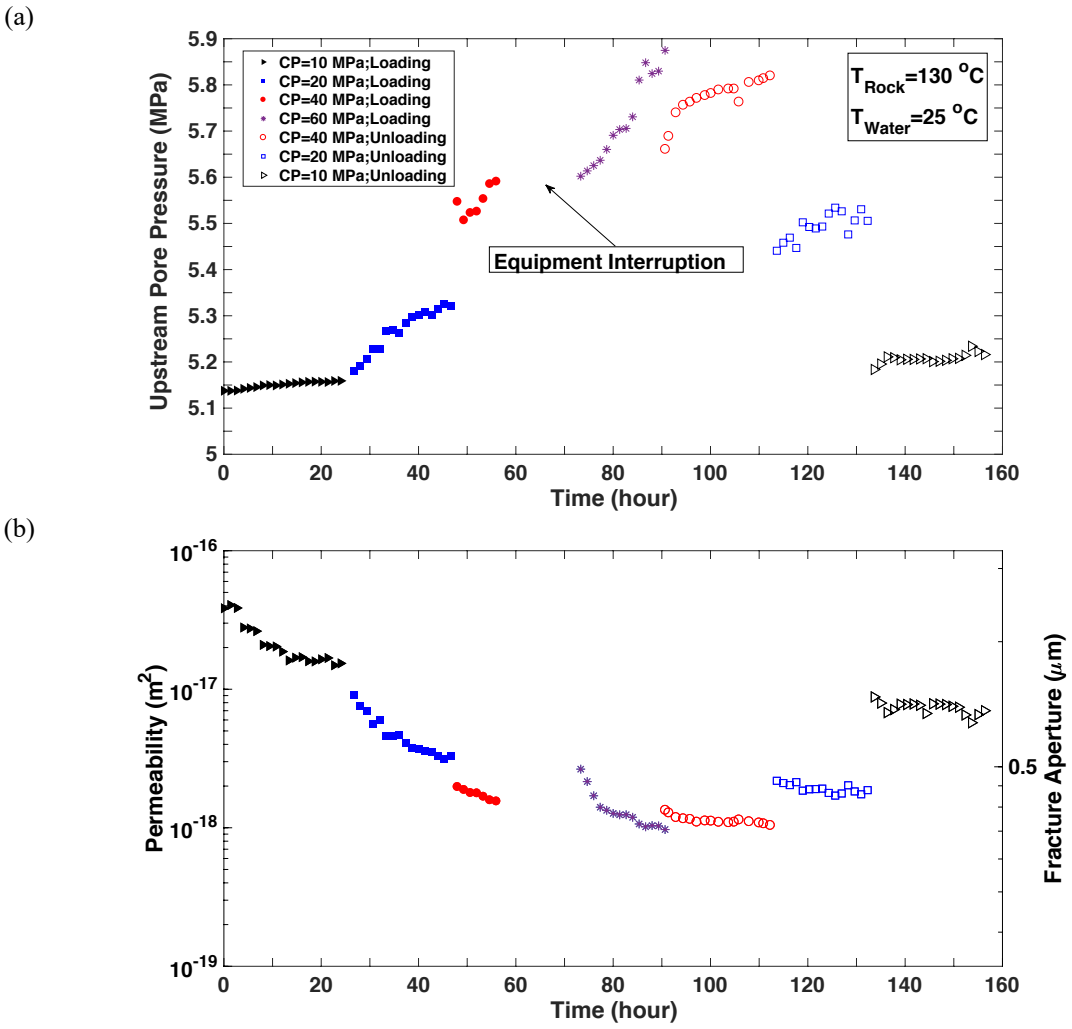


Figure 5-6. Evolution of (a) upstream pore pressure, and (b) fracture permeability and hydraulic aperture during the experiment #3

Figure 5.8a shows the evolution of upstream pore pressure during experiment #4, which exhibits increase rate of 1.74 Pa/s, less than that of experiment #3. This could be attributed to the fact that water has a lower viscosity at higher temperature (i.e. ~75 °C vs

~25 °C) and hence can flow easier through the fracture. In addition, the higher temperature of injected fluid affects the contribution of THMC processes on fracture response. Moreover, the initial fracture surface topography in each experiment is different, which might be another explanation for this observation. As evident in Figure 5.8b, there is relatively-substantial fluctuation in the hydraulic aperture and fracture permeability for the loading stage at CP=10 MPa. This is attributed to the fact that at early stages of the experiment, the equilibrium conditions were not completely achieved and therefore, upstream pore pressure was fluctuating leading to substantial change in differential pore pressure rate in the range of $4.23\times10^{4}$ to $5.73\times10^{4}$ Pa, which is about 36% of the initial differential pressure ($\Delta P$) value. In addition, at lower levels of effective stress, less differential pressure is needed to inject water into the fractured specimen at prescribed rate compared to higher levels of effective stresses. This explains the significant fluctuations of the estimated hydraulic aperture and fracture permeability during loading stage at CP=10 MPa. During loading stages of the experiment, the hydraulic aperture and fracture permeability changes from 1.5 to 0.56 μm, and from $8.9\times10^{-18}$ to $4.9\times10^{-19}$ $m^2$, respectively. During unloading stages, the fracture permeability and hydraulic aperture and fracture permeability have been changed from $4.9\times10^{-19}$ to $3.6\times10^{-18}$ $m^2$, and from 0.56 to 1.2 μm, respectively. This is an indication of incomplete recovery of the hydraulic aperture and fracture permeability, which might be in part due to pressure solution phenomenon. is due to (i) pressure solution (i.e. dissolution of asperities in-contact followed by diffusion and precipitation at free-faces), and (ii) mineral dissolution at free-faces of the fracture surface and precipitation further down the fracture surface.

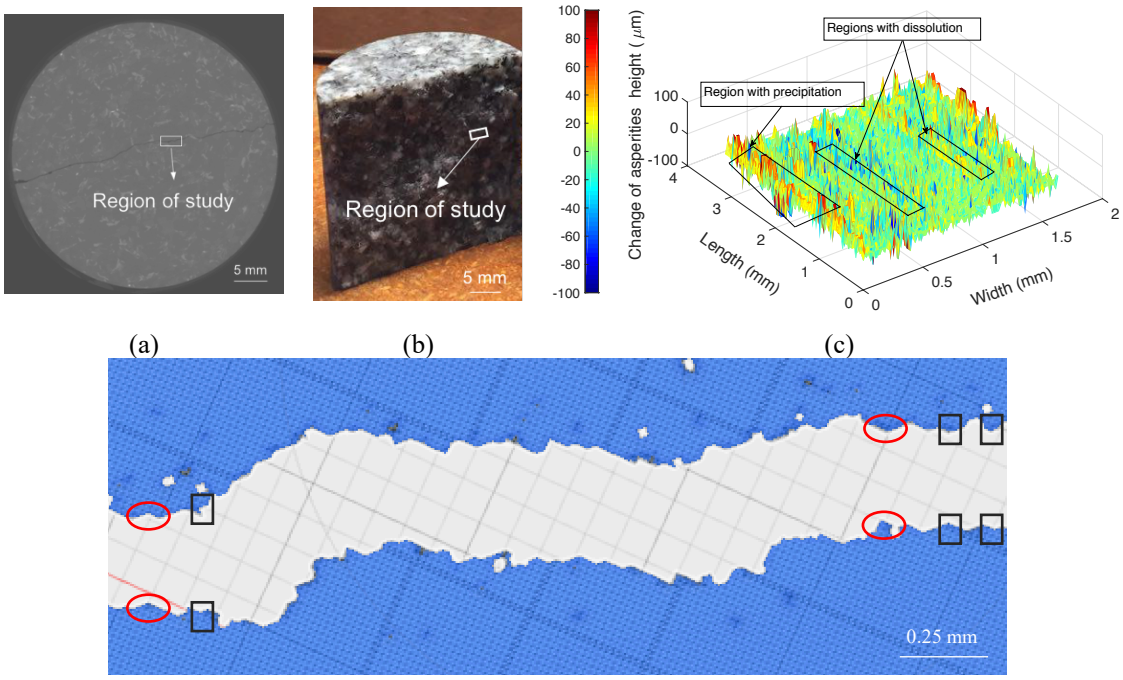


Figure 5-7. (a) 2D CT image of a selected slice of the fractured specimen; (b) selected region on fracture surface for topography analysis; (c) net difference between pre- and post-test 3D topography map of the selected region of fracture surface (note that the negative values represent zones of mineral dissolution, and positive values represent zones of mineral precipitation); and (d) magnified region of study (in a 3D model) with identified possible dissolution/precipitation regions for experiment #3 (note that rectangles show possible regions of dissolution and the circles show possible regions of precipitation.

As presented in Table 5.2, the concentration of different elements in this experiment is noticeably higher than experiments #1 to #3 (except for silica). The temperature of injected fluid in this experiment (i.e. ~75 °C) was higher than that of previous experiments (i.e. ~25 °C), which might contribute to the enhanced dissolution rate of the minerals. It should be noted that most of the sampled effluent for this experiment corresponds to the last three days of the experiment (due to loss of the effluent for the first four days). This might explain the considerably-higher concentration of Ca, and Na and lower concentration

of Si for this experiment compared to the previous experiments and imply a strong kinetic dependency on mineral dissolution rates.

(a)

(b)

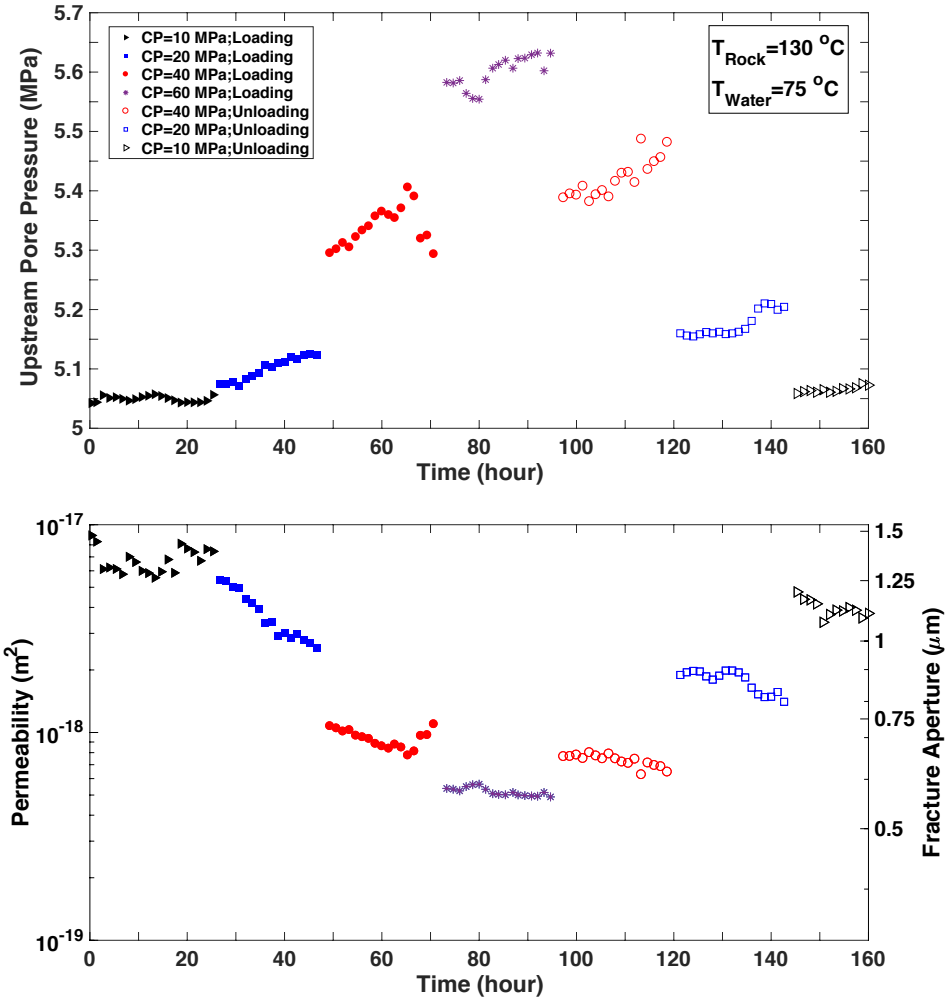


Figure 5-8. Evolution of (a) upstream pore pressure, and (b) fracture permeability and hydraulic aperture during the experiment #4

Figures 5.9a and 5.9b show the evolution of upstream pore pressure, with a rate of 0.82 Pa/s, and hydraulic aperture and fracture permeability during experiment #5, respectively. It can be observed in Figure 5.9b that during loading stages, the fracture

permeability and hydraulic aperture and fracture permeability change from $1.9\times10^{-18}$ to $0.67\times10^{-18}$ $m^2$, and from 0.88 to 0.62 μm, respectively. On the other hand, during unloading stages, the hydraulic aperture and fracture permeability change from $0.67\times10^{-18}$ to $1.3\times10^{-18}$ $m^2$, and from 0.62 to 0.77 μm, respectively.

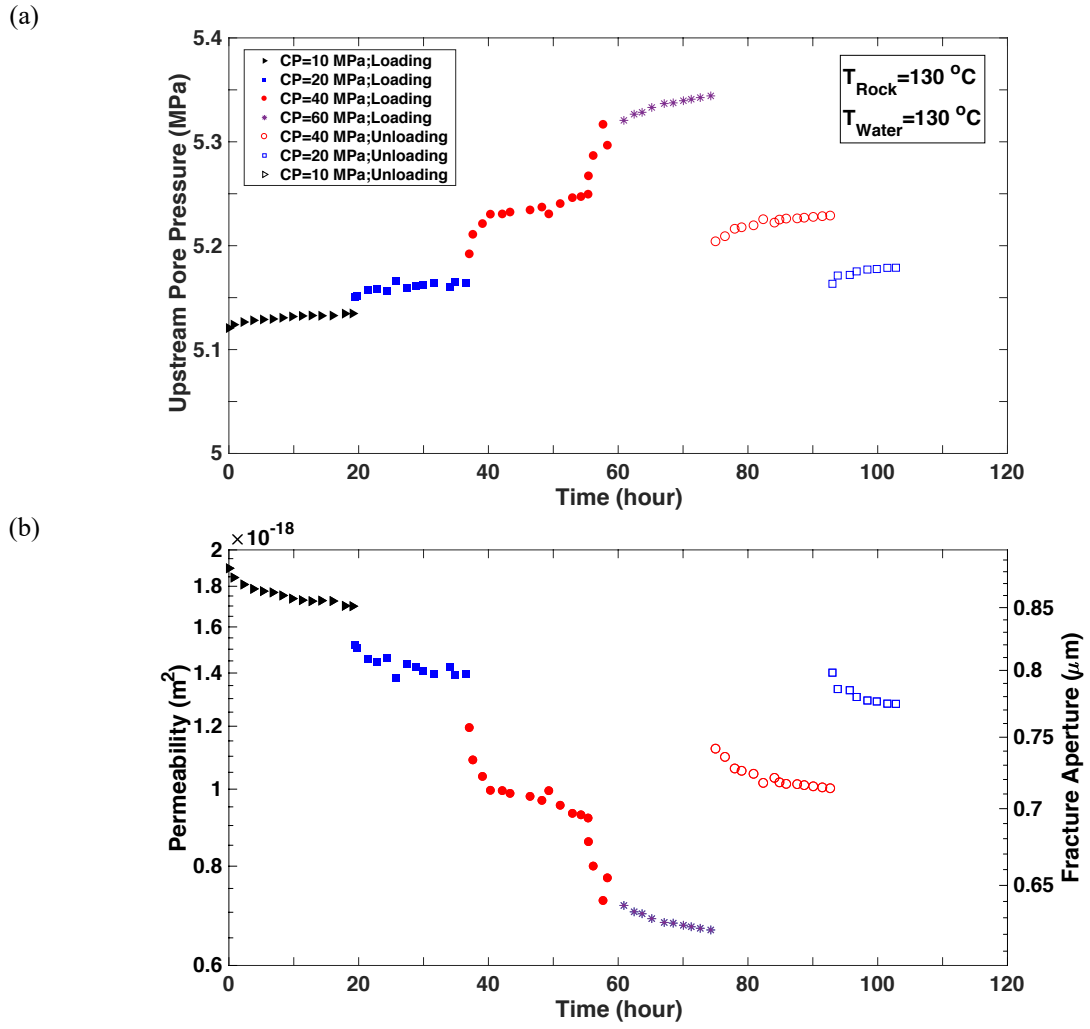


Figure 5-9. Evolution of (a) upstream pore pressure, and (b) fracture permeability and hydraulic aperture during the experiment #5

The evolution of upstream pore pressure for experiment #6 is shown in Figure 5.10a, exhibiting an increase rate of 9.8 Pa/s. Significantly higher upstream pore pressure increase is observed in this experiment compared to experiments #3 to #5. This could be attributed to the higher viscosity of injected fluid at lower temperatures and the effects of lower temperature of injected fluid on THMC processes. As evident in Figure 5.10b, during loading stages, the fracture permeability and hydraulic aperture changed from $1.2\times10^{-17}$ to $2.6\times10^{-19}$ $m^2$, and from 1.6 to 0.46 μm, respectively. During unloading stages, the fracture permeability and hydraulic aperture recover to $1.3\times10^{-18}$ $m^2$ and 0.77 μm, respectively. The lowest recovery of the hydraulic aperture and fracture permeability was observed during this experiment, which is an indication of the effect of temperature on pressure solution. Unfortunately, the effluent analysis could not be conducted in this experiment due to loss of the collected effluent sample during transition.

## 5.4 DISCUSSION

### 5.4.1 HYDRAULIC ANALYSIS

Pressure solution, mineral dissolution/precipitation/dissolution, and mechanical creep can contribute to the observed gradual decrease of the hydraulic aperture and fracture permeability in the reported experiments, as was also observed in other studies (e.g. Polak et al., 2003; Yasuhara et al., 2005; Caulk et al., 2016; Faoro et al., 2016; Vogler et al., 2016). The observed relative fluctuations in the upstream pore pressure during experiments, an indication of the sensitivity of hydraulic data to mechanical/chemical changes at the fracture surface, might be explained by the fact that some new flow paths are created (decrease in upstream pore pressure) or some of the existing flow channels are

blocked (increase in upstream pore pressure) as a result of pressure solution, mineral dissolution/precipitation, and mechanical creep.

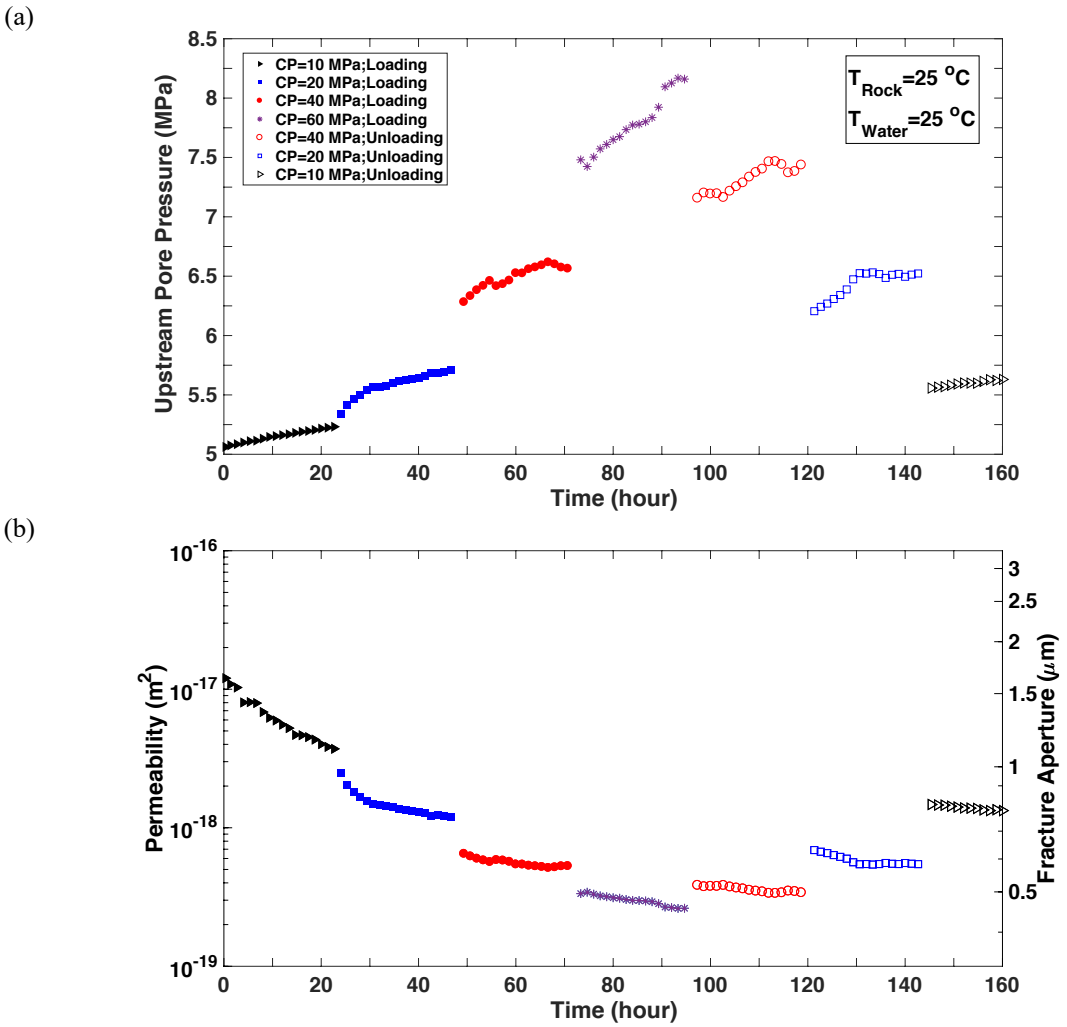


Figure 5-10. Evolution of (a) upstream pore pressure, and (b) fracture permeability and hydraulic aperture during the experiment #6

Higher rate of upstream pore pressure increase in experiment #2 (0.17 Pa/s) compared to experiment #1 (0.14 Pa/s), highlights the role of pressure solution phenomenon at higher effective stresses. The concentration of dissolved elements, as shown in Table 5.2, slightly decreases for experiment #2 compared to experiment #1, while the solubility of feldspars and quartz do not drastically change with confining effective

pressure (Johnson et al., 1998; Dove, 1999). Therefore, the difference in the rate of upstream pore pressure increase between experiments #1 and #2 might not cannot be attributed to the different mineral dissolution/precipitation rates. Higher effective stress leads to higher $R_c$ values, as more asperities come into contact (Taron and Elsworth, 2010). This again highlights dominance of pressure solution at higher effective stresses.

During loading stages of experiments #3 to #6, there is an abrupt increase in upstream pore pressure transitioning from one stage to the other; whereas during unloading, there is an abrupt decrease in upstream pore pressure during effective stress transition. While transitioning from one loading stage to the next, with the abrupt increase in the effective stress, more asperities come into contact at the fracture surface, (i.e. increasing R value) and subsequently enhances pressure solution phenomenon (see Figure 5.2), which in turn leads to potential closure of some of the existing flow paths and crushing of the propping asperities leads to a decrease in hydraulic aperture. Since the injection rate is set constant, the upstream pore pressure intensifier increases the upstream pore pressure to maintain the prescribed constant injection rate. During unloading, with abrupt decrease in the effective stress, the asperities in contact decreases, (i.e. decreasing $R_c$ value) due to stress relaxation, which in turn leads to the observed abrupt decrease in upstream pore pressure. In addition, movement of possible loose grains, created during the process of specimen fracturing, with fluid along the fracture can contribute to closure of fracture. Permeability changes at higher effective stresses are less compared to those at lower effective stresses. This might be explained by the fact that at higher CP levels, the initial permeability value is much less compared to that of lower CP levels and therefore, closure of some of the flow paths do not significantly alter the permeability. As the applied

effective stress increases from the first to the last loading stage, the permeability decreases. Given the initial low fracture permeability value, there is not much room available for further permeability reduction at higher effective stress values.

### 5.4.2 CHEMICAL ANALYSIS

As it can be seen from Table 5.2, the concentration of Ca, K, Na, and Si elements noticeably increased in the collected effluent samples compared to influent (i.e. deionized water). This might can be due to dissolution of feldspar (oligoclase, and microcline) and quartz minerals. The concentration of aluminum in the effluent samples was extremely low, which is consistent with observations of other studies (Caulk et al., 2016; Faoro et al., 2016).

Table 5.3 presents the estimated amounts of dissolved quartz and microcline feldspar minerals that have led to the composition of silicon in the effluent. Using effluent dissolved Si concentration, the range of fracture aperture change representing dissolved quartz or microcline feldspar for the entire duration of experiments #1 and #2 are presented in Table 5.3 and compared against that obtained from hydraulic data. The difference between the fracture aperture change from the two analyses, as presented in Table 5.4, highlights the role of other processes affecting the fracture aperture including mechanical creep, thermal contraction/dilation, and mineral precipitation leading to accumulation of dissolved minerals along the fracture and subsequent increase in pore pressure.

It should be acknowledged that the chemical equilibrium between the injected fluid and the $SiO_2$-rich minerals of the rock affects the spatial distribution of mineral dissolution/precipitation along the fracture. However, this was not the focus of this study. While for experiment #3, the regions of dissolution were identified using negative values on the 3D maps of the fracture surface, in the absence of micro-scale imaging, accurate identification of regions of precipitation could not be performed.

Table 5-3. The estimated amounts of dissolved quartz and microcline feldspar minerals ($x10^{-6}$ mol/kg) that led to the composition of the silicon in the effluent

| | Exp. #1 | Exp. #2 | Exp. #3 | Exp. #4 | Exp. #5 |
|---|---|---|---|---|---|
| Quartz | 8.191 | 3.344 | 6.792 | 0.654 | 11.732 |
| Microcline feldspar | 2.73 | 1.115 | 2.264 | 0.218 | 3.911 |

Table 5-4. Comparison of fracture aperture estimation using hydraulic and chemical analysis between experiments #1 and #2

| Experiment | Hydraulic aperture (μm) | Rc | Aperture from chemical analysis (μm) | Percentage difference between two analyses (%) |
|---|---|---|---|---|
| Exp. #1 | 0.162 | 0.8 | 0.086-0.139 | 31-57% |
| | | 0.4 | 0.173-0.278 | 7-72% |
| Exp. #2 | 0.348 | 0.8 | 0.033-0.053 | 88-93% |
| | | 0.4 | 0.066-0.105 | 70-81% |

### 5.4.3 THERMAL ANALYSIS

The change in the recorded upstream pore pressure values during experiment #5 exhibit much less increase (a rate of 0.82 Pa/s) compared to those for experiments #3 and #4. This, in part, could be attributed to the lower viscosity of water at an approximate temperature of 130 °C compared to 75 °C and 25 °C; and hence, it can flow easier through

the fracture. Moreover, contribution of thermal stresses is minimal in this experiment, which in part can contribute to the substantially-lower differential pore pressure generated during this experiment compared to experiments #3 and #4.

When the temperature of the injected fluid and the fractured specimen are not the same (e.g. experiments #3 and #4), as the fluid is circulated through the fractured specimen, its temperature increases, though the exact temperature of water-rock reactions is unknown in the experiment. It is important to note that the spatial distribution of mineral dissolution along the fracture is affected by the temperature difference between the injected fluid and the rock specimen ($\Delta T$). There is lower dissolution rate toward the beginning of the fracture and higher dissolution rate toward the end of the fracture, where the temperatures of the rock specimen and circulating fluid are closer (i.e. $\Delta T$ is minimized). As presented in Table 5.1, the temperature of the injected fluid at the inlet increases from 25°C in experiment #3, to 75°C in experiment #4, and to 130°C in experiment #5, while the temperature of host rock is the same in these three experiments. As it can be observed from Table 5.2, although not conclusive, the amount of dissolved minerals in experiment #5 is higher compared to experiments #3 and #4. This can be attributed to the effects of higher temperature of water-rock reactions in experiment #5 compared to that in experiments #3 and #4.

The beginning, the minimum, and the ending values of hydraulic aperture and fracture permeability in experiments #3 to #6 appear in Table 5.5, indicating that the values of hydraulic aperture and fracture permeability are not fully recoverable. Figures 5.11a and 5.11b compare the average fracture permeability and average hydraulic aperture for different loading and unloading stages recorded in experiments #3 to #6, respectively. The

general trend observed in Figure 5.11 indicates that with minimizing the thermal effects, (i.e. decrease of temperature difference between injected fluid and rock specimen) the rate of hydraulic aperture and fracture permeability reduction decreases. Lower hydraulic aperture and fracture permeability values are observed during the unloading stages compared to the loading stages, which was found to be present at both room and relatively high temperatures can be contributed to mineral dissolution/precipitation and pressure solution. In each experiment, when comparing loading and unloading stages with the same effective stress, since the effective stress and temperature remain the same, the contribution of mechanical creep and thermal dilation/contraction to the reduction of fracture permeability is expected to be the same. Therefore, pressure solution and mineral dissolution/precipitation can be identified as responsible mechanisms for the observed difference between hydraulic aperture and fracture permeability values during loading and unloading stages with the same effective stress and temperature.

Modeling the fracture permeability reduction as a function of time: (i) minimizes the role of the initial fracture permeability value on fracture response, and (ii) allows one to estimate how long a fracture can remain permeable in an EGS field with conditions similar to those of the experiment. Table 5.6 presents the initial permeability and permeability decay rate in the experiments performed in this study (except that of experiment #4) using an exponential decay function similar to the model presented in Morrow et al. (2001). As it can be seen from Table 5.6, in general, the estimated permeability loss rate during loading stages increases with an increase in effective stress (except in experiment #6). This can be attributed to the fact that the contributions of

mechanical aspect of pressure solution and mechanical creep to the permeability loss rate are enhanced at higher effective stresses.

(a)

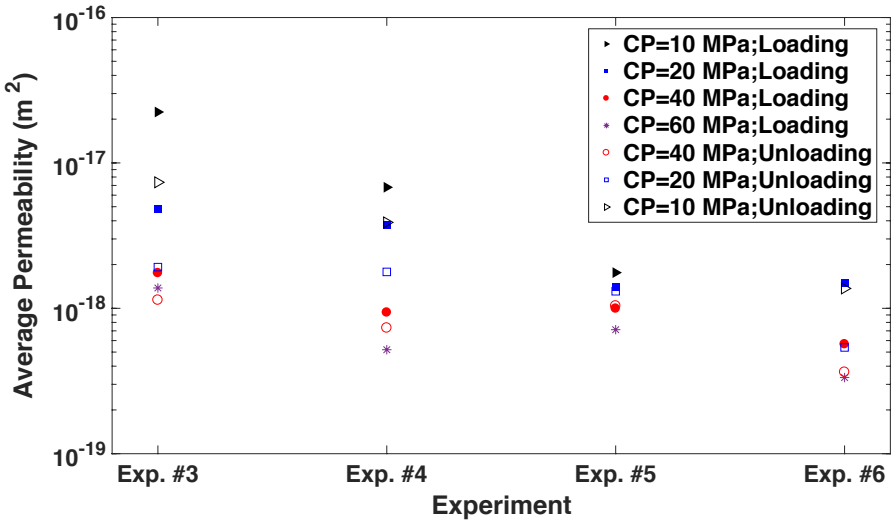


(b)

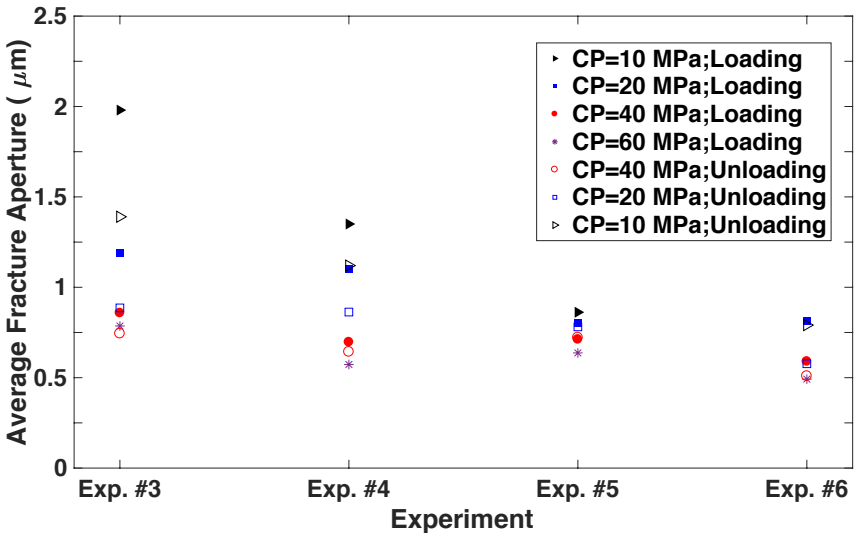


Figure 5-11. Comparison of (a) average permeability, and (b) average fracture aperture estimation during different stages of loading and unloading at different experiments

Although it was desired to compare the values of permeability decay rate from experiments in this study with those of Morrow et al. (2001), the major differences in experimental conditions (i.e. pressure and temperature) limited this comparison to only experiment #2. A decay rate of 0.0142 $day^{-1}$ is reported by Morrow et al. (2001) for an experiment conducted at conditions close to those of experiment #2, with estimated decay rate of 0.0456 $day^{-1}$. This difference in permeability decay rate reflects the fact that the experimental conditions, and the fracture roughness, shape, number, and hardness of asperities in fractured rock specimens are different in the two studies.

Table 5-5. Comparing hydraulic aperture and fracture permeability for experiments #3 to #6

| | | Beginning point (CP: 10 MPa, loading) | Minimum value (CP: 60 MPa) | Ending point (CP: 10 MPa, unloading) | Percentage of recovery |
|---|---|---|---|---|---|
| Permeability ($\times 10^{-18}$ $m^2$) | Exp. #3 | 38 | 0.97 | 7 | 18% |
| | Exp. #4 | 8.9 | 0.49 | 3.6 | 40% |
| | Exp. #5 | 1.9 | 0.67 | 1.3 | 68% |
| | Exp. #6 | 12 | 0.26 | 1.3 | 11% |
| Hydraulic aperture (μm) | Exp. #3 | 2.4 | 0.71 | 1.36 | 57% |
| | Exp. #4 | 1.5 | 0.56 | 1.2 | 80% |
| | Exp. #5 | 0.88 | 0.62 | 0.77 | 87.5% |
| | Exp. #6 | 1.6 | 0.46 | 0.77 | 48% |

Table 5-6. The initial permeability, in units of $\times 10^{-18}$ $m^2$, and permeability loss rate (r), in units of 1/hour, for different experiments

| | | | | | | | | |
|---|---|---|---|---|---|---|---|---|
| Exp. #1 | Initial Perm. | 3.275 | | | | | | |
| | r | 0.0015 | | | | | | |
| Exp. #2 | Initial Perm. | 5.851 | | | | | | |
| | r | 0.0019 | | | | | | |
| | | CP10L | CP20L | CP40L | CP60L | CP40U | CP20U | CP10U |
| Exp. #3 | Initial Perm. | 38.417 | 9.14 | 1.972 | 2.649 | 1.339 | 2.183 | 8.801 |

| | | | | | | | | |
|---|---|---|---|---|---|---|---|---|
| | r | 0.0206 | 0.0275 | N/A | 0.0311 | 0.0058 | 0.0056 | 0.0061 |
| Exp. #5 | Initial Perm. | 1.896 | 1.517 | 1.194 | 0.723 | 1.123 | 1.401 | N/A |
| | r | 0.003 | 0.0027 | 0.0073 | 0.0076 | 0.0035 | 0.0051 | N/A |
| Exp. #6 | Initial Perm. | 12.017 | 2.487 | 0.65 | 0.335 | 0.385 | 0.69 | 1.473 |
| | r | 0.0251 | 0.0178 | 0.0056 | 0.0048 | 0.0028 | 0.0063 | 0.003 |

CP: Confining Pressure; L: Loading Stage; U: Unloading Stage (e.g. CP10L: confining pressure of 10 MPa, loading stage)

### 5.4.4 COMPARISON

Comparing the results of experiment #6 with those of experiments #3 to #5 confirms that THMC processes are coupled and therefore excluding the effect of one of the contributing processes can alter the effects of other processes on fracture response. For example, both experiments #5 and #6 were designed such that the effects of thermal stresses were minimized, however, minimal pressure solution effects on fracture behavior was observed in experiment #5 (i.e. the hydraulic aperture was mostly recovered, see Tables 5.4 and 5.5) and maximum pressure solution effects was observed in experiment #6 (i.e. the minimum recovery of the hydraulic aperture, see Tables 5.4 and 5.5).

As presented in Table 5.2, the concentration of dissolved elements in the effluent samples, mainly Si, Ca, K, Al, and Mg, increased for experiments #4 and #5 compared to experiments #1 to #3. This could be attributed to the elevated temperatures for injected water, which increases the dissolution rate of associated minerals (Johnson et al., 1998; Dove, 1999). The pore pressure measurements and chemical analysis of dissolved elements in this study are consistent with similar experimental conditions/studies reported by Savage et al. (1992), Morrow et al. (2001), Caulk et al. (2016), and Faoro et al. (2016). The comparison between experiment #2 of this study with the experimental studies reported by

Morrow et al. (2001) and Caulk et al. (2016) are presented in Tables 5.5 and 5.7, showing a consistent reduction of fracture permeability. In addition, the comparison between the results of experiment #3 of this study with experimental results (with close experimental conditions) reported by Faoro et al. (2016) are presented in Tables 5.5 and 5.7. Faoro et al. (2016) found that there is a minimal pressure solution effect when either the temperature or the effective stress is at low levels, while, at both high temperature and high effective stress the observed permeability is not fully recoverable. In this study, we found that even at low temperatures there are some effects of pressure solution as observed in experiment #6. This discrepancy between the two studies can be attributed to the differences in rock specimens, and topography of fracture surface, initial permeability value, among others. On the other hand, both studies show substantial pressure solution effects at relatively high temperatures and high effective stresses.

Table 5-7. Comparison of experiment #2 with other studies

| | Constant effective stress | | | Varying effective stress | |
|---|---|---|---|---|---|
| | Exp. #2 | Morrow et al. (2001) | Caulk et al. (2016) | Exp. #3 | Faoro et al. (2016) |
| Granite type | Barre | Westerly | Barre | Barre | Westerly |
| Temperature of injected fluid (°C) | 25 | 150 | 120 | 25 | 25 |
| Temperature of the rock (°C) | 130 | 150 | 120 | 130 | 25 |
| Effective stress (MPa) | 36.6 | 50 | 35 | 5-55 (loading)<br>55-5 (unloading) | 1.35-55 (loading)<br>55-4.8 (unloading) |
| Duration (days) | 10 | 40 | 40 | 7 | 10 |

| | | | | | |
|---|---|---|---|---|---|
| Starting permeability ($\times 10^{-18}$ $m^2$) | 5.9 | 3.87 | 0.336 | 38 | 1650 |
| Minimum permeability ($\times 10^{-18}$ $m^2$) | N/A | N/A | N/A | 0.97 | 1.08 |
| Ending permeability ($\times 10^{-18}$ $m^2$) | 2.4 | 0.211 | 0.133 | 7 | 1120 |
| Percentage decrease | 59.3 | 94.5 | 60.4 | N/A | N/A |
| Irrecoverable percentage | N/A | N/A | N/A | 82% | 32% |

### 5.4.5 APPLICATION TO EGS

Mineral dissolution/precipitation can cause significant problems in EGS reservoirs including (i) reduction of fracture permeability, which leads to production decline (e.g. Morrow et al., 2001; Vogler et al., 2016), (ii) scaling problem in wells (e.g. Xu et al., 2004; Montalvo et al., 2005), and (iii) potential damage to the power plant equipment (Xu et al., 2004; Kumar and Ghassemi, 2005). The experimental results in this study indicated a continuous reduction in the fracture permeability, in part due to mineral precipitation on the fracture surface. Therefore, quantification of the dissolution/precipitation rate in EGS design/operation is very important as it has significant implications for the sustainability of an EGS reservoir.

The experimental results in this study suggest that the amount of mineral dissolution varies with temperature of the injected fluid. In EGS field operation, one has to consider the effects of temperature of injected geothermal fluid on mineral dissolution/precipitation processes and its impact on the evolution of fracture permeability and consequently the reservoir production. In addition, higher initial temperature

difference between the bedrock and the injected geothermal fluid leads to higher thermal stresses, and consequently more pronounced change in the state of stress within the reservoir. This may increase the possibility of an induced seismic event as also reported by other studies (e.g. Ghassemi and Zhou, 2011; Jansen and Miller, 2017).

Fracture roughness, shape, number and hardness of propping asperities affect fracture response to increase in effective stress (Pyrak-Nolte and Morris, 2000; Farough et al., 2016). Crushing of the asperities in-contact accompanied by mineral dissolution due to high localized stresses is a component of pressure solution. The experimental results in this study suggest that the fracture permeability decreases with an increase in effective stress, which in part is attributed to pressure solution. This has a direct implication in EGS field operations as the crushing of asperities, which prop open the natural fractures, at higher effective stresses can lead to significant reduction in fracture permeability, and consequently production decline.

The effects of thermal processes on fracture response occur at shorter time-scales, while, those of chemical processes occur at longer time-scales (e.g. Ghassemi, 2012; Izadi and Elsworth, 2015). Although the performed experiments in this study were relatively-short, useful information can be inferred about the effects of thermal processes on fracture response at earlier stages of the experiments, while, the changes in fracture permeability at later stages can be attributed to chemical processes. The temperature difference between the rock and the injected fluid ($\Delta T$) can affect spatial distribution of mineral dissolution/precipitation along the fracture surface, though not observed explicitly in this study. In EGS field operation, dissolution occurs mostly near the injection well, where $\Delta T$

is maximum; while, precipitation occurs mostly near the production well, where ΔT is minimum (e.g. Ghassemi and Kumar, 2007) and the circulating water has higher concentration of different minerals compared to the injected water.

## 5.5 CONCLUSIONS

In this study, the effects of coupled THMC processes on hydraulic aperture and fracture permeability (with a focus on pressure solution) were studied by conducting a series of flow-through experiments on artificially-fractured Barre granite specimens at different pressures and temperatures. Mechanical, chemical, and thermal processes were identified as potential mechanisms that contribute to different rates of fracture closure and permeability change observed in the suite of experiments.

The estimated fracture permeability and hydraulic aperture gradually decreased over time for relatively-longer term experiments under constant effective stress. In addition, the fracture permeability decreased with increase of effective stresses, while the mineral dissolution/precipitation occurred with a slower rate as shown by ICP-OES analysis, due to less potential for free-face dissolution at higher effective stress. The observed relative changes in the upstream pore pressure during experiments was an indication of the sensitivity of hydraulic data to mechanical/chemical changes at the fracture surface including pressure solution, mineral dissolution/precipitation, and mechanical creep.

The evolution of hydraulic aperture and fracture permeability were not fully recoverable under loading/unloading cycles, pointing to the importance of pressure

solution. At higher temperatures, the fracture hydraulic aperture and fracture permeability recovered the most after unloading in experiments conducted at higher temperatures. Injection of geothermal fluid into the hot bedrock triggers mineral dissolution/precipitation processes. However, the contribution of mineral dissolution/precipitation was not found to be substantial at low temperatures of injected fluid. Increasing the temperature of the injected water led to increased concentration of dissolved elements obtained in the effluents, an indication of enhanced mineral dissolution/precipitation rate.

Chemical analysis and the performed image analysis pointed to the occurrence of dissolution process. The experimental results were found to be consistent and in-line with studies with similar experimental conditions. The findings of this study highlight the role of pressure solution on closure of fractures subjected to hydrothermal conditions, which emphasizes the importance of pressure solution in EGS reservoirs, where fracture closure can lead to substantial production decline.

# CHAPTER 6

# Flow-induced alterations of seismic signatures and fracture aperture under constant state-of-stress in a single-fractured rock

## ABSTRACT

Fluid-fracture surface interactions, caused by different mechanisms, is one of the underlying reasons for permeability reduction over long periods of time in different geo-resources, such as deep geothermal systems and shale gas/oil reservoirs. The sensitivity of the ultrasonic signatures (e.g. frequency content, velocity, amplitude, and attenuation) to the changes in fracture aperture caused by fluid-fracture surface interactions can be considered as a probe for flow-induced fracture aperture evolution. Flow-through tests on an artificially-fractured phyllite specimen from a geothermal reservoir along with the concurrent measurements of ultrasonic signatures of P- and cross-polarized S-waves demonstrated the sensitivity of ultrasonic signatures to the evolution of fracture aperture/permeability under constant state-of-stress (i.e. constant pore and confining pressures). Particularly, the closure of fracture and decrease of permeability led to increase of P-wave velocity, decrease of P-wave attenuation, and increase of S-waves amplitude. In addition, time evolution of the time-frequency maps of the transmitted ultrasonic waves revealed that the partitioning of the frequency content slightly changes, as the fracture aperture/permeability is altered. Specifically, alterations in hydraulic aperture is reflected in the changes of time-frequency partitioning, while, under constant hydraulic aperture, the time-frequency partitioning is unaltered.

## 6.1 INTRODUCTION

Characterizing the aperture size and distribution during operation of fractured reservoirs is a challenging task, and often it is necessary to study the evolution of fracture permeability as it significantly influences reservoir production in geothermal, shale gas, and tight oil reservoirs. The geometry of fracture surface area substantially affects the fracture response and therefore production of fractured reservoirs through different mechanisms/phenomena such as pressure solution (e.g. Kamali-Asl et al., 2018a), mineral dissolution/precipitation (e.g. Faoro et al., 2016), and mechanical creep (e.g. Sone and Zoback, 2013b). Fracture surface roughness and tortuosity of asperities of the rock joints/fractures control the mechanical deformation, while, hydraulic properties (i.e. flow properties) are controlled by aperture size (Cook, 1992; Pyrak-Nolte and Morris, 2000; Acosta-Colon et al., 2009). Important to note, aperture distribution along a fracture, amount and spatial distribution of the asperities, and contact area of the fracture can influence both fracture-specific stiffness and flow through the fracture (Pyrak-Nolte and Morris, 2000). More specifically, uneven distribution of aperture along a fracture can result in larger aperture along the major flow path and/or in critical necks, which in turn leads to higher permeability (e.g. Pyrak-Nolte and Nolte, 2016). Larger aperture, and therefore larger volume of void space, creates more compliant fractures with the same contact area (e.g. Pyrak-Nolte and Nolte, 2016). Since reservoir production is affected by fracture aperture/permeability, it is important to monitor the long-term evolution of fracture aperture over the reservoir's operation period.

Seismic waves can be considered as high-resolution probes to assess the alteration of fractures/joints in fractured formations, as they are sensitive to different elements of geological formations (e.g. overburden and pore pressures, depth of interest, and saturation level) (e.g. Wang, 2001; Knight et al., 2010; Müller et al., 2010; Pyrak-Nolte et al., 2015; Saltiel et al., 2017). Compressional (P-type) and shear (S-type) waves are usually implemented to infer information about the internal structure of intact rocks in different formations such as shale and geothermal reservoirs (e.g. Sayers, 2013; Sone and Zoback, 2013a; Lopes et al., 2014; Kamali-Asl et al., 2018b-d). Propagation of seismic waves in fractured formations gives rise to frequency-dependent elastic interface waves, which exhibit a velocity ranging from shear-wave (upper limit) to Rayleigh-wave (lower limit) (e.g. Pyrak-Nolte et al., 1990; Pyrak-Nolte and Morris, 2000; Batzle et al., 2006). Mechanical deformations at the fracture surface and alteration of hydraulic properties of the fractured formation can significantly affect the seismic response of fractured formations (e.g. Cook, 1992; Mukerji and Mavko, 1994; Mavko, 2009). In addition, a fracture can be weakened/strengthened by the geochemical processes at the fracture surface, and hence, affects the response to shear/slip as well as long-term reservoir production (e.g. Pyrak-Nolte et al., 2015). Therefore, the evolution of the seismic signatures (namely, frequency content, velocity, amplitude, and attenuation) can be used as a proxy to track the evolution of fracture aperture/permeability.

In this study, flow-through experiments were performed to investigate the sensitivity of the ultrasonic signatures to the changes in the aperture size resulted from different physio-chemical processes at fracture surface. In a companion paper, the authors

have reported the results from a suite of flow-through experiments under varying state-of-stress (i.e. varying confining and/or pore pressures). Here, an artificially-fractured phyllite specimen was used to conduct the flow-through-fracture tests with concurrent measurements of the ultrasonic P- and cross-polarized S-waves, along with radial strains. The transmitted ultrasonic P- and cross-polarized S-waves were then analyzed to infer changes in the fracture aperture using velocities, amplitudes, attenuations, and frequency content of these waves. Section 6.2 provides the experimental methodology, section 6.3 provides the results and discussions. Conclusions are provided in section 6.4. Appendix E provides a brief introduction to continuous wavelet transform. Appendix F provides explanations on estimation of fracture aperture/permeability, Appendix G provides experimental procedure for flow-through tests, materials used in this chapter are provided in Appendix H, and propagation of seismic waves in flow-through experiments is provided in Appendix I.

## 6.2 EXPERIMENTAL METHODLOGY

### 6.2.1 ATTACHMENTS OF STRAIN GAUGES AND DIRECTION OF SEISMIC WAVES PROPAGATION

The two halves of the saturated fractured specimen were mated together, and a copper jacket was wrapped around the fractured specimen to facilitate attachment of the strain gauges. Then the specimen was inserted inside a Vitton jacket, with two open cuts at 180°-apart to expose the copper jacket for attachment of the strain gauges. As shown in Figure 6.1b, the strain gauges were attached on each half of the specimen. The interface between the Vitton and copper jacket was sealed using a high- pressure/temperature-

resistant epoxy. The fracture plane of the specimen was oriented at ~45° to the plane of propagation of $S_1$-waves (See Figure A9.1c). Finally, the two ends of the specimen were wire-tightened to the top and bottom ultrasonic velocity core-holders (Figure A6.1b) and the specimen was placed inside the test vessel (Figure A6.1a).

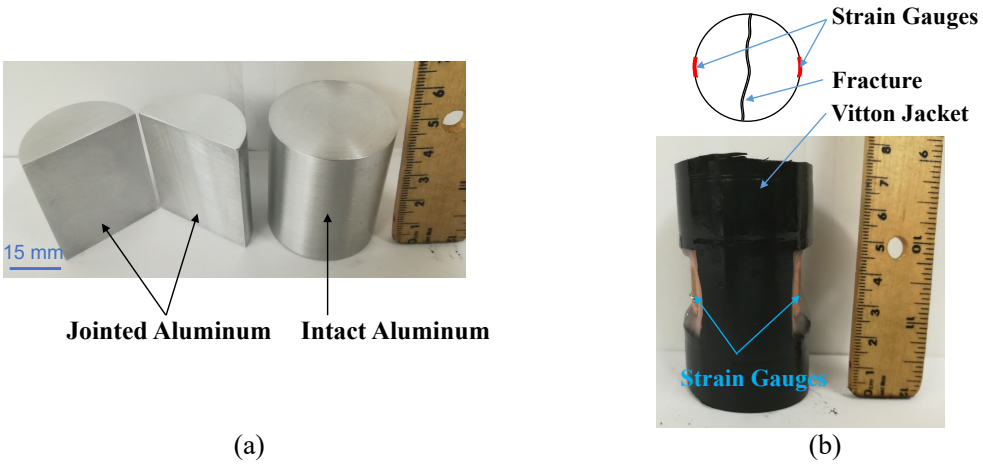


Figure 6-1. Photos of (a) intact and jointed aluminum specimens, and (b) the copper- and Vitton-jacketed specimen with the two rectangular windows (180°-apart) for attachment of strain gauges.

Concurrent with the flow of deionized water through the fracture, seismic waves of the fractured specimen were collected by transmitting the ultrasonic P-wave and cross-polarized S-waves from the bottom (i.e. upstream) core-holder and receiving the signals using top (i.e. downstream) core-holder. As illustrated in Figure A9.1a, the transducers for P, $S_1$, and $S_2$ waves are stacked together and embedded in the hollow-cylindrical-shaped core-holders. Figure A9.1c shows the cross-section of the fractured phyllite specimen and direction of propagation of P- and cross-polarized S-waves. As shown in Figure A9.1c, the fracture plane is oriented ~45° to the plane of propagation of $S_1$-wave.

### 6.2.2 EXPERIMENTAL PROGRAM

Previous studies on flow-through experiments on artificially-fractured granite specimens under reservoir conditions, few days long, showed the gradual decrease in permeability/fracture aperture (e.g. Caulk et al., 2016; Kamali-Asl et al., 2018a). Conducting flow-through tests in PCT closely simulates the flow in fractured reservoir conditions, in that, the flow rate (reflecting permeability) usually declines and hence, the production drops over time. However, it is usually easier to perform DCTs in laboratory experiments. In order to (i) investigate repeatability of the results, and (ii) broaden the potential future experimental studies (e.g. elevated temperatures and different depths of interest), a DCT was also performed. The differential pore pressure in PCT and injection rate in DCT were set such that the injected fluid would have enough residence time to react with the surface and thus, the evolutions of permeability/fracture aperture and ultrasonic signatures can be captured.

In this study, both types of flow-through tests (i.e. PCT and DCT) were performed on a fractured phyllite specimen at room temperature, under constant CP, DS, and pore pressures of 24, 6, and 11 MPa, respectively. These stresses were chosen to represent the in-situ stress conditions, where the phyllite specimen was extracted, in the triaxial test set-up. The differential pore pressure in PCT was maintained constant at 0.6 MPa, and the injection rate in DCT was prescribed at $3.5\times10^{-2}$ ml/sec (with a capillary number of $2.36\times10^{-10}$), while maintaining the downstream pore pressure at 11 MPa during both tests. The evolutions of radial strain, outflow rate (in PCT), and differential pore pressure (in DCT) were recorded every second during the test, while ultrasonic signatures were

collected every 30 min. For clarity in the presentation of results, all data were binned to every 4 hours. The concurrent measurements of the ultrasonic signatures along with the two 180°-apart strain gauges were used to investigate the alterations of permeability/fracture aperture caused by fluid-fracture surface interactions.

Before proceeding to the flow-tests, it was important to ensure that variations in the ultrasonic waves are caused by presence of fracture, and not an artifact of the transducers' error. The variations in the received ultrasonic waves, collected at stress levels similar to those planned for flow-tests on fractured rock specimen, were compared between intact and jointed (two halves with saw-cut, smooth surface area) aluminum specimens (see Figure 1(b)) with identical dimensions as fractured phyllite specimen. It was confirmed that the presence of joint/fracture alters the ultrasonic signatures (i.e. frequency content, velocity, amplitude). It should be noted that both tests were performed at room temperature. The work is still in progress to better quantify the sensitivity of the ultrasonic waves to the alterations of fracture aperture at close-to-field temperatures, particularly for geothermal applications.

## 6.3 RESULTS AND DISCUSSIONS

Section 6.3.1 summarizes the evolutions of ultrasonic velocities, amplitudes, attenuations, time-frequency maps and radial strains in PCT, and Section 6.3.2 summarizes those of DCT.

In order to verify that presence of fracture leads to alterations of ultrasonic waves, the P-, $S_1$-, and $S_2$-waves were measured for an intact phyllite specimen (extracted from

the same core, with the identical dimensions as fractured rock) under CP of 30 MPa. The waveforms of the ultrasonic waves were compared with those of fractured specimen under CP and pore pressures of 30 and 11 MPa. Figure 6.2 shows waveforms for all three ultrasonic waves for intact and fractured specimens, indicating changes in velocities, amplitudes, frequency contents due to presence of fracture and fluid flow. The P-wave arrival time for fractured specimen is less than that of intact specimen, and the amplitude of S-waves become meaningful for fractured specimen compared to very low amplitudes for intact specimen. In addition, the frequency content of the P-wave signals for intact and fractured specimens are slightly different after t=25 μSec.

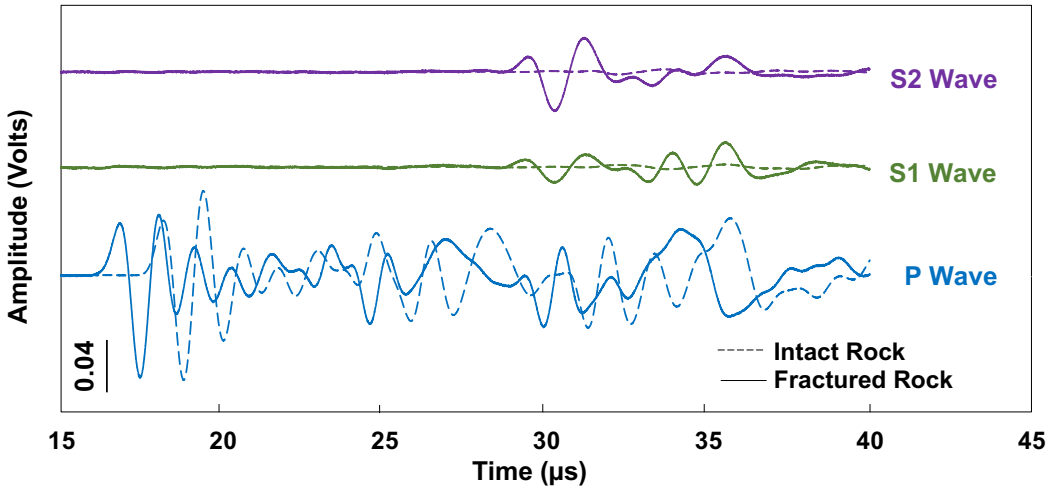


Figure 6-2. Comparison between received ultrasonic signals in fractured and intact water-saturated rock specimens at CP=30 MPa

### 6.3.1 PRESSURE-CONTROLLED TEST (PCT)

#### 6.3.1.1 RADIAL STRAINS

Figure 6.3 shows the evolutions of the average radial strains, flow rate, and the corresponding permeability/fracture aperture (estimated using Darcy's Law/Modified

Cubic Law based on flow rate) during PCT under CP, DS, and pore pressures of 24, 6, and 11 MPa, respectively. The apparent permeabilities of ~$10^{-19}$ $m^2$ suggest that the two halves of the fracture are very well-mated, and they are close to full-contact. It can be observed that during the first 60 hours of the test, the radial strain is increasing as the flow rate is decreasing. Different hydro-chemo-mechanical processes (e.g. stress corrosion, pressure solution, and mineral dissolution/precipitation) triggered by fluid-fracture surface interactions under specified stress conditions lead to decrease in fracture aperture and flow rate (e.g. Caulk et al., 2016; Faoro et al., 2016; Kamali-Asl et al., 2018a), as the two halves of the fractured specimen come together, and therefore, the radial strain increases. It should be, however, noted that between t=64 to 96 hr, the evolution of radial strain cannot be explained based on the evolution of flow rate, which might be due to an experimental error, where, the upstream pore pressure increased for a few hours, leading to a sudden increase in the flow rate at t=68 hr. While, the radial strain data showed a gradual decrease over time, rather than a sudden decrease at t=68 hr. After t=100 hr, radial strain can capture response of fracture, indicating an increasing overall trend in the radial strain.

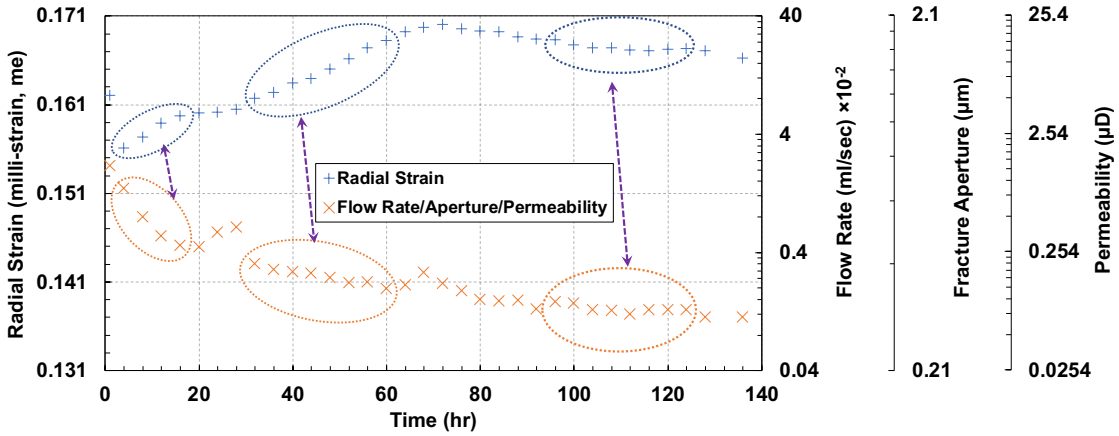


Figure 6-3. Time evolutions of the average radial strain, flow rate and fracture aperture/permeability in PCT

#### 6.3.1.2 ULTRASONIC VELOCITIES, AMPLITUDES, AND ATTENUATIONS

Figure 6.4 shows the evolutions of the measured ultrasonic velocities along with flow rate and the corresponding fracture aperture/permeability during PCT. As stated by Gu (1994), propagation of P-waves parallel to the fracture plane leads to the generation of a compressional-type interface wave by the shear particle displacement. Roy and Pyrak-Nolte (1997) and Nolte et al. (2000) have reported changes in the characteristics of the arrival P-wave, propagating along the fracture plane, as the state of the fracture is altered. In addition, creation of secondary micro-cracks, caused by fracture creation in the Brazilian test, can in part explain the sensitivity of the P-wave velocities. A correspondence between the flow rate/aperture and P-wave velocities (with blue and orange ovals for P-wave velocity and flow rate, respectively) can be observed in Figure 6.4a, where they follow each other with a reverse trend during the test. When the flow rate increases, due to fluid-fracture surface interactions, the P-wave velocity decreases, and vice versa. However, there is a lag between the instances of increase/decrease of flow rate/aperture/permeability compared to decrease/increase of P-wave velocity. That is, when physical changes/processes occur at the fracture surface, P-wave velocity reacts immediately, while, the flow rate/aperture/permeability react at a later time. For cases where the variation in flow rate/aperture is steeper, the change in P-wave velocity is more significant, indicating the sensitivity of P-wave velocity to alterations of fracture surface geometry. On the other hand, rock shifting (due to crushing of contacting asperities), channelized flow, and creation/closure of flow channels can have different impact on flow rate and P-wave velocity, and in part might explain some of the observed inconsistencies/lags between the trends of flow rate and those of P-wave velocity. Figure 6.4b shows the time evolutions of

$S_1$- and $S_2$-waves velocities and flow rate/aperture/permeability, with no identified viable trend for $S_1$- and $S_2$-waves velocities. It appears that alterations of flow rate/aperture/permeability cannot be captured using S-waves velocities. The propagation of the S-wave in the direction parallel to fracture has been found to be insensitive to the state of the fracture, however, the characteristics of S-wave in the direction perpendicular to the fracture plane is affected by the state of the fracture (e.g. Roy and Pyrak-Nolte, 1995; Nolte et al., 2000). In this study, the fracture plane was placed 45° with respect to the propagation direction of each of the two cross-polarized S-waves, and therefore, both S-waves have parallel and perpendicular components to the fracture plane. This can explain observed weak correspondence between differential pore pressure and S-waves velocities.

The maximum amplitude of the collected P-, $S_1$-, and $S_2$-waves at each time instance were analyzed and normalized with respect to their initial value. Figure 6.5 shows the time evolutions of the normalized maximum amplitude of the P-, $S_1$-, and $S_2$-waves, flow rate, and the corresponding fracture aperture/permeability. As it can be seen in Figure 6.5, the normalized maximum amplitude of the P-wave is not sensitive to the changes in flow rate/aperture/permeability, in contrast to the normalized maximum amplitudes of $S_1$- and $S_2$-waves, where an increasing trend can be observed in Figure 6.5. This could be potentially attributed to the fact that the impedance (density times velocity) of water compared to that of the rock matrix is much lower and therefore, the shear-wise propagation of shear waves is affected by the ratio of the impedance of the two media, however, longitudinal-wise propagation of compressional wave is not affected by this ratio.

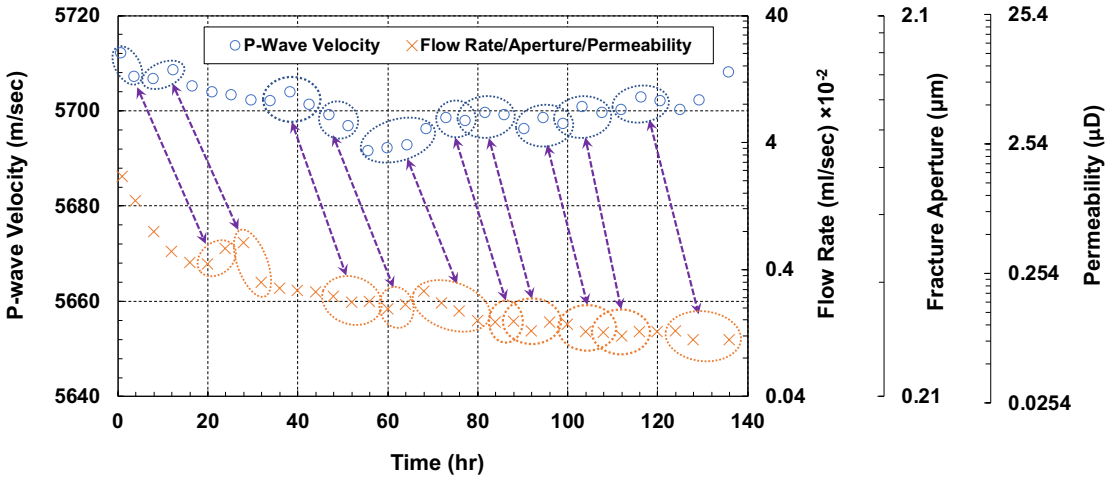


(a)

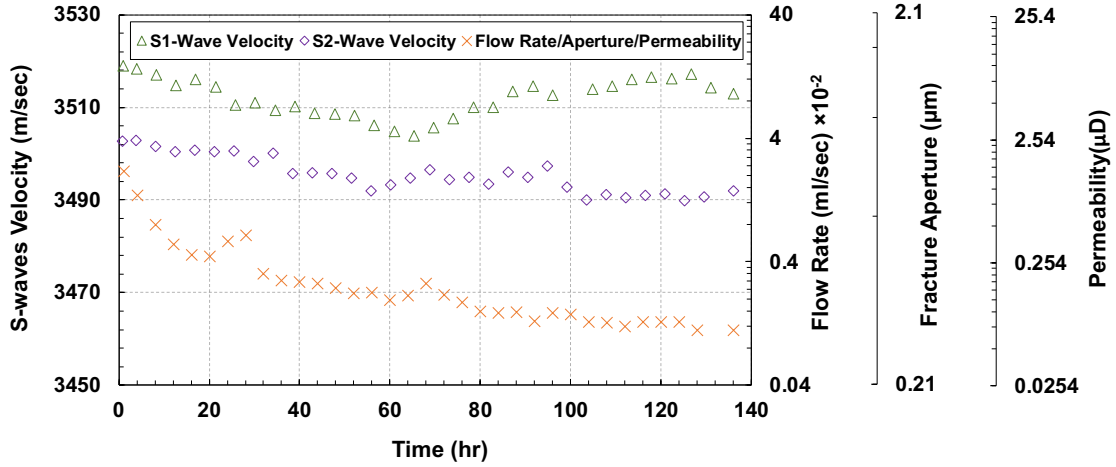


(b)

Figure 6-4. Time evolutions of the ultrasonic velocities (a) P-wave, (b) S-waves with flow rate/aperture/permeability in PCT.

The attenuation analysis for the fractured specimen was performed following the procedure outlined in Pyrak-Nolte et al. (1990), as expressed in Eq. (6.1):

$$Q = -\pi f x/[cln(A/A_l)] \tag{6.1}$$

where, Q is the ultrasonic quality factor, f is the central frequency of the transmitted ultrasonic wave, x is the length of the specimen (i.e. fractured rock), c is the phase velocity

of the ultrasonic wave, A and Al are the maximum spectral amplitudes of the fractured rock and aluminum specimen (with identical dimensions as fractured rock specimen), respectively. For each recorded ultrasonic wave, the Fourier transform was performed on the entire time-series to estimate the maximum spectral amplitude.

Figure 6.6a shows the time evolutions of the attenuation factor (1/Q) for P-wave, flow rate, and the corresponding fracture aperture/permeability in PCT, indicating slightly decreasing trend. This observation implies that P-wave attenuation could also serve as a proxy for changes in fracture aperture over time. However, the variations of $S_1$- and $S_2$-waves attenuations against flow rate/aperture/permeability over time, as shown in Figure 6.6b, do not exhibit an identifiable trend, which indicate that the S-waves attenuation is not sensitive to the changes in fracture aperture.

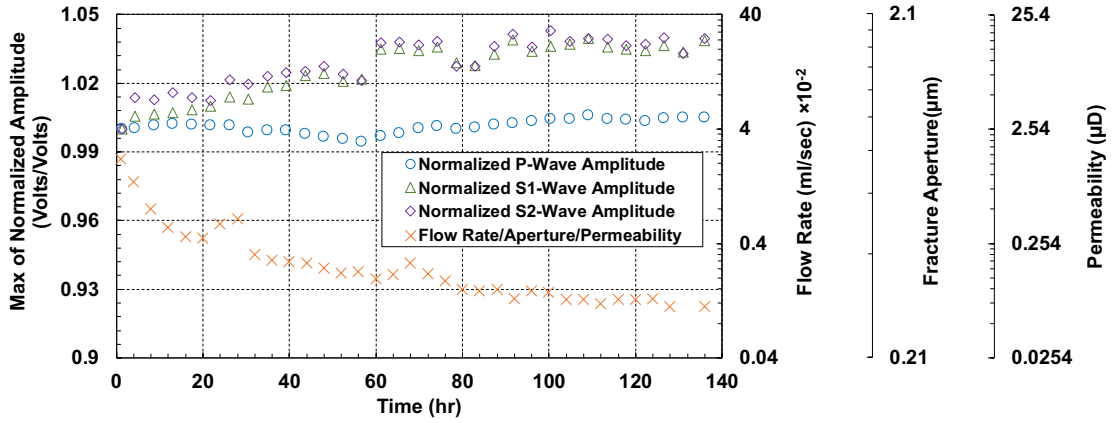


Figure 6-5. Time evolution of the normalized maximum ultrasonic waves amplitudes with flow rate/aperture/permeability in PCT

#### 6.3.1.3 TIME-FREQUENCY ANALYSIS

***P-wave signals:*** Time-frequency analysis of the P-, $S_1$-, and $S_2$-waves can reveal information about their time-dependent frequency content. A Continuous Wavelet Transform (CWT), with Morlet Mother Wavelet, was employed to generate time-frequency maps. It should be noted that CWT is a more robust approach compared to short-time-Fourier-transform, given its adaptive time-frequency resolution (e.g. Dubechies, 1990; Farzampour et al., 2018). Figures 6.7a-d show the time-frequency maps of the transmitted P-wave signals related to the received signals at t =25, 50, 75, and 100 hr. It should be noted that the time-frequency map at t=25 hr was used as a baseline, while, the time evolution of frequency content (during the test) can be inferred by comparing the time-frequency maps at different times. The time-frequency map for P-wave signal recorded at t=25 hr is provided in Figure 6.7a. It can be seen that the energy of the higher frequency range (i.e. ~800 kHz) is higher than that of the lower frequency range (i.e. ~200 kHz). This observation could be, in part, attributed to the fact that the fracture aperture is relatively-low and therefore, the contribution of the rock matrix in transmitting the P-wave is more significant than the fractured volume, as confirmed by comparing the time-frequency map of the transmitted P-wave through intact and fractured rocks. In addition, the majority of the higher frequency portion of the transmitted P-wave arrives at t≈17 μSec, while, a small portion of the higher frequency range arrives at later times (at t≈27 and 32 μSec).

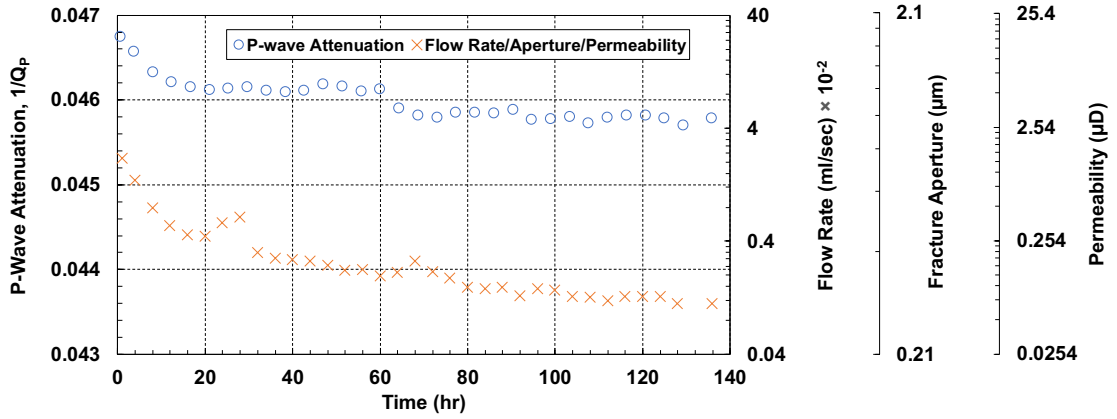


(a)

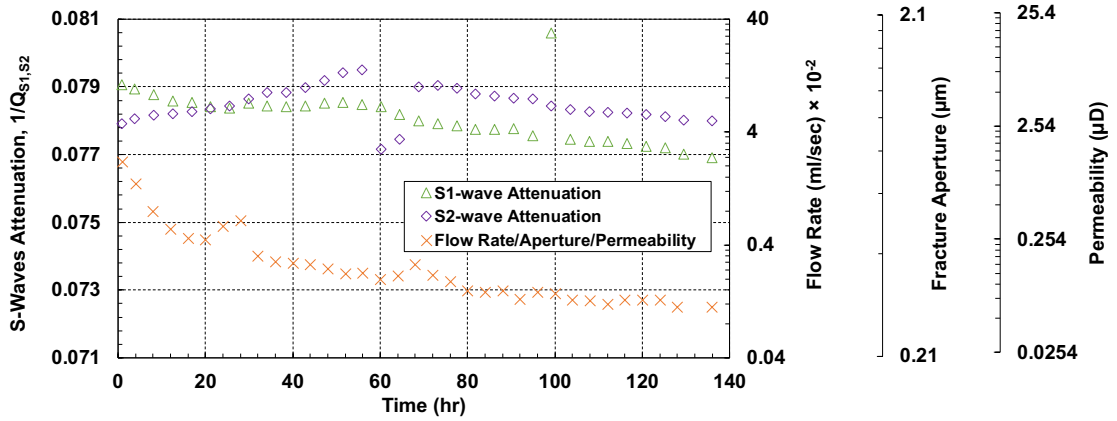


(b)

Figure 6-6. The evolutions of ultrasonic attenuation for P-, $S_1$-, and $S_2$-waves in PCT

In order to investigate the effects of fracture aperture alterations on the evolution of time-frequency content, the transmitted P-wave signal at t=25 hr was subtracted from those at t=50, 75, and 100 hr. Then, the resultant signals were used as the input for wavelet transform to generate the time-frequency maps and illustrated in Figures 6.7b-d, implying that the energy of the P-wave decreases over time. This indicates that the change in energy (i.e. amplitude) of P-wave signal at an earlier time instance (e.g. t=50 hr) compared to those a later time instance (e.g. t=100 hr) is more significant. On the other hand, as the test

proceeds, the frequency partitioning of the resultant P-wave signals is altered. In particular, the energy concentrated in the higher frequency range decreases, and eventually, the lower frequency range has higher concentration of energy compared to the higher frequency range. This indicates that the change in frequency partitioning of P-wave signal is more significant at a later time instance (e.g. t=100 hr) compared to an earlier time instance (e.g. t=50 hr).

***S-waves signals:*** Following the same procedure for P-waves, time-frequency maps for the $S_1$- and $S_2$-waves were developed and shown in Figures 6.7e-h and 6.7i-l. Figure 6.7(e) indicates that the higher amount of energy is stored in the lower frequency band (centered ~ 250 kHz) compared to the higher frequency band (centered ~ 650 kHz). Comparing the time-frequency map for $S_1$-wave with that of P-wave (see Figure 6.7a), it can be observed that the difference between the lower and higher frequency bands is much smaller for $S_1$-wave (~ 400 kHz) compared to that of P-wave (~600 kHz), an inherent characteristic of S-waves.

A comparison between the time-frequency map of $S_1$-wave with that of $S_2$-wave at t=25 hr (i.e. comparing Figure 6.7e with 6.7i) indicates that the higher and lower frequency bands are centered around the same frequency, which are ~650 and ~250 kHz, respectively. This observation indicates that both $S_1$- and $S_2$-waves have the same dominant frequencies. However, the ratio of the peak spectral amplitude in the higher frequency band to that of lower frequency band is lower for $S_2$-wave compared to $S_1$-wave. In addition, the spectral amplitudes for $S_2$-wave (see Figure 6.7i) is less than that of $S_1$-wave (see Figure 6.7e). These differences between the time-frequency maps of $S_1$- and $S_2$-waves might have been

caused by various anisotropic behaviors including (i) material anisotropy of the intact core retrieved from Blue Mountain geothermal reservoir, (ii) anisotropic distribution of asperities in different directions, and (iii) anisotropic flow paths (i.e. channelized flow) in different directions.

Similar to the procedure implemented for the P-waves, the signals recorded at t=25 hr for cross-polarized S-waves were subtracted from those recorded at t=50, 75, and 100 hr, in order to better illustrate the evolution of the time-frequency maps caused by fluid-fracture surface alterations. Figures 6.7f-h and 6.7j-l show the time-frequency maps of the resultant signals (i.e. signal recorded at t=25 hr subtracted from those recorded at t=50, 75, and 100 hr) for $S_1$- and $S_2$-waves, respectively. As the time progresses, similar to P-waves, the maximum amplitude of the $S_{1,2}$-waves decreases, implying that the change in the energy (i.e. amplitude) of the transmitted $S_{1,2}$-waves is less significant at a later time instance (e.g. t=100 hr) compared to an earlier time instance (e.g. t=50 hr). Also, similar to P-waves, the ratio of the spectral amplitude at higher frequency band to that of lower frequency band becomes smaller at a later time instance compared to an earlier time instance, which is more significant for the $S_1$-waves compared to $S_2$-waves. This slight difference between the two cross-polarized S-waves could be attributed to the anisotropy in (i) material, (ii) asperities distribution, and (iii) flow paths, as stated earlier.

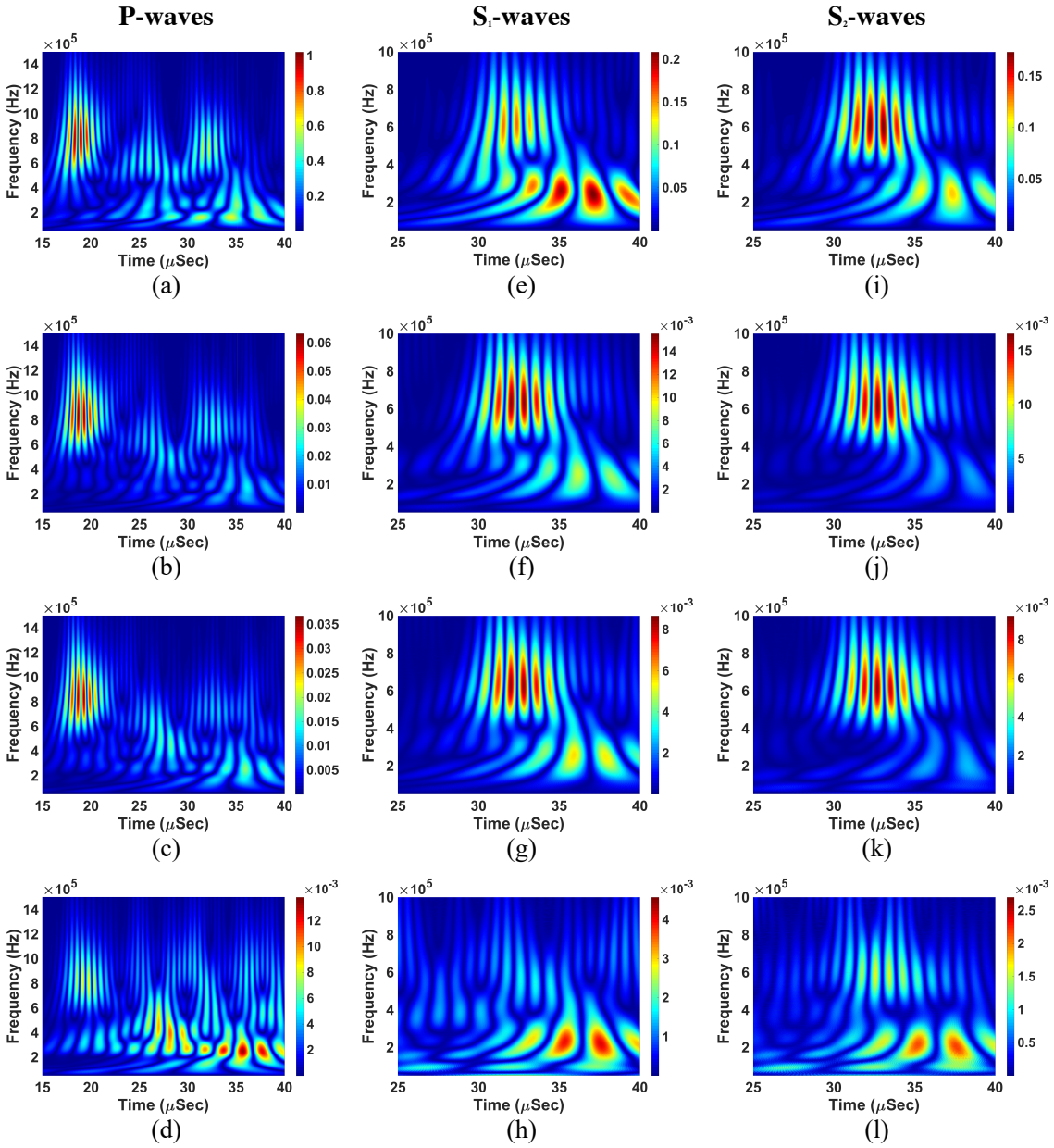


Figure 6-7. Time-frequency maps for the received P-waves in PCT at (a) t=25 hrs, (b) 50hr-25hr, (c) 75hr-25hr, (d) 100hr-25hr; received $S_1$-waves in PCT at (e) t=25 hrs, (f) 50hr-25hr, (g) 75hr-25hr, (h) 100hr-25hr; received $S_2$-waves in PCT at (i) t=25 hrs, (j) 50hr-25hr, (k) 75hr-25hr, (l) 100hr-25hr.

### 6.3.2 DISPLACEMENT-CONTROLLED TEST (DCT)

#### 6.3.2.1 RADIAL STRAINS, ULTRASONIC VELOCITIES, AMPLITUDES, AND ATTENUATIONS

Figure 6.8a illustrates the evolutions of average radial strain and differential pore pressure, indicating that there is a strong correspondence between radial strain and differential pore pressure in DCT. The processes caused by fluid-fracture surface interactions alter fracture permeability/hydraulic aperture, leading to increase/decrease in upstream pore pressure to maintain the constant injection rate and consequently, $\Delta P$ increases/decreases accordingly. For instance, as fracture permeability decreases, the upstream pore pressure intensifier adjusts (i.e. increases) the upstream pore pressure (and subsequently $\Delta P$) to maintain the constant injection rate. Then, the increase in $\Delta P$ leads to increase in fracture aperture (to maintain the constant flow rate), which in turn leads to the decrease in radial strain. The reverse correspondence between fracture aperture and radial strain was also observed in PCT. For example, at the time intervals with increase in $\Delta P$ (e.g. t=48 to 72 hr), the radial strain decreases, and vice versa.

Figure 6.8b shows the evolutions of the P-wave velocity and differential pore pressure, implying a clear correspondence between P-wave velocity and differential pore pressure. When $\Delta P$ increases, the P-wave velocity decreases (e.g. t=20 to 42 hr). This observation could be attributed to the fact that as the fracture opens up, the contribution of the fractured volume becomes more significant, and therefore, the P-wave velocity decreases. The direct correspondence between fracture aperture and P-wave velocity was

also observed in PCT. The evolution of S1- and S2-waves velocities were not found to be sensitive to the changes in fracture aperture, as shown in Figure 6.8c, similar to the PCT. In addition, the evolution of the maximum amplitude of the P-wave was not indicative of the changes in the fracture aperture, as was also observed in PCT.

Figure 6.9a shows the evolution of the normalized maximum amplitude of $S_1$- and $S_2$-waves and differential pore pressure during DCT. It can be observed that there is a gradual increase in the maximum amplitude of both $S_1$- and $S_2$-waves during the test, as the overall trend of differential pore pressure is increasing and hence, the fracture aperture has been increased. The direct correspondence between fracture aperture and maximum amplitude of $S_1$- and $S_2$-waves were also observed in PCT. In addition, the evolution of the maximum amplitude of the P-wave was not indicative of the changes in the fracture aperture, as was also observed in the PCT. Figure 6.9b shows the evolutions of P-wave attenuation and differential pore pressure in DCT, indicating sensitivity of P-wave attenuation to the alterations of fracture aperture/permeability, as was also observed in Figure 6.6a for P-wave attenuation in PCT. The evolutions of $S_1$- and $S_2$-waves attenuations were not found to be sensitive to the changes in fracture aperture, as was the case for PCT.

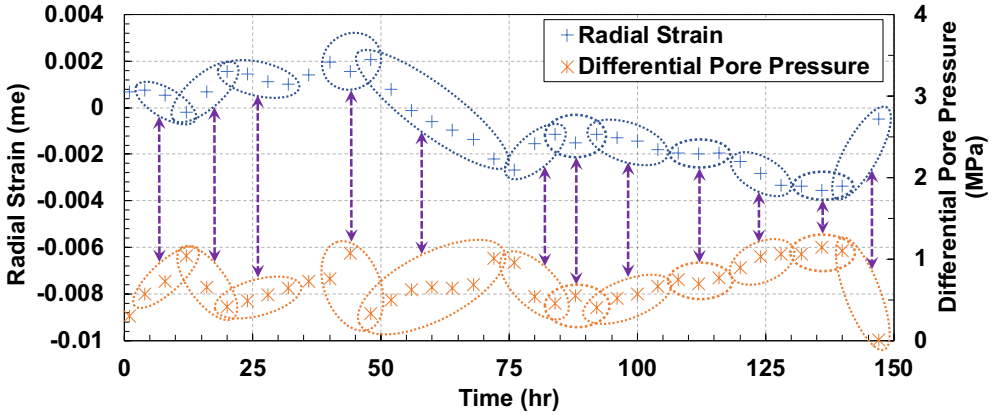


(a)

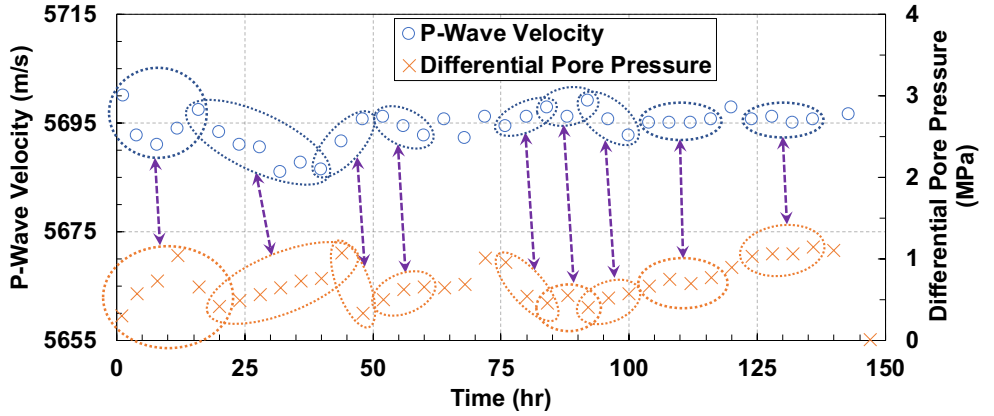


(b)

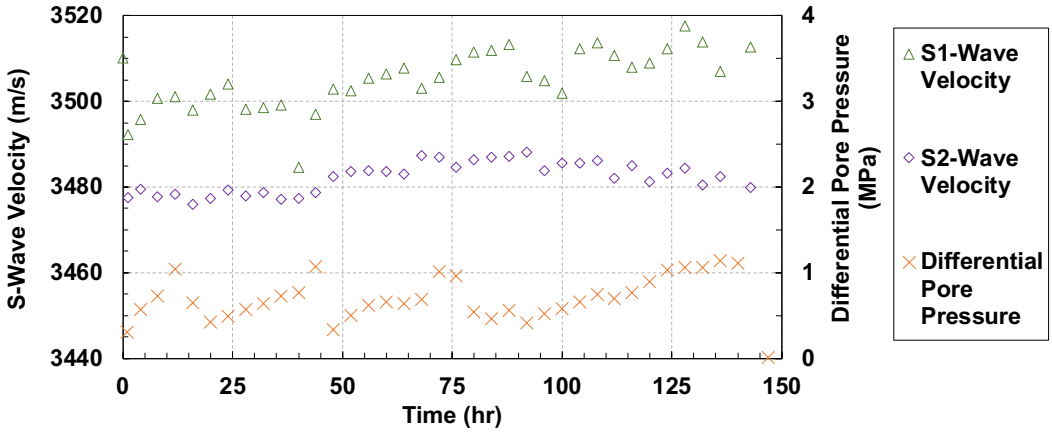


(c)

Figure 6-8. Time evolution of the differential pore pressure with (a) radial strain, (b) P-wave velocity, and (c) normalized maximum amplitude of $S_{1,2}$-waves in DCT

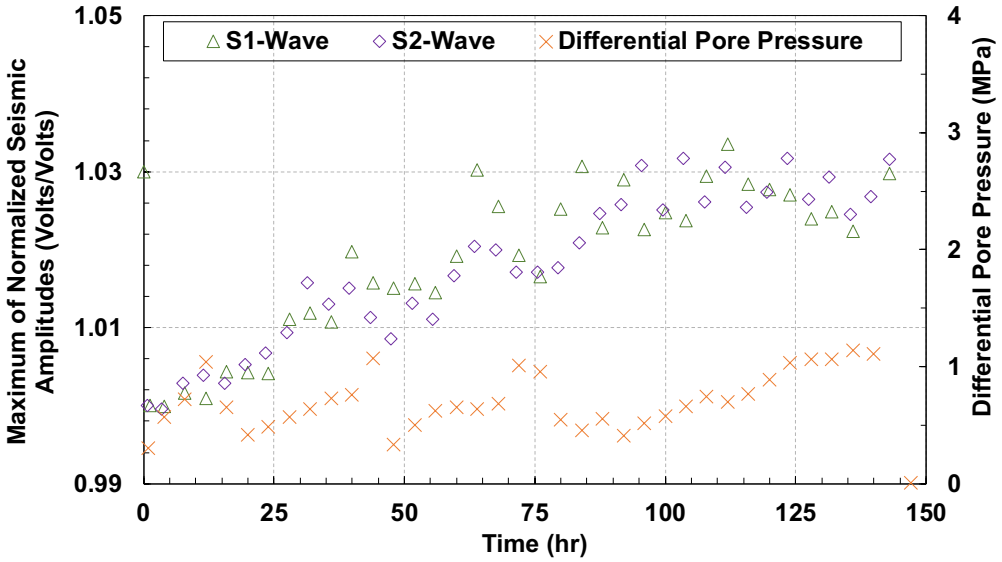


(a)

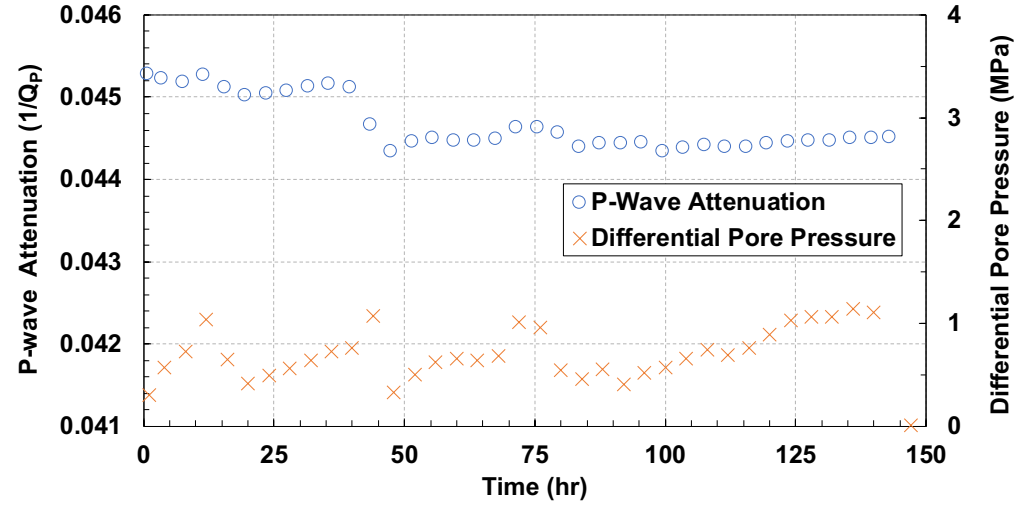


(b)

Figure 6-9. Time evolution of the differential pore pressure with (a) normalized maximum amplitude of $S_{12}$-waves, (b) P-wave attenuation, in the DCT

### 6.3.2.2 TIME-FREQUENCY ANALYSIS

***P-wave signals:*** The time-frequency maps for P-, $S_1$-, and $S_2$-waves for representative time instances of t=30, 60, 90, and 120 hr were generated by implementing wavelet transform.

The time-frequency maps at t=30 hr were shown to establish a baseline for the analysis of changes in frequency content over the course of the test. The ultrasonic signals recorded at t=30 hr were subtracted from those recorded at t=60, 90, and 120 hr. Then, the resultant signals were used as the input for the wavelet transform. Figure 6.10a shows the time-frequency map for the P-wave signal recorded at t=30 hr, indicating higher and lower frequency bands centered ~800 and ~200 kHz, respectively, as also observed during the PCT. The higher frequency band has higher energy (i.e. amplitude) compared to the lower frequency band, with very close amplitudes compared to PCT. The higher frequency band arrives at three different time intervals centered at ~18, ~25, and ~32 μSec, with the first arrival having the highest energy, while the lower frequency band is more distributed from ~25 to 40 μSec, similar to what was observed in PCT.

Figures 6.10b-d illustrate the time-frequency maps of the resultant (subtracted) signals related to t=60, 90, and 120 hr, indicating an increase in the energy (i.e. amplitude) of the transmitted P-wave as time progresses. This observation is opposite to that of PCT, which can be attributed to the different mechanisms of conducting the two types of flow-through test. More precisely, in PCT the upstream and downstream pore pressures are constant and the flow rate changes over time. However, in DCT, the downstream pore pressure and upstream injection rate are set as constant and the upstream pore pressure is

continuously adjusted to maintain the prescribed constant injection rate. Consequently, the decrease in the energy of the transmitted P-wave in a later time compared to an earlier time over the course of the PCT can be attributed to the lower flow rate (i.e. lower fracture aperture). While, the increase in the energy of the transmitted P-wave in a later time instance (e.g. t=120 hr) compared to an earlier time instance (e.g. t=60 hr) over the course of the DCT can be attributed to the higher differential pore pressure (i.e. higher fracture aperture). The frequency partitioning of the resultant signals did not indicate tangible changes over time, as opposed to that of the PCT. This could be attributed to the fact that the volume of the fracture remains almost the same.

***S-waves signals:*** Time-frequency maps for S1- and S2-waves are illustrated in Figures 6.10e-h and 6.10i-l, respectively. Figures 6.10e and 6.10i show the time-frequency maps of S1- and S2-waves at t=30 hr, indicating higher and lower frequency bands centered ~650 and ~250 kHz, respectively, which are similar to those in PCT. The contribution of the higher frequency band is more significant for S1-wave, while, the contribution of lower frequency band is more significant for S2-wave, similar to PCT. The energy (i.e. amplitude) of the S1-wave is slightly more than that of S2-wave, as also observed in PCT.

Figures 6.10f-h and 6.10j-l illustrate the time-frequency maps for the resultant signals (i.e. ultrasonic signal at t=30 hr subtracted from those at t=60, 90, and 120 hr) for $S_1$- and $S_2$-waves, respectively. It can be observed that, comparing time-frequency of the resultant signal at t=120 hr with that of t=60 hr, the change in energy (i.e. amplitude) becomes more pronounced as the test proceeds, as observed for P-wave. This observation is in contrast to those of the PCT, which can be attributed to the difference in mechanisms

of conducting these two modes of flow-through-fracture tests, as explained earlier. Comparing Figures 6.10f, 6.10g, and 6.10h (or equivalently 6.10j, 6.10k, 6.10l), it can be inferred that the frequency partitioning of the S1- and S2-waves does not change over time, similar to that of P-waves in DCT, and in contrast to that of all ultrasonic waves in PCT.

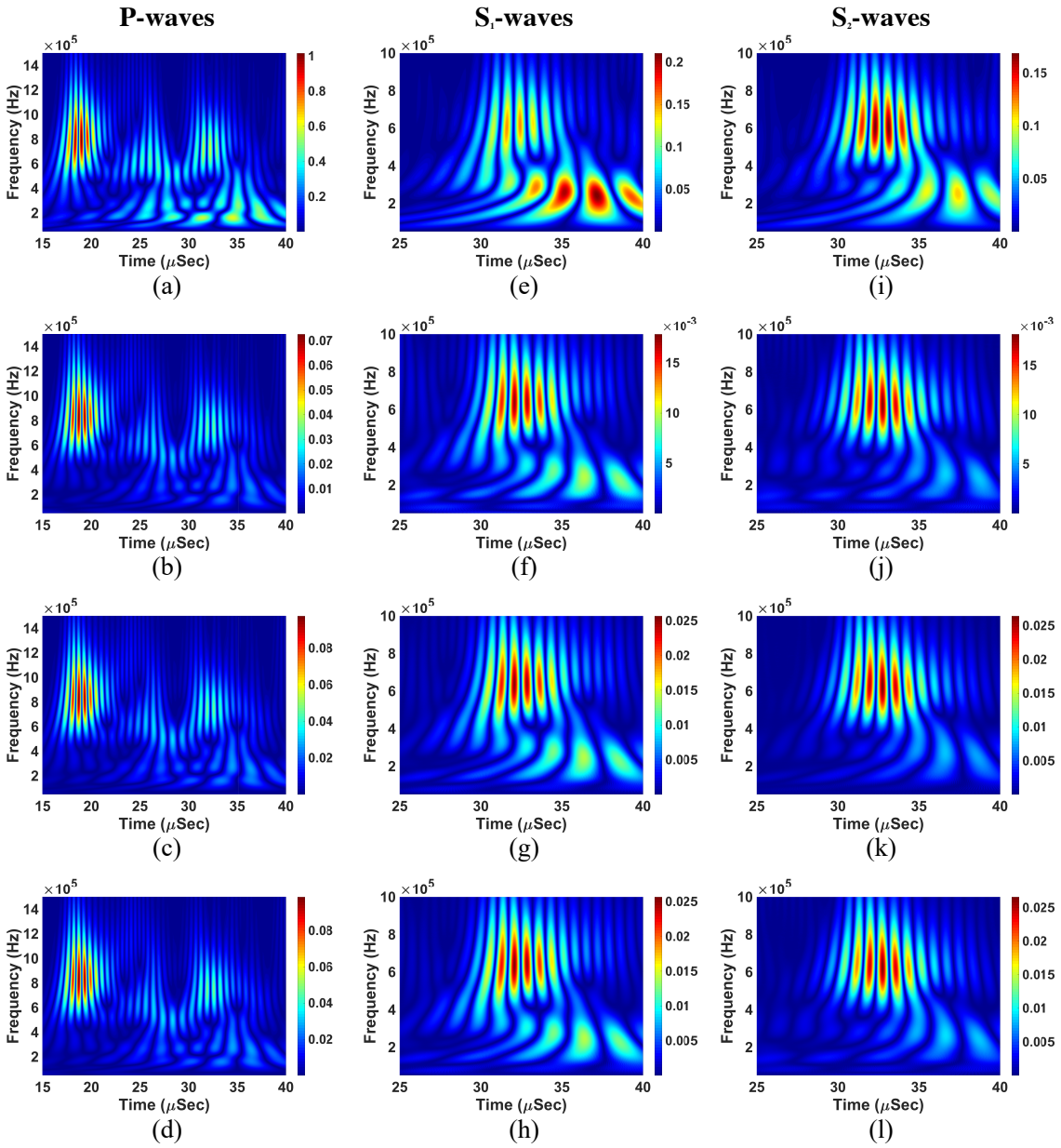


Figure 6-10. Time-frequency maps for the received P-waves in DCT at (a) t=25 hrs, (b) 60hr-30hr, (c) 90hr-30hr, (d) 120hr-30hr; received $S_1$-waves in DCT at (e) t=25 hrs, (f) 60hr-30hr, (g) 90hr-30hr, (h) 120hr-30hr; received $S_2$-waves in DCT at (i) t=25 hrs, (j) 60hr-30hr, (k) 90hr-30hr, (l) 120hr-30hr.

## 6.4 CONCLUSIONS

In this study, the sensitivity of P- and S-wave ultrasonic signatures (e.g. velocity, frequency content, amplitude, and attenuation) to the alterations of hydraulic properties, due to fluid-fracture surface interactions, were investigated. Pressure- and displacement-controlled flow-through-fracture tests were performed on an artificially-fractured reservoir phyllite specimen. The ultrasonic P-, $S_1$-, and $S_2$-waves and radial strain were measured during flow-through-fracture tests to evaluate the correspondence between evolution of fracture aperture to those of ultrasonic signatures.

The results suggested that ultrasonic signatures can potentially be used as a proxy for flow-induced fracture aperture evolution. An increase in fracture aperture led to a decrease in radial strain, with a more pronounced change in radial strain when the change in fracture aperture is significant. The P-wave velocity and attenuation, and the maximum amplitude of $S_1$- and $S_2$-waves can be used as indicators of fracture aperture change in fractured formations. In particular, a decrease in fracture aperture led to (i) increase in the P-wave velocity, (ii) decrease in the P-wave attenuation, and (iii) increase in the maximum amplitude of cross-polarized S-waves. However, the evolutions of $S_1$- and $S_2$-waves velocities/attenuations and the evolution of maximum amplitude of P-wave were not indicatives of the changes in flow rate/aperture/permeability.

The time-frequency maps of the transmitted ultrasonic P-waves revealed higher and lower frequency bands of ~800 and ~200 kHz, while those of both S-waves were ~650 and ~250 kHz. For pressure-controlled test, the frequency partitioning of the transmitted ultrasonic signals (P-, $S_1$-, and $S_2$-waves) showed a slight transition from higher

frequencies to lower frequencies as the test progressed, while those of displacement-controlled test did not show changes in frequency partitioning. The energy of the transmitted ultrasonic waves showed lower increase in energy content as the test progressed for pressure-controlled test, while those of displacement-controlled test indicated higher increase in the energy content.

# CHAPTER 7

# SENSITIVITY OF SEISMIC SIGNATURES TO THE CHANGES OF FRACTURE APERTURE/PERMEABILITY UNDER DIFFERENT STATES-OF-STRESS

## ABSTRACT

Response of fracture networks is a critical factor in the long-term performance of the geo-resources and linked to significant permeability reduction over long period of time resulted from fluid-fracture surface interactions. In this study, we evaluate the sensitivity of ultrasonic signatures (i.e. frequency content, velocity, amplitude, and attenuation) to the changes in fracture aperture caused by fluid-fracture surface interactions. Flow-through tests on artificially-fractured phyllite specimens from the Blue Mountain geothermal field, along with the concurrent measurements of ultrasonic signatures of P- and cross-polarized S-waves demonstrated the sensitivity of ultrasonic signatures to the evolution of fracture aperture/permeability under different state-of-stress (i.e. different pore fluid and/or confining pressures). It was found that ultrasonic velocities, amplitudes, and fracture specific stiffness increase, whereas attenuation decreases with the increase in the confining pressure. Increase in pore pressure led to decrease in ultrasonic velocities, ultrasonic amplitudes, and fracture specific stiffness, and increase in ultrasonic attenuations. In addition, it was found that time-frequency partitioning depends on hydraulic aperture. Three-Element rheological model and Power-Law model successfully predicted the time-

dependent fracture displacement, with the latter being less accurate at higher levels of pore pressures.

## 7.1 INTRODUCTION

Different geo-resources including (un)conventional oil/gas resources, geothermal exploitation, geological $CO_2$ storage, and nuclear waste disposal are closely tied with flow and transport properties of the enclosed reservoir (Pyrak-Nolte et al., 2015; Falcon-Suarez et al., 2016). Reservoir formations are to-some-extent fractured porous media, sensitive to perturbations in state-of-stress and chemical equilibrium alterations of the original physico-chemical properties, such as pore pressures and fluid geochemistry, respectively (Yasuhara et al., 2004; Majer et al., 2007; Ghassemi, 2012). These perturbations lead to changes in porosity and permeability (e.g. Benson and Orr, 2008; Ghassemi, 2012; Falcon-Suarez et al., 2017), which in turn, may lead to deformation, damage, fracturing, and eventually, micro-seismicity (e.g. Majer et al., 2007; Ellsworth 2013; Johnson and Majer, 2017).

The characterization of the fracture network is crucial to understand and predict the reservoir behavior during both (re)stimulation and long-term production stages. Different coupled thermo-hydro-mechanical-chemical (THMC) processes can affect the response of reservoirs, including pressure solution caused by high stress concentrations at asperities in-contact (e.g. Yasuhara et al., 2004), mineral dissolution/precipitation (e.g. Bachler et al., 2005), mechanical creep (e.g. Sone and Zoback, 2013b), hydraulic fracturing (e.g. Bazant et al., 2014), and shear/slip along fractures/faults (e.g. Ghassemi, 2012). For example, in geothermal reservoirs, the temperature-assisted chemical dissolution/precipitation processes contribute to reduce the permeability (e.g. Caulk et al., 2016; Faoro et al., 2016;

Kamali-Asl et al., 2018a); while in shale gas formations, the hydraulically-created fractures are prone to closure during production stage, caused by mechanical creep (e.g. Delle Piane et al., 2011; Sone and Zoback, 2013a and 2013b; Kamali-Asl et al., 2018b and 2018c).

Fractures geometry, distribution, and connectivity determine the fracture permeability of the reservoir, which is directly linked to its production efficiency (Pyrak-Nolte and Nolte, 2015; Kamali-Asl et al., 2018d). The hydraulic properties of a single fracture are controlled by aperture size, while, the mechanical characteristics are controlled by the geometry of the fracture surface (i.e. fracture surface roughness/tortuosity) (Cook, 1992; Pyrak-Nolte and Morris, 2000; Acosta-Colon et al., 2009). These two characteristics define a full fracture geometry description and are mutually controlled by (i) contact area of the fracture, (ii) amount and spatial distributions of the asperities, and (iii) aperture distribution along the fracture (Cook, 1992; Pyrak-Nolte and Morris, 2000; Choi et al., 2009). It is important to note that apertures and asperities are complementary aspects of fracture surface (Pyrak-Nolte and Nolte, 2016).

Geophysical signals can propagate in long distances and reveal information about the fractured formation (e.g. Pyrak-Nolte and Nolte, 2016). In particular, the alteration of the flow characteristics in fractured formations can be monitored using seismic waves as high-resolution probes, sensitive to different geological conditions such as temperature, overburden and pore pressures, saturation level, and depth of interest (e.g. Vlastos et al., 2006; Mavko, 2009; Pyrak-Nolte and Nolte, 2016).

The internal micro-structure of the rock can be investigated using seismic waves in different geo-energy applications such as shale gas formations (e.g. Fjaer, 2008; Sone and

Zoback, 2013a; Kamali-Asl et al., 2018c), geological carbon storage (e.g. Falcon-Suarez et al. 2017) and geothermal reservoirs (e.g. Anderson et al., 1974; Kamali-Asl et al., 2018e). In addition, seismic-wave velocity and attenuation can be used to infer the degree of saturation in oil/gas fields and to distinguish between water and steam in geothermal reservoirs (e.g. Jones et al., 1980; Bodau and Long, 1996; Szewczyk et al., 2018).

As seismic waves propagate through a fractured media, frequency-dependent elastic interface waves are generated, which are categorized into fast and slow interface waves with velocities ranging from shear-wave (upper limit) to Rayleigh-wave (lower limit) (e.g. Biot, 1956a and 1956b; Pyrak-Nolte et al., 1990; Delle Piane et al., 2014). While, the energy of these interface waves depends on state-of-stress and fracture geometry (e.g. Pyrak-Nolte et al., 1990), there exists a direct relationship between fracture-specific stiffness and propagation of interface waves (e.g. Cook, 1992; Roy and Pyrak-Nolte, 1995). Hence, seismic response of fractured formations is substantially-affected by both alteration of hydraulic and mechanical properties (e.g. Cook, 1992; Brajanovski et al., 2006). In this regard, geochemical processes at the fracture surface might weaken/strengthen the fracture shearing behavior, which in turn, might affect the outcome of hydro-shearing process in geo-energy resources (Pyrak-Nolte et al., 2015). Therefore, fracture aperture/permeability dependencies and evolution can be potentially assessed and monitored using remote sensing tools (i.e. seismic signatures).

In this study, we performed flow-through tests under variable stress conditions on artificially-fractured phyllite specimens to investigate the sensitivity of ultrasonic signatures to stress-induced changes in hydraulic/mechanical properties of fracture

reservoirs analogues. During the tests, we measured ultrasonic P- and cross-polarized S-waves along with radial strains to investigate the sensitivity of ultrasonic velocities, amplitudes, attenuations, and frequency-dependency to changes in the state of stress.

## 7.2 MATERIALS AND METHODS

### 7.2.1 ROCK SAMPLE PREPARATION

Two specimens, namely PL1 and PL2, were used in flow-through tests with the two halves of the saturated fractured specimens mated together. PL1 was directly inserted inside the Vitton jacket used to prevent the contact between the confining fluid of the triaxial vessel and the rock sample; while, PL2 was wrapped in a copper jacket to facilitate attachment of the strain gauges prior to inserting it inside the Vitton jacket with two open cuts at 180°-apart (Figure A9.1a). Note that strain gauges were attached only on PL2. The fracture plane in both samples was oriented at ~45° to the $S_1$-waves propagation plane (Figure A9.1c). Finally, the two ends of the sample were wire-tightened to the top and bottom ultrasonic velocity core-holders, before being placed inside the triaxial vessel for the tests (Figure A6.1a).

### 7.2.2 EXPERIMENTAL PROCEDURE

The flow-through experiments were run with DIW at room temperature, during ~120 and ~160 h for PL1 and PL2, respectively. During this time, we collected ultrasonic P-wave and cross-polarized S-waves. The P, $S_1$, and $S_2$ waves transducers were stacked together and embedded in the hollow-cylindrical-shaped core-holders (Figure A9.1b),

transmitting the signal from the bottom (i.e. upstream) to the top (i.e. downstream) core-holder.

The attenuation analysis for the fractured samples was performed following the procedure outlined in Pyrak-Nolte et al. (1990), as expressed in Eq. (7.1):

$$Q = -\pi f x/[c ln(A/A_l)] \quad (7.1)$$

where, Q is the seismic quality factor, f is the central frequency of the transmitted seismic wave, x is the length of the specimen (i.e. fractured rock), c is the phase velocity of the seismic wave, and A and $A_l$ are the maximum spectral amplitudes of the fractured rock and aluminum specimen (with identical dimensions as fractured rock specimen), respectively. Fourier transform analysis was performed to estimate the maximum spectral amplitude of the seismic waves at each time instance. Note that a brief introduction to continuous wavelet transform is provided in Appendix E.

### 7.2.3 EXPERIMENTAL PROGRAM

We conducted a PCT on PL1, and a DCT on PL2 to investigate the effect of confining pressure and pore water pressure on fracture response and wave propagation through fracture. For the PCT, the differential pore pressure ($\Delta P_p = P_{up} - P_{down}$) was the imposed parameter, while the evolution of the outflow rate was recorded and used to estimate the corresponding fracture permeability and aperture during the test. In the case of DCT, the injection flow rate was set to $2.65\times10^{-11}$ $m^3$ $s^{-1}$ and the $P_{down}$ was set constant, while the $P_{up}$ was the monitoring parameter. The evolution of $\Delta P_p$ was used to infer fracture permeability and aperture. It should be noted that in the PCT, the flow rate is changing,

and therefore, the hydraulic aperture is not constant. By contrary, in the DCT the injection rate and hence the hydraulic aperture is constant throughout the test.

In addition, to assess the particular effect of the saturated fracture on the ultrasonic properties, the P-, $S_1$-, and $S_2$-waves were measured on a third intact (non-fractured) phyllite sample (with same dimensions as PL1) under $P_c$ = 15 MPa.

Figure 7.1 shows the stress paths used in the DCT and PCT. For the DCT, $\sigma_{dev}$ was set to 6 MPa, with $P_C$ = 60 MPa, while $P_{down}$ was increased 10 MPa (9 MPa for the first step) step-wise from 1 to 40 MPa. Each step of the stress path was held constant for 24 h. This test was performed in order to investigate the net effects of pore pressure changes on ultrasonic signatures, including velocity, amplitude, attenuation, and time-frequency dependency. For the PCT, hydrostatic confining conditions were applied ($P_C$), to simulate overburden and pore pressures equivalent to 630, 1260, and 1890 m depth, using adopting 24.1 and 8.8 MPa/km rates for $P_c$ and $P_p$, respectively. The stress path for this test is consisted of 10 stages. As it can be seen in Figure 7.1b, there is an ~8 h delay between variations of $P_p$ and $P_c$. This delay was considered in the design of stress path in order to (i) distinguish the effects of each stress component on the evolution of fracture aperture, and (ii) evaluate the influence of the effective stress (i.e., $P_c$ - $P_p$) on the ultrasonic properties. In addition, the stress path for PCT was designed to capture the effects of stress corrosion at higher effective pressures. Figure 7.2 illustrates a schematic of the concept of stress corrosion, in which, as higher effective pressures are applied, the asperities come in-contact and eventually crush, leading to lower fracture aperture/permeability.

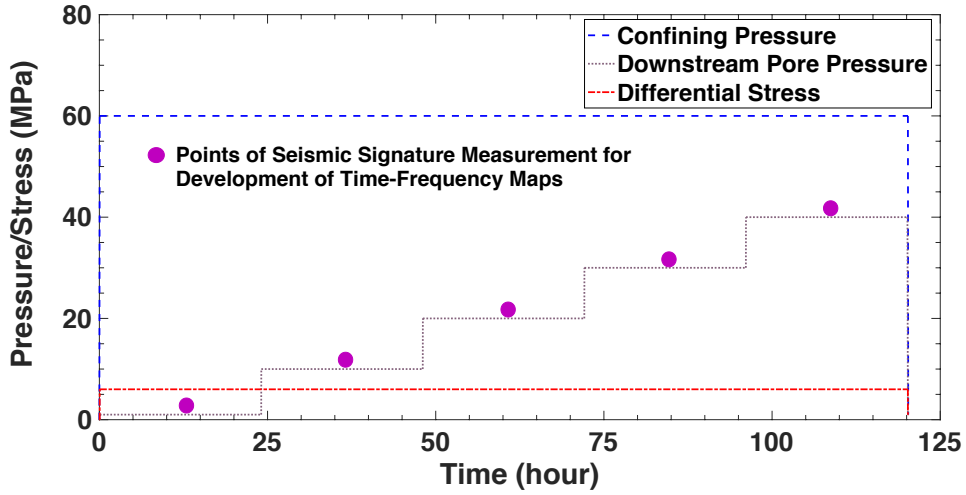


(a)

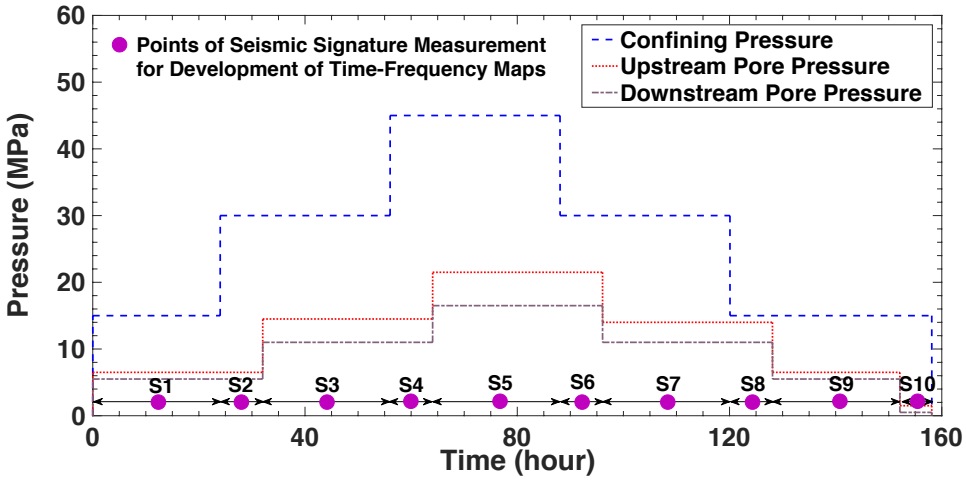


(b)

Figure 7-1. Stress path followed in (a) the PCT and (b) the DCT. The purple points indicate the time instances that seismic waves were selected for time-frequency analysis within a given stage (S), while, for all other analyses (i.e. velocity, amplitude and attenuations), the 30-minute collected seismic signatures were used.

The evolutions of radial strains, differential pore pressure (in DCT), and outflow rate (in PCT) were recorded every second, while ultrasonic responses were collected every 0.5 h. Further, for clarity in the presentation of results, all data were binned to every 2 h.

## 7.3 RESULTS

Figure 7.3 shows waveforms for all three seismic waves for intact and fractured specimens, indicating changes in velocities, amplitudes, attenuations, and frequency spectrum due to presence of fracture and fluid flow. The P-wave arrival time for fractured specimen is less than that of intact specimen, and the amplitudes of S-waves are observable for fractured specimen compared to very low amplitudes for intact specimen. In addition, the frequency content of the P-wave signals for intact and fractured specimens are slightly different after t=25 μs.

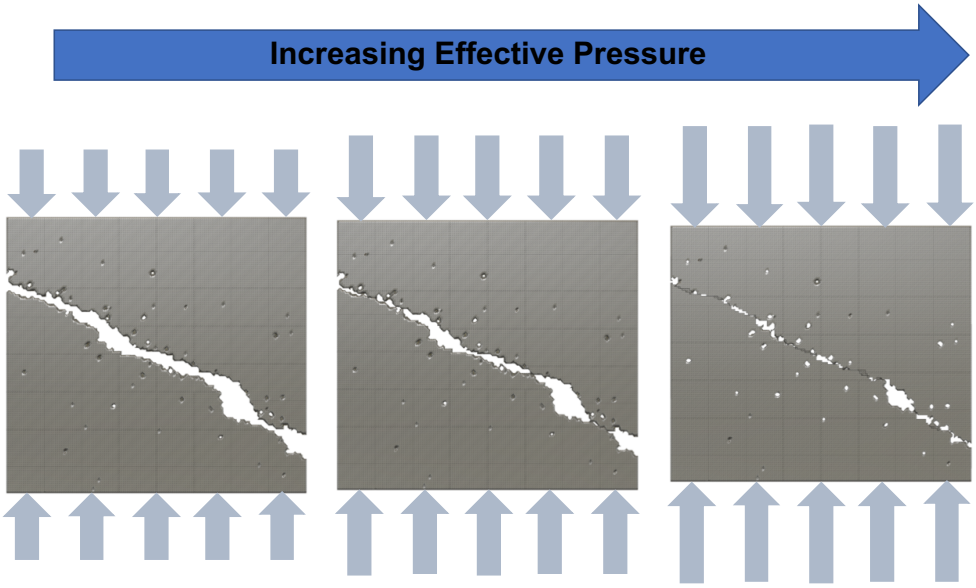


Figure 7-2. Schematic of the concept of stress corrosion

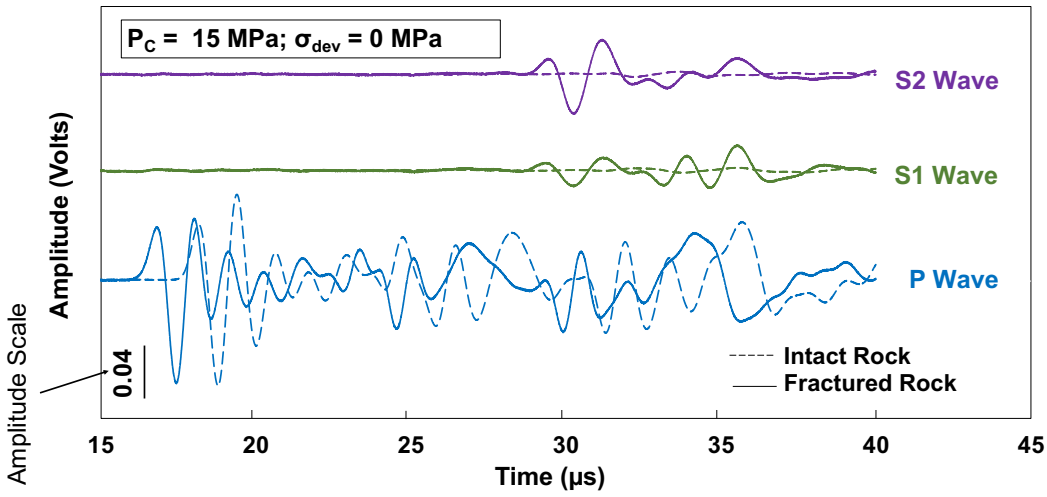


Figure 7-3. Signal comparison between fractured and intact rocks

### 7.3.1 DISPLACEMENT-CONTROLLED TEST (DCT)

#### 7.3.1.1 MECHANICAL EVIDENCES

Figure 7.4 shows the time evolutions of average radial strains along with differential pore pressure at different stages of DCT (dilation/reduction). Within each stage of the test (with constant $P_{down}$), the fracture aperture varies with the $P_{up}$ is automatically adjusted (in most cases increases) by the instrument to maintain the constant injection rate. As a result of the increase/decrease in the upstream pore pressure and consequently in differential pore pressure, the mechanical aperture of the fracture increases/decreases, while the hydraulic aperture/permeability is maintained constant during the test. This, in turn, leads to increase in radial strain or opening of the fracture. Transitioning from one $P_{down}$ step to the next, there is a sudden increase in radial strain. This could be attributed to the fact that as $P_{down}$ increases, the fracture opens up and therefore, the radial strain

increases, as also observed by Nooraeipour et al. (2018). It should be noted that negative $\Delta P_p$ values are attributed to the fact that this test was performed in displacement-controlled mode and therefore, $P_{up}$ cannot be increased with the same rate as $P_{down}$ increases, due to constant injection rate in the upstream side. The gradual increase of radial strain within each stage and the sudden increase of radial strain with $P_{down}$ changes are more significant at higher $P_{down}$. Immediately after the $P_{down}$ increases, the $\Delta Pp$ is practically-null, indicating permeability is maximum. In general, with increasing the pore pressure the effective pressure reduces and permeability increases (e.g. Al-Wardy and Zimmerman, 2004). We observe that $\Delta Pp$ is decreasing by increasing the $P_{down}$, with the exception of the transition from 10 to 20 MPa.

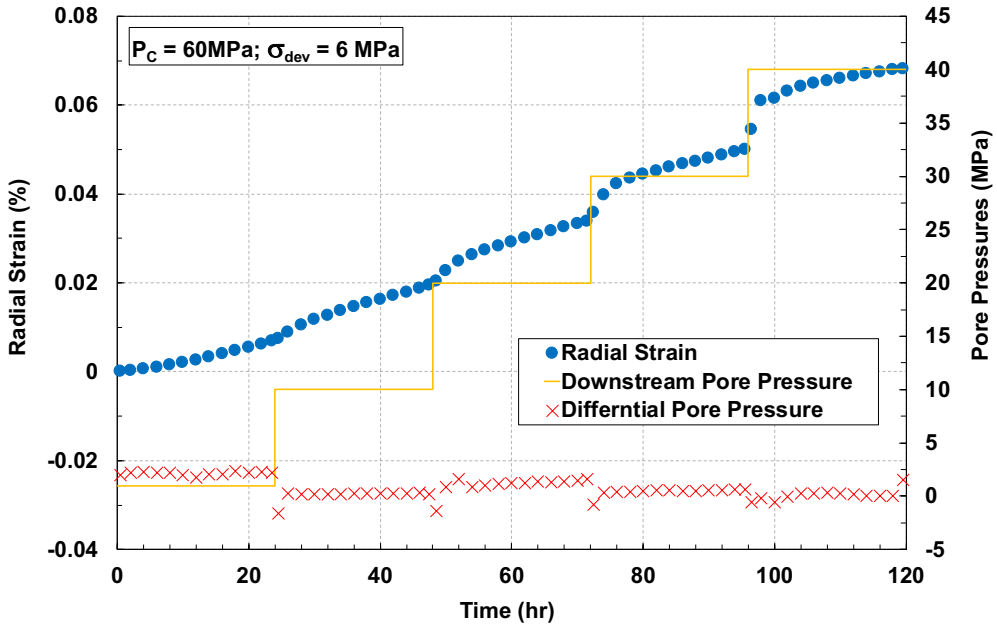


Figure 7-4. Evolutions of radial strain data at different stages of the DCT

#### 7.3.1.2 ULTRASONIC EVIDENCES

Figure 7.5 shows time evolutions of permeability and ultrasonic velocities (Figure 7.5a), normalized maximum acoustic amplitudes (Figure 7.5b), and ultrasonic attenuations (Figure 7.5c) at different levels of downstream pore pressure. The ultrasonic velocities are relatively-constant within each stage and increase between two consecutive stages as the effective stress increases, by <2% for $V_P$ and ~5% for $V_S$, as also observed by Nooraeipour et al. (2018). Similar to ultrasonic velocities, ultrasonic amplitudes and attenuations exhibit constant value at each stage, however, they show an increasing trend at higher $P_{down}$ levels.

### 7.3.2 PRESSURE-CONTROLLED TEST

#### 7.3.2.1 ULTRASONIC EVIDENCES

Figure 7.6 shows the time evolutions of permeability and the ultrasonic velocities (Figure 7.6a), normalized maximum acoustic amplitudes (Figure 7.6b), and ultrasonic attenuations (Figure 7.6c) at different stages of this test. Similar to the DCT, all three ultrasonic signatures (namely velocities, amplitudes, and attenuations) are relatively-constant at each stage, while, they are sensitive to the changes in confining/pore pressures. The range of ultrasonic seismic velocities for the fractured PL1 specimen in PCT (see Figure 7.6a) is slightly higher than that measured for PL2 specimen in DCT (see Figure 7.5a), which can be interpreted as the effect of the anisotropy reported for this rock (Kamali-Asl et al., 2018d). S-waves amplitude shows stronger effective stress dependency than P-waves. It can be observed that S-waves attenuations are sensitive to the changes in the state-of-stress, however, P-wave attenuations are not as conclusive as those in DCT.

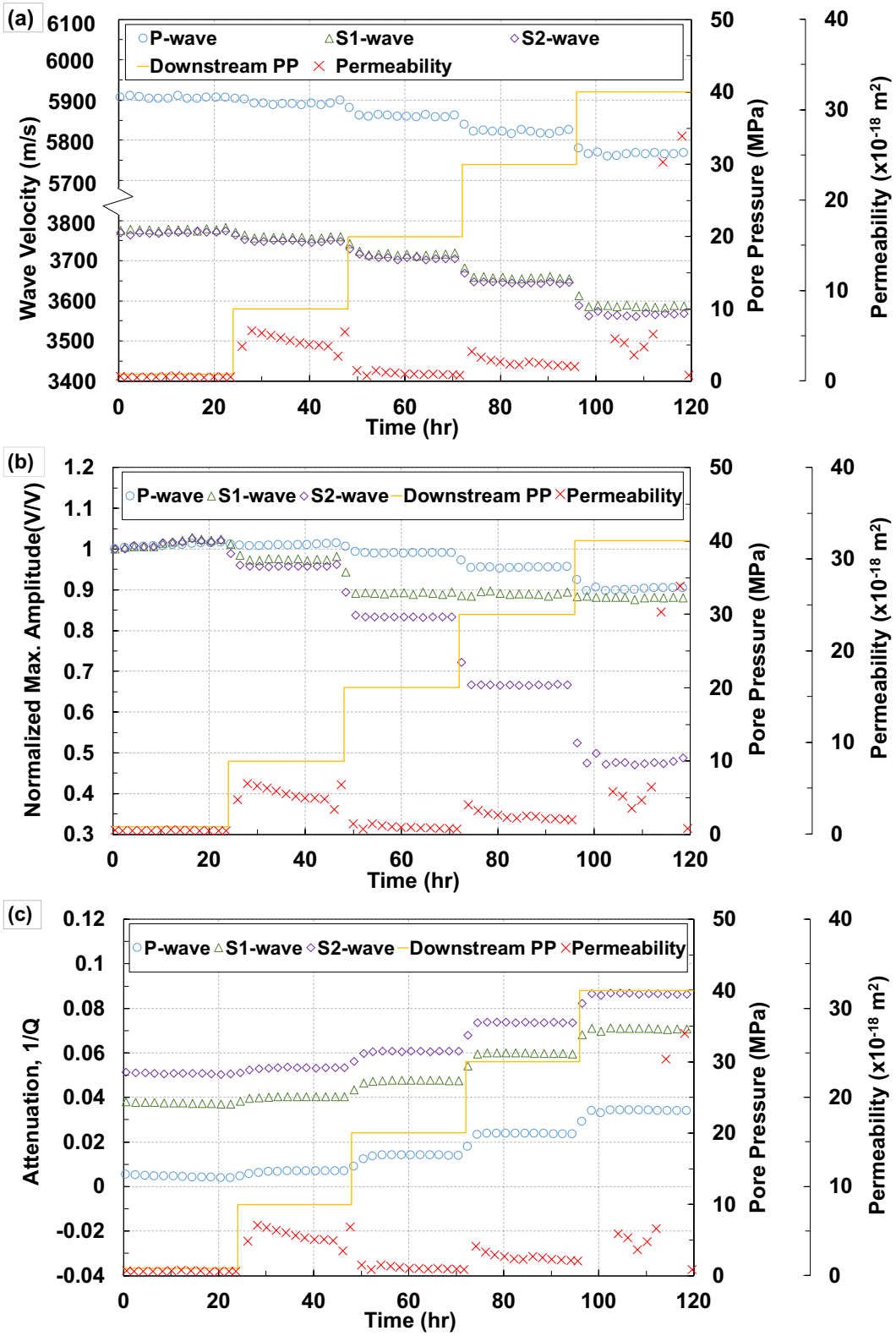


Figure 7-5. Variation of ultrasonic (a) velocities, (b) maximum normalized amplitudes, and (c) attenuations for P-, $S_1$-, and $S_2$-waves, together with the permeability evolution in the DCT.

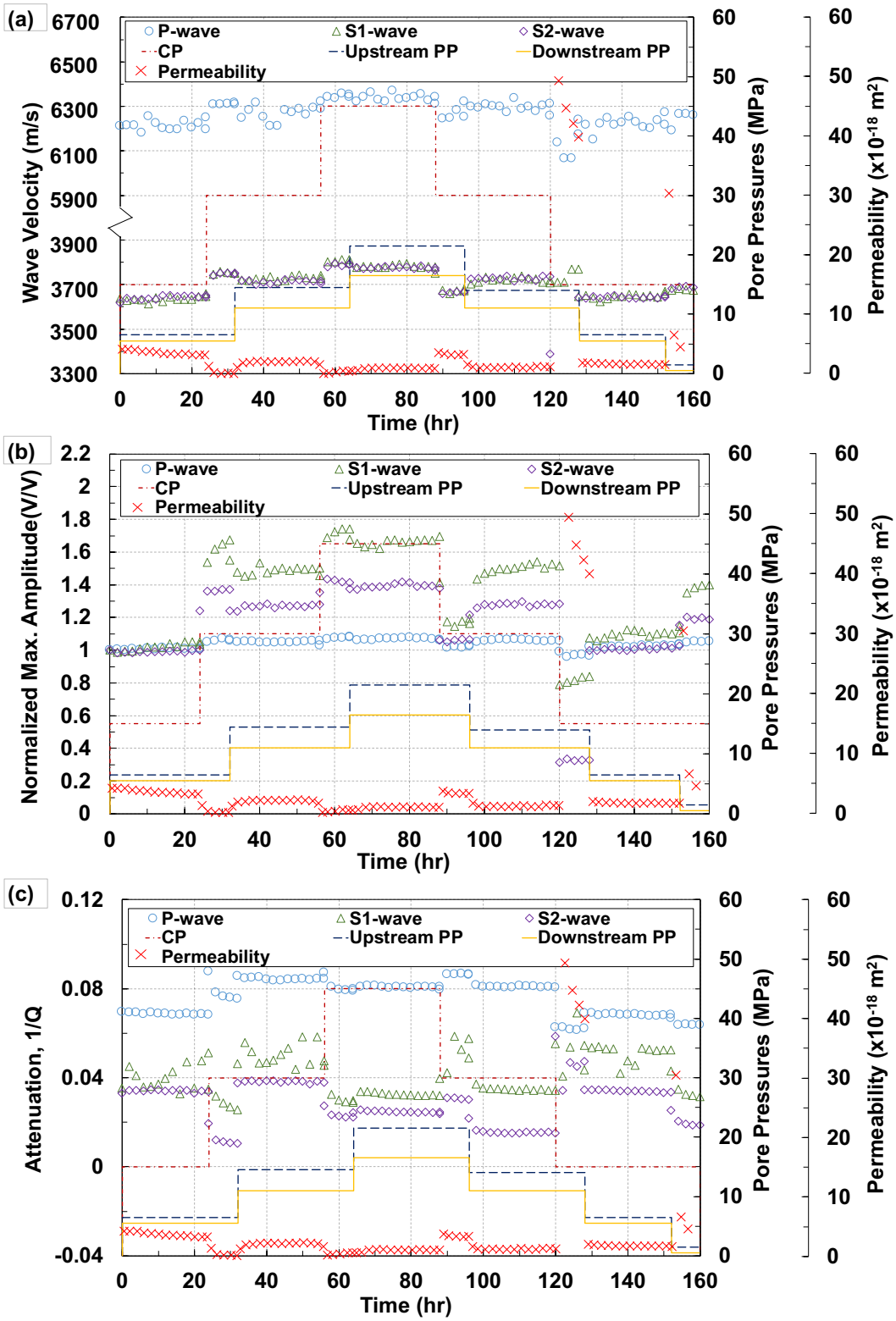


Figure 7-6. Variation of ultrasonic (a) velocities, (b) maximum normalized amplitudes, and (c) attenuations for P-, $S_1$-, and $S_2$-waves, together with the permeability evolution in the PCT

### 7.3.3 TIME-FREQUENCY ANALYSIS

#### 7.3.3.1 P-WAVES

Figure 7.7a-d shows that the higher frequency range (i.e. ~800 kHz) has higher contribution in the time-frequency partitioning compared to the lower frequency range (i.e. ~200 kHz). This observation can be attributed to the fact that the fracture aperture is extremely small (~0.6 μm) and therefore, the body of the rock with higher transmitted frequency has a more significant contribution to the transmission of the P-waves. As the pore pressure increases from 1 to 40 MPa, the peak amplitude of the time-frequency maps decreases by 20%, which indicates ultrasonic wave dissipation increase with the pore pressure. As previously mentioned, this test was performed in displacement-controlled mode, where the injection rate and the available fracture volume for fluid to flow is constant throughout the test. Hence, hydraulic permeability and aperture do not change over the course of the experiment. Therefore, the ratio of the available volume within the fracture for fluid to flow to the volume of the rock matrix is constant, and the insensitivity of frequency partitioning of time-frequency maps to the changes in the pore pressures reflect the constant hydraulic aperture (and not mechanical) in the DCT. However, in the PCT (as will be discussed), where the hydraulic aperture is variable, the frequency partitioning of time-frequency maps will be altered by the changes in pore pressure and consequently permeability and hydraulic aperture.

Figure 7.7e-l shows that in all the stages of the PCT, the higher frequency content of the P-wave signals (~800 kHz) arrive earlier compared to lower frequency content (~200 kHz). This phase lag reveals the energy of the P-wave signals is transmitted within the high

frequency domain, as we observed in the DCT. It appears that the lower frequency part of the wavelet-transformed (hereafter referred as WT) transmitted P-waves is symmetric (fast) interface wave.

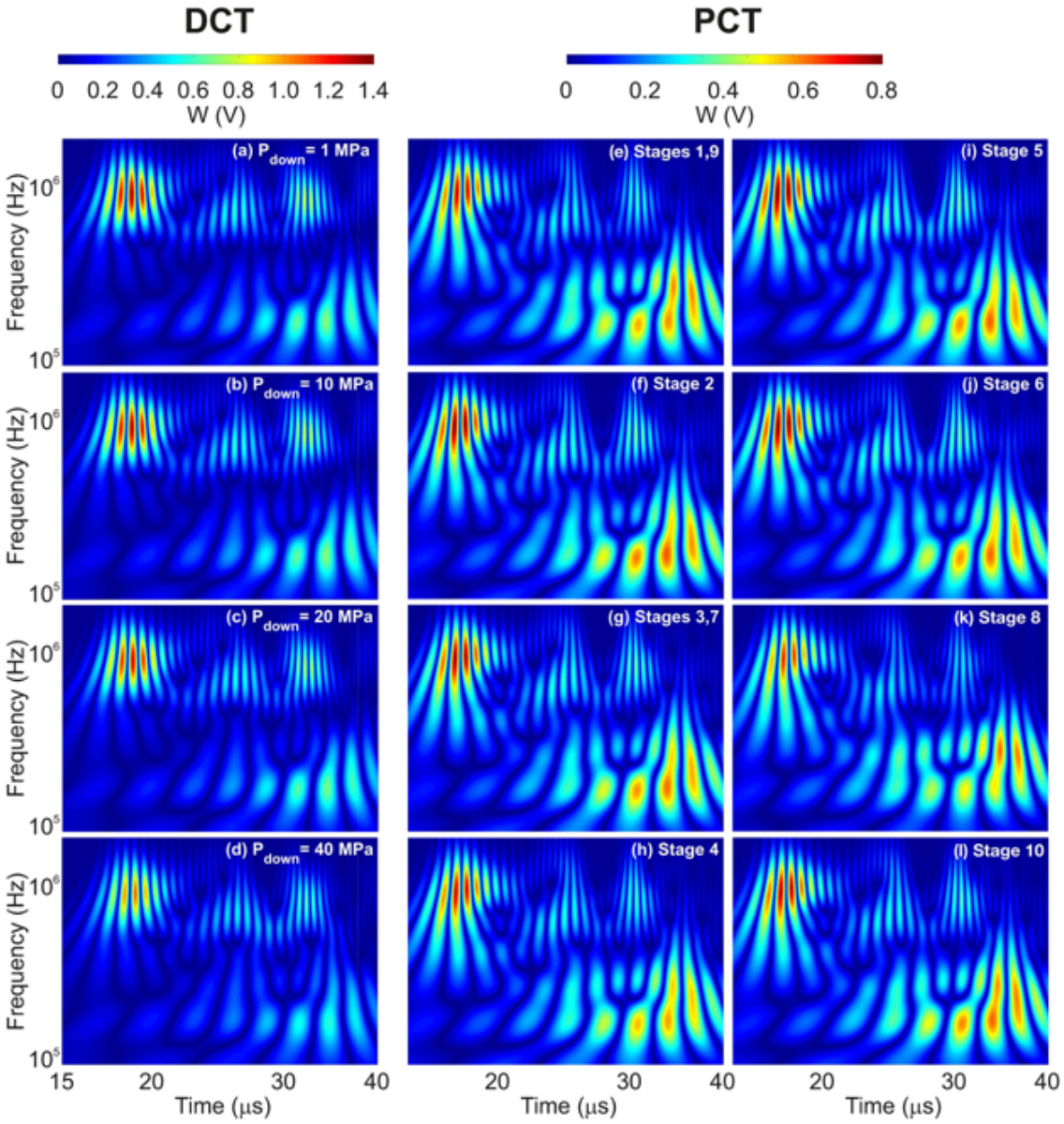


Figure 7-7. Time-frequency maps for the received P-waves in DCT at pore pressures of (a) 1, (b) 10, (c) 20, (d) 40 MPa; and received P-waves in PCT at stages 1 to 10 in (e)-(l). Stages 1 and 9 as well as 3 and 7 are combined, since stages 9 and 7 had the same pressures as 1 and 3 in the unloading path. Note that both axes are in logarithmic scale.

* W(V) below the colorbars refers to Eq. (A5.2), where $W_{a,b}(z)$ was defined as the wavelet-transformed amplitude with the unit of volts.

At higher confining pressures and/or lower pore pressures, the contribution of the higher frequency portion of the WT transmitted P-waves becomes more significant. This can be attributed to the fact that at higher specific stiffness values (i.e. higher effective stress), the contribution of the body P-waves compared to the fast interface waves is more significant (Roy and Pyrak-Nolte, 1995; Pyrak-Nolte et al., 1996). In addition, as specific stiffness increases the upper lobe in the lower frequency range tends to approach to the lower lobe. However, no significant change in the frequency partitioning of the higher frequency range can be observed. These two observations are consistent with the fact that the lower frequency range corresponds to fast interface wave and hence, alterations in flow characteristics (i.e. flow rate, asperities in contact, and fracture aperture) lead to notable changes in the time-frequency content of the fast interface waves obtained from WT transmitted P-waves. However, body P-waves (not interface waves) propagate through the matrix of the rock and therefore, the changes in fracture stiffness (caused by changes in the effective stress) do not affect body P-waves.

At higher confining pressures (while the pore pressure is constant), the amplitude of the WT transmitted wave increases. This might imply that the energy of the transmitted wave is conserved more at higher levels of effective stress. However, increase of pore pressure led to decreased amplitude of the WT transmitted P-waves. As pore pressure increases, the two halves of the fractured specimen get farther away and fracture aperture increases, which leads to larger fluid-filled fractured volume. Therefore, energy dissipation due to interaction with higher volumes of water present in the fracture is more significant.

#### 7.3.3.2 S-WAVES

The time-frequency maps of the $S_1$- (in the DCT; Figure 7.8a-d) and $S_2$-waves (in the PCT; Figure 7.8e-l) exhibit concentration of energy around the lower frequency range (i.e. ~250 kHz) and higher frequency range (i.e. ~600 kHz), respectively. This difference in frequency partitioning of the two cross-polarized S-waves can be attributed to the fact that there is a 90° difference in their propagation direction and the dominant wave propagation mode is interface wave for $S_1$-wave, while, that of $S_2$-wave is body wave. It should be noted that, to be concise, the time-frequency maps of $S_2$-waves in the DCT and $S_1$-waves in the DCT are not presented as their trend were found to be very similar to the time-frequency maps of $S_1$-waves in the DCT and $S_2$-waves in the PCT, respectively.

In the DCT, at higher pore pressures, the peak amplitude of WT transmitted S-waves decreases by ~20%, as also observed for P-waves. More importantly, the frequency partitioning of S-waves also remains unaltered by the variation of pore pressure. As previously explained, this can be attributed to the fact that this test was performed in displacement-controlled mode and hence, the available fracture volume for fluid flow is constant throughout the test. Therefore, the frequency partitioning of time-frequency maps is sensitive to the changes in hydraulic aperture and not pore pressure itself.

Figure 7.8e-l shows that the peak amplitudes of the WT transmitted S-waves occur at two different frequencies during the PCT. The higher frequency range, centered at ~600 kHz, corresponds to the transmitted body S-wave and the lower frequency range, centered at ~250 kHz, corresponds to the transmitted slow (antisymmetric) interface wave. As fracture stiffness increases with the effective stress, the contribution of transmitted energy

through slow interface wave becomes less significant. For example, a comparison between Figure 7.8h, stage 4 (CP=45, Pp=11 MPa), and Figure 7.8k, stage 8 (CP=15, Pp=11 MPa) reveals that when fracture specific stiffness is high (i.e. Figure 7.8h: Stage 4), the higher frequency has a more significant contribution to energy of the transmitted signal. As also observed in WT transmitted P-waves, the amplitude of WT transmitted S-waves increases with the fracture specific stiffness (i.e. confining pressure increases and/or pore pressure decreases). This could be attributed to the fact that at higher fracture specific stiffness, fracture aperture is lower, and therefore the medium is less energy-dispersive.

## 7.4 DATA ANALYSIS AND DISCUSSIONS

### 7.4.1 PRESSURE-DEPENDENCY OF ULTRASONIC PROPERTIES

The results indicate that the ultrasonic properties of our fractured samples are strongly stress-dependent parameters. The state of stress conditions we have imposed in the tests applied for changes in the confining and pore pressure. In this section, we investigate the individual contribution of each of them on the ultrasonic properties.

#### 7.4.1.1 PORE PRESSURE EFFECTS

In order to investigate the correlation between pore pressure and ultrasonic signatures (i.e. velocity, maximum amplitude, and attenuation), the average values of ultrasonic signatures in each stage of the DCT (i.e. under constant pore pressure) were plotted against pore pressure for P- and average S-waves. Figure 7.9a shows the ultrasonic velocities decreases linearly with pore pressure, with relatively-high regression values for both P- and average S-waves ($R^2$ ~0.96 in both cases). This could be attributed to the fact

that at higher pore pressures, the mechanical aperture increases (with unaltered hydraulic aperture) and the contribution of the fluid-filled fractured volume on the propagation of ultrasonic waves becomes more significant compared to that of body of the rock.

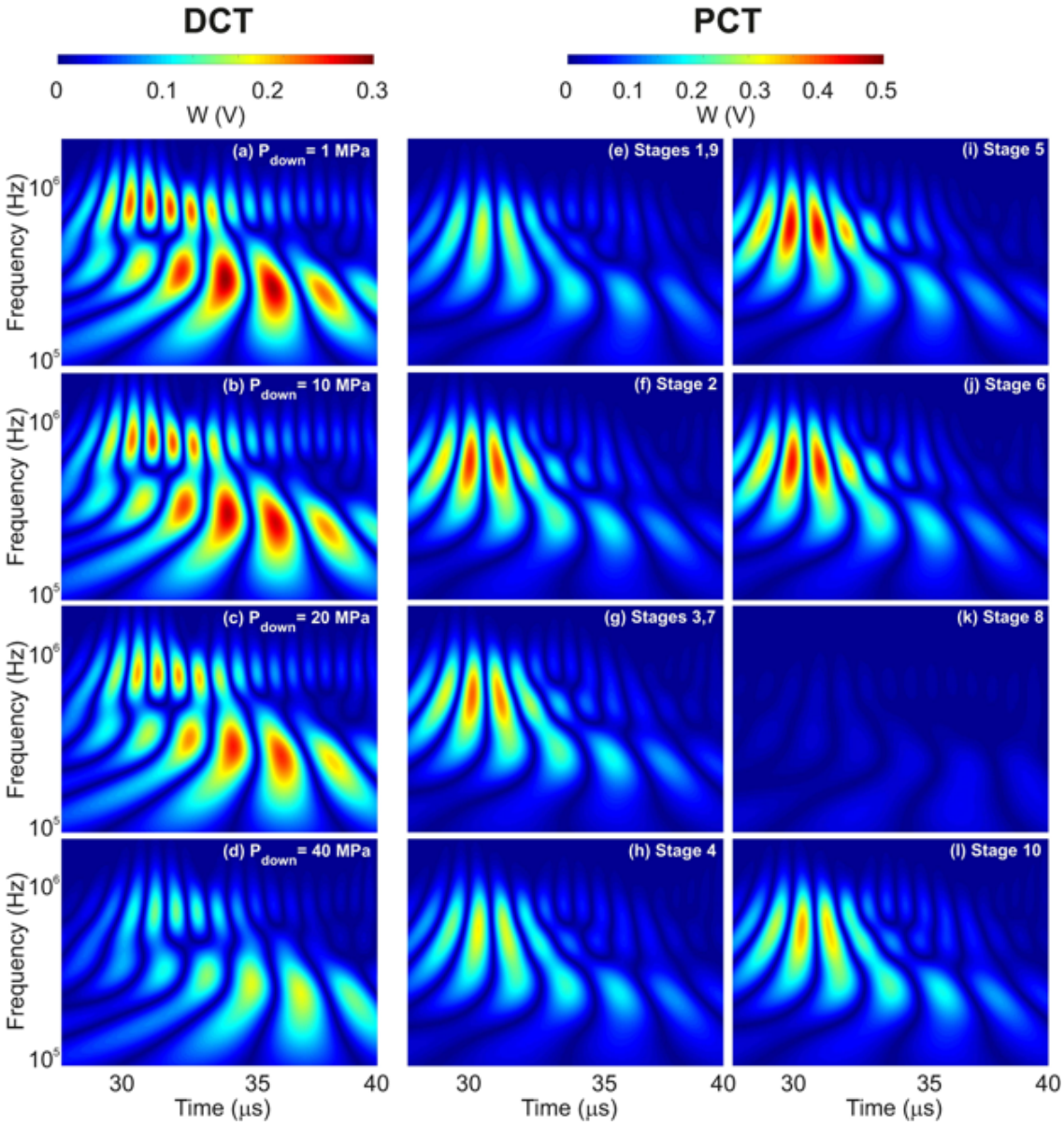


Figure 7-8. Time-frequency maps for the received $S_1$-waves in the DCT at pore pressures of (a) 1, (b) 10, (c) 20, (d) 40 MPa; and received $S_2$-waves in the PCT at stages 1 to 10 in (e)-(l). Stages 1 and 9 as well as 3 and 7 are combined, since stages 9 and 7 had the same pressures as 1 and 3 in the unloading path. Note that both axes are in logarithmic scale.

* W(V) below the colorbars refers to Eq. (A5.2), where $W_{a,b}(z)$ was defined as the wavelet-transformed amplitude with the unit of volts.

Figure 7.9b shows a good correlation between the (normalized) amplitudes for P- and S-waves and pore pressure ($R^2$ ~0.87 and $R^2$ ~0.99, respectively). Although both the P- and S-waves attenuations decrease linearly with the pore pressure, S-waves are more sensitive to the changes. This effect could be attributed to the nature of the torsional-wise propagation of shear waves (e.g. Biot 1956a,b), i.e. several repeated cycles of movement of particles from one solid half-space (i.e. rock) to fluid and then movement from fluid to another solid half-space. However, P-wave propagates in a longitudinal fashion, where the particles do not typically change their medium (e.g. Pyrak-Nolte et al., 1990; Cook, 1992).

The higher the applied pore pressures, the greater the relative contribution of the fluid-filled fractured volume on wave attenuation increases, and therefore, the quality factor decreases (Figure 7.9c). The P-wave quality factor ($Q_P$) shows higher sensitivity to the changes in pore pressure, compared to the quality factor of average S-waves ($Q_S$), as also observed in other studies (e.g. Kamali-Asl et al., 2018d). In addition, the range of $Q_P$-values lies between ~40 to ~250, while that of $Q_S$-values lies between ~12 to ~23, similar to other studies (e.g. Amalokwu, 2016). The lower values of quality factor for average S-waves compared to P-wave can be attributed to the different nature of the propagation of shear waves compared to compressional waves, as explained earlier.

#### 7.4.1.2 CONFINING PRESSURE VERSUS PORE PRESSURE EFFECTS

In order to investigate the effects of different depths of interest (i.e. different pore pressures and overburden stresses), the average ultrasonic signatures in all 10 stages of PCT for both P- and average S-waves were plotted with respect to pore pressure and confining pressure.

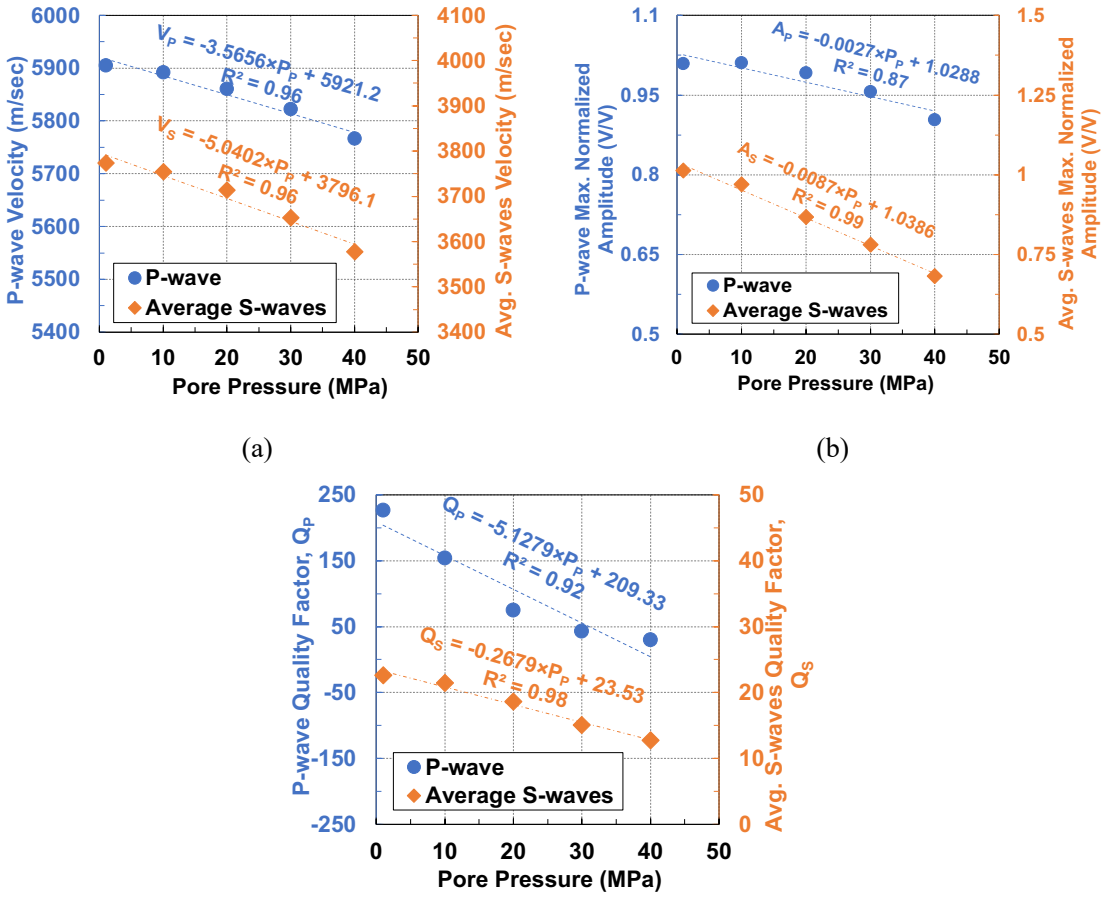


Figure 7-9. Variation of average seismic (a) velocities, (b) amplitudes, (c) quality factors against pore pressures in DCT

Figure 7.10a shows that as confining pressure increases/decreases, and under the same pore pressure, the wave velocities increase/decrease. For example, transitioning from CP=15 to 30 MPa, the P- and average S-waves velocities increase by ~1.5% and ~2.5%, respectively. This observation could be attributed to (i) closure of fracture at higher levels of confining pressure, and (ii) closure of stress-release induced micro-fractures, given the fact that the rock core was retrieved from a depth of 1.26 km (Kamali-Asl et al., 2018d). Same variations of effective stress at constant confining pressure (the DCT conditions),

carried P- and average S-wave velocities increases by ~1.2% and up to 4%, respectively. Hence, S-waves are more sensitive to the pore pressure than the confining pressure, while P-waves have a similar dependency to both.

The ultrasonic velocities show some degree of hysteresis associated with the unloading. The stiffening applied to the samples during the loading stress-path is not completely recovered during the unloading, resulting in little increases of both the Vp (~0.1%) and Vs (~0.3%), under the same state-of-stress. This observation could be attributed to the fact that stress corrosion occur as higher effective pressures are applied, and irreversible changes occur in the fracture aperture, leading to lower fracture aperture in the unloading cycle compared to the loading cycle (Yasuhara et al., 2004; Kamali-Asl et al., 2018a).

Figure 7.10b shows the maximum normalized amplitude increases for both P- and average S-waves with effective stress. For example, transitioning from $P_C$ = 30 to 15 MPa, the average normalized maximum P- and average S-waves amplitudes decrease by ~8% and ~65%, respectively. While, transitioning from $P_{down}$=11 to 0.5 MPa, the normalized maximum P- and S-waves amplitudes increase by ~8% and 166%, respectively.

Effective stress has more significant effects on the normalized maximum amplitudes of average S-waves compared to $_{that}$ of P-wave, and therefore, the range of variation is more significant, as also observed in the DCT. For example, the range of the normalized maximum amplitude for P- and average S-waves lies from 1.29 to 1.42 and 1.05 to 3.37, respectively. As for the ultrasonic velocities, hysteresis in maximum amplitude values for both P- and average S-waves from loading to unloading stages

suggests that the stress corrosion plays a crucial role in the stress-induced fracture response (e.g. Yasuhara et al. 2004; Faoro et al. 2016; Kamali-Asl et al. 2018a).

Figure 7.10c shows the variation of the average ultrasonic quality factors in each stage of the PCT against pore and confining pressure. As stated above, the P-wave attenuations (or equivalently quality factors) show significant scattering. The average S-waves ultrasonic quality factors increase with the confining and decrease with pore pressure, as also observed for ultrasonic velocities and amplitudes. For example, from $P_C$ = 30 to 45 MPa, the average value of attenuation for average S-waves increase by ~54%. While, from $P_{down}$ = 11 to 5.5 and then 0.5 MPa, the average attenuation of S-waves increases by ~19% and then ~82%. However, comparing the loading and unloading stress paths provides no evidences of the sensitivity of ultrasonic quality factors to stress corrosion.

### 7.4.2 FRACTURE-SPECIFIC STIFFNESS

Fracture-specific stiffness is defined as the slope of the stress-displacement curve (e.g. Cook 1992). Alternatively, the ultrasonic velocities and attenuations can be implemented to calculate fracture-specific stiffness (κ) using Eq. (7.2) (Choi et al., 2014):

$$\kappa = \frac{\omega \rho V_s}{\sqrt{\frac{1}{T_S^2} - 1}} \tag{7.2}$$

where $\kappa$ is the fracture-specific stiffness (Pa/m), $\omega$ is the central frequency of the signal (Hz), $\rho$ is the density of the rock specimen (kg/m$^3$), $V_S$ is the S-wave velocity (m/s), and $T_S$ is the unitless S-wave transmission coefficient.

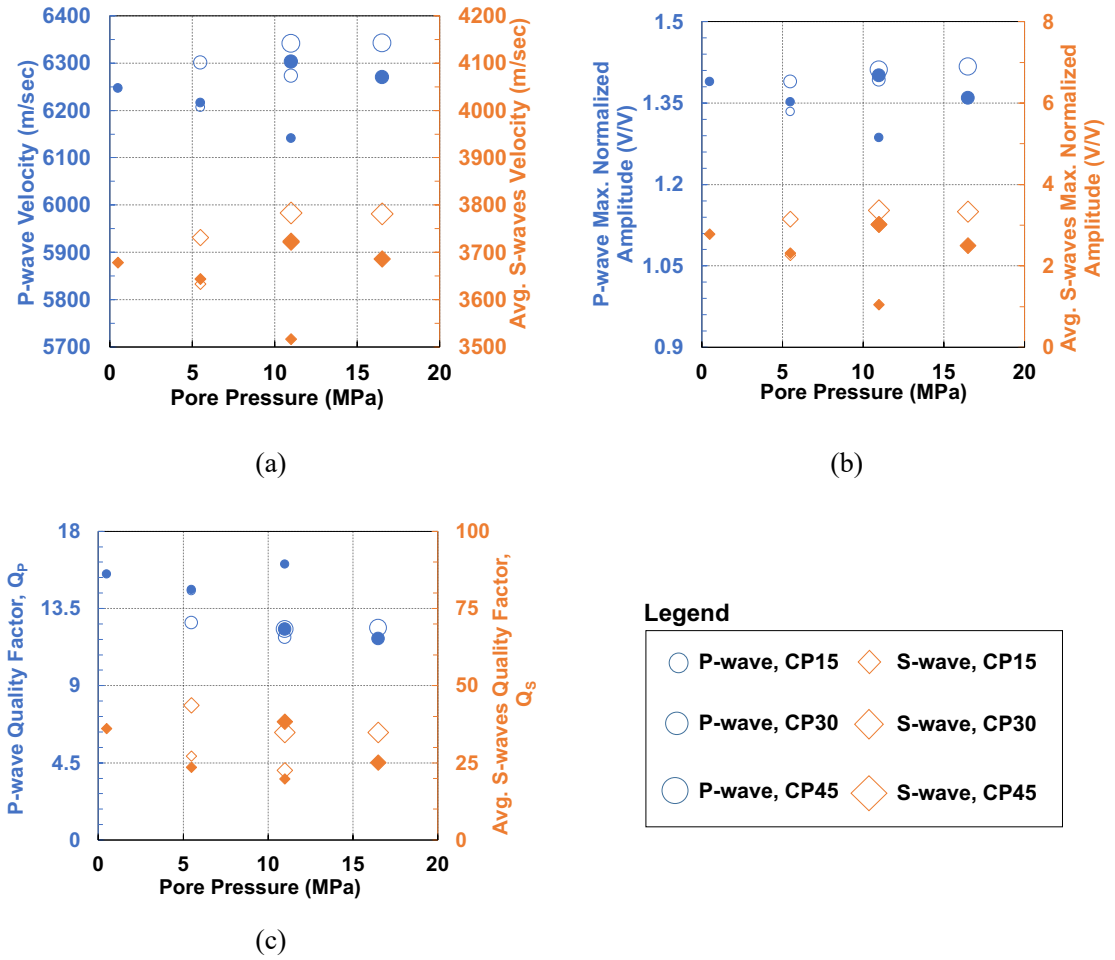


Figure 7-10. Variation of average seismic (a) velocities, (b) amplitudes, (c) quality factors against confining/pore pressures in the PCT. For better clarity, the horizontal axis is selected to reflect pore pressure and the size of the scatter points in the plots (circle for P-wave and diamond for average S-waves) reflect the confining pressure, with the smallest size referring to CP=15 MPa, the intermediate size referring to CP=30 MPa, and the biggest size referring to CP=45 MPa. It should be noted that the empty and filled scatter points (circles for P-wave and diamonds for average S-waves) reflect the loading and unloading stages, respectively.

Applying Eq. (7.2) for the DCT data, we observe that as pore pressure increases, the fracture specific stiffness decreases (Figure 7.11a). At lower pore pressures (i.e. higher effective pressures), the fluid-filled fracture volume is more reduced, and the fractured specimen is likely to deform less. Then, the effective stress contributes to increase the slope

of stress-displacement at the fracture interface and, in turn, fracture-specific stiffness. For example, from $P_{down}$ = 20 to 30 MPa, the fracture-specific stiffness decreases by ~23%.

Figure 7.11b shows the variation of fracture-specific stiffness at different stages of PCT, indicating an increase in κ values at higher levels of effective pressure (either when confining pressure increases or pore pressure decreases). This is consistent with the fact that at higher effective pressures, the fracture is being closed, and hence, the fractured specimen is likely to deform less. Therefore, fracture-specific stiffness values are higher, as also observed in the DCT. We observe that the individual contribution of each the confining and pore pressure lead to similar results. For instance, from $P_c$ = 30 to 45 MPa in the loading cycle, the fracture-specific stiffness increases by ~200%; while, from $P_{down}$ = 11 to 5.5 MPa and further to 0.5 MPa, in the unloading cycle, the fracture specific stiffness increases by ~200% in both cases.

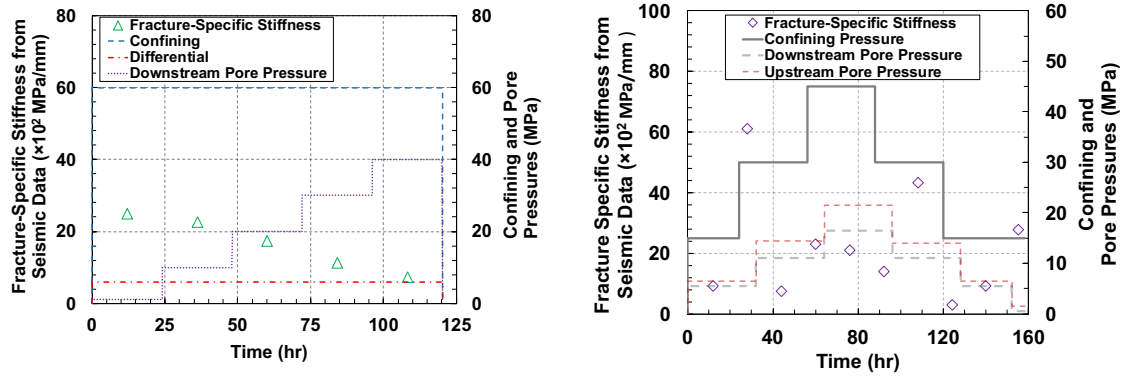


(a) (b)

Figure 7-11. Fracture-specific stiffness estimated from seismic data in (a) the DCT and (b) the PCT.

### 7.4.3 TIME-DEPENDENT RADIAL DISPLACEMENT MODELING

During DCT, the radial strains at the fracture surface were measured and used as an additional indication that fracture is closing under constant state-of-stress at different pore pressures levels. Two models known as Three-Element model and Power-Law model (Zoback 2010) were used to predict the longer-time time-dependent fracture displacement (perpendicular to the flow direction; see Figure A9.1c) of the fractured sample. The Three-Element model is composed of a dashpot and a Maxwell model (a spring and a dashpot in parallel) in series configuration, as shown in Figure 7.12. Eq. (7.3) shows the differential equation for this model (Zoback 2010):

$$\sigma + \frac{\eta_1 + \eta_2}{E}\dot{\sigma} = \eta_1\dot{\varepsilon} + \frac{\eta_1\eta_2}{E}\ddot{\varepsilon} \tag{7.3}$$

where σ is the applied pressure, ε is the time-dependent strain, $\eta_1$ is the dashpot coefficient, and $(\eta_2, E)$ are the dashpot and spring coefficients for Maxwell unit.

Solving Eq. (7.3) will result in the following expression for strain as Eq. (7.4) (Zoback 2010):

$$\varepsilon = \sigma\left[\frac{1}{\eta_1}t + \frac{1}{E}\left(1 - e^{-\frac{E}{\eta_2}t}\right)\right] \tag{7.4}$$

Power-Law model is defined as Eq. (7.5) (Zoback 2010):

$$\varepsilon = \sigma \times Bt^n \tag{7.5}$$

where ε is the time-dependent strain, σ is the applied pressure, and B and n are empirical parameters.

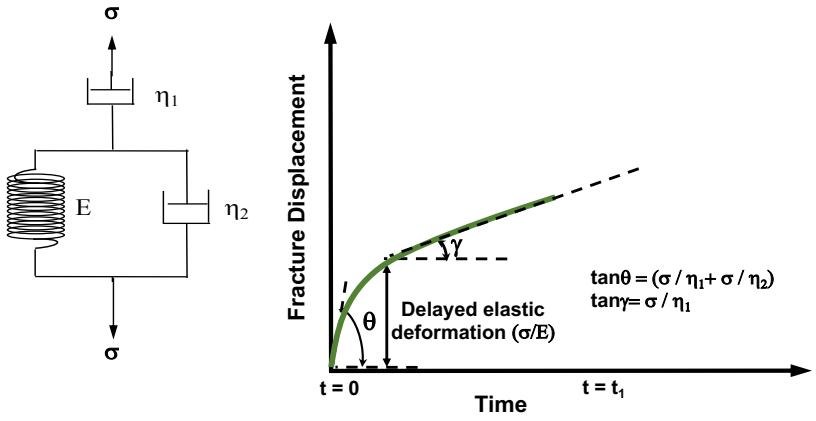


Figure 7-12. Schematic of Three-Element model and the displacement at the fracture surface perpendicular to the fracture surface

The experimental data (i.e. radial strains) were used to fit Three-Element rheological and Power-Law models and find the associated parameters (i.e. $\eta_1$, $\eta_2$, and E in the former and B and n in the latter). These five parameters were found at pore pressures of 10, 20, 30, and 40 MPa (see Table 7.1). In general, $B$ increases with the pore pressure, while $E$, $\eta_1$, $\eta_2$, and $n$ decrease. Figure 7.13 shows the variation of radial displacement at the fracture surface obtained from experimental data against the predicted curve using Three-Element rheological and Power-Law models, indicating that these two models successfully predict the time-dependent fracture displacement in flow-through experiments. It should be, however, noted that as the pore pressure increases the accuracy of the Power-Law model in long-term prediction decreases.

Table 7-1. Parameters of Three-Element and Power-Law Models

| Model | Parameter | Pore Pressure (MPa) | | | |
|---|---|---|---|---|---|
| | | 10 | 20 | 30 | 40 |
| Three-Element | E (GPa) | 1667 | 794 | 403 | 169 |
| | $\eta_1$ (GPa.h) | 12535 | 10288 | 8333 | 5447 |
| | $\eta_2$ (GPa.h) | 7590 | 2594 | 659 | 886 |
| Power-Law | n | 0.730 | 0.587 | 0.403 | 0.230 |
| | B ($MPa^{-1}$) $\times 10^{-6}$ | -0.622 | -0.777 | -1.04 | -1.55 |

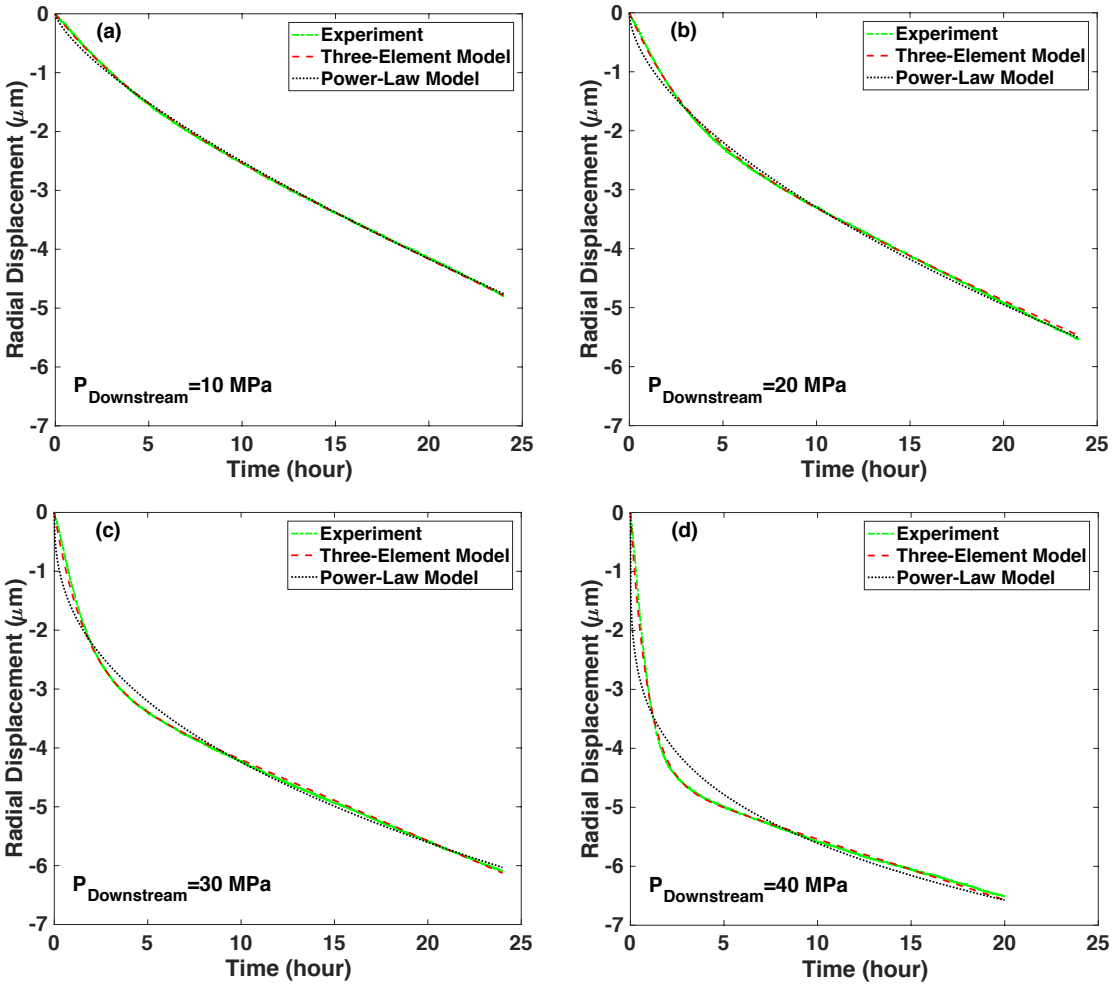


Figure 7-13. Modelling time-dependent fracture displacement at each stage of DCT using Three Element and Power-Law models for $P_{down}$ of (a) 10, (b) 20, (c) 30, and (d) 40 MPa

### 7.4.4 IMPLICATION FOR FIELD APPLICATIONS

The ultrasonic characteristics of fractured reservoirs is affected by the state-of-stress, i.e. overburden/pore pressures. We found that ultrasonic velocities, amplitudes, attenuations, and time-frequency maps change at different states-of-stress. In particular, the velocities decrease as the level of pore pressure changes, while, the ultrasonic amplitudes and attenuations increase. It is important to quantify the ultrasonic signatures at different states-of-stress, when ultrasonic measurements are to be made in the field to infer information about the field-of-interest. These geophysical signals propagate in long distances at different depths, and hence different levels of confining and/or pore pressures. Therefore, the interpretation of these geophysical measurements can be performed better if they are well-characterized at different levels of overburden/pore pressures. On the other hand, the long-term fracture closure under constant state-of-stress is important to evaluate as it reveals information about the long-term productivity of the fractured formations such as enhanced geothermal systems.

## 7.5 CONCLUSIONS

In this paper, fluid-fracture surface interactions at variable state-of-stress (i.e. pore and confining pressures) were investigated by conducting flow-through experiments on artificially-fractured phyllite samples, retrieved from Blue Mountain geothermal field. In particular, sensitivity of P- and cross-polarized S-waves ultrasonic signatures (i.e. velocity, amplitude, attenuation, and frequency content) and radial strains under variable state-of-stress were studied.

The results suggested that ultrasonic signatures can be potentially used as a proxy for fracture aperture alterations caused by the change in confining and pore pressures. An increase in pore pressure led to the opening of the fracture as indicated by increase in radial strains (during displacement-controlled test). The P-wave velocity and attenuation, and the velocity and maximum amplitude of cross-polarized S-waves can be potentially used as indicators of change in fracture aperture. In particular, a decrease in fracture aperture (due to increase of confining stress or decrease of pore pressure) led to (i) increase in the P- and S-wave velocity, (ii) decrease in the P-wave attenuation, and (iii) increase in the maximum amplitude of cross-polarized S-waves. However, the P-wave amplitude and S-waves attenuations exhibited less sensitivity to the change in the fracture aperture.

The time-frequency maps of the transmitted ultrasonic P-waves revealed two distinct higher and lower frequency bands of ~800 and ~200 kHz, while both S-waves revealed a higher and lower frequencies of ~650 and ~250 kHz, respectively. The higher frequency band might correspond to the body wave and the lower band to the fast interface wave (in case of P-wave) and slow interface waves (in case of S-waves). Frequency partitioning of the time frequency maps is sensitive to the changes in hydraulic aperture as the frequency partitioning is unchanged in DCT with constant hydraulic aperture. However, in PCT, where the hydraulic aperture is not constant during the experiment, the frequency partitioning is altered. At higher fracture specific stiffness values (i.e. confining pressure increases or pore pressure decreases), the body waves substantially contribute to the transmitted wave, while at lower fracture specific values (i.e. confining pressure decreases or pore pressure increases), the interface waves become more dominant.

Closure of fracture at a constant level of confining and pore pressures lead to reduction in the permeability of the fractured rock. Three-Element rheological and Power-Law models were used to predict the longer-term behavior of chemo-mechanical creep (i.e. radial displacement at the fracture surface) in flow-through experiments under constant pressures during DCT. It was found that both of these models can successfully predict the radial displacement at the fracture surface, with a reduced accuracy for the Power-Law model at higher pore pressures.

# CHAPTER 8

# EFFECTS OF CIRCULATING FLUID TYPE ON RESPONSE OF FRACTURED ROCKS IN GEOTHERMAL RESERVOIRS: AN EXPERIMENTAL STUDY

## ABSTRACT

In geothermal reservoirs, coupled thermal-hydrological-mechanical-chemical processes lead to gradual closure of fractures and consequent production decline. The objective of this study was to investigate the effects of injected fluid type on the evolution of fracture aperture/permeability at various stress levels through a series of flow-through experiments were performed on a fractured phyllite specimen, retrieved from Blue Mountain geothermal field. The injected fluids included deionized water, super- and under-saturated silica fluids, and the geothermal fluid extracted from the Blue Mountain geothermal field. It was found that fracture aperture/permeability reduction was the highest in the experiment with the injected geothermal fluid and the lowest in the experiment with the injected super-saturated silica fluid. In addition, the degree of permeability recovery, controlled by pressure solution, was lower in the experiment using geothermal fluid compared to the experiment using super-saturated silica fluid. On the other hand, chemical analysis of the effluent samples revealed that feldspars and quartz dissolution occurred in the experiment with injected deionized water and precipitation of silica in the experiment with injected geothermal fluid. The post-test observation by scanning electron microscopy of fracture surface area in the test with the injected super-saturated silica fluid indicated

some degree of mineral precipitation. A comparison between pre- and post-test computer tomography scan images for the experiment with injected super-saturated silica showed that mostly fracture sealing and/or mineral precipitation occurred, with minor mineral dissolution. Finally, the Three-Element Rheological model successfully predicted the fracture permeability decay. The results of this study suggested that precipitation of silica, a major problem in permeability loss of deep geothermal systems, can be potentially minimized by using fluid for injection that is closer to chemical equilibrium state with the host rock.

## 8.1 INTRODUCTION AND BACKGROUND

Reservoir production decline is one of the challenges in commercialization of deep geothermal systems (e.g. Polak et al., 2003; Yasuhara et al., 2004; Ghassemi et al., 2008; Ghassemi, 2012; Caulk et al., 2016; Faoro et al., 2016; Kamali-Asl et al., 2018a). Typically, large amounts of water are injected in operation of deep geothermal reservoirs, though large portion of the used water is recycled (MIT report, 2006; Kaya et al., 2011). As the so-called "cold fluid" (~ 60 to 90 °C when reaching depths of 3 to 5 km) is injected into the reservoir, it flows through the network of fractures and interacts with the host bedrock, triggering coupled Thermal-Hydrological-Mechanical-Chemical (THMC) processes that leads to alteration of permeability and typical reservoir production rate (e.g. Polak et al., 2003; Taron and Elsworth, 2010; Ishibashi et al., 2013; Caulk et al., 2016). Stress corrosion (i.e. crushing of contacting asperities due to stress concentration; see Figure 8.1a), free-face mineral dissolution/precipitation, pressure solution, thermal deformations/stresses, and mechanical creep are among the involved mechanisms that affect the permeability of

geothermal reservoirs (e.g. Yasuhara et al., 2013; Farough et al., 2016; Kamali-Asl et al., 2018b, 2018c).

Several studies have investigated the effects of coupled THMC processes on permeability decline in geothermal reservoirs (e.g. Ghassemi et al., 2008; Tao et al., 2011; Pandey et al., 2015; Caulk et al., 2016; Kamali-Asl et al., 2018a). The coupled THMC processes act at different time-scales (Taron et al., 2010; Vogler et al., 2016) and generally contribute to fracture permeability reduction. Thermal processes affect the response of geothermal reservoirs in short time-scales (e.g. Polak et al., 2003), while mechanical processes act in intermediate time-scales (e.g. Safari and Ghassemi, 2015), and chemical processes in prolonged time-scales (e.g. Faoro et al., 2016). The role of thermo-elastic stresses and heat conduction on permeability evolution significantly depends on the thermal expansion coefficient and porosity of rock mass (Germanovich et al., 2001), with higher permeability reduction in fractured rocks compared to intact rocks. This can be attributed to mineral dissolution and particle (grain) crushing at the propping asperities, with higher rates of dissolution/precipitation at higher temperatures (e.g. Savage et al., 1992; Morrow et al., 2001; Polak et al., 2003; Yasuhara et al., 2015). At higher rock temperatures, the contacting asperities are progressively compacted (Elsworth and Yasuhara, 2006), and heat extraction can be enhanced due to the creation of secondary thermal cracks (Tarasovs and Ghassemi, 2010; Ghassemi, 2012).

Pressure solution, a chemo-mechanical creep process, is reported to contribute to the permeability evolution in fractured reservoirs (e.g. Yasuhara et al., 2004), which is dominant in earlier times, leading to permeability reduction. However, free-face

dissolution is dominant in later times, resulting in slight increase of fracture permeability (Polak et al., 2003; Yasuhara et al., 2005; Liu et al., 2006; Yasuhara et al., 2006). Moreover, it is worth noting that fracture permeability reduction due to pressure solution is also directly influenced by the applied stress levels (e.g. Tao et al., 2011, Caulk et al., 2016, Kamali-Asl et al., 2018a) as shown schematically in Figure 8.1(a). Pressure solution phenomenon is dominant at low temperatures, while, at high temperatures (i) mineral dissolution/precipitation is another contributing mechanism to the permeability reduction (Faoro et al., 2016), (ii) permeability recovery is enhanced (Kamali-Asl et al., 2018a), and (iii) dissolution rate is increased for quartz (Savage et al., 1992) and calcite in (Rabemanana et al., 2003) in geothermal rocks.

The composition of injected fluid significantly influences the amount/rate of mineral dissolution/precipitation in geothermal reservoirs (Kumar and Ghassemi, 2005; Rawal and Ghassemi, 2014; Pandey et al., 2015). Precipitation/scaling of amorphous silica in reservoir/wells/power plant is one of the challenges in commercialization of deep geothermal systems (e.g. Xu et al., 2004; Kumar and Ghassemi, 2005). If the silica concentration in the injected water is less than that of the rock in equilibrium state (i.e. injected water is under-saturated), some of the silica minerals in the rock dissolve into the circulating water due to lower concentration of silica in the injectate. On the other hand, if the silica concentration of the injected water is higher than that of the rock in equilibrium state (i.e. injected water is super-saturated), then some of the minerals in the water precipitate on the fracture surface (e.g. Ghassemi and Kumar, 2007; Rawal and Ghassemi, 2014). Injection of over- and under-saturated silica fluids into a fractured reservoir leads to precipitation near production well and dissolution near injection well, respectively

(Pandey et al., 2015) and hence, lower permeability near the production well compared to injection well in both short- and long-terms scales (Rawal and Ghassemi, 2014). Therefore, the composition of the injected fluid can be designed to be at-equilibrium with the host rock (Xiong et al., 2013) in an attempt to potentially minimize the production decline caused by mineral precipitation in the fractured reservoir.

In our previous studies, the effects of different states-of-stress (Caulk et al., 2016), and different temperatures of injected fluid (Kamali-Asl et al., 2018a) on the evolution of fracture aperture/permeability have been investigated. Other studies have investigated the effects of chemo-mechanical processes on the response of fractured reservoirs through numerical modelling (Liu et al., 2006; Tao et al., 2011; Pandey et al., 2015; Rutqvist, 2015). However, very limited studies have focused on the effects of injected fluid type on the evolution of fracture aperture/permeability. The importance of the composition of the circulating fluid in potentially minimizing the production decline caused by mineral precipitation in fractured reservoirs warrants further investigation to gain more insight into the potential role it can play in optimizing geothermal reservoir production.

The Blue Mountain geothermal reservoir, a hot brine geothermal field, contains neutral-pH, dilute alkaline-chlorine waters (Casteel et al., 2009), with high injectivity potential according to the injection test at a depth of 5600 ft, where the maximum initial temperature is in the order of 210 °C (Casteel et al., 2009). Aeromagnetic and gravity data have indicated that the geothermal field is located along a pre-existing crustal fracture (Ponce et al., 2009), which mostly consists of mafic dike. The characterization of fracture connectivity demonstrated that calcite scaling could occur at an average temperature of 160

°C, which is a common temperature at the Blue Mountain geothermal field (Sumner et al., 2015). The reservoir has experienced over 20 °F temperature drop from 2009 to 2011 and consequent power output decrement due to the initial injection strategy (Swyer et al., 2016). In a new injection strategy, the injection flow was moved to the wells located in northern part of the field and the western deep wells were closed, leading to improved power output (Swyer et al., 2016).

AltaRock Energy Inc. provided a phyllite rock core (see Figure A8.1a), retrieved from DB-2 well at a depth of 1260 m in Blue Mountain geothermal field, which was sub-cored into 4 specimens (two intact and two fractured). The results on (i) mechanical characterization of intact specimens, and (ii) sensitivity of seismic signatures under constant and varying state-of-stress for one of the fractured specimens are reported in companion papers (Kamali-Asl et al., 2018b, 2018c, 2018d). In this study four injection fluids including deionized water, super- and under-saturated silica fluids, and geothermal fluid (extracted from Blue Mountain field) were used in flow-through experiments. The evolution of hydraulic properties (i.e. fracture aperture/permeability) were investigated using hydraulic data, SEM and X-Ray CT-scan images, and chemical composition of the effluent samples.

## 8.2 MATERIALS

The phyllite rock core had a diameter and length of 2.5 and 9 inches, respectively, as shown in Figure A8.1a, a bulk dry density of 2.69 g/cm$^3$, a porosity of 0.74%, and is relatively-homogenous and isotropic, with no apparent micro-cracks in the texture of the core. Quantitative X-Ray Diffraction (XRD) analysis showed that the core contained

67.4% quartz, 18.8% albite, 10.5% biotite, and 3.2% chlorite. A vertical sub-core was drilled with a diameter and a length of 1.5 and 1.88 inches, which was used in this study and shown in Figure A8.1b.

Four different fluids, with their composition provided in Table 8.1, were used as circulating fluid in flow-through experiments to investigate different patterns/rates of mineral dissolution/precipitation caused by composition variation of the circulating fluid. Deionized water, super- and under-saturated fluids with respect to silica, and geothermal fluid extracted from Blue Mountain geothermal field were used as the circulating fluid and the effluent was collected upon completion of each experiment. The compositions of the influent and effluent fluids were analyzed using ICP-OES and are reported in Table 8.1.

## 8.3 EXPERIMENTAL METHODOLOGY

The experiments of this study were performed in displacement-controlled mode, as explained in Appendix F.

### 8.3.1 CHEMICAL ANALYSIS

Analysis of the influent and effluent samples collected at the end of each experiment was performed using a JY Horiba Optima 2 ICP-OES instrument housed at the Geology Department, University of Vermont. Samples were acidified with 1% ultrapure $HNO_3$ and concentrations of Al, Ca, Fe, K, Mg, Mn, Na, and Si were determined.

### 8.3.2 IMAGE ANALYSIS

A Brucker SkyScan 1173 Micro-Computed Tomography (CT), housed in the Imaging Laboratory at the Department of Civil and Environmental Engineering, University of Vermont, was used to scan the pre- and post-test specimens with a resolution of 20.1 microns. The boundary greyscale thresholding of the pre- and post-CT scans were equally performed following the standard approach for CT-image processing (ASTM, 1992). Although it was desired to use pre- and post-test CT images to accurately estimate the change in fracture aperture along the length of the specimen, the fact that the pre- and post-test CT images were obtained at atmospheric pressure and room temperature (not experimental condition) prevented performing this analysis. However, the pre- and post-CT-images at few sections along the length of the rock specimen were compared to identify regions with mineral dissolution/precipitation and fracture sealing.

In addition, secondary and back-scattered Scanning Electron Microscopy (SEM) images of a selected region of fracture surface were taken using a JEOL 6060 housed in Microscopy Imaging Center at the University of Vermont. Images acquired in secondary electron mode can reveal patterns of mineral dissolution/precipitation regions, while, backscattered electron mode images can reveal valuable information about the composition of the elements in a selected region.

### 8.3.3 EXPERIMENTAL CONDITIONS

As the rock core was extracted from a depth of ~1260 m, considering overburden stress and pore pressure gradients of 24.1 and 8.8 MPa/km, the in-situ overburden stress

and pore pressure were estimated as 30 and 11 MPa, respectively (Cladouhos et al., 2016). To better study the permeability evolution during loading and unloading at states-of-stress lower, equal, and higher than in-situ conditions, a generic stress path shown in Figure 8.1b was designed and followed during the experiments. Effective pressure was increased step-wise (i.e. 9.5, 19, and 28.5 MPa) during loading stages and decreased step-wise (i.e. 19 and 9.5 MPa) during unloading stages and was kept constant for 27 to 36 hours during each stage. The unloading stages were performed as it was desired to evaluate the reversibility of hydraulic aperture and fracture permeability due to pressure solution. The loading increase/decrease rate during transition from one loading/unloading stage to the next was 0.333 MPa/sec.

The stress path followed in all four experiments were very similar, except few changes, which were made to better understand the involved mechanisms in the permeability evolution. In the test with deionized water as circulating fluid, confining and downstream pore pressure were increased/decreased simultaneously. However, in the rest of the experiments, in order to separately study the effects of confining and pore pressures on the evolution of fracture aperture/permeability, a time-lag of 3 to 8 hours was considered between instances of increase/decrease in confining pressure with those of downstream pore pressure.

The temperatures of the bedrock and circulated fluid in the field were determined as 155 and 75 °C, respectively. In the experiments, the temperature of the rock specimen and the circulated fluid were set at 130 and 65 °C, respectively. Effort was made to keep the temperature difference between circulated fluid and the rock specimen close to field

conditions, given the instrument limitation for temperature's upper bound of 130 °C for the rock specimen.

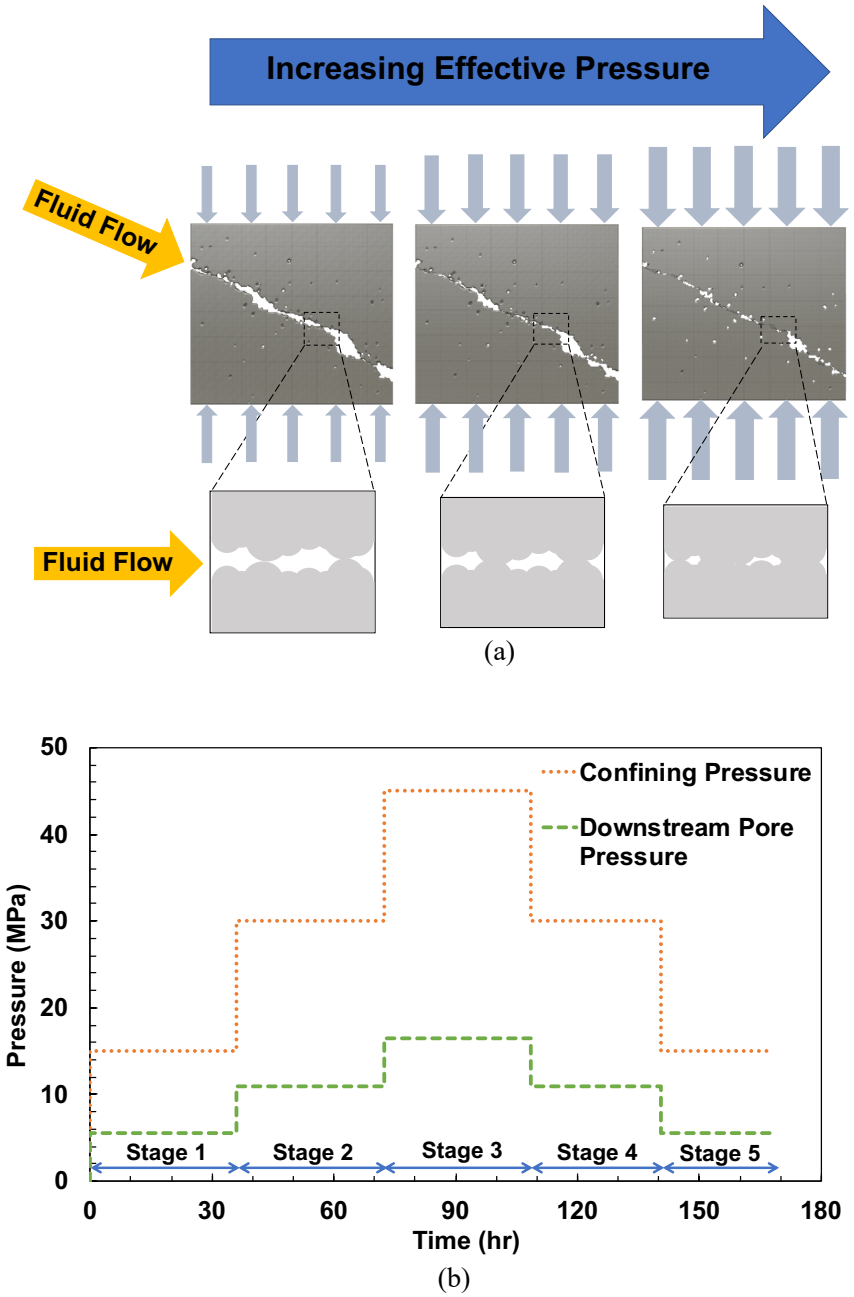


Figure 8-1. (a) Schematic of fracture closure due to stress corrosion at the contacting asperities, and (b) generic stress path followed during the experiments of this study

## 8.4 RESULTS

The upstream and downstream pore pressure measurements were collected every 1 second during the experiments and binned to every 2 hours for better clarity in the presented figures, where the evolution of differential pore pressure (ΔP) during each experiment is super-imposed on the stress path. Sections 8.4.1 to 8.4.4 present the results of flow-through experiments using deionized water, geothermal fluid, and super- and under-saturated fluids, respectively.

### 8.4.1 DEIONIZED WATER AS CIRCULATING FLUID

Figure 8.2a shows the evolution of differential pore pressure super-imposed on the stress path. It can be observed that the differential pore pressure (ΔP) increases during the first three stages of the test, i.e. loading stages. This might be explained by the fact that at higher effective pressure levels, in addition to the increased number of contacting asperities (see Figure 8.1a), the effect of pressure solution is more pronounced, which leads to higher fracture closure rates. Subsequently, fractured volume decreases, and hence, differential pore pressure increases to maintain the constant pre-scribed injection rate.

It should be noted that, since the downstream pore pressure is constant during each stage, the increase of ΔP resulted from increase of upstream pore pressure. This increase in ΔP is an indication of the partial closure of the fracture and in turn, permeability loss. As it can be seen in Figure 8.2b, the fracture permeability and hydraulic aperture of the specimen decreased from $9.14\times10^{-20}$ to $4.90\times10^{-20}$ $m^2$ and from 0.32 to 0.26 μm, respectively, in the first stage of the test. In the first 3 to 4 hours of each stage, the hydraulic

equilibrium was not achieved, and ΔP values are very low. Hence, the data for this time period do not provide reliable estimation of permeability. Likewise, transitioning from one CP/PP stage to another, the data for the first 3 to 4 hours are not true indicatives of permeability. But rather, the upstream pore pressure intensifier attempts to catch up the prescribed injection rate by increasing the upstream pore pressure. The fracture permeability and hydraulic aperture at the end of the third stage reach to $4.28\times10^{-21}$ $m^2$ and 0.12 μm, respectively. The unloading stages, namely stages 4 and 5, show a decreasing trend of ΔP, which is an indication of permeability enhancement during each stage. This observation could have resulted from rock shifting as a consequence of mechanical creep and/or mineral dissolution/precipitation. The fracture permeability and hydraulic aperture at the end of the experiment reached to $3.69\times10^{-20}$ $m^2$ and 0.24 μm, indicating 60% and 25% reduction, respectively.

### 8.4.2 GEOTHERMAL FLUID AS CIRCULATING FLUID

Figure 8.3a shows the measured differential pore pressures super-imposed on stress path for the test with geothermal fluid as the circulating fluid. The stress path for this experiment was slightly modified to de-couple the effects of increase in confining pressure and downstream pore pressure on the evolution of fracture permeability and hydraulic aperture. After performing the first stage of the stress path, the confining pressure was first increased to the next desired level and then kept constant; while, the downstream pore pressure was not increased. The values of upstream pore pressure were measured for 3 hours and then, the downstream pore pressure was increased to the proportionate value of confining pressure (with a ratio of 11:30 as stated in section 3.5). Then, the upstream pore

pressure was measured for 30 hours during each stage. As shown on Figure 8.3a, the values of ΔP are one order of magnitude lower than those measured in the test with deionized water as circulating fluid. This can imply that since the geothermal fluid was obtained from the field and was chemically-equilibrated with the reservoir rock, the chemical composition of the geothermal fluid is more compatible with this reservoir rock and therefore, less mineral dissolution/precipitation was observed. In addition, it was found that the downstream pore pressure has an effect on permeability evolution, since ΔP is higher at a lower downstream pore pressure. The fracture permeability and hydraulic aperture were changed from $3.32\times10^{-19}$ to $3.39\times10^{-20}$ $m^2$ and from 0.49 to 0.23 μm, respectively; and recovered back to $5.48\times10^{-20}$ $m^2$ and 0.27 μm, as shown in Figure 8.3b, which shows one order of magnitude irrecoverable decrease in the permeability. Moreover, as evident in Figure 8.3b, during both loading and unloading stages, and at each stage, permeability decreases, which could be an indication of mineral dissolution/precipitation. In addition, the geothermal fluid has been already chemically-equilibrated with the geothermal bedrock, and therefore, fewer chemical reactions are expected to occur, and hence, the initial permeability of the specimen is not altered significantly.

In addition, it was found that the downstream pore pressure has an effect on permeability evolution, since ΔP is higher at a lower downstream pore pressure. The fracture permeability and hydraulic aperture were changed from $3.32\times10^{-19}$ to $3.39\times10^{-20}$ $m^2$ and from 0.49 to 0.23 μm, respectively; and recovered back to $5.48\times10^{-20}$ $m^2$ and 0.27 μm, as shown in Figure 8.3b, which shows one order of magnitude irrecoverable decrease in the permeability. Moreover, as evident in Figure 8.3b, during both loading and unloading

stages, and at each stage, permeability decreases, which could be an indication of mineral dissolution/precipitation. In addition, the geothermal fluid has been already chemically-equilibrated with the geothermal bedrock, hence, fewer chemical reactions are expected to occur, and hence, the initial permeability of the specimen is not altered significantly.

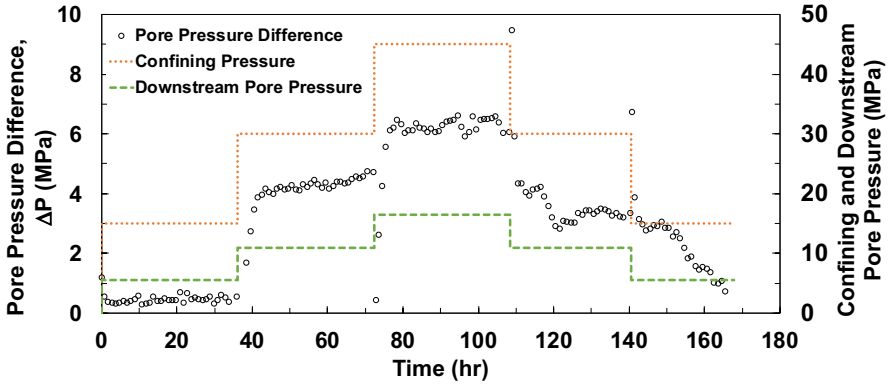


(a)

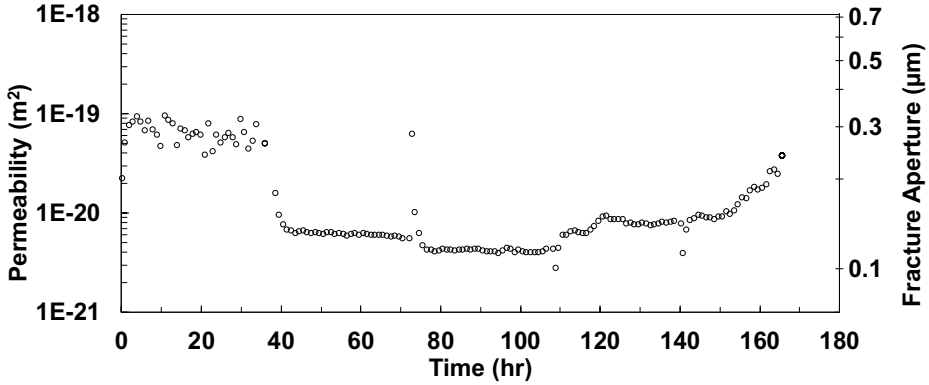


(b)

Figure 8-2. Hydraulic data during experiment with deionized water as circulating fluid: (a) differential pore pressure data super-imposed on stress path, (b) evolution of fracture aperture/permeability

### 8.4.3 SUPER-SATURATED $SiO_2$ FLUID

The measurements of ΔP super-imposed on stress path (same with the experiment with circulated geothermal fluid) for the test with super-saturated $SiO_2$ circulating fluid are

provided in Figure 8.4a. Compared to tests with deionized water and geothermal fluids as circulating fluids, the highest differential pore pressure was observed in this test, which in part can be attributed to mineral dissolution/precipitation as a result of injection of super-saturated silica fluid. The fracture permeability and hydraulic aperture decrease from $5.17\times10^{-20}$ to $1.33\times10^{-21}$ $m^2$ and from 0.27 to 0.08 µm, respectively, and recovered back to $4.13\times10^{-21}$ and 0.11 µm, respectively, as illustrated in Figure 8.4b. Similar to the experiment with geothermal fluid, the permeability dropped one order of magnitude, indicating importance of stress corrosion phenomena on fracture response.

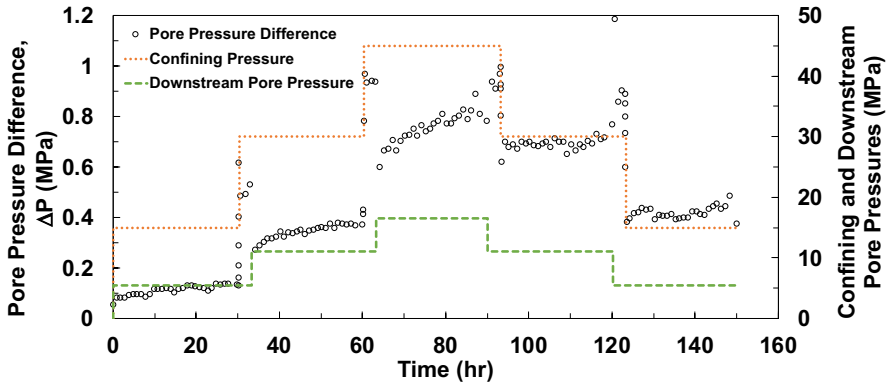


(a)

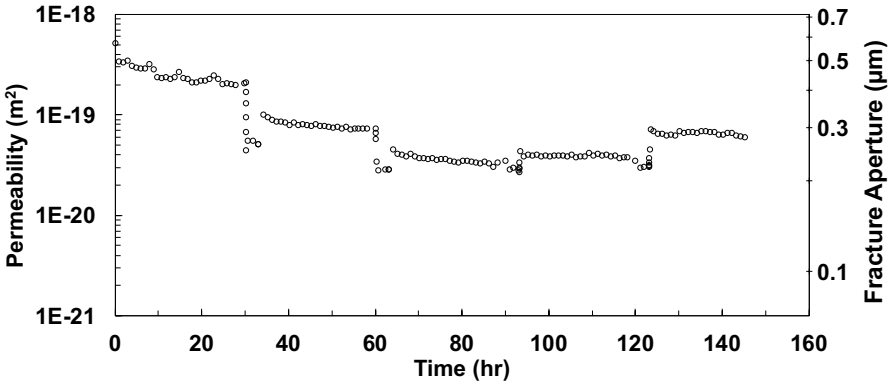


(b)

Figure 8-3. Hydraulic data during experiment with geothermal fluid as circulating fluid: (a) differential pore pressure data super-imposed on stress path, (b) evolution of fracture aperture/permeability

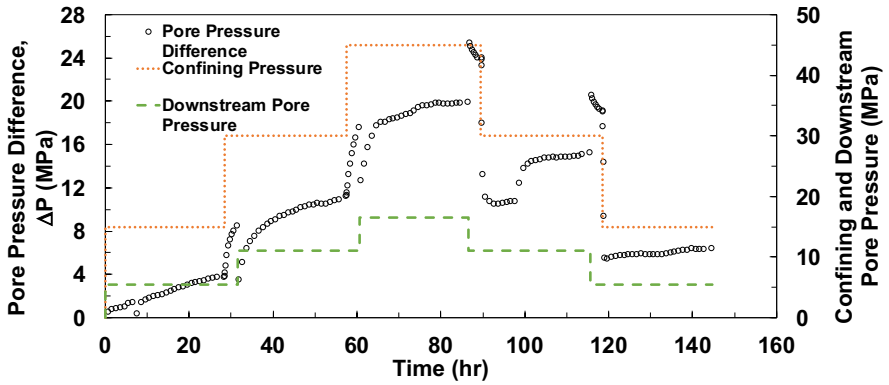


(a)

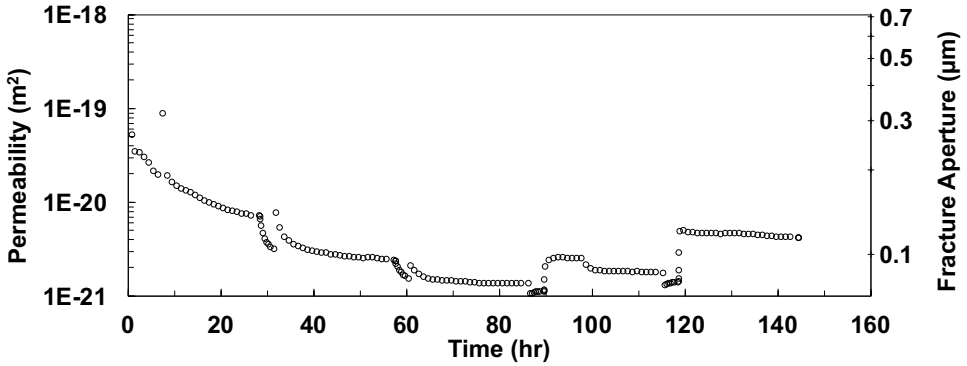


(b)

Figure 8-4. Hydraulic data during experiment with super-saturated silica circulating fluid: (a) differential pore pressure data super-imposed on stress path, (b) evolution of fracture aperture/permeability

### 8.4.3.1 ANALYSIS OF CT-SCAN AND SEM IMAGES

Figure 8.5 shows the pre- and post- test CT-scan images for the experiment using super-saturated silica fluid, indicating regions with mineral dissolution/precipitation and fracture sealing at four sections along the core with different distances (9.5, 19, 28.5, and 38 mm) from the inlet (i.e. downstream). At each location, a small region is magnified to better illustrate the mineral dissolution/precipitation and/or fracture sealing. It can be

inferred that, in all four locations along the core, the fracture experiences closure, though with different patterns/rates, depending on the distance from the inlet/outlet. This observation is in-agreement with the hydraulic data, which showed a significant decrease in fracture aperture/permeability in the experiment using super-saturated silica fluid.

Figure 8.6a shows the BSE image of a selected region near the outlet, where the effluent fluid is collected, taken after the experiment using super-saturated silica circulating fluid. Figure 8.6b is a magnified region of Figure 8.6a, where it can be seen in some spots (closer to the outlet) that some particles have not been washed out by circulated fluid. Figure 8.6c shows the results of EDS for different elements of Al, Fe, K, Mg, O, and Si in five different regions. It can be inferred that the primary minerals are (i) plagioclase in Region 1, (ii) muscovite in Region 2, (iii) biotite and/or chlorite in Region 3, (iv) K-feldspar and/or iron-oxide in Region 4, and (v) quartz in Region 5, have occurred. Figures 8.6d-f show the SEM images of different regions on the fracture surface at three different scales, indicating mineral precipitation in all of them. Figure 8.6f indicates the existence of a crystal, which might be attributed to precipitation of quartz.

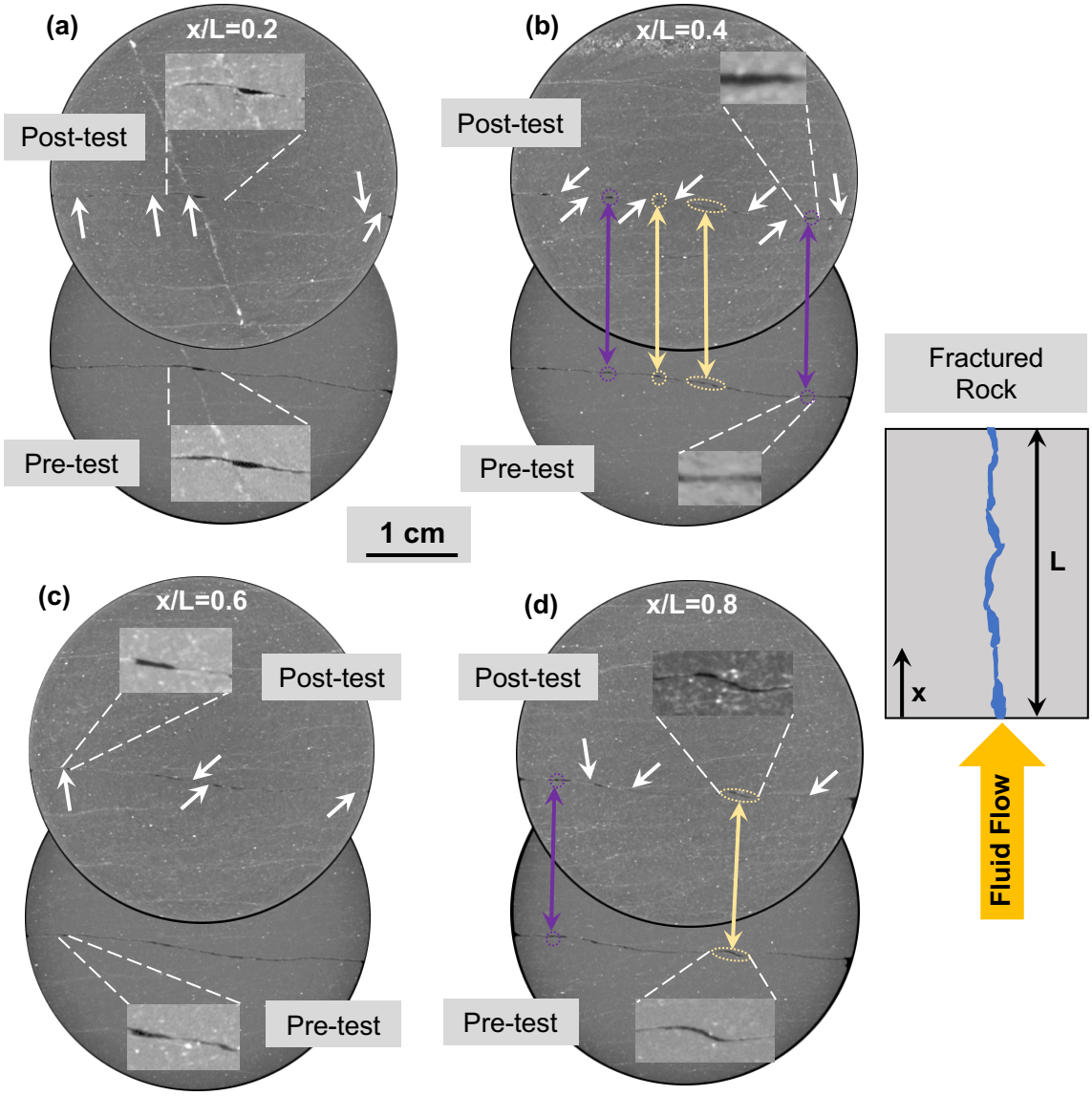


Figure 8-5. Pre- and post- test X-Ray Micro-CT images of the cross section (one near outlet, two in middle sections, and one near inlet) of the specimen in the experiment using super-saturated silica circulating fluid.

Note #1: The white arrows show regions with sealing, the purple circles indicate regions with dissolution, and yellow ovals show regions with precipitation (not necessarily sealing).

Note #2: Some regions were magnified to better show dissolution/precipitation and/or fracture sealing

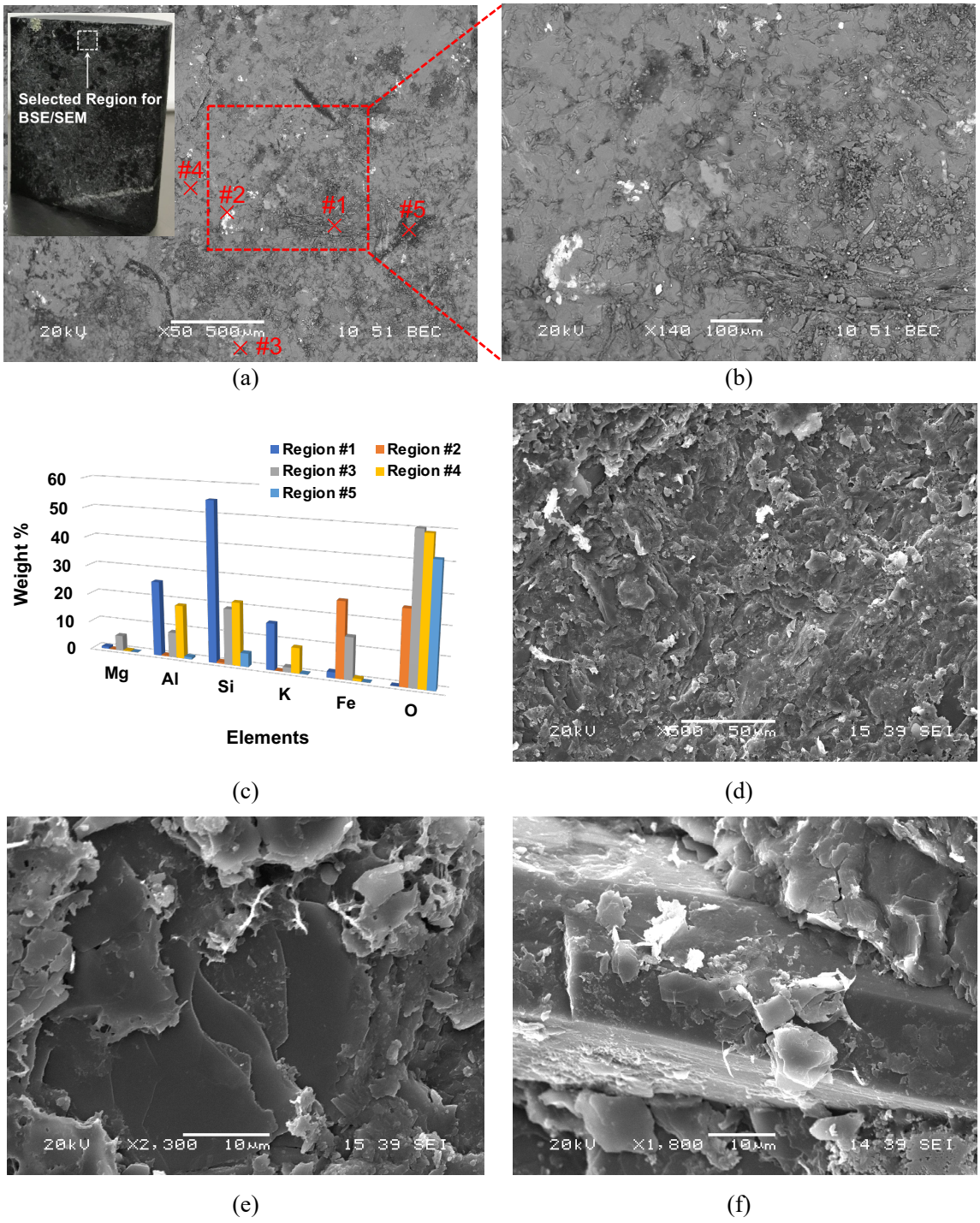


Figure 8-6. Backscattered electron microscopy images at (a) X50 and (b) X140; (c) the distribution of elements in the five spots of BSE image (at X50) using energy dispersive X-Ray spectroscopy (EDS); and secondary electron microscopy images at (d) X500, (e) X2300, and (f) X1800; after the experiment with circulated super-saturated silica fluid.

### 8.4.4 UNDER-SATURATED $SiO_2$ FLUID

Figure 8.7a shows the measurements of differential pore pressure super-imposed on stress path for the test with under-saturated $SiO_2$ circulating fluid. The same stress path as that of experiment with super-saturated fluid was followed, except that the initial equilibrium time was set higher as 36 hours. The results show that the values of differential pore pressure do not imply a uniform pattern of mineral dissolution/precipitation, which could be in part attributed to the fact that the circulated fluid was under-saturated with respect to silica. However, in some time instances, further precipitation in flow veins which were not saturated with respect to silica might occur. In addition, it appears that the values of $\Delta P$ in this test are significantly lower than those measured during the test with injection of super-saturated silica fluid. This is an indication of less mineral precipitation in this experiment compared to that of experiment with super-saturated silica fluid. As illustrated in Figure 8.7b, during loading stages the fracture permeability and hydraulic aperture increase from $5.97\times10^{-21}$ to $9.0\times10^{-21}$ $m^2$ and from 0.13 to 0.15 μm, respectively, and further increased to $11.1\times10^{-21}$ and 0.16 μm during unloading stages.

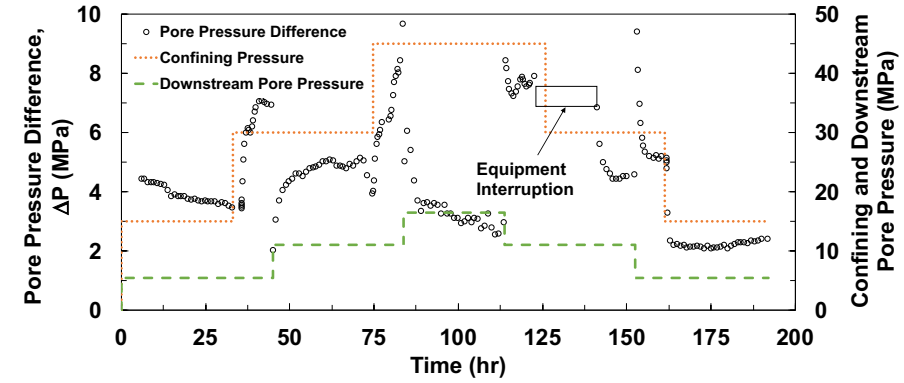


(a)

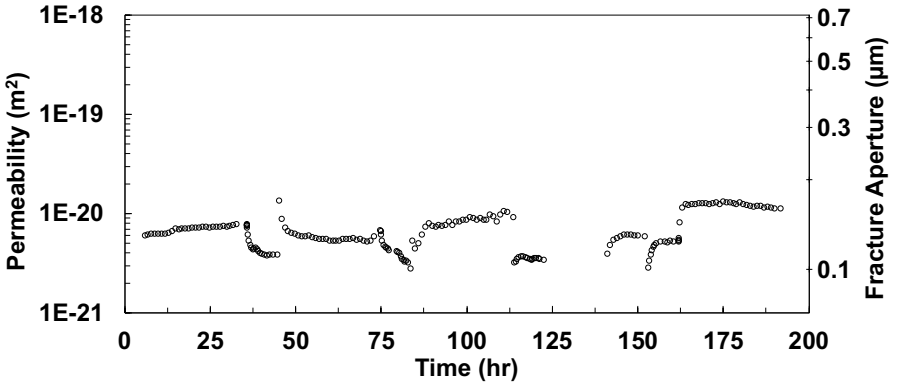


(b)

Figure 8-7. Hydraulic data during experiment with super-saturated silica circulating fluid: (a) differential pore pressure data super-imposed on stress path, (b) evolution of fracture aperture/permeability

### 8.4.5 ICP RESULTS

The elemental compositions of the influent and effluent samples are provided in Table 8.1. It can be inferred that there is a net dissolution of quartz and feldspars in the experiment using deionized water, as the concentration of all elements are increasing in the effluent compared to its influent. In the experiment using geothermal fluid, the precipitation of silica occurred, as it is not an exchangeable element. For the experiments with circulated under- and super-saturated silica fluids, comparing the ICP analysis for

influent and effluent samples indicate cation-exchanging between different elements rather than mineral dissolution/precipitation, as opposed to the experiments with circulated deionized water and geothermal fluid. In addition, the concentration of Na in both super- and under-saturated silica fluids is very high in influent and effluent samples, which is originating from the fact that these fluids are brine.

Table 8-1. Chemical composition of the influents and effluents of the four circulating fluids using ICP-OES analysis

| | | Al | Ca | Fe | K | Mg | Mn | Na | Si | pH |
|---|---|---|---|---|---|---|---|---|---|---|
| Deionized Water | Inf. | BDL | < 0.5 | BDL | < 0.5 | BDL | BDL | < 0.5 | <0.3 | 7.29 |
| | Effl. | 0.03 | 2.15 | BDL | 1.25 | 0.37 | 0.013 | 1.41 | 0.64 | 7.90 |
| Geothermal Fluid | Inf. | 0.19 | 44.98 | 1.09 | 457.7 | 2.2 | 0.085 | 3453.67 | 76.15 | 7.63 |
| | Effl. | 0.24 | 43.09 | 0.14 | 434.46 | 0.56 | 0.052 | 3330.44 | 62.92 | 7.23 |
| Super-saturated Si-Fluid | Inf. | 0.12 | 1.09 | 0.1 | 16.36 | 0.12 | 0.011 | 2682.55 | 183.03 | 10.67 |
| | Effl. | 1.57 | 0.94 | 0.23 | 60.15 | 0.01 | 0.008 | 2537.91 | 183.83 | 10.90 |
| Under-saturated Si-Fluid | Inf. | 0.04 | 0.25 | 0.03 | 0.42 | 0.01 | 0.006 | 7.46 | 5.39 | 3.46 |
| | Effl. | 0.07 | 4.91 | BDL | 3.12 | 0.37 | 0.025 | 6.23 | 5.85 | 7.19 |

Note: Inf.: Influent; Effl.: Effluent

## 8.5 DISCUSSION

### 8.5.1 DECOUPLING THE EFFECTS OF CONFINING AND PORE PRESSURES ON FRACTURE PERMEABILTY

Increasing effective pressure leads to an increase in differential pore pressure, as also observed in other studies (e.g. Faoro et al., 2016; Kamali-Asl et al., 2018a). This is attributed to the fact that at higher effective pressure levels: (i) some of the flow paths are

blocked, and (ii) the number of asperities in-contact increases, as shown in Figure 8.1a. This in turn, causes crushing of the contacting asperities, which is an essential part of pressure solution phenomenon, followed by diffusion and precipitation of the crushed particles along the flow path (Yasuhara et al., 2003; Taron and Elsworth, 2010). Eventually, the permeability of the specimen decreases, and therefore, the upstream pore pressure intensifier increases the upstream pore pressure to maintain the prescribed constant injection rate. In Stages 4 and 5 (i.e. during unloading path), the permeability does not recover back to the same values as in Stages 2 and 1, respectively, as also reported in other studies (e.g. Faoro et al., 2016; Kamali-Asl et al., 2018a). This, in part, can be attributed to the contribution of pressure solution/stress corrosion, which cause some degree of irreversible permeability decay. In addition, movement of possible loose grains, created during the process of specimen fracturing, with fluid along the fracture can contribute to closure of fracture.

One might expect that the permeability of the fractured specimen continuously decreases as the experiments are ongoing, however, inspecting the permeability data indicates that there are time instances where the specimen experiences a sudden increase in its permeability. This can be attributed to the fact that, as the upstream pore pressure intensifier increases the upstream pore pressure to maintain the prescribed constant injection rate, it is likely that: (i) some of the blocked flow paths are reopened, and/or (ii) some new flow paths are created, as also reported in other studies (Caulk et al., 2016; Kamali-Asl et al., 2018a). The initial fracture geometry, particularly, the shape, number and spatial distribution of asperities; hardness of asperities; and the way that the two pieces of the fracture have been mated together are among important factors that influence (i) the

initial fracture permeability (Pyrak-Nolte and Morris, 2000; Farough et al., 2016), (ii) mechanical aspect of pressure solution phenomenon (Yasuhara and Elsworth, 2008; Yasuhara et al., 2011); and (iii) the percentage of permeability recovery (Kamali-Asl et al., 2018a).

During the experiments with geothermal, super-, and under-saturated silica fluids, there was a time-lag between instances of increase/decrease of confining pressure and those of downstream pore pressure. It appeared that increasing/decreasing the downstream pore pressure, under constant confining pressure, leads to a sudden increase/decrease in the permeability of the fractured specimen. This, in part, is attributed to the fact that some of the contacting asperities open up at higher levels of downstream pore pressure, which in turn, leads to lower number of contacting asperities at higher levels of downstream pore pressure. For example, transitioning from $P_{down}$=5.5 to 11 MPa, at a constant confining pressure of 30 MPa, the permeability of the specimen for experiments with geothermal and super-saturated silica fluids increase by 97% and 142%, respectively.

On the other hand, increasing/decreasing the confining pressure, under constant downstream pore pressure, controls the rate of the permeability reduction within each stage. At higher levels of confining pressure, the rate of permeability decay is less than that of lower confining pressures. For example, in the experiment using super-saturated silica fluid, permeability decay of the specimen at a confining pressure of 30 MPa, for $P_{down}$=5.5 and 11 MPa are 55.8% and 53.5%, respectively; while, the permeability decay at a confining pressure of 45 MPa, for $P_{down}$=11 and 16.5 MPa are 36.3% and 35.9%, respectively. This could be attributed to the fact that at higher confining levels, the

specimen has already experienced some degree of stress corrosion and hence, there is less potential for additional particle crushing at contacting asperities by stress corrosion. In addition, the total available free-face for mineral dissolution/precipitation is reduced at higher confining levels, as schematically shown in Figure 8.1a.

### 8.5.2 TIME-DEPENDENT PERMEBILITY EVOLUTION

Modeling permeability decay can provide insight into the long-term response of fracture and in some cases can potentially be used for long-term fracture response prediction under reservoir conditions. While empirical correlations for permeability decay can be developed by fitting different functions (e.g. power, exponential) to experimental data (Kamali-Asl et al., 2018a), models that capture fracture deformation and subsequently permeability decay can potentially represent fracture response more realistically. Traditionally, Burger's and Power-Law models are used to predict the mechanical creep in rocks with high amount of clay (e.g. Sone and Zoback, 2013b). We propose to use Three-Element Rheological model to predict longer-term chemo-mechanical creep (i.e. fracture closure) and then estimate corresponding permeability decay using modified cubic law (Eq. (A7.2)). Three-Element model is composed of a dashpot and a Maxwell model (a spring and a dashpot in parallel) in series configuration, as shown in Figure 8.8a. Eq. (8.1) shows differential equation for this model (Zoback, 2010):

$$\sigma + \frac{\eta_1 + \eta_2}{E}\dot{\sigma} = \eta_1 \dot{b} + \frac{\eta_1 \eta_2}{E}\ddot{b} \tag{8.1}$$

where σ is the applied pressure, b is time-dependent fracture aperture, $\eta_1$ is the dashpot coefficient, and $(\eta_2, E)$ are the dashpot and spring coefficients for Maxwell unit.

Solving Eq. (8.1) will result in the following expression for hydraulic aperture:

$$b = \sigma\left[\frac{1}{\eta_1}t + \frac{1}{E}\left(1 - e^{-\frac{E}{\eta_2}t}\right)\right] \tag{8.2}$$

The permeability decay for the experiment using supersaturated silica fluid as representative experiment was modelled. First the best-fit parameters for $\eta_1$, $\eta_2$, and $E$ were estimated for the five stages of the experiment with circulated super-saturated silica fluid. These three parameters were then used to plot the model predictions against experimental data for each of the five ~24-hour stages, as shown in Figures 8.8b-f.

It can be inferred that as higher effective pressures are applied to the specimen, the values of $\eta_1$, $\eta_2$, and $E$ increase. The parameters $E$ and $\eta_1$ indicate how fast the hydraulic aperture of the specimen decreases over a very short period of time. We propose that these parameters can be considered as measures of the rate of how fast stress corrosion. Hence, the increase of these parameters with effective pressure implies that it is less likely that stress corrosion occurs at higher levels of effective pressure. This, in part, might be attributed to the fact that at higher effective pressures, the initial permeability of the specimen is lower and therefore, stress corrosion is less influential. Parameter $\eta_2$ can be considered as a proxy on longer-time mineral dissolution/precipitation rates. As effective pressure increases, the two halves of the fractured specimen get closer, and permeability decreases. Hence, there is less potential for: (i) free-face dissolution, and (ii) precipitation of diffused particles after stress corrosion. Consequently, the increase of parameter $\eta_2$ with effective pressure indicates lower rates of mineral dissolution/precipitation. In addition, it can be observed that in all stages, for both loading and unloading paths, the Three-Element

Rheological model can successfully predict the permeability decay at different effective pressure levels. It should be, however, noted that longer-term experiments (weeks to months) are necessary to better predict the permeability decay in fractured formations.

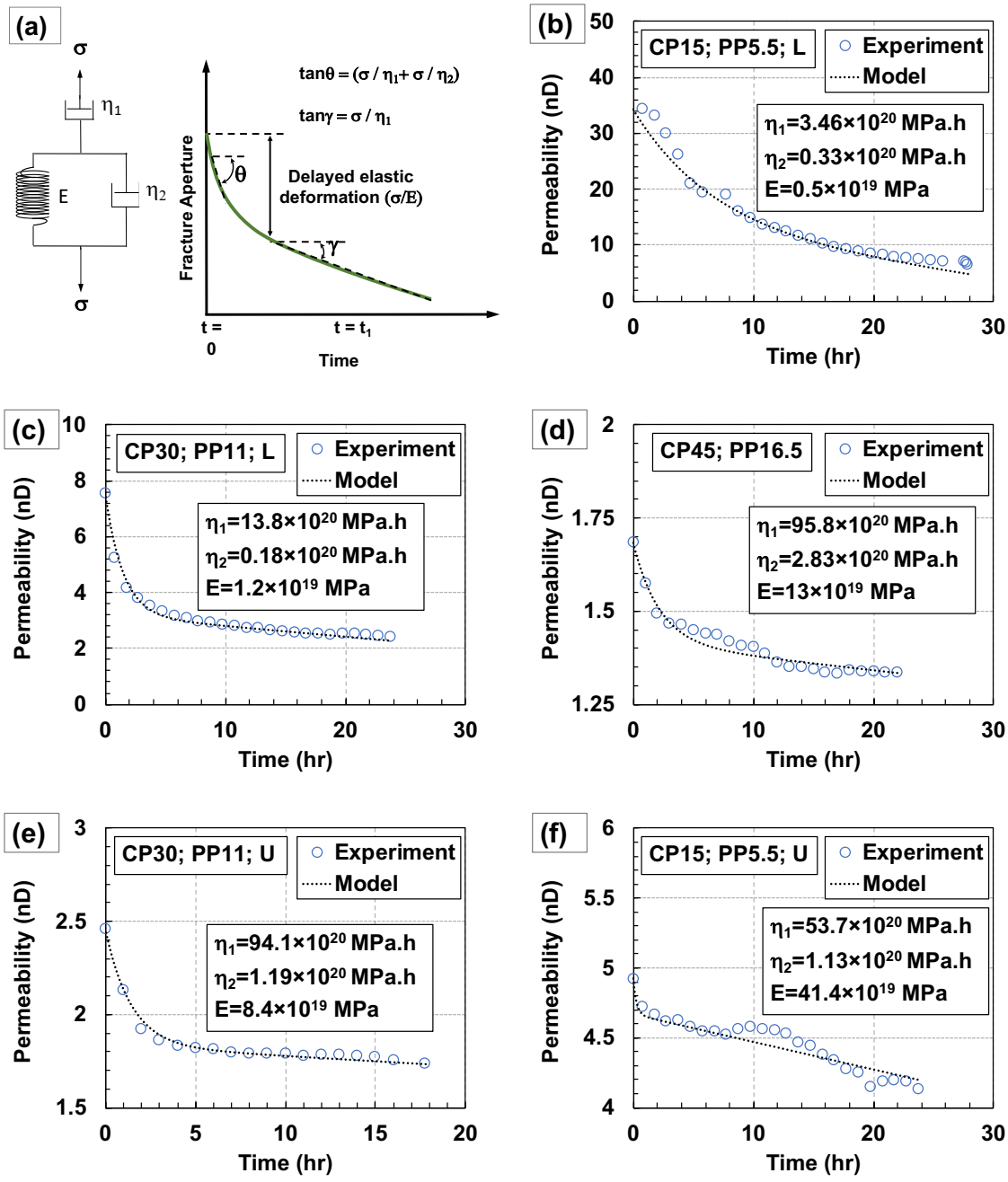


Figure 8-8. (a) Schematic of the Three-Element Rheological model and the displacement at the fracture surface (perpendicular to the fracture surface), and (b) to (f) comparison between experimental data with

the time-dependent model of permeability decay in Stages 1 to 5 of the experiment with super-saturated silica circulating fluid. Note: L and U denotes loading and unloading stages, respectively

### 8.5.3 PERMEABILITY WITH DIFFERENT CIRCULATED FLUIDS

To better illustrate the effects of circulated fluid on the evolution of fracture permeability, the average values of permeability in each stage of the experiments are shown in Figure 8.9. The experiment with geothermal fluid can be considered as an upper bound for the permeability values in all five stages of each test, while, the average permeability values for the experiment using super-saturated silica fluid can be considered as a lower bound. For instance, at the highest effective pressure level (i.e. Stage 3), the permeability in the experiment with injected super-saturated silica fluid is more than one order of magnitude less than that of the experiment with geothermal fluid. This can be attributed to the different compositions of the circulating fluid, given the fact that the temperatures and stress paths of the two experiments are exactly the same. The chemical disequilibrium between the host rock and super-saturated silica fluid can be considered as the main reason for the observed small values of fracture aperture/permeability. In particular, due to presence of quartz in the composition of the phyllite rock and aqueous silica in the circulating fluid, the precipitation of the silica is highly likely to occur.

As discussed in section 8.1, pressure solution is one of the contributing mechanisms to the permeability decline in geothermal reservoirs. Comparing the average permeability of the specimen at the same effective pressure during loading and unloading paths provides a measure of the degree of permeability recovery, which is, in part, controlled by pressure solution phenomenon. For example, in the experiments using geothermal and super-

saturated silica fluids, the average permeabilities for an effective pressure of 19 MPa (i.e. comparing Stages 2 and 4) have decreased by 54% and 32%, respectively. For the effective pressure of 9.5 MPa (i.e. comparing Stages 1 and 5), they have decreased by 74% and 63%, respectively. This observation shows that applying high levels of effective pressure has a more pronounced effect on the permeability drop compared to intermediate levels.

On the other hand, the experiment using geothermal fluid indicates less degree of permeability recovery after experiencing the higher level of effective pressure (i.e. Stage 3 in Figure 8.1a with effective pressure of 28.5 MPa) compared to that of the experiment using super-saturated silica fluid. This can, in part, be attributed to the fact that, at low (i.e. 9.5 MPa) and/or intermediate (i.e. 19 MPa) levels of effective pressure, the initial permeability of the former experiment is higher compared to the latter experiment, and hence, more non-contacting asperities exist. Consequently, as the higher level of effective pressure (i.e. 28.5 MPa) is applied, it is more likely that the increase in the number of contacting asperities in the former experiment (i.e. geothermal fluid) is higher compared to the latter experiment (i.e. super-saturated silica fluid). Therefore, there is more potential for the occurrence of pressure solution phenomenon, which is essentially-dependent on the amount of the crushed grains/particles due to stress corrosion. Nevertheless, the total number of asperities in-contact in the experiment using geothermal fluid appears to be less than that of the experiment using super-saturated silica fluid, regardless of the level of the effective pressure, as the average permeability of the former experiment is always higher than the latter experiment in all five stages of the experiments.

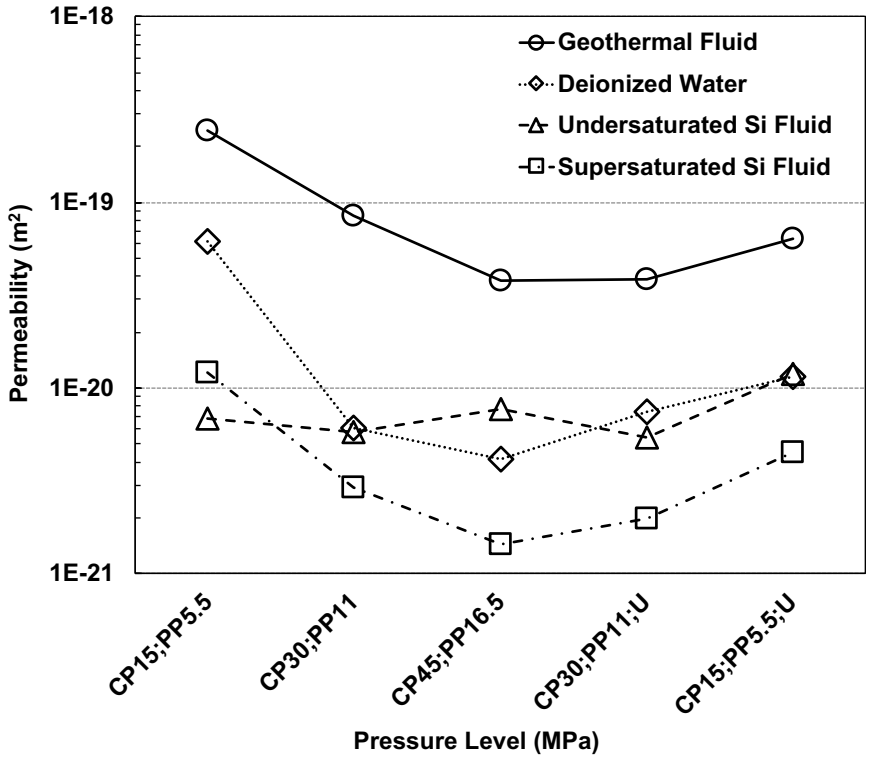


Figure 8-9. Average permeability at each stage of the stress path for all experiments

Note: CP, PP, and U denotes confining pressure, pore pressure and unloading path, respectively.

### 8.5.4 IMPLICATIONS TO THE DEVELOPMENT OF FUTURE GEOTHERMAL FIELDS

Geothermal reservoir production decline due to permeability reduction poses a significant challenge to the development of this renewable energy source. One of the contributing mechanisms to the permeability reduction is mineral dissolution/precipitation, which is controlled by the rate of kinetic reactions between the minerals present in the rock fracture surface and the circulating fluid. The composition of the circulating fluid, and hence, how far the circulating fluid is from chemical equilibrium with the minerals present in the rock fracture surface, plays a significant role in the rate of mineral

dissolution/precipitation. The results of this study imply that the permeability reduction caused by mineral dissolution/precipitation can be potentially minimized by designing and employing a synthetic fluid that is very close to chemical equilibrium with respect to the minerals present in the rock fracture surface in the reservoir. In addition, the rate of permeability decay in fractured formations is a function of the overburden stress, which should be accounted for in numerical simulations of the effects of THMC processes on permeability decline in geothermal reservoirs. Finally, the long-term prediction of permeability decline can potentially be modeled using Three-Element Rheological model, which is essential in evaluating the long-term production decline in deep geothermal reservoirs.

## 8.6 CONCLUSIONS

In this study, a suite of flow-through experiments was performed on a fractured phyllite specimen, retrieved from Blue Mountain geothermal field at a depth of 1.26 km. In order to study the effects of different circulating fluids on fracture aperture/permeability evolution at lower, equal, and higher pressures than in-situ levels, deionized water, geothermal fluid, and super- and under-saturated silica fluids were used. The absolute values of permeability were the lowest and highest in the experiments using super-saturated and geothermal fluids, respectively. In addition, the degree of permeability recovery was lower in the experiment using geothermal fluid. On the other hand, the rate of permeability decay was found to decrease at higher levels of confining pressure, while, changing pore pressure led to a sudden change in the permeability. The Three-Element Rheological model

was employed and successfully predicted the long-term permeability decay at different confining/pore pressure levels.

The analysis of chemical composition of the effluent indicated that dissolution of feldspars and quartz occurred in the experiment with circulated deionized water and precipitation of quartz in the experiment using circulated geothermal fluid. The pre- and post-test X-Ray Micro-CT images for the experiment using super-saturated silica circulating fluid revealed the regions with mineral dissolution/precipitation and fracture sealing at different locations along the rock core. In addition, the SEM images indicated that mineral precipitation in the experiment with circulated super-saturated silica fluid.

# CHAPTER 9

# CONLUSIONS AND FUTURE WORK

In this dissertation, the effects of thermal-hydrological-mechanical-chemical processes on the mechanical/transport properties of intact/fractured rock specimens from deep/shallow reservoirs were experimentally investigated.

Mechanical characterization of intact Marcellus Shale cores (a depth of ~7500 ft) and a phyllite reservoir core (a depth of ~4133 ft) were conducted through multi-stage elastic, cyclic, creep, and multi-stage failure tests with the concurrent measurements of ultrasonic signatures. It should be, however, noted that the attempts for thermal-hydrological-mechanical characterization of intact shale and phyllite cores were not successful.

The effects of different mineralogical content for the Marcellus Shale rocks were studied by comparing the elastic, hysteresis, viscoelastic, and failure characteristics of clay- and carbonate-rich cores. It was found that clay content plays a major role in the mechanical characteristics of shale gas rocks. In particular, when the rock core has higher clay content: (i) Young's and shear moduli are lower, (ii) the rate of viscoelastic deformation is higher, (iii) the percentage of plastic deformations after unloading is more significant, (iv) the degree of non-linearity increases, (v) the ratio of dynamic to static moduli is lower, and (vi) the range of P- and S-wave ultrasonic velocities are lower; compared to a rock core with lower clay content. Regardless of the clay content, it was found that: (i) the degree of non-linearity is more significant at lower levels of confining pressure and/or differential

stress, due to open microcracks, (ii) the Young's modulus is higher in unloading sub-cycles compared to loading and reloading sub-cycles, (iii) ultrasonic velocities slightly increase after each stage of hydrostatic and triaxial creep, and (iv) ultrasonic velocities are sensitive to changes in the micro-structure of the specimen due to changes in confining pressure and/or differential stress, with a more pronounced change during hydrostatic loading compared to triaxial loading.

On the other hand, the effects of material anisotropy of phyllite reservoir rocks were found to be significant on their mechanical characteristics, in particular: (i) different levels of non-linearity in elastic response, (ii) alterations of both static and dynamic moduli with a more pronounced effect on the latter, (iii) different degrees of alteration in the ultrasonic velocities during hydrostatic creep, (iv) discrepancy in viscoelastic deformation in different directions. In addition, time-frequency content of the ultrasonic waves was: (a) significantly altered by confining pressure, (b) unaffected by differential stress, and (c) slightly affected during triaxial creep loading.

A comparison between the characteristics of shale and phyllite rocks indicated that, compared to shale rocks, phyllite exhibits: (i) higher elastic moduli, (ii) less viscoelastic deformations, (iii) lower degree of plastic deformations, (iv) higher ultrasonic velocities and less significant changes due to application of confining pressure and/or differential stress, (v) higher strength, higher coefficient of internal friction, higher failure deformation, and a more brittle response.

In addition, the effects of thermal-hydrological-mechanical-chemical processes on the response of fractured Barre granite and phyllite reservoir rocks at different simulated

conditions were experimentally investigated with the concurrent recording of the ultrasonic signatures as a potential proxy for fracture aperture/permeability evolution.

The Mechanical (M) component of the coupled THMC processes was found to affect the rate of mineral dissolution and the rate of fracture aperture/permeability reduction. In particular, it was found that at higher stress levels the rate of mineral dissolution is lower, and the rate of fracture aperture/permeability reduction is higher, compared to lower stress levels. In addition, stress corrosion/pressure solution phenomena (as a subset of Chemo-Mechanical processes) were found to affect fracture response by irrecoverable fracture closure after unloading. The Thermal (T) component of the coupled THMC processes was found to affect the degree of recovery upon unloading, with a higher recovery when the temperature difference between the injected fluid and the host rock is minimal. Lastly, the Chemical (C) component of THMC processes affects the fracture aperture/permeability loss, mainly due to mineral dissolution/precipitation. In particular, it was found that when the composition of the injected fluid is closer to the chemical equilibrium state with the host rock (i.e. geothermal fluid; extracted from a production well), the fracture aperture/permeability decay is minimal. While injection of a fluid with a composition farther from equilibrium state with the host rock (i.e. super-saturated silica fluid) leads to a higher decay in fracture aperture/permeability.

In addition, ultrasonic signatures (namely velocity, amplitude, attenuation, and time-frequency content) in both constant and varying states-of-stress were found to be sensitive proxies for flow-induced changes in fracture aperture/permeability. In particular, P-wave velocity and attenuation, and maximum amplitude of S-waves can be potentially

used as indicators of fracture aperture/permeability evolution caused by interaction of fluid with rock's fracture surface. Time-frequency content of ultrasonic waves was found to be sensitive to the changes in hydraulic aperture (i.e. flow characteristics), but not sensitive to the changes in mechanical aperture (i.e. strain measurements).

Some suggestions for future work are:

- Experimental investigation of the hydraulic fracturing process at various states-of-stress in shale and granite/phyllite rocks is important to better design the stimulation and/or production program in shale gas and geothermal reservoirs. Increasing the pore pressure to the fracturing threshold and recording ultrasonic signatures before and after onset of fracturing can be very useful.
- Modelling chemical reactions and a more in-depth analysis of influent and effluent fluid samples are important components of a thorough analysis of the chemical components of THMC processes. This can lead to the better design of a synthetic fluid close to chemical-equilibrium with the host bedrock, which minimizes the rate of mineral dissolution/precipitation.
- As provided in chapter 8, a geothermal fluid (extracted from a production well at Blue Mountain geothermal field) was used as the circulated fluid into fractured rock and led to the highest values of permeability change. One can collect effluent from a series of tests with injected geothermal fluid and re-inject into the same fractured rock specimen to further investigate the effects of chemical-equilibrium between the rock minerals and the injected fluid.

- This dissertation provides a unique dataset on the response of intact/fractured shale/phyllite rocks. Numerical and/or conceptual models can be further improved using the results of the suite of experiments reported in this dissertation.

- Because of the existing limitations, the ultrasonic signatures were recorded at room temperature. It is very important to evaluate the ultrasonic signatures and their evolutions in flow-through experiments at field conditions, where the temperatures of the rock and injected fluid are close to field conditions.

- The propagation of ultrasonic waves in intact/fractured rocks can be modeled using analytical and/or numerical simulations, given the known mineralogical content of the rock specimen. Furthermore, they can be compared to experimental results obtained from this study.

REFERENCES


Acosta-Colon, A., Pyrak-Nolte, L. J., & Nolte, D. D. (2009). Laboratory-scale study of field of view and the seismic interpretation of fracture specific stiffness. *Geophysical Prospecting*, 57, 209-224.

Albaric, J., Oye, V., Langet, N., Hasting, M., Lecomte, I., Iranpour, K. & Reid, P. (2014). Monitoring of induced seismicity during the first geothermal reservoir stimulation at Paralana, Australia. *Geothermics*, 52, 120–131.

Al-Wardy, W., & Zimmerman, R. W. (2004). Effective stress law for the permeability of clay-rich sandstones. *Journal of Geophysical Research*, 109.

Amalokwu, K.I. (2016). *Saturation effects on frequency-dependent seismic anisotropy in fractured porous rocks.* PhD Thesis, University of Southampton, UK.

Ameli, P., Elkhoury, J. E., Morris, J. P., & Detwiler, R. L. (2014). Fracture permeability alteration due to chemical and mechanical processes: a coupled high-resolution model. *Rock Mechanics and Rock Engineering*, 47(5), 1563-1573.

Ameli, P., Elkhoury, J. E., & Detwiler, R. L. (2013). High-resolution fracture aperture mapping using optical profilometry. *Water Resources Research*, 49(10), 7126-7132.

Anderson, D.L., Minster, B., & Cole, D. (1974). The effect of oriented cracks on seismic velocities. *Journal of Geophysical Research*, 79, 4011-4015.

André, L., Rabemanana, V., & Vuataz, F. D. (2006). Influence of water–rock interactions on fracture permeability of the deep reservoir at Soultz-sous-Forêts, France. *Geothermics*, 35(5), 507-531.

Arnold, T., Zorn, T., Bernhard, G., & Nitsche, H. (1998). Sorption of uranium (VI) onto phyllite. *Chemical Geology*, *151*(1-4), 129-141.

ASTM. (1992). Standard Guide for Computed Tomography (CT) Imaging, ASTM Designation E 1441 - 92a. In: 1992 Annual Book of ASTM Standards, Section 3: Metals Test Methods and Analytical Procedures. ASTM, Philadelphia, 690-713.

Avary, K.L., and Lewis, J.E., 2008, New interest in cores taken thirty years ago: the Devonian Marcellus Shale in northern West Virginia: http://www.papgrocks.org/avary_pp.pdf, accessed September 2016.

Ayling, M. R., Meredith, P. G., & Murrell, S. A. (1995). Microcracking during triaxial deformation of porous rocks monitored by changes in rock physical properties, I. Elastic-wave propagation measurements on dry rocks. *Tectonophysics*, *245*(3-4), 205-221.

Bachrach, R., & Avseth, P. (2008). Rock physics modeling of unconsolidated sands: Accounting for nonuniform contacts and heterogeneous stress fields in the effective media approximation with applications to hydrocarbon exploration. *Geophysics*, *73*(6), E197-E209.

Bächler, D., & Kohl, T. (2005). Coupled thermal–hydraulic–chemical modelling of enhanced geothermal systems. *Geophysical Journal International*, 161, 533-548.

Barton, N. (2007). *Rock Quality, Seismic Velocity, Attenuation and Anisotropy*. CRC press.

Batzle, M. L., Han, D. H., & Hofmann, R. (2006). Fluid mobility and frequency-dependent seismic velocity—Direct measurements. *Geophysics*, 71, N1-N9.

Bažant, Z. P., Salviato, M., Chau, V. T., Viswanathan, H., & Zubelewicz, A. (2014). Why fracking works. *Journal of Applied Mechanics*, *81*(10), 101010.

Benson, S. M., & Orr, F. M. (2008). Carbon dioxide capture and storage. *MRS Bull.*, 33(4), 303-305.

Biot, M.A. (1956a). Theory of propagation of elastic waves in a fluid-saturated porous solid. I. Low-frequency range. *Journal of Acoustic Society of America*, 28(2), 168-178.

Biot, M.A. (1956b). Theory of propagation of elastic waves in a fluid-saturated porous solid. II. Higher frequency range. *Journal of Acoustic Society of America*, 28 (2), 179-191.

Blaisonneau, A., Peter-Borie, M., & Gentier, S. (2016). Evolution of fracture permeability with respect to fluid/rock interactions under thermo-hydro-mechanical conditions: development of experimental reactive percolation tests. *Geothermal Energy*, 4(1), 3.

Boadu, F. K., & Long, L. T. (1996). Effects of fractures on seismic-wave velocity and attenuation. *Geophysical Journal International*, 127(1), 86-110.

Brace, W. F. (1980, October). Permeability of crystalline and argillaceous rocks. In *International Journal of Rock Mechanics and Mining Sciences & Geomechanics Abstracts* (Vol. 17, No. 5, pp. 241-251). Pergamon.

Bradford, J., McLennan, J., Moore, J., Podgorney, R., Nash, G., Mann, M., ... & Glaspey, D. (2016). Numerical Modeling of the Stimulation Program at RRG-9 ST1, a DOE EGS. In *Proceedings, 41st Workshop on Geothermal Reservoir Engineering* (pp. 953-961).

Brajanovski, M., Müller, T.M., & Gurevich, B. (2006). Characteristic frequencies of seismic attenuation due to wave-induced fluid flow in fractured porous media. *Geophysical Journal International*, 166(2), 574-578.

Brantut, N., Baud, P., Heap, M. J., & Meredith, P. G. (2012). Micromechanics of brittle creep in rocks. *Journal of Geophysical Research: Solid Earth*, *117*(B8).

Britt, L. K., & Schoeffler, J. (2009, January). The geomechanics of a shale play: What makes a shale prospective. In *SPE Eastern Regional Meeting*. Society of Petroleum Engineers.

Calvin, W., Lamb, A., & Kratt, C. (2010). Rapid characterization of drill core and cutting mineralogy using infrared spectroscopy. *Geotherm. Resour. Counc. Trans*, *34*, 761-764.

Castagna, J. P., Batzle, M. L., & Eastwood, R. L. (1985). Relationships between compressional-wave and shear-wave velocities in clastic silicate rocks. *Geophysics*, *50*(4), 571-581.

Casteel, J., Trazona, R., Melosh, G., Niggemann, K., & Fairbank, B. (2009). A Preliminary conceptual model for the Blue Mountain geothermal system, Humboldt County, Nevada. *Transactions Geothermal Resources Council*, *33*, 917-920.

Catalli, F., Meier, M. A., & Wiemer, S. (2013). The role of Coulomb stress changes for injection-induced seismicity: The Basel enhanced geothermal system. *Geophysical Research Letters*, 40(1), 72-77.

Caulk, R. A., Ghazanfari, E., Perdrial, J. N., & Perdrial, N. (2016). Experimental investigation of fracture aperture and permeability change within Enhanced Geothermal Systems. *Geothermics*, 62, 12-21.

Caulk, R. A., & Tomac, I. (2017). Reuse of abandoned oil and gas wells for geothermal energy production. *Renewable Energy*, 112, 388-397.

Cha, M., Alqahtani, N. B., Yin, X., Kneafsey, T. J., Yao, B., & Wu, Y. S. (2017). Laboratory system for studying cryogenic thermal rock fracturing for well stimulation. *Journal of Petroleum Science and Engineering*, *156*, 780-789.

Chabora, E., Zemach, E., Spielman, P., Drakos, P., Hickman, S., Lutz, S., ... & Rose, P. (2012, January). Hydraulic stimulation of well 27-15, Desert Peak geothermal field, Nevada, USA. In *Proceedings of thirty-seventh workshop on geothermal reservoir engineering, Stanford University, Stanford* (Vol. 30).

Chang, C., Moos, D., & Zoback, M. D. (1997). Anelasticity and dispersion in dry unconsolidated sands. *International Journal of Rock Mechanics and Mining Sciences*, *34*(3-4), 48-e1.

Chang, C., & Zoback, M. D. (2009). Viscous creep in room-dried unconsolidated Gulf of Mexico shale (I): Experimental results. *Journal of Petroleum Science and Engineering*, *69*(3), 239-246.

Chapman, M. (2003). Frequency-dependent anisotropy due to meso-scale fractures in the presence of equant porosity. *Geophysical Prospecting*, *51*(5), 369-379.

Choi, M. K., Bobet, A., & Pyrak-Nolte, L. J. (2014). The effect of surface roughness and mixed-mode loading on the stiffness ratio κ x/κ z for fractures. *Geophysics*, *79*(5), D319-D331.

Cholach, P. Y., & Schmitt, D. R. (2006). Intrinsic elasticity of a textured transversely isotropic muscovite aggregate: Comparisons to the seismic anisotropy of schists and shales. *Journal of Geophysical Research: Solid Earth*, *111*(B9).

Cladouhos, T., Petty, S., Larson, B., Iovenitti, J., Livesay, B., & Baria, R. (2009). Toward more efficient heat mining: A planned enhanced geothermal system demonstration project. *GRC Transactions*, *33*, 165-170.

Cladouhos, T. T., Petty, S., Swyer, M. W., Uddenberg, M. E., Grasso, K., & Nordin, Y. (2016). Results from Newberry Volcano EGS Demonstration, 2010–2014. *Geothermics*, 63, 44-61.

Cliffs Minerals, Inc. 1980, Phase II Report, Preliminary Laboratory Results, Eastern Gas Shales Project, West Virginia #6 well, Monongalia County.

Cook, N. G. (1992, May). Natural joints in rock: mechanical, hydraulic and seismic behaviour and properties under normal stress. In *International Journal of Rock Mechanics and Mining Sciences & Geomechanics Abstracts* (Vol. 29, No. 3, pp. 198-223). Pergamon.

Croize, D., Renard, F., & Gratier, J. P. (2013). *Advances in Geophysics*. Elsevier Inc.

Curtis, J. B. (2002). Fractured shale-gas systems. *AAPG bulletin*, *86*(11), 1921-1938.

Deichmann, N., & Giardini, D. (2009). Earthquakes induced by the stimulation of an enhanced geothermal system below Basel (Switzerland). *Seismological Research Letters*, 80(5), 784-798.

Daubechies I. 1992 *Ten Lectures on Wavelets*. Society for Industrial and Applied Mathematics: Philadelphia, PA, USA.

Davey, H. (2012). *Geomechanical characterization of the Montney Shale northwest Alberta and northeast British Columbia, Canada*. Colorado School of Mines.

Davies, R. J., Mathias, S. A., Moss, J., Hustoft, S., & Newport, L. (2012). Hydraulic fractures: How far can they go?. *Marine and petroleum geology*, *37*(1), 1-6.

Delle Piane, C. D., Dewhurst, D., Siggins, A., & Raven, M. (2009). Geomechanical and rock physics properties of an Australian Northwest shelf shale. In *SEG Technical*

*Program Expanded Abstracts 2009* (pp. 2213-2217). Society of Exploration Geophysicists.

Delle Piane, C., Dewhurst, D.N., Siggins, A.F., & Raven, M.D. (2011). Stress-induced anisotropy in brine saturated shale. *Geophysical Journal International*, 184(2), 897-906.

Dewhurst, D. N., & Siggins, A. F. (2006). Impact of fabric, microcracks and stress field on shale anisotropy. *Geophysical Journal International*, *165*(1), 135-148.

Dewhurst, D. N., Siggins, A. F., Kuila, U., Clennell, M. B., Raven, M. D., & Nordgard-Bolas, H. M. (2008, January). Elastic, geomechanical and petrophysical properties of shales. In *The 42nd US Rock Mechanics Symposium (USRMS)*. American Rock Mechanics Association.

Dewhurst, D. N., Siggins, A. F., Sarout, J., Raven, M. D., & Nordgård-Bolås, H. M. (2011). Geomechanical and ultrasonic characterization of a Norwegian Sea shale. *Geophysics*, *76*(3), WA101-WA111.

Ding, Q. L., & Song, S. B. (2016). Experimental Investigation of the Relationship between the P-Wave Velocity and the Mechanical Properties of Damaged Sandstone. *Advances in Materials Science and Engineering*, *2016*.

Dobson, P. F., Kneafsey, T. J., Sonnenthal, E. L., Spycher, N., & Apps, J. A. (2003). Experimental and numerical simulation of dissolution and precipitation: implications for fracture sealing at Yucca Mountain, Nevada. *Journal of Contaminant Hydrology*, 62, 459-476.

Dove, P. M. (1999). The dissolution kinetics of quartz in aqueous mixed cation solutions. *Geochmica et Cosmochimica Acta*, 63(22), 3715–3727.

Eberhart-Phillips, D., Han, D. H., & Zoback, M. D. (1989). Empirical relationships among seismic velocity, effective pressure, porosity, and clay content in sandstone. *Geophysics*, *54*(1), 82-89.

Edwards, B., & Douglas, J. (2014). Magnitude scaling of induced earthquakes. *Geothermics*, 52, 132–139.

EIA, U. (2013). Annual energy outlook 2013. *US Energy Information Administration, Washington, DC*, 60-62.

EIA Report, (2017). Annual Energy Outlook 2017. *US Energy Information Administration*.

EIA Report, (2018). Annual Energy Outlook 2018 with projections to 2050. *US Energy Information Administration*.

Ellsworth, W. L. (2013). Injection-induced earthquakes. *Science*, *341*(6142), 1225942.

Elsworth, D., & Yasuhara, H. (2010). Mechanical and transport constitutive models for fractures subject to dissolution and precipitation. *International Journal for Numerical and Analytical Methods in Geomechanics*, 34(5), 533-549.

Eshkalak, M. O., Aybar, U., & Sepehrnoori, K. (2015). On the feasibility of re-stimulation of shale wells. *Petroleum Science*, *12*(3), 553-559.

Eslami, J., Grgic, D., & Hoxha, D. (2010). Estimation of the damage of a porous limestone from continuous (P-and S-) wave velocity measurements under uniaxial loading and different hydrous conditions. *Geophysical Journal International*, *183*(3), 1362-1375.

Falcon-Suarez, I., North, L., & Best, A. (2014). Experimental rig to improve the geophysical and geomechanical understanding of $CO_2$ reservoirs. *Energy Procedia*, 59, 75-81.

Falcon-Suarez, I., Marín-Moreno, H., Browning, F., Lichtschlag, A., Robert, K., North, L. J., & Best, A. I. (2017). Experimental assessment of pore fluid distribution and geomechanical changes in saline sandstone reservoirs during and after $CO_2$ injection. *International Journal of Greenhouse Gas Control*, 63, 356-369.

Fang, Y., den Hartog, S. A., Elsworth, D., Marone, C., & Cladouhos, T. (2016). Anomalous distribution of microearthquakes in the Newberry Geothermal Reservoir: Mechanisms and implications. *Geothermics*, 63, 62-73.

Faoro, I., Vinciguerra, S., Marone, C., Elsworth, D., & Schubnel, A. (2013). Linking permeability to crack density evolution in thermally stressed rocks under cyclic loading. *Geophysical Research Letters*, 40(11), 2590-2595.

Faoro, I., Elsworth, D., & Candela, T. (2016). Evolution of the transport properties of fractures subject to thermally- and mechanically-activated mineral alteration and redistribution. *Geofluids*. 16(3), 396-407.

Farough, A., Moore, D. E., Lockner, D. A., & Lowell, R. P. (2016). Evolution of fracture permeability of ultramafic rocks undergoing serpentinization at hydrothermal conditions: An experimental study. *Geochemistry, Geophysics, Geosystems*, 17(1), 44-55.

Farzampour, A., Kamali-Asl, A., & Hu, J. W. (2018a). Unsupervised identification of arbitrarily-damped structures using time-scale independent component analysis: Part I. *Journal of Mechanical Science and Technology*, *32*(2), 567-577.

Farzampour, A., Kamali-Asl, A., & Hu, J. W. (2018b). Unsupervised identification of arbitrarily-damped structures using time-scale independent component analysis: Part II. *Journal of Mechanical Science and Technology*, *32*(9), 4413-4422.

Faulds, J. E., & Melosh, G. (2008, October). A preliminary structural model for the blue mountain geothermal field, Humboldt County, Nevada. In *Proceedings of the Geothermal Resources Council Annual Meeting 2008: "Geothermal-Gaining Steam* (pp. 234-239).

Feng, X. T. (Ed.). (2017). *Rock Mechanics and Engineering Volume 2: Laboratory and Field Testing*. CRC Press.

Fisher, K. (2010). Data confirm safety of well fracturing. *The American Oil & Gas Reporter*.

Fjaer, E., Holt, R. M., Raaen, A. M., Risnes, R., & Horsrud, P. (2008). *Petroleum related rock mechanics* (Vol. 53). Elsevier.

Fortin, J., Stanchits, S., Dresen, G., & Guéguen, Y. (2006). Acoustic emission and velocities associated with the formation of compaction bands in sandstone. *Journal of Geophysical Research: Solid Earth*, *111*(B10).

Fortin, J., Guéguen, Y., & Schubnel, A. (2007). Effects of pore collapse and grain crushing on ultrasonic velocities and Vp/Vs. *Journal of Geophysical Research: Solid Earth*, *112*(B8).

Frash, L. P., Gutierrez, M., & Hampton, J. (2014). True-triaxial apparatus for simulation of hydraulically fractured multi-borehole hot dry rock reservoirs. *International Journal of Rock Mechanics and Mining Sciences*, 70, 496-506.

Frash, L. P., Gutierrez, M., Hampton, J., & Hood, J. (2015). Laboratory simulation of binary and triple well EGS in large granite blocks using AE events for drilling guidance. *Geothermics*, 55, 1-15.

Gao, Q., Tao, J., Hu, J., & Yu, X. B. (2015). Laboratory study on the mechanical behaviors of an anisotropic shale rock. *Journal of Rock Mechanics and Geotechnical Engineering*, *7*(2), 213-219.

Garcia, J., Hartline, C., Walters, M., Wright, M., Rutqvist, J., Dobson, P. F., & Jeanne, P. (2016). The Northwest Geysers EGS Demonstration Project, California: Part 1: Characterization and reservoir response to injection. *Geothermics*, 63, 97-119.

Gatelier, N., Pellet, F., & Loret, B. (2002). Mechanical damage of an anisotropic porous rock in cyclic triaxial tests. *International Journal of Rock Mechanics and Mining Sciences*, *39*(3), 335-354.

Genter A., Goerke X., Graff J. J., Cuenot N., Krall G., Schindler M., & Ravier G. (2010). Current status of the EGS Soultz geothermal project (France). *World Geothermal Congress*, WGC2010, Bali, Indonesia, April 2010.

Germanovich, L. N., Lowell, R. P., & Astakhov, D. K. (2001). Temperature-dependent permeability and bifurcations in hydrothermal flow. *Journal of Geophysical Research: Solid Earth*, *106*(B1), 473-495.

Ghassemi, A. & Zhang, Q. (2004). A Transient Fictitious Stress Boundary Element Method for Porothermoelastic Media. *Engineering Analysis with Boundary Elements*, 28(11), 1363-1373.

Ghassemi, A., & Kumar, G. S. (2007). Changes in fracture aperture and fluid pressure due to thermal stress and silica dissolution/precipitation induced by heat extraction from subsurface rocks. *Geothermics*, 36(2), 115-140.

Ghassemi, A., Nygren, A., & Cheng, A. (2008). Effects of heat extraction on fracture aperture: A poro–thermoelastic analysis. *Geothermics*, 37(5), 525-539.

Ghassemi, A., & Zhou, X. (2011). A three-dimensional thermo-poroelastic model for fracture response to injection/extraction in enhanced geothermal systems. *Geothermics*, 40(1), 39-49.

Ghassemi, A. (2012). A review of some rock mechanics issues in geothermal reservoir development. *Geotechnical and Geological Engineering*, 30(3), 647-664.

Ghassemi, A., & Suarez-Rivera, R. (2012). Sustaining fracture area and conductivity of gas shale reservoirs for enhancing long-term production and recovery. *College Station*.

Ghassemi, A., Zhou, X. X., & Rawal, C. (2013). A three-dimensional poroelastic analysis of rock failure around a hydraulic fracture. *Journal of Petroleum Science and Engineering*, *108*, 118-127.

Ghassemi, A. & Tao, Q. (2016). Thermo-poroelastic effects on reservoir seismicity and permeability change. *Geothermics*, 63, 210-224.

Ghorbani, A., Zamora, M., & Cosenza, P. (2009). Effects of desiccation on the elastic wave velocities of clay-rocks. *International Journal of Rock Mechanics and Mining Sciences*, *46*(8), 1267-1272.

Gischig, V. S. (2015). Rupture propagation behavior and the largest possible earthquake induced by fluid injection into deep reservoirs. *Geophysical Research Letters*, 42(18), 7420-7428.

Goertz-Allmann, B. P., Goertz, A., & Wiemer, S. (2011). Stress drop variations of induced earthquakes at the Basel geothermal site. *Geophysical Research Letters*, 38(9).

Gritto, R., & Jarpe, S. P. (2014). Temporal variations of Vp/Vs ratio at The Geysers geothermal field, USA. *Geothermics*, 52, 112–119.

Gu, B. (1994) Interface Waves on a Fracture in Rock. Ph.D. Thesis, University of California, Berkeley.

Hedayat, A., Pyrak-Nolte, L. J., & Bobet, A. (2014). Precursors to the shear failure of rock discontinuities. *Geophysical Research Letters*, *41*(15), 5467-5475.

Hedayat, A., & Walton, G. (2016). Laboratory determination of rock fracture shear stiffness using seismic wave propagation and digital image correlation. *Geotechnical Testing Journal*, *40*(1), 92-106.

Hedayat, A., & Hinton, J. Geophysical Waveform's Frequency Attenuation as a Precursor to Rock Shear Failure. In *Geotechnical Frontiers 2017* (pp. 633-642).

Hedayat, A., Hinton, J., Haeri, H., and Masoumi, H. (2018) Geophysical Signatures of Shear Induced Damage and Frictional Processes on Rock Joints. *Journal of Geophysical Research*. DOI: 10.1002/2017JB014773.

Hiraiwa, M., Wallen, S. P., & Boechler, N. (2017). Acoustic wave propagation in disordered microscale granular media under compression. *Granular Matter*, *19*(3), 62.

Hoek, E., & Martin, C. D. (2014). Fracture initiation and propagation in intact rock–a review. *Journal of Rock Mechanics and Geotechnical Engineering*, *6*(4), 287-300.

Holt, R. M., Fjær, E., Stenebråten, J. F., & Nes, O. M. (2015). Brittleness of shales: relevance to borehole collapse and hydraulic fracturing. *Journal of Petroleum Science and Engineering*, *131*, 200-209.

Hossain, M. M., Rahman, M. K., & Rahman, S. S. (2000). Hydraulic fracture initiation and propagation: roles of wellbore trajectory, perforation and stress regimes. *Journal of Petroleum Science and Engineering*, *27*(3), 129-149.

Hu, L., Winterfeld, P. H., Fakcharoenphol, P., & Wu, Y. S. (2013). A novel fully-coupled flow and geomechanics model in enhanced geothermal reservoirs. *Journal of Petroleum Science and Engineering*, 107, 1-11.

Huang, X., & Zhao, Y. P. (2017). Characterization of pore structure, gas adsorption, and spontaneous imbibition in shale gas reservoirs. *Journal of Petroleum Science and Engineering*, *159*, 197-204.

Ishibashi, T., McGuire, T. P., Watanabe, N., Tsuchiya, N., & Elsworth, D. (2013). Permeability evolution in carbonate fractures: Competing roles of confining stress and fluid pH. *Water Resources Research*, *49*(5), 2828-2842.

Islam, M. A., & Skalle, P. (2013). An experimental investigation of shale mechanical properties through drained and undrained test mechanisms. *Rock Mechanics and Rock Engineering*, *46*(6), 1391-1413.

Izadi, G., & Elsworth, D. (2015). The influence of thermal-hydraulic-mechanical-and chemical effects on the evolution of permeability, seismicity and heat production in geothermal reservoirs. *Geothermics*, 53, 385-395.

Jansen, G., & Miller, S. A. (2017). On the Role of Thermal Stresses during Hydraulic Stimulation of Geothermal Reservoirs. *Geofluids*, 2017.

Jarvie, D. M., Hill, R. J., Ruble, T. E., & Pollastro, R. M. (2007). Unconventional shale-gas systems: The Mississippian Barnett Shale of north-central Texas as one model for thermogenic shale-gas assessment. *AAPG bulletin*, *91*(4), 475-499.

Jia, X. (2004). Codalike multiple scattering of elastic waves in dense granular media. *Physical Review Letters*, *93*(15), 154303.

Jin, Z., Li, W., Jin, C., Hambleton, J., & Cusatis, G. (2017). Elastic, strength, and fracture properties of Marcellus shale. *arXiv preprint arXiv:1712.02320*.

Johnson, J. W., Knauss, K. G., Glassley, W. E., DeLoach, L. D., & Tompson, A.F.B. (1998). Reactive transport modeling of plug- flow reactor experiments: quartz and tuff dissolution at 240 8C. *Journal of Hydrology*, 209(1–4), 81–111.

Johnson, L. R., & Majer, E. L. (2017). Induced and triggered earthquakes at The Geysers geothermal reservoir. *Geophysical Journal International*, 209(2), 1221-1238.

Johri, M., & Zoback, M. D. (2013, August). The evolution of stimulated reservoir volume during hydraulic stimulation of shale gas formations. In *Unconventional Resources Technology Conference* (pp. 1661-1671). Society of Exploration Geophysicists, American Association of Petroleum Geologists, Society of Petroleum Engineers.

Jones, L. E., & Wang, H. F. (1981). Ultrasonic velocities in Cretaceous shales from the Williston Basin. *Geophysics*, 46(3), 288-297.

Jones, T., Murphy, W., & Nur, A. (1980). Effects of temperature and saturation on the velocity and attenuation of seismic waves in rocks: applications to geothermal reservoir evaluation. In *Proceedings of the Sixth Workshop on Geothermal Reservoir Engineering* (pp. 16-18).

Josh, M., Esteban, L., Delle Piane, C., Sarout, J., Dewhurst, D. N., & Clennell, M. B. (2012). Laboratory characterisation of shale properties. *Journal of Petroleum Science and Engineering*, *88*, 107-124.

Kamali-Asl A, Ghazanfari E. Investigating the creep response of Marcellus Shale formations. *In: Proceedings of the Geotechnical Frontiers*. Orlando; 12-15 March 2017. p. 562-569.

Kamali-Asl A, Ghazanfari E. Response of Marcellus Shale specimens to cyclic loading. *In: Proceedings of the International Foundation Congress and Equipment Exp.* Orlando; 5-10 March 2018. p. 399-407.

Kamali-Asl, A., Ghazanfari, E., Newell, P., & Stevens, M. (2018a). Elastic, viscoelastic, and strength properties of Marcellus Shale specimens. *Journal of Petroleum Science and Engineering*, 171, 662-679.

Kamali-Asl, A., Ghazanfari, E., Newell, P., and Stevens, M. (2018b). Elastic, viscoelastic, and strength properties of Marcellus Shale specimens. *Journal of Petroleum Science and Engineering*, 171, 662-679.

Kamali-Asl, A., Ghazanfari, E., Hedayat, A., and Deering, L (2018c). Investigation of static/dynamic moduli and plastic response of shale specimens. *International Journal of Rock Mechanics and Mining Sciences*, 110, 231-245.

Kamali-Asl, A., Kc, B., Ghazanfari, E., & Hedayat, A. (2018d). Flow-induced alterations of seismic signatures and fracture aperture under constant state-of-stress in a single-fractured rock. *Under Review. Geophysics*.

Kamali-Asl, A., Kc, B., Foroutan, M., Ghazanfari, E., Cladouhos, T., & Stevens, M. (2018e). Stress-strain response and seismic signature analysis of phyllite reservoir rocks from Blue Mountain geothermal field. *Geothermics*, 77, 204-223.

Kanagawa, K., Cox, S. F., & Zhang, S. (2000). Effects of dissolution-precipitation processes on the strength and mechanical behavior of quartz gouge at high-temperature hydrothermal conditions. *Journal of Geophysical Research: Solid Earth*, 105(B5), 11115-11126.

Kaya, E., Zarrouk, S. J., & O'Sullivan, M. J. (2011). Reinjection in geothermal fields: a review of worldwide experience. *Renewable and Sustainable Energy Reviews*, *15*(1), 47-68.

Kelkar, S., Lewis, K., Hickman, S., Davatzes, N. C., Moos, D., & Zyvoloski, G. (2012, January). Modeling coupled thermal-hydrological-mechanical processes during shear stimulation of an EGS well. In *Thirty-Seventh Workshop on Geothermal Reservoir Engineering, Stanford University, Stanford*.

Kim, M. M., & Ko, H. Y. (1979). Multistage triaxial testing of rocks.

Kim, J., Sonnenthal, E., & Rutqvist, J. (2015). A sequential implicit algorithm of chemo-thermo-poro-mechanics for fractured geothermal reservoirs. *Computers and Geosciences*, 76, 59-71.

Kivi, I. R., Ameri, M. J., & Ghassemi, A. (2015). Chemoporoelastic characterization of Ghom shale. *Journal of Petroleum Science and Engineering*, *127*, 115-123.

Knight, R., Pyrak-Nolte, L. J., Slater, L., Atekwana, E., Endres, A., Geller, J., ... & Straley, C. (2010). Geophysics at the interface: Response of geophysical properties to solid-fluid, fluid-fluid, and solid-solid interfaces. *Reviews of Geophysics*, 48.

Koh, J., Roshan, H., & Rahman, S. S. (2011). A numerical study on the long term thermo-poroelastic effects of cold water injection into naturally fractured geothermal reservoirs. *Computers and Geotechnics*, 38(5), 669-682.

Kovári, K., & Tisa, A. (1975). Multiple failure state and strain controlled triaxial tests. *Rock Mechanics*, *7*(1), 17-33.

Kranz, R. L., Frankel, A. D., Engelder, T., & Scholz, C. H. (1979, August). The permeability of whole and jointed Barre granite. In *International Journal of Rock Mechanics and Mining Sciences & Geomechanics Abstracts* (Vol. 16, No. 4, pp. 225-234). Pergamon.

Kuila, U., Dewhurst, D. N., Siggins, A. F., & Raven, M. D. (2011). Stress anisotropy and velocity anisotropy in low porosity shale. *Tectonophysics*, *503*(1-2), 34-44.

Kumar, P., & Foufoula-Georgiou, E. (1997). Wavelet analysis for geophysical applications. *Reviews of Geophysics*, 35(4), 385-412.

Kumar, G. S., & Ghassemi, A. (2005). Numerical modeling of non-isothermal quartz dissolution/precipitation in a coupled fracture–matrix system. *Geothermics*, 34(4), 411-439.

Kwiatek, G., Martínez-Garzón, P., Dresen, G., Bohnhoff, M., Sone, H., & Hartline, C. (2015). Effects of long-term fluid injection on induced seismicity parameters and maximum magnitude in northwestern part of The Geysers geothermal field. *Journal of Geophysical Research: Solid Earth*, 120(10), 7085–7101.

Legarth, B., Huenges, E., & Zimmermann, G. (2005). Hydraulic fracturing in a sedimentary geothermal reservoir: Results and implications. *International Journal of Rock Mechanics and Mining Sciences*, *42*(7-8), 1028-1041.

Li, T., Shiozawa, S. and McClure, M. W. 2016. Thermal breakthrough calculations to optimize design of a multiple-stage Enhanced Geothermal System, *Geothermics*, 64, 455-465 https://doi.org/10.1016/j.geothermics.2016.06.015.

Li, Y., & Ghassemi, A. (2012, January). Creep behavior of Barnett, Haynesville, and Marcellus shale. In *46th US Rock Mechanics/Geomechanics Symposium*. American Rock Mechanics Association.

Li, W., Petrovitch, C., & Pyrak-Nolte, L. J. (2009, January). Seismic wave propagation in fractured carbonate rock. In *43rd US Rock Mechanics Symposium & 4th US-Canada Rock Mechanics Symposium*. American Rock Mechanics Association.

Liang, W., Zhang, C., Gao, H., Yang, X., Xu, S., & Zhao, Y. (2012). Experiments on mechanical properties of salt rocks under cyclic loading. *Journal of Rock Mechanics and Geotechnical Engineering*, *4*(1), 54-61.

Liu, J., Sheng, J., Polak, A., Elsworth, D., Yasuhara, H., & Grader, A. (2006). A fully-coupled hydrological–mechanical–chemical model for fracture sealing and preferential opening. *International Journal of Rock Mechanics and Mining Sciences*, *43*(1), 23-36.

Liu, Z. B., Xie, S. Y., Shao, J. F., & Conil, N. (2015). Effects of deviatoric stress and structural anisotropy on compressive creep behavior of a clayey rock. *Applied Clay Science*, *114*, 491-496.

Liu, Z. B., & Shao, J. F. (2016). Moisture effects on damage and failure of Bure claystone under compression. *Geotechnique Letters*, *6*(3), 182-186.

Liu, Z. B., Shao, J. F., Liu, T. G., Xie, S. Y., & Conil, N. (2016). Gas permeability evolution mechanism during creep of a low permeable claystone. *Applied Clay Science*, *129*, 47-53.

Liu, Z. B., Xie, S. Y., Shao, J. F., & Conil, N. (2017). Multi-step triaxial compressive creep behaviour and induced gas permeability change of clay-rich rock. *Géotechnique*, 1-9.

Liu, Z., Shao, J., Xie, S., Conil, N., & Zha, W. (2018). Effects of relative humidity and mineral compositions on creep deformation and failure of a claystone under compression. *International Journal of Rock Mechanics and Mining Sciences*, *103*, 68-76.

Lockner, D. A., Summers, R., Moore, D., & Byerlee, J. D. (1982, April). Laboratory measurements of reservoir rock from the Geysers Geothermal Field, California. In *International Journal of Rock Mechanics and Mining Sciences & Geomechanics Abstracts* (Vol. 19, No. 2, pp. 65-80). Pergamon.

Loucks, R. G., Reed, R. M., Ruppel, S. C., & Jarvie, D. M. (2009). Morphology, genesis, and distribution of nanometer-scale pores in siliceous mudstones of the Mississippian Barnett Shale. *Journal of Sedimentary Research*, *79*(12), 848-861.

Luo, J., Zhu, Y., Guo, Q., Tan, L., Zhuang, Y., Liu, M., Zhang, C., Xiang, W., & Rohn, J. (2017). Experimental investigation of the hydraulic and heat-transfer properties of artificially fractured granite. *Scientific reports*, 7.

Lovekin, J., Morrison, M. Champneys, G. and Morrow, J., 2017, Temperature Recovery after Long-term Injection: Case History from Soda Lake, Nevada, *Geothermal Resources Council Transactions*, v. 41, 2770-2779.

Lutz, S. J., Hickman, S., Davatzes, N., Zemach, E., Drakos, P., & Robertson-Tait, A. (2010, February). Rock mechanical testing and petrologic analysis in support of well stimulation activities at the Desert Peak Geothermal Field, Nevada. In *Proceedings 35th workshop on geothermal reservoir engineering*.

Majer, E. L., Baria, R., Stark, M., Oates, S., Bommer, J., Smith, B., & Asanuma, H. (2007). Induced seismicity associated with enhanced geothermal systems. *Geothermics*, 36(3), 185-222.

Manepally, C., Fedors, R., Basagaoglu, H., Ofoegbu, G., & Pabalan, R. (2011). *Coupled Processes Workshop Report*. Technical Report. Center for Nuclear Waste Regulatory Analyses and the US Nuclear Regulatory Commission.

Manjunath, M., Awasthi, A. P., & Geubelle, P. H. (2012). Wave propagation in random granular chains. *Physical Review E*, *85*(3), 031308.

Martínez-Garzón, P., Kwiatek, G., Sone, H., Bohnhoff, M., Dresen, G., & Hartline, C. (2014). Spatiotemporal changes, faulting regimes, and source parameters of induced seismicity: A case study from The Geysers geothermal field. *Journal of Geophysical Research: Solid Earth*, 119(11), 8378-8396.

Matek, B. (2016). 2016 Annual U.S. & Global Geothermal Power Production Report. Geothermal Energy Association.

Mavko, G., Mukerji, T., & Dvorkin, J. (2009). *The rock physics handbook: Tools for seismic analysis of porous media*. Cambridge University Press.

Maxwell, S. (2011). Microseismic hydraulic fracture imaging: The path toward optimizing shale gas production. *The Leading Edge*.

McClure, M. W., & Horne, R. N. (2014). An investigation of stimulation mechanisms in Enhanced Geothermal Systems. *International Journal of Rock Mechanics and Mining Sciences*, 72, 242-260.

McLamore, R., & Gray, K. E. (1967). The mechanical behavior of anisotropic sedimentary rocks. *Journal of Engineering for Industry*, *89*(1), 62-73.

Meier, P. M., Rodríguez, A. A., & Bethmann, F. (2015). Lessons learned from Basel: new EGS projects in Switzerland using multistage stimulation and a probabilistic traffic light system for the reduction of seismic risk. In *Proceedings of World Geothermal Congress 2015*, Melbourne, 19-25 April 2015.

Melosh, G., Cumming, W., Casteel, J., Niggemann, K., & Fairbank, B. (2010, April). Seismic reflection data and conceptual models for geothermal development in Nevada. In *Proceedings world geothermal congress, Bali, Indonesia* (Vol. 6).

Menéndez, B., Zhu, W., & Wong, T. F. (1996). Micromechanics of brittle faulting and cataclastic flow in Berea sandstone. *Journal of Structural Geology*, *18*(1), 1-16.

Modiriasari, A., Bobet, A., & Pyrak-Nolte, L. J. (2017). Active Seismic Monitoring of Crack Initiation, Propagation, and Coalescence in Rock. *Rock Mechanics and Rock Engineering*, *50*(9), 2311-2325.

Momeni, A., Karakus, M., Khanlari, G. R., & Heidari, M. (2015). Effects of cyclic loading on the mechanical properties of a granite. *International Journal of Rock Mechanics and Mining Sciences*, *77*, 89-96.

Montague, J. A., & Pinder, G. F. (2015). Potential of hydraulically induced fractures to communicate with existing wellbores. *Water Resources Research*, *51*(10), 8303-8315.

Montalvo, F., Xu, T., & Pruess, K. (2005, April). TOUGHREACT code applications to problems of reactive chemistry in geothermal production-injection wells. First exploratory model for Ahuachapan and Berlin geothermal fields. In *Proceedings of World Geothermal Congress*, 2005 Antalya, Turkey.

Montgomery, C. T., & Smith, M. B. (2010). Hydraulic fracturing: history of an enduring technology. *Journal of Petroleum Technology*, *62*(12), 26-40.

Moore, D. E., & Lockner, D. A. (2004). Crystallographic controls on the frictional behavior of dry and water-saturated sheet structure minerals. *Journal of Geophysical Research: Solid Earth*, *109*(B3).

Morrow, C. A., Moore, D. E., & Lockner, D. A. (2001). Permeability reduction in granite under hydrothermal conditions. *Journal of Geophysical Research*, 106(B12), 30-55130551-30560.

Mukerji, T., & Mavko, G. (1994). Pore fluid effects on seismic velocity in anisotropic rocks. *Geophysics*, 59, 233-244.

Müller, T. M., Gurevich, B., & Lebedev, M. (2010). Seismic wave attenuation and dispersion resulting from wave-induced flow in porous rocks—A review. *Geophysics*, 75, 75A147-75A164.

Nasseri, M. H. B., Rao, K. S., & Ramamurthy, T. (2003). Anisotropic strength and deformational behavior of Himalayan schists. *International Journal of Rock Mechanics and Mining Sciences*, *40*(1), 3-23.

Niandou, H., Shao, J. F., Henry, J. P., & Fourmaintraux, D. (1997). Laboratory investigation of the mechanical behaviour of Tournemire shale. *International Journal of Rock Mechanics and Mining Sciences*, *34*(1), 3-16.

Nolte, D. D., Pyrak-Nolte, L. J., Beachy, J., & Ziegler, C. (2000). Transition from the displacement discontinuity limit to the resonant scattering regime for fracture interface waves. *International Journal of Rock Mechanics and Mining Sciences*, 37(1-2), 219-230.

Pagoulatos, A. (2004). *Evaluation of multistage triaxial testing on Berea sandstone* (Doctoral dissertation, University of Oklahoma).

Pandey, S. N., Chaudhuri, A., Rajaram, H., & Kelkar, S. (2015). Fracture transmissivity evolution due to silica dissolution/precipitation during geothermal heat extraction. *Geothermics*, 57, 111-126.

Passey, Q. R., Bohacs, K., Esch, W. L., Klimentidis, R., & Sinha, S. (2010, January). From oil-prone source rock to gas-producing shale reservoir-geologic and petrophysical characterization of unconventional shale gas reservoirs. In *International Oil and Gas Conference and Exhibition in China*. Society of Petroleum Engineers.

Paterson, M. S., & Wong, T. F. (2005). *Experimental rock deformation-the brittle field*. Springer Science & Business Media.

Pellet, F. L., & Fabre, G. (2007). Damage evaluation with P-wave velocity measurements during uniaxial compression tests on argillaceous rocks. *International Journal of Geomechanics*, *7*(6), 431-436.

Petty, S., Fairbanks, B., and Bauer, S., 2005, Lessons learned in the drilling of DB-1 and DB-2, Blue Mountain, NV. Thirtieth Workshop on Geothermal Resource Engineering, Stanford, University, Proceedings, SGP-TR-176.

Pireh, A., Alavi, S. A., Ghassemi, M. R., & Shaban, A. (2015). Analysis of natural fractures and effect of deformation intensity on fracture density in Garau formation for shale gas development within two anticlines of Zagros fold and thrust belt, Iran. *Journal of Petroleum Science and Engineering*, *125*, 162-180.

Polak, A., Elsworth, D., Yasuhara, H., Grader, A. S., & Halleck, P. M. (2003). Permeability reduction of a natural fracture under net dissolution by hydrothermal fluids. *Geophysical Research Letters*, 30(20).

Ponce, D.A., Watt, J.T. Casteel, J., and Logsdon, G. (2008). *Physical property measurements on core samples from drill-holes DB-1 and DB-2, Blue Mountain Geothermal Prospect, north-central Nevada* (NO. 2009-1022) U.S. Geological survey.

Ponce, D. A., Glen, J. M. G., & t Watt, J. (2009, December). Geophysical setting of the blue Mountain Geothermal Area, North-central Nevada and its relationship to a crustal-scale Fracture Associated with the Inception of the Yellowstone Hotspot. In *AGU Fall Meeting Abstracts*.

Ponce, D. A. (2012). *Geophysical studies in the vicinity of Blue Mountain and Pumpernickel Valley near Winnemucca, north-central Nevada* (No. 2012-1207). U.S. Geological Survey.

Puzrin, A. (2012). *Constitutive Modelling in Geomechanics: Introduction*. Springer Science & Business Media.

Pyrak-Nolte, L. J., Myer, L. R., Cook, N. G., & Witherspoon, P. A. (1987, January). Hydraulic and mechanical properties of natural fractures in low permeability rock. In *Proceedings of 6th ISRM Congress*. International Society for Rock Mechanics.

Pyrak-Nolte, L. J., Myer, L. R., & Cook, N. G. (1990). Transmission of seismic waves across single natural fractures. *Journal of Geophysical Research: Solid Earth*, 95, 8617-8638.

Pyrak-Nolte, L. J., & Morris, J. P. (2000). Single fractures under normal stress: The relation between fracture specific stiffness and fluid flow. *International Journal of Rock Mechanics and Mining Sciences*, 37(1), 245-262.

Pyrak-Nolte, L. J., DePaolo, D. J., & Pietraß, T. (2015). Controlling subsurface fractures and fluid flow: a basic research agenda. *USDOE Office of Science* (SC)(United States).

Pyrak-Nolte, L. J., & Nolte, D. D. (2016) Approaching a universal scaling relationship between fracture stiffness and fluid flow. *Nature communications*, 7, 10663.

Rabemanana, V., Durst, P., Bächler, D., Vuataz, F. D., & Kohl, T. (2003). Geochemical modelling of the Soultz-sous-Forêts Hot Fractured Rock system: comparison of two reservoirs at 3.8 and 5 km depth. *Geothermics*, *32*(4-6), 645-653.

Ramamurthy, T. (1993). Strength and modulus responses of anisotropic rocks. *Comprehensive rock engineering*, *1*(13), 313-329.

Rassouli, F. S., & Zoback, M. D. (2015, November). Long-term creep experiments on Haynesville shale rocks. In *49th US Rock Mechanics/Geomechanics Symposium*. American Rock Mechanics Association.

Rassouli, F. S., & Zoback, M. D. (2017, August). Multi-Stage Creep Experiments on the Wolfcamp Shale, Permian Basin, West Texas, USA. In *51st US Rock Mechanics/Geomechanics Symposium*. American Rock Mechanics Association.

Rassouli, F. S., & Zoback, M. D. (2018). Comparison of Short-Term and Long-Term Creep Experiments in Shales and Carbonates from Unconventional Gas Reservoirs. *Rock Mechanics and Rock Engineering*, 1-20.

Rawal, C., & Ghassemi, A. (2014). A reactive thermo-poroelastic analysis of water injection into an enhanced geothermal reservoir. *Geothermics*, 50, 10-23.

Report, M.I.T. (2006). The future of geothermal energy. Impact of Enhanced Geothermal Systems (EGS) on the United States in the 21st Century, Massachusetts Institute of Technology, Cambridge, MA, 372.

Rezaee, R. (2015). *Fundamentals of gas shale reservoirs*. John Wiley & Sons.

Roy, S., & Pyrak-Nolte, L. J. (1995). Interface waves propagating along tensile fractures in dolomite. *Geophysical Research Letters*, 22, 2773-2776.

Roy, S., & Pyrak-Nolte, L. J. (1997). Observation of a distinct compressional-mode interface wave on a single fracture. *Geophysical Research Letters*. 24(2), 173-176.

Rutqvist, J., Majer, E., Oldenburg, C., Peterson, J., & Vasco, D. (2006). Integrated modeling and field study of potential mechanisms for induced seismicity at The Geysers Goethermal Field, California. Lawrence Berkeley National Laboratory.

Rutqvist, J. (2015). Fractured rock stress-permeability relationships from in situ data and effects of temperature and chemical-mechanical couplings. *Geofluids*, *15*(1-2), 48-66.

Safari, R., & Ghassemi, A. (2015). 3D thermo-poroelastic analysis of fracture network deformation and induced micro-seismicity in enhanced geothermal systems. *Geothermics*, 58, 1-14.

Saltiel, S., Selvaduari, P. A., Bonner, B. P., Glaser, S. D., & Ajo-Franklin, J. B. (2017). Experimental development of low-frequency shear modulus and attenuation measurements in mated rock fractures: Shear mechanics due to asperity contact area changes with normal stress. *Geophysics*, 82(2), M19-M36.

Sarout, J., Molez, L., Guéguen, Y., & Hoteit, N. (2007). Shale dynamic properties and anisotropy under triaxial loading: Experimental and theoretical investigations. *Physics and Chemistry of the Earth, Parts A/B/C*, *32*(8), 896-906.

Savage, D., Bateman, K., & Richards, H. G. (1992). Granite-water interactions in a flow-through experimental system with applications to the Hot Dry Rock geothermal system at Rosemanowes, Cornwall, UK. Applied Geochemistry, 7(3), 223-241.

Sayers, C. M., Van Munster, J. G., & King, M. S. (1990, October). Stress-induced ultrasonic anisotrophy in Berea sandstone. In *International Journal of Rock Mechanics and Mining Sciences & Geomechanics Abstracts* (Vol. 27, No. 5, pp. 429-436). Pergamon.

Sayers, C. M. (2013). The effect of kerogen on the elastic anisotropy of organic-rich shales. *Geophysics*, 78, D65-D74.

Schmittbuhl, J., Lengliné, O., Cornet, F., Cuenot, N., & Genter, A. (2014). Induced seismicity in EGS reservoir: the creep route. *Geothermal Energy*, *2*(1), 14.

Schoenball, M., Dorbath, L., Gaucher, E., Wellmann, J. F., & Kohl, T. (2014). Change of stress regime during geothermal reservoir stimulation. *Geophysical Research Letters*, 41(4), 1163-1170.

Schön, J. H. (2015). *Physical properties of rocks: Fundamentals and principles of petrophysics* (Vol. 65). Elsevier.

Schubnel, A., & Guéguen, Y. (2003). Dispersion and anisotropy of elastic waves in cracked rocks. *Journal of Geophysical Research: Solid Earth*, 108(B2).

Sieminski, A. (2017). Annual Energy Outlook 2017. US Energy Information Administration.

Simmons, G., & Brace, W. F. (1965). Comparison of static and dynamic measurements of compressibility of rocks. *Journal of Geophysical Research*, *70*(22), 5649-5656.

Shapiro, S. A., Rothert, E., Rath, V., & Rindschwentner, J. (2002). Characterization of fluid transport properties of reservoirs using induced microseismicity. *Geophysics*, *67*(1), 212-220.

Slatt, R. M., & Abousleiman, Y. (2011). Merging sequence stratigraphy and geomechanics for unconventional gas shales. *The Leading Edge*, *30*(3), 274-282.

Soeder, D. J. (2018). The successful development of gas and oil resources from shales in North America. *Journal of Petroleum Science and Engineering*.

Sondergeld, C. H., & Rai, C. S. (2011). Elastic anisotropy of shales. *The Leading Edge*.

Sone, H. (2012). Mechanical properties of shale gas reservoir rocks, and its relation to the in-situ stress variation observed in shale gas reservoirs (Doctoral dissertation, Stanford University).

Sone, H., & Zoback, M. D. (2013a). Mechanical properties of shale-gas reservoir rocks—Part 1: Static and dynamic elastic properties and anisotropy. *Geophysics*.

Sone, H., & Zoback, M. D. (2013b). Mechanical properties of shale-gas reservoir rocks—Part 2: Ductile creep, brittle strength, and their relation to the elastic modulus. *Geophysics*, *78*(5), D393-D402.

Sone, H., & Zoback, M. D. (2014). Time-dependent deformation of shale gas reservoir rocks and its long-term effect on the in-situ state of stress. *International Journal of Rock Mechanics and Mining Sciences*, *69*, 120-132.

Standard, A. S. T. M. D4543-01,2001, "Standard Practices for Preparing Rock Core Specimens and Determining Dimensional and Shape Tolerances," ASTM International, West Conshohocken, PA.

Standard, A. S. T. M. D5777-00, 2011,"Standard Guide for Using the Seismic Refraction Method for Subsurface Investigation," ASTM International, West Conshohocken, PA.

Standard, A. S. T. M. D7012, 2014, "Standard Test Methods for Compressive Strength and Elastic Moduli of Intact Rock Core Specimens under Varying States of Stress and Temperatures," ASTM International, West Conshohocken, PA.

Stephenson, L. P., Plumley, W. J., & Palciauskas, V. V. (1992). A model for sandstone compaction by grain interpenetration. *Journal of Sedimentary Research*, 62(1).

Stimac, J., Nordquist, G., Suminar, A., & Sirad-Azwar, L. (2008). An overview of the Awibengkok geothermal system, Indonesia. *Geothermics*, *37*(3), 300-331.

Sumner, K.K., Camp, E.R., Huntington, K.W., Cladouhos, T.T., M., U., (2015). Assessing Fracture Connectivity using Stable and Clumped Isotope Geochemistry of Calcite. *Fortieth Workshop on Geothermal Reservoir Engineering*, Stanford Univ.

Swyer, M. W., Uddenberg, M., Nordin, Y., Cladouhos, T. T., & Petty, S. (2016). New Injection Strategies at Blue Mountain, Nevada Through Tracer Test Analysis, Injection-Production Correlation, and an Improved Conceptual Model. In *Proceedings of 41st Workshop on Geothermal Reservoir Engineering* (pp. 22-24).

Szewczyk, D., Bauer, A., & Holt, R. M. (2017). Stress-dependent elastic properties of shales—laboratory experiments at seismic and ultrasonic frequencies. *Geophysics Journal International*, 212(1), 189-210.

Tao, Q., Ghassemi, A., & Ehlig-Economides, C. A. (2011). A fully coupled method to model fracture permeability change in naturally fractured reservoirs. *International Journal of Rock Mechanics and Mining Sciences*, *48*(2), 259-268.

Tarasovs, S., & Ghassemi, A. (2010). A study of propagation of cooled cracks in a geothermal reservoir. In *Geothermal Resources Council Annual Meeting*, Sacramento (Vol. 34, pp. 428-431).

Taron, J., & Elsworth, D. (2010). Coupled mechanical and chemical processes in engineered geothermal reservoirs with dynamic permeability. *International Journal of Rock Mechanics and Mining Sciences*, 47(8), 1339-1348.

Templeton, D. C., Matzel, E., & Cladouhos, T. (2017). *Evolution of Microseismicity at the Blue Mountain Geothermal Site* (No. LLNL-CONF-732407). Lawrence Livermore National Lab.(LLNL), Livermore, CA (United States).

Tenthorey, E., Cox, S. F., & Todd, H. F. (2003). Evolution of strength recovery and permeability during fluid–rock reaction in experimental fault zones. *Earth and Planetary Science Letters*, 206(1), 161-172.

Tester, J. W., Anderson, B. J., Batchelor, A. S., Blackwell, D. D., DiPippo, R., Drake, E., ... & Petty, S. (2006). The future of geothermal energy: Impact of enhanced geothermal systems (EGS) on the United States in the 21st century. *Massachusetts Institute of Technology*, *209*.

Tien, Y. M., & Kuo, M. C. (2001). A failure criterion for transversely isotropic rocks. *International Journal of Rock Mechanics and Mining Sciences*, *38*(3), 399-412.

Toksöz, M. N., Cheng, C. H., & Timur, A. (1976). Velocities of seismic waves in porous rocks. *Geophysics*, *41*(4), 621-645.

Tomac, I., & Gutierrez, M. (2017). Coupled hydro-thermo-mechanical modeling of hydraulic fracturing in quasi-brittle rocks using BPM-DEM. *Journal of Rock Mechanics and Geotechnical Engineering*, 9(1), 92-104.

Torrence, C., & Compo, G. P. (1998). A practical guide to wavelet analysis. *Bulletin of the American Meteorological society*, *79*(1), 61-78.

Vermylen, J. P. (2011). *Geomechanical studies of the Barnett shale, Texas, USA*. Stanford University.

Villamor Lora, R., & Ghazanfari, E. (2014). Geomechanical Characterization of Shale Formations for Sustainable Production. In *Shale Energy Engineering 2014: Technical Challenges, Environmental Issues, and Public Policy* (pp. 133-143).

Villamor Lora, R. (2015). *Geomechanical Characterization of Marcellus Shale* (Doctoral Dissertation, University of Vermont).

Villamor Lora, R., Ghazanfari, E., & Izquierdo, E. A. (2016). Geomechanical characterization of Marcellus shale. *Rock Mechanics and Rock Engineering*, *49*(9), 3403-3424.

Vlastos, S., Liu, E., Main, I. G., Schoenberg, M., Narteau, C., Li, X. Y., & Maillot, B. (2006). Dual simulations of fluid flow and seismic wave propagation in a fractured network: effects of pore pressure on seismic signature. *Geophysical Journal International*, 166(2), 825-838.

Vogler, D., Amann, F., Bayer, P., & Elsworth, D. (2016). Permeability Evolution in Natural Fractures Subject to Cyclic Loading and Gouge Formation. *Rock Mechanics and Rock Engineering*, 49(9), 3463-3479.

Walton G., Hedayat A., Kim E., & Labrie D. (2017) Post-yield strength and dilatancy evolution across the Brittle–Ductile transition in Indiana limestone. *Rock Mechanics and Rock Engineering*, 50(7):1691-1710.

Wang, Z. (2001). Fundamentals of seismic rock physics. *Geophysics*, 66, 398-412.

Wang, T., Xu, D., Elsworth, D., & Zhou, W. (2016). Distinct element modeling of strength variation in jointed rock masses under uniaxial compression. *Geomechanics and Geophysics for Geo-Energy and Geo-Resources*, *2*(1), 11-24.

Wichtmann, T., & Triantafyllidis, T. (2009). Influence of the grain-size distribution curve of quartz sand on the small strain shear modulus G max. *Journal of Geotechnical and Geoenvironmental Engineering*, *135*(10), 1404-1418.

Witherspoon, P. A., Wang, J. S., Iwai, K., & Gale, J. E. (1980). Validity of cubic law for fluid flow in a deformable rock fracture. *Water Resources Research*, 16(6), 1016-1024.

Wong, I., Pezzopane, S., Dober, M., & Terra, F. (2010). Evaluations of induced seismicity/seismic hazards and risk for the Newberry volcano EGS demonstration. A report prepared by URS for AltaRock Energy Inc., CA, USA.

Xiong, Y., Hu, L., & Wu, Y. S. (2013, February). Coupled geomechanical and reactive geochemical simulations for fluid and heat flow in enhanced geothermal reservoirs. In *PROCEEDINGS, Thirty-Eighth Workshop on Geothermal Reservoir Engineering Stanford University*.

Xu, T., Sonnenthal, E., Spycher, N., Pruess, K., Brimhall, G., & Apps, J. (2001). Modeling multiphase non-isothermal fluid flow and reactive geochemical transport in variably saturated fractured rocks: 2. Applications to supergene copper enrichment and hydrothermal flows. *American Journal of Science*, 301(1), 34-59.

Xu, T., Ontoy, Y., Molling, P., Spycher, N., Parini, M., & Pruess, K. (2004). Reactive transport modeling of injection well scaling and acidizing at Tiwi field, Philippines. *Geothermics*, 33(4), 477-491.

Yang, S. Q. (2012). Strength and deformation behavior of red sandstone under multi-stage triaxial compression. *Canadian Geotechnical Journal*, *49*(6), 694-709.

Yang, J., & Gu, X. Q. (2013). Shear stiffness of granular material at small strains: Does it depend on grain size?. *Géotechnique*, *63*(2), 165.

Yang, Y., & Zoback, M. (2016). Viscoplastic deformation of the Bakken and adjacent formations and its relation to hydraulic fracture growth. *Rock Mechanics and Rock Engineering*, *49*(2), 689-698.

Yang, S. Q., Tian, W. L., & Ranjith, P. G. (2017). Experimental investigation on deformation failure characteristics of crystalline marble under triaxial cyclic loading. *Rock Mechanics and Rock Engineering*, *50*(11), 2871-2889.

Yasuhara, H., Elsworth, D., & Polak, A. (2004). Evolution of permeability in a natural fracture: Significant role of pressure solution. *Journal of Geophysical Research: Solid Earth*, 109(B3).

Yasuhara, H., Polak, A., Mitani, Y., Grader, A., Halleck, P., & Elsworth, D. (2005). Evolution of fracture permeability through reactive flow at elevated temperatures. *Transactions of Geothermal Research Council*, 29, 437-441.

Yasuhara, H., & Elsworth, D. (2006). A numerical model simulating reactive transport and evolution of fracture permeability. *International Journal for Numerical and Analytical Methods in Geomechanics*, 30(10), 1039-1062.

Yasuhara, H., & Elsworth, D. (2008). Compaction of a rock fracture moderated by competing roles of stress corrosion and pressure solution. *Pure and Applied Geophysics*, 165(7), 1289-1306.

Yasuhara, H., Kinoshita, N., Ohfuji, H., Lee, D. S., Nakashima, S., & Kishida, K. (2011). Temporal alteration of fracture permeability in granite under hydrothermal conditions and its interpretation by coupled chemo-mechanical model. *Applied Geochemistry*, 26(12), 2074-2088.

Youn, H., & Tonon, F. (2010). Multi-stage triaxial test on brittle rock. *International Journal of Rock Mechanics and Mining Sciences*, *47*(4), 678-684.

Yu, Y., Zhang, J., & Zhang, J. (2009). A modified Brazilian disk tension test. *International Journal of Rock Mechanics and Mining Sciences*, 46(2), 421-425.

Zang, A., Oye, V., Jousset, P., Deichmann, N., Gritto, R., McGarr, A., Majer, E., & Bruhn, D. (2014). Analysis of induced seismicity in geothermal reservoirs–An overview. *Geothermics*, 52, 6-21.

Zhou, X., Fan, L., & Wu, Z. (2017). Effects of Microfracture on Wave Propagation through Rock Mass. *International Journal of Geomechanics*, *17*(9), 04017072.

Zhuang, L., Kim, K. Y., Jung, S. G., Nam, Y. J., Min, K. B., Park, S., ... & Yoon, J. S. (2017, August). Laboratory evaluation of induced seismicity reduction and permeability enhancement effects of cyclic hydraulic fracturing. In *51st US Rock Mechanics/Geomechanics Symposium*. American Rock Mechanics Association.

Zhu, W., Baud, P., & Wong, T. F. (2010). Micromechanics of cataclastic pore collapse in limestone. *Journal of Geophysical Research: Solid Earth*, *115*(B4).

Zimmermann, G., & Reinicke, A. (2010). Hydraulic stimulation of a deep sandstone reservoir to develop an Enhanced Geothermal System: Laboratory and field experiments. *Geothermics*, 39(1), 70-77.

Zoback, M. D. (2010). *Reservoir geomechanics*. Cambridge University Press.

Zoback, M. D., & Byerlee, J. D. (1975). The effect of microcrack dilatancy on the permeability of Westerly granite. *Journal of Geophysical Research*, *80*(5), 752-755.

Zou, C., Dong, D., Wang, S., Li, J., Li, X., Wang, Y., Li, D., & Cheng, K. (2010). Geological characteristics and resource potential of shale gas in China. *Petroleum exploration and development*, 37(6), 641-6.

# APPENDIX A: MATERIALS FOR MECHANICAL CHARACTERIZATION OF SHALE ROCKS

West Virginia Geological and Economic Survey provided the shale plugs, which were retrieved from a deep well (~2270 m) drilled in Marcellus Shale formation in Morgantown, West Virginia (Figure A1.1a). The plugs were cored perpendicular to the bedding (Avary et al., 2008), and stored at room temperature and ambient humidity conditions (Figure A1.1b). Using these plugs, it was desired to extract several sub-cores, both perpendicular and parallel to the bedding planes, and with aspect ratios of close to 2. However, despite the fact that precautionary measures were taken during drilling, due to their brittle nature, we were only able to retrieve four sub-cores (diameter of 1.5 inches), with horizontal bedding planes (Figures A1.1c and A1.1d). Information about the depth, mineralogical composition (using X-Ray Diffraction (XRD) analysis), and dimensions of the retrieved specimens are provided in Tables 2.1 and 3.1. CL1, CL2, R3, and R4 specimens are clay-rich, while, CR1, CR2, R1, and R2 are calcite/quartz-rich, as indicated in Tables 2.1 and 3.1. The Scanning Electron Microscopy (SEM) images are provided in Figures A1.1e and A1.1f, which indicate presence of micro-cracks sub-parallel to beddings, void and inclusions. TOC was determined using sample combustion method (Passey et al., 2010) as 2.7%. The porosity of the specimens was estimated using the comparison between the bulk density of the specimen with average grain density (Mavko et al., 2009) obtained from XRD and TOC tests, and found to be on average close to 6%. It should be acknowledged that no attempt was made to re-hydrate the specimens, as they are very

brittle, and no information about the chemical composition of in-situ pore fluid was available.

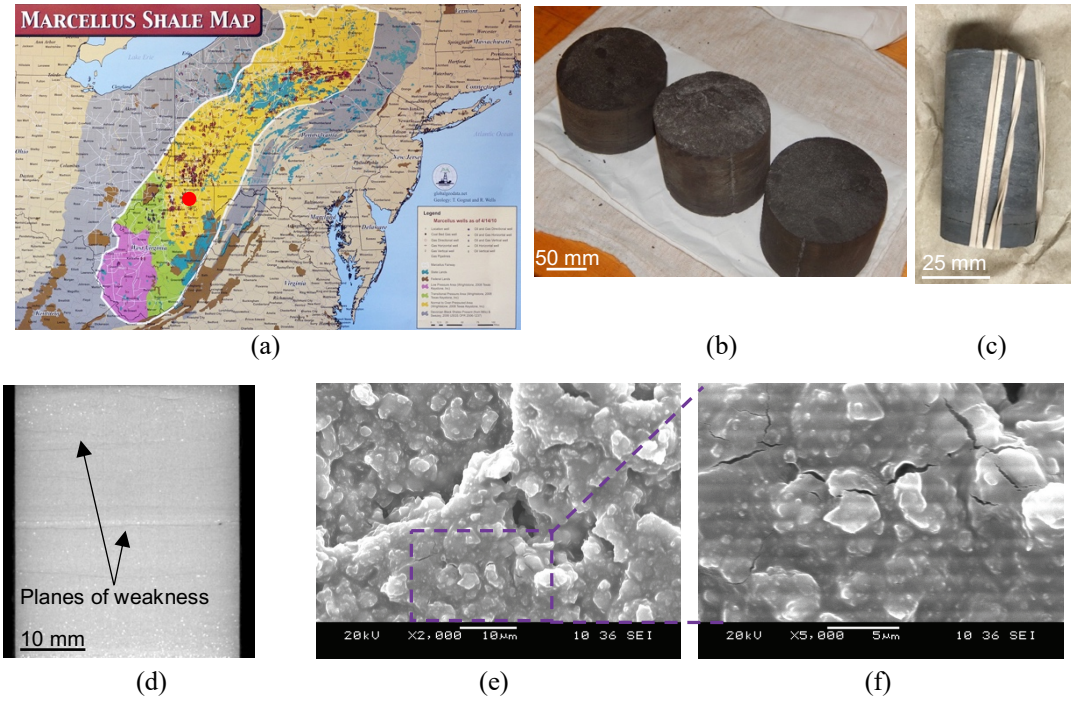


Figure A1-1. (a) location of drilled cores (West Virginia, EGSP well#6) as red dot superimposed on the map of Marcellus formation (Source: http://www.gallawaysafety.com/Marcellus-Shale-Map-Which-states-are-Impacted); (b) shale cores provided by West Virginia Geological and Economic Survey; (c) phot of a sub-cored specimen (1.5-inch diameter); (d) X-Ray CT image showing the bedding planes in sub-cored specimens; (e) and (f) scanning electron microscopy images showing different features including micro-fractures sub-parallel to the bedding, voids and inclusions (Note: Fig A1.1(f) is a magnified rectangular region of Figure A1.1(e)).

# APPENDIX B: SPECIMEN PREPARATION FOR MECHANICAL CHARACTERIZATION TESTS

For preparation of a rock specimen, ASTM D4543 standard was followed. After lapping the two ends of the specimen, it was wrapped in copper jacket (Figure A2.1a). Then, two pairs of axial and radial strain gauges, placed 90 degrees apart with respect to each other, were attached on the copper jacket as shown in Figure A2.1b. Then, the Vitton jackets were attached at the two ends of the copper-jacketed specimen. To improve the transmissivity of ultrasonic waves, couplant was used at the interface of rock and ultrasonic core holders. Finally, the prepared test column was mounted on the base plug (Figure A2.1c) to be placed inside the test vessel.

(a) (b) (c)

Figure A2-1. (a) photo of a sub-core specimen (1.5-inch diameter) wrapped in copper jacket; (b) prepared specimen with two pairs of strain gauges attached on the copper jacket (placed 90 degrees apart) and the two ends wrapped in Vitton jacket mounted on the base plug; (c) prepared specimen placed between the two ultrasonic core holders ready to be inserted into the test vessel.

# APPENDIX C: EXPERIMENTAL PROCEDURE FOR MECHANICAL CHARACTERIZATION TESTS

The mechanical testing of rock specimens was performed using AutoLab 1500 instrument (Figure A3.1a). Confining Pressure (CP) of up to 70 MPa, and Differential Stress (DS) of up to 580 MPa (for 1.5-inch diameter specimens) can be applied using this high-pressure fully servo-controlled triaxial equipment. The Linear Variable Differential Transformer (LVDT), which is attached to the loading piston, provides axial deformation of the specimen, in addition to those from axial strain gauges. The applied differential stress on the specimen is measured using the load cell located in the upper chamber of the test vessel. Both stress- and strain-control modes can be performed using the instrument. Figure A3.1b shows a schematic of the different components of AutoLab 1500.

During triaxial testing of the specimens, the ultrasonic P-wave and cross-polarized S-waves (perpendicular to the bedding planes) can be transmitted/received using ultrasonic transducers embedded in core holders. The pulse generator, manufactured by New England Research (NER) Inc., generates pulses with frequency of 10 pulses per second. The P- and cross polarized S-wave transducers, manufactured by NER, had a central frequency of 750 kHZ. Tektronix TDS 3000 Series Oscilloscope was used as digitizer. ASTM D5777 was followed in order to pick the arrival time of P- and S-waves, and subsequently, estimate the P- and S-wave velocities ($V_p$ and $V_s$).

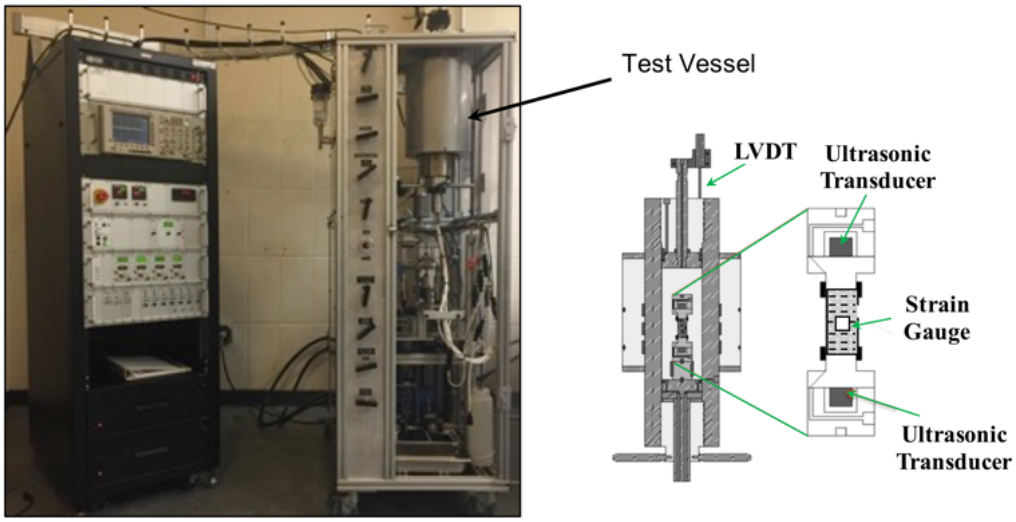


(a) (b)

Figure A3-1. (a) Autolab 1500 instrument, and (b) schematic of the specimen inside the test vessel.

# APPENDIX D: ESTIMATION OF STATIC AND DYNAMIC MODULI

Stress-strain curves can be used to estimate static moduli, and ultrasonic wave velocities can be used to estimate dynamic moduli (e.g. Fjar, 2008). When the characteristics of the material is symmetric about an axis normal to the plane of isotropy (e.g. Puzrin, 2012), the medium is referred to Vertical Transverse Isotropic (VTI). The linear elastic VTI theory, with z axis the symmetry axis, can be expressed with five elastic constants in a matrix representation format, shown in Eq. (A4.1):

$$\begin{Bmatrix} \varepsilon_{xx} \\ \varepsilon_{yy} \\ \varepsilon_{zz} \\ \varepsilon_{xy} \\ \varepsilon_{yz} \\ \varepsilon_{xz} \end{Bmatrix} = \begin{bmatrix} \frac{1}{E_h} & -\frac{\nu_{hh}}{E_h} & -\frac{\nu_{vh}}{E_v} & 0 & 0 & 0 \\ -\frac{\nu_{hh}}{E_h} & \frac{1}{E_h} & -\frac{\nu_{vh}}{E_v} & 0 & 0 & 0 \\ -\frac{\nu_{vh}}{E_v} & -\frac{\nu_{vh}}{E_v} & \frac{1}{E_v} & 0 & 0 & 0 \\ 0 & 0 & 0 & \frac{1}{G_{vh}} & 0 & 0 \\ 0 & 0 & 0 & 0 & \frac{1}{G_{vh}} & 0 \\ 0 & 0 & 0 & 0 & 0 & \frac{2(1+\nu_{hh})}{E_h} \end{bmatrix} \times \begin{Bmatrix} \sigma_{xx} \\ \sigma_{yy} \\ \sigma_{zz} \\ \sigma_{xy} \\ \sigma_{yz} \\ \sigma_{xz} \end{Bmatrix} \quad \text{(A4.1)}$$

$\nu_{\mathrm{vh}}$ and $E_{\mathrm{v}}$ are Young's modulus and Poisson's ratio in vertical direction (Figure A4.1b), $\nu_{\mathrm{hh}}$ and $E_{\mathrm{h}}$ are Young's modulus and Poisson's ratio in horizontal direction (Figure A4.1c), and $G_{\mathrm{vh}}$ is the shear modulus in the vertical plane (Figure A4.1d). Shale specimens can be modeled as VTI medium at the macroscopic scale (Villamor Lora et al., 2016).

In a triaxial test, stress and strain relationship can be expressed as (Puzrin, 2012):

$$\begin{Bmatrix}\delta\varepsilon_a\\ \delta\varepsilon_r\end{Bmatrix}=\begin{bmatrix}1/E_{\mathrm{v}} & -2\,\nu_{\mathrm{vh}}/E_{\mathrm{v}}\\ -2\,\nu_{\mathrm{vh}}/E_{\mathrm{v}} & -(1-\nu_{\mathrm{hh}})/E_{\mathrm{h}}\end{bmatrix}\begin{Bmatrix}\delta\sigma_a\\ \delta\sigma_r\end{Bmatrix} \tag{A4.2}$$

where $\varepsilon_a$ and $\varepsilon_r$ are axial and radial strains, respectively; $\sigma_a$ and $\sigma_r$ are axial and radial stresses, respectively. To study the anisotropic response of a VTI material in a triaxial test, and to estimate shear/coupling moduli, Eq. (A4.1) can be re-written as (Puzrin, 2012):

$$\begin{Bmatrix}\delta\varepsilon_v\\ \delta\varepsilon_s\end{Bmatrix}=\begin{bmatrix}1/K & -1/J\\ -1/J & 1/3G\end{bmatrix}\begin{Bmatrix}\delta p\\ \delta q\end{Bmatrix} \tag{A4.3}$$

where $\varepsilon_v$ is the volumetric strain; $\varepsilon_s$ is the distortional strain; $p$ is the mean stress; $q$ is the differential stress; and, $K$, $J$, and $G$ are bulk, coupling, and shear moduli, respectively.

For static measurements, bulk ($K$) and coupling ($J$) moduli can be estimated based on the stress-strain curve during the hydrostatic stage of the experiment (as depicted in Figures A4.1e and A4.1f), while, Poisson's ratio ($\nu$), and Young's ($E$) modulus can be estimated using the stress-strain curve during the triaxial stage of the experiment (as shown in Figures A4.1g and A4.1h). In this study, $K$ and $J$ were estimated from isotropic compression (hydrostatic) stage of creep tests on CL1 and CR1 specimens. It should be acknowledged that at small differential stress levels, some irreversible deformations occur in the specimen. Therefore, to avoid elastic term for the reported moduli, we refer to them as static moduli (Fjar, 2008). For an elastic, homogeneous, and isotropic material, dynamic moduli can be estimated using ultrasonic wave velocities, expressed as (Zoback, 2010):

$$E_{\mathrm{v}}=\frac{\rho V_S^2(3V_P^2-4V_S^2)}{V_P^2-V_S^2} \tag{A4.4}$$

$$\nu_{\mathrm{vh}} = \frac{V_P^2 - 2V_S^2}{2(V_P^2 - V_S^2)} \tag{A4.5}$$

$$G_{\mathrm{vh}} = \rho V_S^2 \tag{A4.6}$$

where $E_{\mathrm{v}}, G_{\mathrm{vh}}$ and $\nu_{\mathrm{vh}}$ are, Young's and shear moduli, and Poisson's ratio in the vertical direction, respectively; $V_p$ and $V_s$ are P- and S-wave velocities in the vertical direction, respectively; and $\rho$ is the bulk density of the material (Zoback, 2010). The measured P- and S-wave velocities in the vertical direction at different stress levels along the stress path were used to estimate the dynamic moduli of rock specimens using Eqs. (A4.4) - (A4.6).

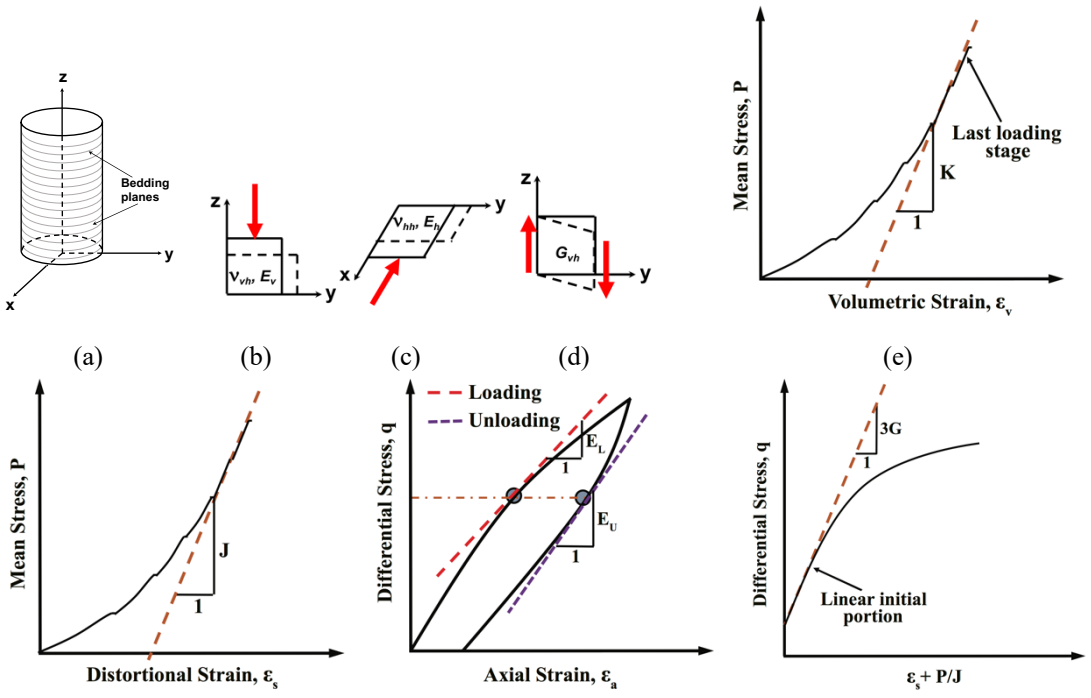


Figure A4-1. Schematics of: (a) VTI medium with the z-axis being the symmetry axis, (b) Poisson's effect in vertical direction, (c) Poisson's effect in horizontal direction, (d) shearing in vertical plane, (e) bulk modulus, and (f) coupling modulus are estimated using the tangent modulus from the stress-strain response during the isotropic compression stage; (g) Young's modulus (tangent) during loading/unloading; and (h) shear modulus (tangent) using the initial portion of the stress-strain curve during triaxial stage (adapted and modified from Villamor Lora et al., 2016).

# APPENDIX E: WAVELET TRANSFORM

Wavelets are defined as basis functions that are used to decompose the signals and extract their time and frequency content. Unlike the short-time Fourier transform, CWT takes advantage of variable time-frequency resolution to provide accurate representations at both low and high ends of the considered frequency range (e.g. Daubechies, 1992; Torrence and Compo, 1998; Farzampour et al., 2018a,b). In addition, a rather large selection of available basis wavelets makes CWT more versatile in decomposing various signals. Consider an analytic signal $z(t)$ with both time-varying amplitude $A(t)$ and phase $\phi(t)$ over time given by:

$$z(t) = A(t)e^{i\phi(t)} \tag{A5.1}$$

The standard form of the CWT of this signal is then defined as (Daubechies, 1992):

$$W_{a,b}(z) = \langle z(t), \psi_{a,b}(t) \rangle = \int_{-\infty}^{\infty} z(t)\psi^{*}_{a,b}(t)\mathrm{d}t \tag{A5.2}$$

where $\psi_{a,b}$ is the basis wavelet. In this equation, the asterisk superscript denotes complex conjugate. The parameters a and b are called the scale and shift parameters, respectively. This transform is named continuous in the sense that the scales are chosen in a continuous fashion. The basis wavelet $\psi_{a,b}(t)$ is defined as:

$$\psi_{a,b}(t) = \frac{1}{\sqrt{a}}\psi\left(\frac{t-b}{a}\right) \tag{A5.3}$$

in which the term $1/\sqrt{a}$ is used in order to normalize the energy of the basis wavelet at all scales and ψ(.) is the square-integrable, zero-mean and admissible mother wavelet (e.g. Daubechies, 1992). It can be observed that the basis wavelet is a dilated and shifted version of mother wavelet that facilitates the decomposition of signals into a set of wavelets at different scales and times (e.g. Torrence and Compo, 1998). In fact, like any other convolution-based transform, CWT correlates the signal with a set of scaled and shifted wavelets through coefficients that represent the similarity between the signal and the wavelet at a particular scale and time (e.g. Daubechies, 1992). This leads to a scalogram of the square moduli of the coefficients, where the scales are inversely related to frequencies. Time-frequency maps can then be extracted from these scalograms. The time and frequency resolutions of the transform are given by:

$$\Delta t_{\psi(a)} = |a| \Delta t_{\psi} \tag{A5.4}$$

$$\Delta \omega_{\Psi(a)} = \frac{\Delta \omega_{\Psi}}{|a|} \tag{A5.5}$$

where $\Delta t_{\psi}$ and $\Delta \omega_{\Psi}$ are time and frequency resolutions of mother wavelet, and $\Delta t_{\psi(a)}$ and $\Delta \omega_{\Psi(a)}$ are time and frequency resolutions of the baby wavelet at scale a, respectively. Based on the Heisenberg's uncertainty principle, these values are limited to:

$$\Delta t_{\psi} \Delta \omega_{\Psi} \geq \frac{1}{2} \tag{A5.6}$$

Eq. (A5.6) implies that the time and frequency resolutions cannot be arbitrarily high.

# APPENDIX F: EXPERIMENTAL PROCEDURE FOR FLOW-THROUGH TESTS

AutoLab 1500 instrument, housed in the Geo-energy Laboratory at the Department of Civil and Environmental Engineering, University of Vermont, a high-pressure/temperature fully servo-controlled triaxial equipment capable of applying Confining Pressure (CP) and pore pressure of up to 70 MPa, and temperatures of up to 130 °C (modified O-rings/sealings allows safe operation of flow experiments at temperatures of up to 130 °C), was used to perform the flow-through experiments (Figure A6.1a). During the experiments, downstream and upstream pore pressure intensifiers were used to apply the desired pore pressures with a resolution of 10 Pa. The instrument enables performing flow-through experiments with constant injection rate (i.e. displacement control) or constant pore pressure (i.e. pressure control) with a precision of ±0.1 MPa and errors of ±0.2 %. The pore pressure intensifiers are also equipped with linear variable differential transformers (LVDTs) that allow continuous monitoring of the amount of injected fluid.

Prior to the experiment, all pore pressure tubings were cleaned using alcohol and hot soapy water. Before initiating each experiment, the fractured rock specimen was saturated by placing it in a desiccator filled with deionized water under vacuum for 7 days. Weights were measured until the weight change was equal or less than 0.005 g (scale precision). The gain in the weight of the specimen before and after saturation was calculated and used to ensure that saturation was achieved. A Vitton jacket was then wrapped around the specimen, followed by placing the jacketed specimen between the two core holders (Figure A6.1b). Then, the mounted specimen was placed into the test vessel

(Figures A6.1a and A6.1c). Pore pressure tubes were then vacuum-saturated with circulating fluid to ensure that there is no air in the system prior to flow initiation. Then flow-through tests are performed in two modes of displacement- and pressure-controlled.

In displacement-controlled test (DCT), downstream pore pressure and upstream injection rate are set as prescribed values and the evolution of upstream pore pressure is used to estimate permeability evolution. On the other hand, in pressure-controlled test (PCT), both downstream and upstream pore pressures are set as prescribed values and the outflow rate is used to estimate permeability evolution. Using the temperature control module of the instrument, the desired temperature is applied to the test vessel. The temperature of the injected fluid is controlled using an electrical heat band wrapped around the upstream pore pressure tubing before entering the fractured specimen (Figure A6.1d). It should be acknowledged that although the temperature of the test vessel (reflecting the temperature of the rock specimen) was continuously measured during the experiments, the temperature of the electrical heat band wrapped around the upstream pore pressure tubing (reflecting the temperature of the injected fluid) was not recorded during the experiments. In addition, it should be acknowledged that the fluctuations in the laboratory room temperature affects the temperature of the rock specimen and the injected water and that the reported temperatures do not reflect these fluctuations.

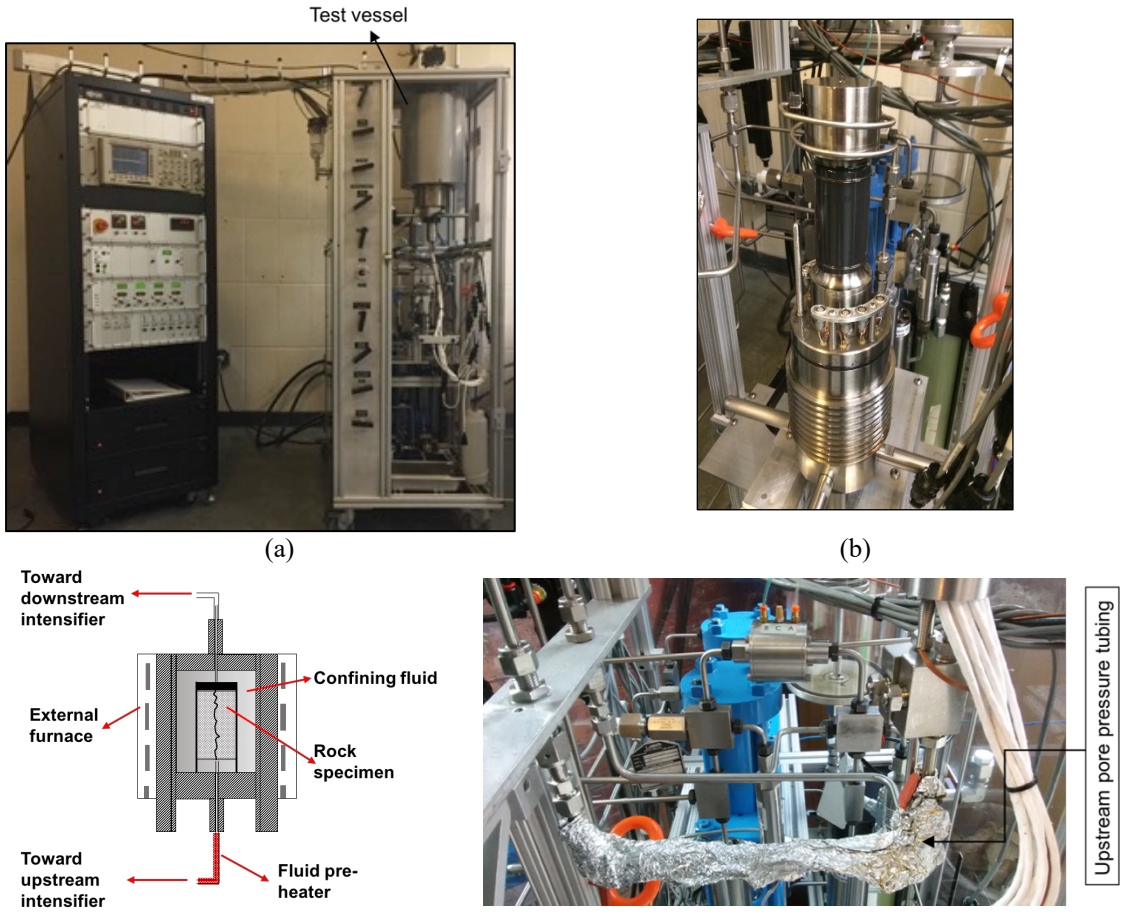


Figure A6-1. (a) AutoLab 1500 equipment, (b) jacketed specimen between the upstream and downstream core holders outside the test vessel, (c) schematic of the rock specimen in the test vessel, and (d) the electrical heat band wrapped around the upstream pore pressure tubing to control the temperature of injected fluid

# APPENDIX G: ESTIMATION OF HYDRAULIC FRACTURE AND FRACTURE PERMEABILITY

The pore pressure measurements during the experiments were used to estimate the permeability using Darcy's law expressed as:

$$k = \frac{Q\mu L}{A\Delta P} \tag{A7.4}$$

where, $Q$ is the flow rate ($m^3/sec$), $\mu$ is the dynamic viscosity of the fluid ($Pa.s$), $L$ is the length of the specimen ($m$), $A$ is the cross-section area of the specimen ($m^2$), and $\Delta P$ is the differential pore pressure across the two ends of the specimen ($Pa$).

Since the specimens had very low porosity (i.e. 0.72%), with virtually-impermeable matrix, the modified cubic law with parallel plate approximation was used to evaluate the hydraulic aperture expressed as (Whiterspoon et al., 1980; Polak et al., 2003):

$$b = \sqrt[3]{\frac{12\mu LQ}{\Delta P.D}} \tag{A7.5}$$

where $b$ is the hydraulic aperture ($m$), and $D$ is the diameter of the specimen ($m$).

# APPENDIX H: MATERIALS AND SPECIMEN PREPARATION FOR FRACTURED PHYLLITE SPECIMENS USED IN FLOW-THROUGH TESTS

Phyllite rock core, shown in Figure A8.1 was retrieved from DB-2 well (depth of 1260 m) at Blue Mountain geothermal field (Nevada, USA) and sub-cored to obtain a rock specimen with a diameter of 38 mm, and a length of 49 mm. The rock had a dry density of 2.69 g/cm$^3$ and porosity of 0.74%. The X-Ray Diffraction (XRD) analysis indicated that the rock contained 67.4% quartz, 18.8% albite, 10.5% biotite, and 3.2% chlorite. The specimen was saw-cut, and the two ends were lapped to 0.001 inches. A modified Brazilian test (Yu et al., 2009) was performed to induce a longitudinal tensile fracture in the specimen (Figure A8.1).

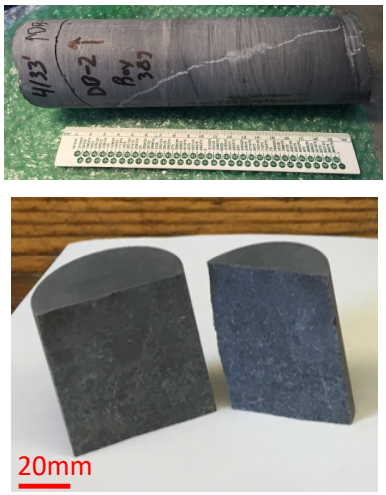


Figure A8-1. Photos of the core rock and fractured phyllite specimen

The fracture surface was characterized using SkyScan 1173 X-Ray micro-CT instrument. Figure A8.2 shows 3D images of the two halves of the fractured specimen and

the generated surface profiles. The fractured specimen was placed in a desiccator filled with deionized water under vacuum condition. To ensure the full saturation of the specimen, weights were measured every day until the change in weight was equal to or less than 0.005 g (scale precision).

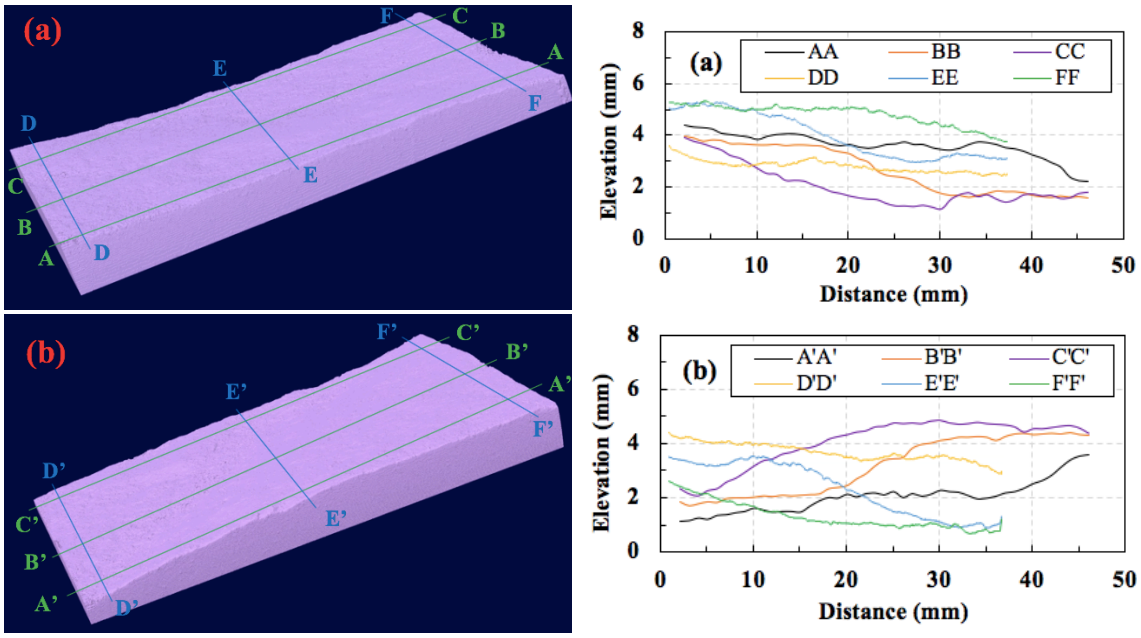


Figure A8-2. 3D surface maps and surface profiles of: (a) fracture surface 1, and (b) fracture surface 2. Lines AA, BB and CC are the lines along which the surface profiles are taken. Lines AA and CC are 3 mm inside the corresponding edges, while line BB is at the center of the surface. Similarly, lines DD and FF are 5 mm inside the corresponding edges, while line EE is at the center.

# APPENDIX I: PROPAGATION OF SEISMIC WAVES IN FLOW-THROUGH TESTS

We used P, $S_1$, and $S_2$ transducers (Boston Piezo-Optics Inc.) of 22.2 mm diameter and 2 mm (for P) and 1 mm (for S) thickness, respectively, with a Tektronix TDS 3000 Series Oscilloscope digitizer. The central frequency was set to 750 kHz with a pulse generation and acquisition rate of 10 $s^{-1}$. ASTM D5777 Standard was used to manually pick the arrival time of P- and cross-polarized S-waves, which were then used for estimation of P- and S-waves velocities ($V_P$, $V_{S1}$, and $V_{S2}$). In addition to velocities, the amplitudes, attenuations, and time-frequency analysis provide indications of the change in ultrasonic properties (e.g. Cook, 1992; Brajanovski et al., 2006; Kamali-Asl et al., 2018d). The amplitude of first-peak in time-domain for P- and cross-polarized S-waves at each of the recording points (i.e. each half-an-hour) throughout flow-through experiments were recorded. Then, these maximum amplitudes were normalized using their first value (i.e. at $t \sim 0.5$ h).

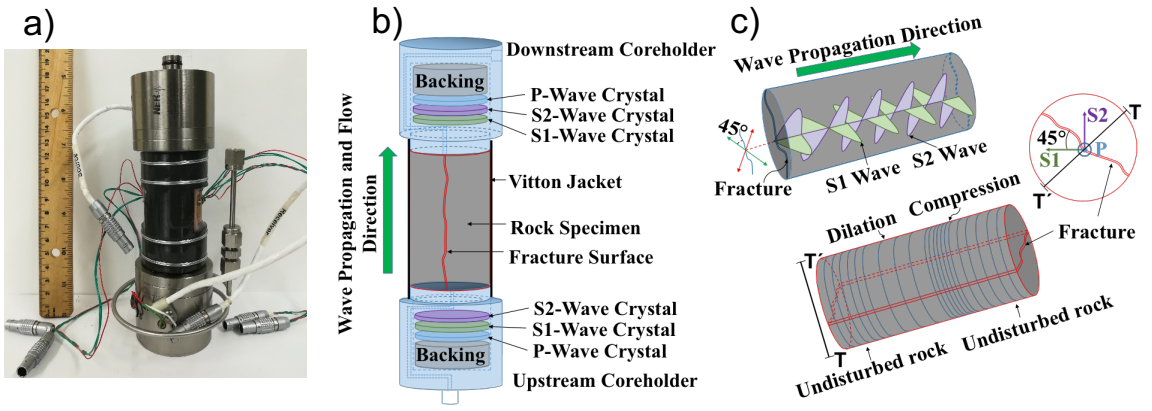


Figure A9-1. Schematics of (a) jacketed fractured specimen placed between the two core-holders, (b) the configuration of P, $S_1$, and $S_2$ piezo-ceramics in top and bottom core-holders, and (c) direction of propagation of P-, $S_1$-, and $S_2$-waves in the fractured specimen.